A Comprehensive Finite Element Model of the Human Masticatory System

Zur Erlangung des akademischen Grades eines
DOKTOR-INGENIEURS
von der Fakultät für
Bauingenieur-, Geo- und Umweltwissenschaften
des Karlsruher Instituts für Technologie (KIT)
genehmigte
DISSERTATION
von
M.Sc. Simon Ernesto Martinez Choy
aus Merida, Venezuela

Tag der mündlichen Prüfung: 13.03.2018

Hauptreferent:	Prof. Karl Schweizerhof
Korreferent:	Prof. Hans J. Schindler
Korreferent:	Prof. Oliver Röhrle

Karlsruhe -

Abstract

Understanding the role and mutual influence of the different components of the masticatory system during biting tasks is crucial for the improvement of the occlusal configuration of antagonistic teeth concerning CAD/CAM produced tooth reconstructions. The aim of this thesis is the creation of a comprehensive model of the stomatognathic system, which permits the reproduction of mandibular movements during the chewing act, including the micromovements of the teeth. The numerical model is based on the finite element method (FEM), which makes use of an explicit scheme for time discretization. The different tissues are represented by both, linear and non-linear material models, while contact is defined between the articular surfaces of the temporomandibular joint. A detailed explanation of the construction of the model is given, which includes the creation of the geometry of each component, the assembly process, the meshing process, and, finally, the proper allocation of material laws. Studies regarding the mineral tissue of the system focus on the first and third principal stresses developed in the mandibular bone during bilateral and unilateral biting as well as incisive biting. An analysis of tooth mobility while biting a deformable bolus is carried out for both, molar and incisive teeth, employing two different hyperelastic material models that lead to realistic force-displacement results. Since in soft tissues compressive loads are handled through a different mechanism than tensile loads, first and third principal stresses are investigated. A study of the performance of the temporomandibular joint follows, which gives attention to the behavior of the different attachments, and to the distribution of loads between the teeth and the joints, when different bite conditions are introduced in the mandible. Stress distributions in the articular disc are studied under several conditions, as well. A study of the role of the muscles ensues, regarding both the production of force as well as their passive reaction to stretching. Since investigations in the literature show a large variety of parameters for the muscles, multiple configurations are investigated involving different characteristic curves for the active and passive behavior of the muscles. Additionally, the kinetic mastication process is reproduced with the help of experimental data concerning the kinematics of the jaw and the measured electrical activity of the muscles during different biting tasks. Finally, the evolution of the movements and the forces on the teeth while in contact with the bolus, is investigated. In particular, the chewing simulations provide insight into the short-range kinetic interactions between antagonistic teeth during mastication, thus representing data of essential importance for ensuring interference-free fixed dental reconstructions. Furthermore, the model allows to examine the effect of rigid spacers between the jaws on the stress patterns in the articular discs, thus delivering information on the mechanism of various occlusal support conditions in the context of prosthetic reconstructions and splint therapy.

Kurzfassung

Das Verständnis der Rolle und der gegenseitigen Beeinflussung der verschiedenen Komponenten des Kausystems bei Beiaufgaben ist zur Verbesserung der okklusalen Konfiguration von antagonistischer Zähne bei CAD / CAM-hergestelltem Zahnrekonstruktionen wichtig. Das Ziel dieser Arbeit ist die Erstellung eines umfassenden Modells des stomatognathen Systems, das die Reproduktion der Unterkieferbewegungen beim Kauakt einschlielich der Mikrobewegungen der Zähne ermöglicht. Das numerische Modell basiert auf der Finite-Elemente-Methode (FEM), bei Verwendung eines expliziten Schemas für die zeitliche Diskretisierung. Die verschiedenen Gewebe werden sowohl durch lineare als auch nichtlineare Materialmodelle repräsentiert. Auch der Kontakt zwischen den Gelenkflächen des Kiefergelenks wird durch entsprechende Definierung erlass. Zum genauen Verständnis wird eine detaillierte Erklärung der Konstruktion des Modells gegeben, die die Erzeugung der Geometrie jeder Komponente, den Montageprozess, den Vernetzungsprozess und schlielich die korrekte Zuordnung der Materialgesetze beinhaltet. Untersuchungen des mineralischen Bestandteiles des Systems konzentrieren sich auf die ersten und dritten Hauptspannungen, die im Unterkieferknochen beim beidseitigen und einseitigen Beien entwickelt werden. Eine Analyse der Zahnbeweglichkeit während des Beiens eines verformbaren Bolus wird sowohl für Molaren als auch für Schneidezähne durchgeführt, die zu realistischen Kraft-Verschiebungs-Ergebnissen führen. Da in weichen Geweben Druckbelastungen mittels eines verschiedenen Mechanismus als Zugbelastungen gehandhabt werden, werden die ersten und dritten Hauptspannungen untersucht. Es folgt eine Untersuchung des Verhaltens des Kiefergelenks, die auf die Interaktion der verschiedenen Attachments und auf die Verteilung der Lasten zwischen den Zähnen und den Gelenken eingeht, wenn im Unterkiefer verschiedene Einschränkungen eingeführt werden. Spannungsverteilungen in den Zwischengelenkscheiben werden ebenfalls unter verschiedenen Bedingungen untersucht. Eine Untersuchung der Rolle der Muskeln wird durchgeführt, die sowohl die Krafterzeugung als auch ihre passives Reaktion auf Dehnung betreffen. Da Untersuchungen in der Literatur eine groe Vielzahl von Parametern für die Muskeln beinhalten, werden mehrere Konfigurationen studiert, die über verschiedene charakteristische Kurven das aktive und passive Verhalten der Muskeln abbilden. Zusätzlich wird der kinetische Kauvorgang mit Hilfe von experimentellen Daten bezüglich der Kinematik des Kiefers und der gemessenen elektrischen Aktivität der Muskeln während verschiedener Beiaufgaben reproduziert. Schlielich wird die Entwicklung der Verschiebungen der Zähne sowie der Kräfte auf die Zähne während des Kontakts mit dem Bolus untersucht. Für die klinische Nutzung geben die Kausimulationen einen Einblick in die kurzen kinetischen Wechselwirkungen zwischen antagonistischen Zähnen während des Kauens und liefern so Daten von essentieller Bedeutung, um störungsfreie fixe Zahnrekonstruktionen zu gewährleisten. Darüber hinaus erlaubt das Modell, die Wirkung von starren Abstandshaltern zwischen den Kiefern auf die Spannungsverteilungen in den Zwischengelenkscheiben zu untersuchen. Damit liegen umfängliche Informationen über den Mechanismus verschiedener okklusaler Auflagerbedingungen im Zusammenhang mit prothetischen Rekonstruktionen und einer Schienentherapie vor.

Acknowledgements

The present thesis was completed during research work at the Institute of Mechanics of the Karlsruhe Institute of Technology. Financial support for this research was provided by the German Federal Ministry of Economics and Technology as part of an AIF project, carried out from 2012 until 2014, according to a decision of the German Bundestag. At the end of this project, further financial support was provided by Zebris Medical GmbH Isny, Prof. Karl Schweizerhof, Prof. Hans J. Schindler and the Deutsche Forschungsgemeinschaft (DFG) under grants SCHM 2456/5-1 and SCHW 307/30-1. I am very grateful for all these contributions, which allowed the successful completion of this thesis.

First, I wish to thank Prof. Dr.-Ing. Karl Schweizerhof, as my main supervisor and referee. I express my sincere gratitude for his essential suggestions and discussions of diverse technical aspects of this study. I also acknowledge his generous support and motivation for the completion of the present work.

I would like to express my sincere gratitude to Prof. Dr. med. Hans J. Schindler, as supervisor and co-reviewer. His dedication and personal interest to cooperate with the engineering field produced critical data for the calibration and validation of the current work. His guidance and discussions of the medical aspects of the work were also invaluable for this study.

I am extremely grateful to Dr. rer. nat. Jürgen Lenz for his role as a supervisor, offering his expertise and scientific guidance, as well as holding numerous discussions of different aspects of the work. On addition to his scientific input, he scrutinized this thesis in order to polish its writing and presentation. His efforts made a very large impact in this work.

I wish to thank Prof. Dr. rer. nat. Oliver Röhrle for carefully reviewing this work and for his numerous suggestions, as well as for accepting to be a co-reviewer. I thank Prof. Dr.-Ing. habil Peter Betsch and Prof. Dr.Ing habil. Thomas Seelig for being my examiners.

I am grateful to PD Dr. habil. Alexander Konyukhov for standing as an examiner and for his helpful guidance in the field of contact mechanics.

I would like to express special thanks to Christopher Fingerhut with whom I collaborated closely at the initial stages of this work. Due to his guidance and support as well as the numerous insightful conversations we held, some of the most difficult challenges of this research were resolved.

Furthermore, I wish to express my thanks to all the members of the Institute of Mechanics at the Karlsruhe Institute of Technology. I would like to express additional thanks to Michael Strobl, Ridvan Izi, Christoph Schmied and Marlon Franke for their kind support and help. I am especially grateful to Rosemarie Krikis and Gabriele Herrmann for their administrative support and friendly assistance.

Finally, I thank my family for the loving support they have provided throughout my life. I will always be grateful to my parents for their motivation and encouragement during my studies. Most of all, I wish to thank my wife Maria, who is both my greatest source of inspiration and the driving force of my life. Thanks to her warm

affection and kind support, I have been able to overcome the most difficult challenges in my life.

Karlsruhe, July 2018 Simon Ernesto Martinez Choy

Contents

List of Figures

Introduction

The main function of the human masticatory system is to process food in order to make it edible. This process, known as mastication, begins with the transfer of food from the tongue to the teeth, subsequently broken down through rhythmic chewing, finalizing the process with clearance and swallowing. Mastication is mostly an unconscious act, controlled by a motor program that continuously adapts to changes in the stomatognathic system, such as tooth loss or introduction of dental implants. Over decades the kinematic behavior of the system was investigated and the revealed data implemented in the reconstruction of missing or lesioned teeth. However, the kinetics of the chewing system are not accessible to direct measurements, but have to be studied based on realistic models of the complete system. Such comprehensive models are currently not available. The goal of this thesis is the creation of a comprehensive model of the stomatognathic system in order to expand the available knowledge substantially regarding the role and influence of the different components of the masticatory system during biting, especially to improve the occlusal configuration of antagonistic teeth regarding CAD/CAM produced tooth reconstructions. In particular, micromovements in the near range of intercuspation are of essential interest in this context in order to avoid interferences during the chewing act.

The human masticatory system is composed of several structures: the mandibula, the maxilla, the temporomandibular joint (TMJ), the teeth, the periodontal ligament (PDL), and the masticatory muscles. The maxilla (upper jaw) is attached to the bones that form the skull. The mandible (lower jaw) is attached to the skull via the temporomandibular joints (TMJ) and muscles. The mandible moves with respect to the skull via the mastication muscles. The mandible and the maxilla have teeth attached which are used for cutting and grinding foodstuffs during the mastication process. The teeth themselves are attached to the alveolar bone through the periodontal ligament (PDL).

These components have been extensively studied in the literature. Many of these studies focus on a single component, generally ignoring or greatly simplifying the rest of the system. A significant number of these studies show discrepancies in their results. Additionally, some authors do not display enough data to allow for a meaningful comparison. The current state is, however, understandable: The sheer complexity of the masticatory system generates difficulties for the commonly employed tests to measure material behavior. Proper tests require deep understanding of the diverse parts that compose it, which demands cooperation between the fields of medicine and physics.

The TMJ is one of the most complicated joints of the human body. It is composed

mainly of the articular disc, the temporal fossa, the condyles, the capsule and the cartilage layers of the condyles and the fossa. These components have their own unique roles and behaviors during the complex movement the TMJ undergoes during chewing and biting. The articular disc is composed of a solid and fluid phase, the fluid phase handling most of the loads during compression and dissipating the energy from sudden loads. The fluids in the disc flow through the collagen fibers of the solid phase, whose permeability changes depending on the arrangement and strain of the fibers. This behavior has been modeled in the literature with linear elastic, hyperelastic, viscoelastic and multi-phase models. Even if the same material models are employed, parameters may greatly vary between authors. Further complications can be found in the validation process: experimental data are limited, in vivo measurements of strains and stresses may be difficult to produce, a large amount of samples is required due to the variation between patients, and so forth. Similar challenges can be found for the remaining tissues that compose the TMJ.

Comparable problems are connected with the remaining components of the masticatory system. The PDL, which has a similar composition as the articular disc, possesses also a liquid and solid phase which work together to optimally handle the loads on the tooth. So far material tests on this tissue only capture the response of the collagen fibers and ignore the load-bearing capacity of its fluid. The PDL, in particular, shows large discrepancies in both, material models and stiffness parameters. Several approaches to model the muscles can be found in the literature. When the sole aim is to place the muscle forces on the model, then the muscles' geometries are usually omitted by directly prescribing the forces as boundary conditions. One of the most prevalent approaches is to use Hill's muscle model in order to capture the characteristic passive and active behavior of the muscles. More sophisticated models may include the volume and the orientation of the muscle' fibers. Lastly, the bone material parameters find better agreement in the literature, although most authors do not incorporate its anisotropic behavior.

The introduction of numerical models allows the estimation of strains, stresses and loads experienced by the masticatory system. However, additional challenges intrinsic to the modeling process must also be considered. Older models suffered from the limitations of the existing technology: geometries needed to be simplified and the number of elements reduced in order to achieve reasonable computational time. Current segmentation softwares permit the generation of realistic geometries from CT-scans of patients. The increasingly available computational power allows for more complex and refined models to be run, improving the accuracy of the obtained solutions. The creation of a numerical model is still, however, a complicated process: incorporating slight changes that modify the geometry require remeshing most of the model, and thus several definitions such as boundary conditions as well as node and segment sets. As the model increases in complexity, errors and numerical insta-

bilities are introduced which become more difficult to find as the input file increases in size.

This work aims to provide a meticulous description of the modeling process, the comparison of the results obtained when using different parameters provided by the literature, and the relationship between the different components of the masticatory system.

In **Chapter 1** the fundamentals of continuum mechanics, required to define the equations of balance of our structural problem, are introduced. Afterwards, the basics of finite element method (FEM) are explained, focusing on the elements and time discretization used in the model. Employed material models are then defined, which requires concepts from hyperelasticity and rheology to be defined. The chapter ends with an overview of contact mechanics with emphasis on the options that produced optimal results for the simulation.

Chapter 2 covers the process of creating a geometry from the CT-scan of a patient. A detailed explanation of the required steps with the different programs is presented in order to obtain a high quality geometry. This geometry is afterwards converted into a compatible format with standard CAD software. The creation of components which could not be obtained with the standard process, e.g those not visible in the CT-scan, are subsequently covered. The chapter continues by showing the generation of the mesh, the types of element formulation for each component, the boundary conditions and the contact definitions. A general survey of the model is shown at the end of the chapter.

Chapter 3 describes the mechanical properties of bone, specifically those of mandibular bone. The literature concerning the stiffness parameters for both, cortical and spongy bone, is presented. Since the capacity of the bones to resist compressive forces are significantly higher than their capacity to resist tensile forces, the simulations in this chapter focus on the first and third principal stresses of the jaw during bilateral and unilateral molar biting as well as incisive biting.

Chapter 4 provides an overview of the mechanical behavior of the PDL and explains the source for the discrepancies of the available material models and parameters in the literature. The chapter describes the calibration of a material model that achieves realistic force-displacement results for different teeth as well as for different tasks. The material model is compared to other models in the literature that also produce accurate results. The behavior of the PDL is studied with purely axial and horizontal forces, during incisive as well as unilateral molar biting. Since failure of the collagen fibers of the PDL occurs during tension, the first and third principal stresses in the tissue are presented.

Chapter 5 depicts the temporomandibular joint, detailing the mechanical behavior and motional scope of its different components. Since several tissues of the joint are

not visible in the CT-scans, the different strategies employed to model each of the components are explained. The behavior of the different components of the joint is then calibrated through the enforcement of proper movement of the jaw during tasks such as jaw opening and strong biting forces. A specific study is finally performed to study the forces on the joints when small variable gaps are introduced that disturb the balance between the joint.

In **Chapter 6** the masticatory muscles are introduced. At first, an overview of the literature is presented regarding the characteristic behavior of the muscles. Hill's muscle model is described in more detail as it was chosen as the optimal approach in this study. The material data required for Hill's model are presented: coordinates of the muscles' origin and insertion point, fiber and tendon length, physiological cross-area, active and passive length-force relationship and velocity-force relationship for each muscle. Since the literature shows discrepancies regarding the length-force relationship and the stretching status of the muscles during occlusion, three different configurations are defined in order to compare the effect of these differences on the behavior of the system. Additional studies are carried out to determine the effect of the bolus size and the origin points of the muscles on both the joint forces and the bite forces.

Chapter 7 focuses on the reproduction of the mastication cycle with the model. The experimental recordings performed by several authors, which include muscle activation levels and the kinematics of a point of the jaw during the cycle, are reviewed at the beginning of the chapter. This cycle is first performed with simplified kinematics, in order to observe and correct existing limitations on the model. An enhanced chewing cycle is then performed trying to replicate the displacements and velocities seen in experimental recordings.

Chapter 8, finally, summarizes the results and most important conclusions of the simulations. The implications and possible applications of the obtained results are discussed. Finally, the limitations of the model and the outlook on future developments are provided.

Some exemplars of this dissertation contain a DVD presenting several of the most important results of this work.

Chapter 1:
Theoretical Background

Continuum mechanics deals with the behavior of materials that can be approximated as continuous for certain lengths and time scales. The equations that govern the mechanics of such materials include the balance laws for mass, momentum, and energy. Kinematic relations and constitutive equations are required to complete the system of governing equations. We now introduce the kinematic relations, balance laws and the constitutive equations for linear, hyperelastic and viscoelastic materials. A more detailed discussion of these topics can be found in [1] and [2].

1.1 Fundamentals of Continuum Mechanics

1.1.1 Kinematics of a Deformable Body

Material Body Configurations

A body undergoing motion is pictured in figure 1.1, Ω representing the body and Γ its boundary. Each point $\mathcal{P}$ has a unique position $\mathbf{x}$ at any time t. This position is given by the placement function:

$$\mathbf{x} = \boldsymbol{\chi}(\mathcal{P}, t)\,. \tag{1.1}$$

We refer to $\mathbf{X}$ as the position of $\mathcal{P}$ in the reference configuration and $\mathbf{x}$ as the position in the actual configuration. The motion of the body can be described by a material formulation (Lagrange) as in (1.1) or by a spatial description (Euler) which follows the inverse motion:

$$\mathbf{X} = \boldsymbol{\chi}^{-1}(\mathbf{x}, t)\,. \tag{1.2}$$

Displacement, Velocity and Acceleration

The displacement of a body is defined as

$$\mathbf{u} = \mathbf{x} - \mathbf{X} \quad \rightarrow \quad \mathbf{u} = \mathbf{u}(\mathbf{X}, t)\,. \tag{1.3}$$

The material formulation of velocity and acceleration are given by

$$\mathbf{v} := \dot{\mathbf{x}} = \frac{\mathrm{d}}{\mathrm{d}t}\boldsymbol{\chi}(\mathbf{X}, t) = \dot{\mathbf{x}}(\mathbf{X}, t)\,. \tag{1.4}$$

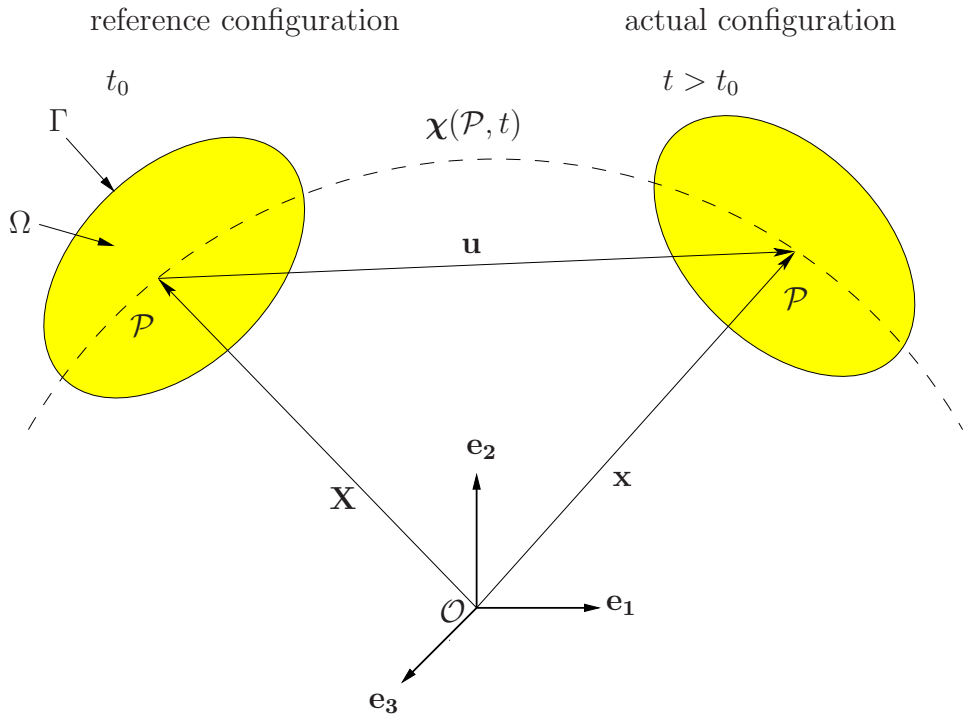

Figure 1.1: Kinematics of a body

$$\mathbf{a} := \ddot{\mathbf{x}} = \frac{\mathrm{d}^2}{\mathrm{d}t^2}\boldsymbol{\chi}(\mathbf{X}, t) = \ddot{\mathbf{x}}(\mathbf{X}, t)\,. \tag{1.5}$$

In the spatial formulation with $\mathbf{X}$ as a function of $\boldsymbol{\chi}^{-1}(\mathbf{x}, t)$ velocity and acceleration are given by

$$\mathbf{v} := \dot{\mathbf{x}}(\mathbf{X}, t) = \dot{\mathbf{x}}(\mathbf{X}(\mathbf{x}, t), t) = \dot{\mathbf{x}}(\mathbf{x}, t)\,, \tag{1.6}$$

$$\mathbf{a} := \ddot{\mathbf{x}}(\mathbf{X}, t) = \ddot{\mathbf{x}}(\mathbf{X}(\mathbf{x}, t), t) = \ddot{\mathbf{x}}(\mathbf{x}, t)\,. \tag{1.7}$$

The material time derivative for a scalar valued quantity is defined as follows

$$\dot{(\cdot)} := \frac{\mathrm{d}(\cdot)(\mathbf{x}, t)}{\mathrm{d}t} = \frac{\partial(\cdot)}{\mathrm{d}t} + \frac{\partial(\cdot)}{\partial \mathbf{x}} \cdot \frac{\mathrm{d}(\mathbf{x})}{\mathrm{d}t} = \frac{\partial(\cdot)}{\mathrm{d}t} + \operatorname{grad}(\cdot) \cdot \mathbf{v} \tag{1.8}$$

The material description is usually employed for solid problems, while a spatial description is generally used for fluid type problems. When using a material description, in Finite Element Analyses the mesh follows the same motion as the body. In a spatial description, the mesh is static, depicting the motion of the body through it. We now define the following notation:

$$\begin{aligned} \operatorname{grad}(\cdot) &= \frac{\mathrm{d}(\cdot)}{\mathrm{d}\mathbf{x}}\,, \\ \operatorname{Grad}(\cdot) &= \frac{\mathrm{d}(\cdot)}{\mathrm{d}\mathbf{X}}\,. \end{aligned} \tag{1.9}$$

Deformation and Strain Tensors

To measure the deformation and strain at a material point, we introduce the material deformation gradient $\mathbf{F}$ and its inverse $\mathbf{F}^{-1}$. $\mathbf{F}$ is defined as the gradient of the motion function with respect to the reference configuration

$$\mathbf{F} := \frac{\mathrm{d}\boldsymbol{\chi}(\mathbf{x}, t)}{\mathrm{d}\mathbf{X}} = \frac{\mathrm{d}\mathbf{x}}{\mathrm{d}\mathbf{X}} = \mathrm{Grad}\,\mathbf{x}\,. \tag{1.10}$$

$\mathbf{F}$ is a second-order tensor which allows the comparison of line elements between the reference and actual configuration,

$$\mathrm{d}\mathbf{x} = \mathbf{F}\,\mathrm{d}\mathbf{X}: \quad \text{push forward of } \mathrm{d}\mathbf{X}\,. \tag{1.11}$$

$$\mathrm{d}\mathbf{X} = \mathbf{F}^{-1}\,\mathrm{d}\mathbf{x}: \quad \text{pull back of } \mathrm{d}\mathbf{x}\,. \tag{1.12}$$

The push-forward operation for the area and volume element are defined as:

$$\mathrm{d}\mathbf{a} = (\mathrm{cof}\,\mathbf{F})\,\mathrm{d}\mathbf{A}\,. \tag{1.13}$$

$$\mathrm{d}v = (\det \mathbf{F})\,\mathrm{d}V\,, \tag{1.14}$$

where cof and det denote the cofactor and determinant of a tensor, respectively, and are defined in index notation as:

$$\mathrm{cof}\,\mathbf{A} = \frac{1}{2} a_{ik} a_{no} (\mathbf{e}_i \times \mathbf{e}_n) \otimes (\mathbf{e}_k \times \mathbf{e}_o) \tag{1.15}$$

$$\det \mathbf{A} = \frac{1}{3} (\mathrm{cof}\,\mathbf{A}) \cdot \mathbf{A}\,. \tag{1.16}$$

Here, $\mathbf{e}_i$ are the basis vectors. The operation $\det \mathbf{F}$ describes the following properties:

$$\det \mathbf{F} \begin{cases} > 0 : \text{this implies a contraction/extension of the volume element } \mathrm{d}v \\ = 0 : \text{implies shrinking to a material point} \\ < 0 : \text{implies an “inversion of the volume”} \end{cases} \tag{1.17}$$

One can determine the change of distance between two infinitesimally adjacent points in a body during deformation with the help of the deformation gradient. The distance between two points in the actual configuration is given by

$$\begin{aligned} \|\mathrm{d}\mathbf{x}\|^2 &= \mathrm{d}\mathbf{x} \cdot \mathrm{d}\mathbf{x} = (\mathbf{F}\,\mathrm{d}\mathbf{X}) \cdot (\mathbf{F}\,\mathrm{d}\mathbf{X}) = \mathrm{d}\mathbf{X} \cdot (\mathbf{F}^T \mathbf{F}) \mathrm{d}\mathbf{X} \\ &=: \mathrm{d}\mathbf{X} \cdot \mathbf{C}\,\mathrm{d}\mathbf{X}\,, \end{aligned} \tag{1.18}$$

where $\mathbf{C}$ is defined as the *right Cauchy-Green* deformation tensor. Analogously, the *left Cauchy-Green* deformation tensor $\mathbf{B}$ is obtained by expressing the reference line element in the actual configuration

$$\begin{aligned}\|\mathrm{d}\mathbf{X}\|^2 = \mathrm{d}\mathbf{X}\cdot\mathrm{d}\mathbf{X} = (\mathbf{F}^{-\mathbf{1}}\,\mathrm{d}\mathbf{x})\cdot(\mathbf{F}^{-1}\,\mathrm{d}\mathbf{x}) = \mathrm{d}\mathbf{x}\cdot(\mathbf{F}^{T-1}\mathbf{F}^{-1})\mathrm{d}\mathbf{x}\\ =: \mathrm{d}\mathbf{x}\cdot\mathbf{B}^{-\mathbf{1}}\,\mathrm{d}\mathbf{x}\,.\end{aligned} \tag{1.19}$$

This gives us the following definitions:

$$\mathbf{C} := \mathbf{F}^T\mathbf{F} \quad \text{and} \quad \mathbf{B} := \mathbf{F}\,\mathbf{F}^T\,. \tag{1.20}$$

We can now define the *Green-Lagrangean* strain tensor $\mathbf{E}$ and the *Almansian* strain tensor $\mathbf{A}$ by comparing the square of the line elements between both configurations

$$\|\mathrm{d}\mathbf{x}\|^2 - \|\mathrm{d}\mathbf{X}\|^2 = \mathrm{d}\mathbf{X}\cdot\mathbf{C}\,\mathrm{d}\mathbf{X} - \mathrm{d}\mathbf{X}\cdot\mathrm{d}\mathbf{X} = \mathrm{d}\mathbf{X}\cdot(\mathbf{C}-\mathbf{I})\,\mathrm{d}\mathbf{X}\,, \tag{1.21}$$

$$\|\mathrm{d}\mathbf{x}\|^2 - \|\mathrm{d}\mathbf{X}\|^2 = \mathrm{d}\mathbf{x}\cdot\mathrm{d}\mathbf{x} - \mathrm{d}\mathbf{x}\cdot\mathbf{B}^{-1}\,\mathrm{d}\mathbf{x} = \mathrm{d}\mathbf{x}\cdot(\mathbf{I}-\mathbf{B}^{-1})\,\mathrm{d}\mathbf{x}\,. \tag{1.22}$$

One finally defines

$$\mathbf{E} := \frac{1}{2}(\mathbf{C}-\mathbf{I}) \quad \text{and} \quad \mathbf{A} := \frac{1}{2}(\mathbf{I}-\mathbf{B}^{-1})\,, \tag{1.23}$$

where $\mathbf{I}$ is the second-order identity tensor. One can also express $\mathbf{E}$ and $\mathbf{A}$ using the material deformation gradient $\mathbf{F}$:

$$\mathbf{E} := \frac{1}{2}((\mathrm{Grad}\,\mathbf{u})^T + \mathrm{Grad}\,\mathbf{u} + (\mathrm{Grad}\,\mathbf{u})^T\,\mathrm{Grad}\,\mathbf{u})\,, \tag{1.24}$$

$$\mathbf{A} := \frac{1}{2}((\mathrm{grad}\,\mathbf{u})^T + \mathrm{grad}\,\mathbf{u} + (\mathrm{grad}\,\mathbf{u})^T\,\mathrm{grad}\,\mathbf{u})\,. \tag{1.25}$$

$\mathbf{E}$ and $\mathbf{A}$ are related by

$$\mathbf{E} := \mathbf{F}^T\mathbf{A}\,\mathbf{F} \quad \leftrightarrow \quad \mathbf{A} := \mathbf{F}^{T-1}\mathbf{E}\,\mathbf{F}^{-1}\,. \tag{1.26}$$

Here, $\mathbf{F}^T(\cdot)\,\mathbf{F}$ and $\mathbf{F}^{T-1}(\cdot)\,\mathbf{F}^{-1}$ denote "contravariant" pull-back and push-forward transportation, respectively.

In the case of small strains and rotations, one can use the so-called infinitesimal strain tensor $\boldsymbol{\varepsilon}$. Following the Taylor expansion and retaining only first order terms, one arrives at

$$\boldsymbol{\varepsilon} = \frac{1}{2}(\mathrm{Grad}\,\mathbf{u} + (\mathrm{Grad}\,\mathbf{u})^T)\,. \tag{1.27}$$

Since $\mathrm{Grad}\,(\cdot) \approx \mathrm{grad}\,(\cdot)$ for geometrically linear regimes, the linearization of $\mathbf{A}$ yields the same result.

Stress Concepts

Cauchy introduced his Lemma and theorem in 1823. It states that a traction vector $\mathbf{t}$ can be found in any cut surface of a body, as function of space, time and orientation such that the distribution of these traction vectors in the cut surface restores the original shape of the intact body in the loaded configuration. These vectors acting on opposing sides of the same cut surface are equal in magnitude and opposite in direction (Fig 1.2).

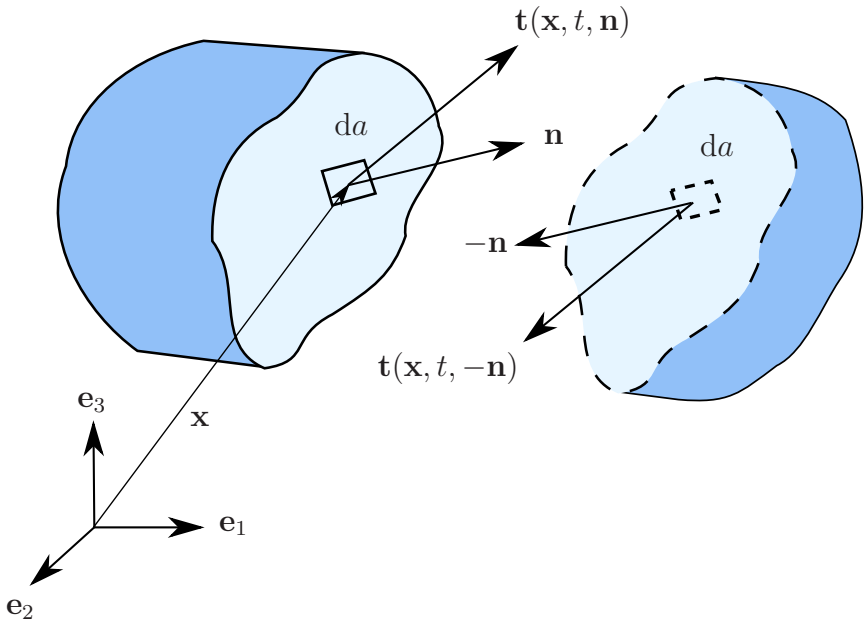

Figure 1.2: Stress vector on an internal surface of a loaded body

The Cauchy Lemma is expressed as:

$$\mathbf{t}(\mathbf{x}, t, \mathbf{n}) = -\mathbf{t}(\mathbf{x}, t, -\mathbf{n})\,. \tag{1.28}$$

According to Cauchy's theorem, merely by knowing the stress vectors in three mutually perpendicular planes, the stress vector on any other plane passing through that point can be found through coordinate transformation equations. The theorem states that there exists a second-order tensor field $\mathbf{T}(\mathbf{x}, t)$, called the *Cauchy* stress tensor, independent of $\mathbf{n}$, such that $\mathbf{T}$ is a linear function of $\mathbf{n}$:

$$\mathbf{t}(\mathbf{x}, t, \mathbf{n}) = \mathbf{T}(\mathbf{x}, t)\,\mathbf{n}\,. \tag{1.29}$$

The differential surface force is

$$\mathrm{d}\mathbf{f} = \mathbf{t}\,\mathrm{d}a = (\mathbf{T}\,\mathbf{n})\mathrm{d}a = \mathbf{T}\,(\mathbf{n}\,\mathrm{d}a) = \mathbf{T}\mathrm{d}\mathbf{a}\,. \tag{1.30}$$

To obtain the *Kirchoff* stress (weighted stress) tensor $\boldsymbol{\tau}$ one introduces a weighted surface element $\mathrm{d}\bar{\mathbf{a}} = \frac{\mathrm{d}V}{\mathrm{d}v}\mathrm{d}\mathbf{a} = (\mathrm{det}\mathbf{F})^{-1}\mathrm{d}\mathbf{a}$

$$\mathrm{d}\mathbf{f} = \mathbf{T}(\mathrm{det}\mathbf{F})\mathrm{d}\bar{\mathbf{a}} =: \boldsymbol{\tau}\mathrm{d}\bar{\mathbf{a}}\,, \quad \boldsymbol{\tau} = (\mathrm{det}\mathbf{F})\mathbf{T}\,. \tag{1.31}$$

The *first Piola-Kirchoff* stress $\mathbf{P}$ (nominal stress) is obtained by performing a covariant pull-back of the second "basis" (set of linearly independent vectors that can represent any vector through linear combination) of the *Kirchoff* stress,

$$\mathbf{P} := \boldsymbol{\tau}\,\mathbf{F}^{T-1} = (\mathrm{det}\mathbf{F})\mathbf{T}\,\mathbf{F}^{T-1}\,. \tag{1.32}$$

Finally, the *second Piola-Kirchoff* stress $\mathbf{S}$ is obtained by pulling back the first basis of the *first Piola-Kirchoff* stress, since now this stress tensor has both its bases in the reference configuration, it is symmetric such as $\mathbf{T}$ and $\boldsymbol{\tau}$

$$\mathbf{S} = \mathbf{F}^{-1}\mathbf{P} = (\mathrm{det}\mathbf{F})\mathbf{F}^{-1}\mathbf{T}\,\mathbf{F}^{T-1}\,. \tag{1.33}$$

In geometrically-linear theories, all stress tensors are approximately identical:

$$\boldsymbol{\sigma} :\approx \mathbf{S} \approx \mathbf{P} \approx \boldsymbol{\tau} \approx \mathbf{T}\,. \tag{1.34}$$

1.1.2 Mechanical Balance Laws

Mass Balance

In a closed system, the mass of a body is constant. Thus, the global form (when employing Eulerian coordinates) is given by

$$\frac{\mathrm{d}}{\mathrm{d}t}\int_{\Omega} \rho\,\mathrm{d}v = 0\,, \tag{1.35}$$

where ρ is the density of the body. The local form of mass balance is given by

$$\dot{\rho} + \rho\,\mathrm{div}\,\dot{\mathbf{x}} = 0\,. \tag{1.36}$$

The mass balance states that the temporal change of mass in a closed system must be zero.

Linear Momentum Balance

Newton's second law of motion states that the temporal change of the body's momentum $\rho\,\dot{\mathbf{x}}$ equals the sum of all forces acting on the body, i.e. of the cutting forces $\bar{\mathbf{t}}$ and the body forces $\mathbf{b}$:

$$\frac{\mathrm{d}}{\mathrm{d}t}\int_{\Omega} \rho\,\dot{\mathbf{x}}\,\mathrm{d}v = \int_{\Gamma} \mathbf{T}\,\mathbf{n}\,\mathrm{d}a + \int_{\Omega} \rho\,\mathbf{b}\,\mathrm{d}v\,. \tag{1.37}$$

which leads to the following local form

$$\rho\,\ddot{\mathbf{x}} = \operatorname{div}\mathbf{T} + \rho\,\mathbf{b}\,. \tag{1.38}$$

Moment of Momentum Balance

The temporal change of the body's moment of momentum $\mathbf{x} \times (\rho\,\dot{\mathbf{x}})$ equals the sum of moments of all forces acting on the body taken with respect to an arbitrary but fixed point (for instance, the origin):

$$\frac{\mathrm{d}}{\mathrm{d}t}\int_{\Omega} \mathbf{x} \times (\rho\,\dot{\mathbf{x}})\,\mathrm{d}v + \int_{\Gamma} (\mathbf{x} \times \mathbf{T}\,\mathbf{n})\mathrm{d}a = \int_{\Omega} (\mathbf{x} \times \rho\,\mathbf{b})\,\mathrm{d}v\,. \tag{1.39}$$

The investigation of the local form shows that

$$\mathbf{0} = \mathbf{I} \times \mathbf{T} \leftrightarrow \mathbf{T} = \mathbf{T}^T\,. \tag{1.40}$$

The main conclusion of the moment of momentum of balance is that the *Cauchy* stress tensor is symmetric. Thus, only six components of the stress tensor are independent. Note, however, that the first *Piola-Kirchoff* stress is not symmetric since its bases are in different configurations. $\mathbf{T} = \mathbf{T}^T \rightarrow \boldsymbol{\tau} = \boldsymbol{\tau}^T, \mathbf{P} \neq \mathbf{P}^T, \mathbf{S} = \mathbf{S}^T$.

1.2 Material Models

The relationship between strain and stress in a given material body is described by the material law

$$\boldsymbol{\sigma} = \boldsymbol{\sigma}(\mathbf{F})\,. \tag{1.41}$$

These constitutive equations are mathematical representations of the different material behaviors which are validated through experimental results. A material is said to be isotropic when its material properties are the same in all directions and anisotropic if they depend on the direction in the material body. This work focuses on linear elastic (isotropic and anisotropic), hyperelastic and viscoelastic material models.

1.2.1 Linear Elastic

Elastic materials completely reverse deformation produced from applied forces once these force are removed. The behavior of the material depends only on the current state of deformation and is independent from the strain path. Linear elastic material models obey Hooke's law with stress being linearly proportional to the strain.

$$\boldsymbol{\sigma} = \mathbb{C}\boldsymbol{\varepsilon}\,. \tag{1.42}$$

Linear Elastic Anisotropic

In the case of material properties not having any planes of symmetry in any direction, the number of components of the fourth-order tensor $\mathbb{C}$ in (1.42) is 81. However, due to the components C_{ijkl} satisfying the following symmetry conditions due to $\boldsymbol{\sigma} = \boldsymbol{\sigma}^T$ and $\boldsymbol{\varepsilon} = \boldsymbol{\varepsilon}^T$:

$$C_{ijkl} = C_{klij} = C_{ijkl} = C_{jilk}\,. \tag{1.43}$$

the number of independent components is reduced to 21:

$$\begin{bmatrix} C_{1111} & C_{1122} & C_{1133} & C_{1123} & C_{1113} & C_{1112} \\ & C_{2222} & C_{2233} & C_{2223} & C_{2213} & C_{2212} \\ & & C_{3333} & C_{3323} & C_{3313} & C_{3312} \\ & & & C_{2323} & C_{2313} & C_{2312} \\ & & & & C_{1313} & C_{1312} \\ & & & & & C_{1212} \end{bmatrix}. \tag{1.44}$$

Using the Voigt notation (1.42) can be represented in the following manner

$$\begin{bmatrix} \boldsymbol{\sigma}_{11} \\ \boldsymbol{\sigma}_{22} \\ \boldsymbol{\sigma}_{33} \\ \boldsymbol{\sigma}_{23} \\ \boldsymbol{\sigma}_{13} \\ \boldsymbol{\sigma}_{12} \end{bmatrix} = \begin{bmatrix} C_{11} & C_{12} & C_{13} & C_{14} & C_{15} & C_{16} \\ C_{21} & C_{22} & C_{23} & C_{24} & C_{25} & C_{26} \\ C_{31} & C_{32} & C_{33} & C_{34} & C_{35} & C_{36} \\ C_{41} & C_{42} & C_{43} & C_{44} & C_{45} & C_{46} \\ C_{51} & C_{52} & C_{53} & C_{54} & C_{55} & C_{56} \\ C_{61} & C_{62} & C_{63} & C_{64} & C_{65} & C_{66} \end{bmatrix} \begin{bmatrix} \boldsymbol{\varepsilon}_{11} \\ \boldsymbol{\varepsilon}_{22} \\ \boldsymbol{\varepsilon}_{33} \\ 2\boldsymbol{\varepsilon}_{23} \\ 2\boldsymbol{\varepsilon}_{13} \\ 2\boldsymbol{\varepsilon}_{12} \end{bmatrix}. \tag{1.45}$$

Here the coefficients C_{ij} are symmetric ($C_{ij} = C_{ji}$) resulting in 21 independent stiffness coefficients (1.43).

Linear Elastic Orthotropic

Orthotropic materials involve three mutually orthogonal planes of material symmetry. The number of independent stiffness coefficients is then reduced to 9. Equation

(1.42) takes the following form

$$\begin{bmatrix} \sigma_{11} \\ \sigma_{22} \\ \sigma_{33} \\ \sigma_{23} \\ \sigma_{13} \\ \sigma_{12} \end{bmatrix} = \begin{bmatrix} C_{11} & C_{12} & C_{13} & 0 & 0 & 0 \\ C_{21} & C_{22} & C_{23} & 0 & 0 & 0 \\ C_{31} & C_{32} & C_{33} & 0 & 0 & 0 \\ 0 & 0 & 0 & C_{44} & 0 & 0 \\ 0 & 0 & 0 & 0 & C_{55} & 0 \\ 0 & 0 & 0 & 0 & 0 & C_{66} \end{bmatrix} \begin{bmatrix} \varepsilon_{11} \\ \varepsilon_{22} \\ \varepsilon_{33} \\ 2\varepsilon_{23} \\ 2\varepsilon_{13} \\ 2\varepsilon_{12} \end{bmatrix} . \tag{1.46}$$

Here we denote the inverse relation of Eq. (1.42) with the compliance matrix $\mathbb{C}^{-1}$ (the inverse of the stiffness matrix)

$$\boldsymbol{\varepsilon} = \mathbb{C}^{-1}\boldsymbol{\sigma} \,, \tag{1.47}$$

which leads to the inverse relation

$$\begin{bmatrix} \varepsilon_{11} \\ \varepsilon_{22} \\ \varepsilon_{33} \\ 2\varepsilon_{23} \\ 2\varepsilon_{13} \\ 2\varepsilon_{12} \end{bmatrix} = \begin{bmatrix} \frac{1}{E_1} & \frac{-\nu_{12}}{E_2} & \frac{-\nu_{13}}{E_3} & 0 & 0 & 0 \\ \frac{-\nu_{12}}{E_1} & \frac{1}{E_2} & \frac{-\nu_{12}}{E_3} & 0 & 0 & 0 \\ \frac{-\nu_{12}}{E_1} & \frac{-\nu_{12}}{E_2} & \frac{1}{E_3} & 0 & 0 & 0 \\ 0 & 0 & 0 & \frac{1}{G_{23}} & 0 & 0 \\ 0 & 0 & 0 & 0 & \frac{1}{G_{13}} & 0 \\ 0 & 0 & 0 & 0 & 0 & \frac{1}{G_{12}} \end{bmatrix} \begin{bmatrix} \sigma_{11} \\ \sigma_{22} \\ \sigma_{33} \\ \sigma_{23} \\ \sigma_{13} \\ \sigma_{12} \end{bmatrix} , \tag{1.48}$$

where E_1, E_2, E_3 are the Young's moduli in the individual directions, G_{23}, G_{13}, G_{12} are the shear moduli and ν_{23}, ν_{13} and ν_{12} are the Poisson's ratios in the corresponding directions. Inversion of the strain-stress relations in (1.48) leads to the components

in Eq. (1.42):

$$
\begin{aligned}
C_{11} &= \frac{E_1}{C_v}(1-\nu_{23}\nu_{32}), \qquad C_{12} = \frac{E_1}{C_v}(\nu_{21}-\nu_{23}\nu_{31}),\\
C_{13} &= \frac{E_1}{C_v}(\nu_{31}+\nu_{21}\nu_{32}), \quad C_{22} = \frac{E_2}{C_v}(1-\nu_{13}\nu_{31}),\\
C_{23} &= \frac{E_2}{C_v}(\nu_{32}+\nu_{31}\nu_{12}), \quad C_{33} = \frac{E_3}{C_v}(1-\nu_{12}\nu_{21}),\\
C_{44} &= G_{23}, \quad C_{55} = G_{31}, \quad C_{66} = G_{12},\\
C_v &= 1-\nu_{12}\nu_{21}-\nu_{23}\nu_{32}-\nu_{31}\nu_{13}-2\nu_{31}\nu_{32}\nu_{13}.
\end{aligned}
\tag{1.49}
$$

Linear Elastic Isotropic

If the material properties are independent of the direction then the material is known as isotropic and the only parameters needed are Young's modulus, E, and an additional parameter, usually, Poisson's ratio ν. Eq (1.47) then reduces to

$$
\begin{bmatrix} \varepsilon_{11} \\ \varepsilon_{22} \\ \varepsilon_{33} \\ 2\varepsilon_{23} \\ 2\varepsilon_{13} \\ 2\varepsilon_{12} \end{bmatrix}
= \frac{1}{E}
\begin{bmatrix}
1 & -\nu & -\nu & 0 & 0 & 0 \\
-\nu & 1 & -\nu & 0 & 0 & 0 \\
-\nu & -\nu & 1 & 0 & 0 & 0 \\
0 & 0 & 0 & 2(1+\nu) & 0 & 0 \\
0 & 0 & 0 & 0 & 2(1+\nu) & 0 \\
0 & 0 & 0 & 0 & 0 & 2(1+\nu)
\end{bmatrix}
\begin{bmatrix} \sigma_{11} \\ \sigma_{22} \\ \sigma_{33} \\ \sigma_{23} \\ \sigma_{13} \\ \sigma_{12} \end{bmatrix}
\tag{1.50}
$$

1.2.2 Non-Linear Elastic Material Models

If the material recovers all its deformation once the loads have been removed but the stress-strain relation is not linear, then Hooke's law is no longer valid. Materials such as elastomers, foams and biological tissues are often modeled using hyperelastic material models. Hyperelastic material models assume that the material behavior can be described by means of a strain energy density function W, from which the stress-strain relationship can be derived.

The *second Piola-Kirchoff* stress is expressed in the following way:

$$
\mathbf{S} = \frac{\partial W}{\partial \mathbf{E}}\,. \tag{1.51}
$$

Most of these models are based on the invariants of the *Cauchy-Green* deformation tensor. These can be obtained using the principal stretch ratios. A stretch ratio is

defined as

$$\lambda = \frac{l}{l_o} \tag{1.52}$$

where l is the deformed length and l_o is the original length. Analogously to the principal strains, the three principal stretch ratios λ_1, λ_2 and λ_3 correspond to the values in the principal axes. The invariants are given as

$$\begin{aligned} I_1 &= {\lambda_1}^2 + {\lambda_2}^2 + {\lambda_3}^2 \,, \\ I_2 &= {\lambda_1}^2{\lambda_2}^2 + {\lambda_2}^2{\lambda_3}^2 + {\lambda_3}^2{\lambda_1}^2 \,, \\ I_3 &= {\lambda^2}_1{\lambda^2}_1{\lambda^2}_1 = J^2 \,, \end{aligned} \tag{1.53}$$

where

$$J = \det \mathbf{F} \,. \tag{1.54}$$

When dealing with incompressible and nearly incompressible materials, it is convenient to split the strain energy density into a deviatoric and volumetric part

$$W = W_{Dev}(\bar{I}_1, \bar{I}_2) + W_{Vol}(J) \,, \tag{1.55}$$

where $\bar{I}_1$, $\bar{I}_2$ are modified invariants with the volume change eliminated and $\bar{\lambda_1}$, $\bar{\lambda_2}$ and $\bar{\lambda_3}$ are the modified principal stretch ratios. They are defined in the following manner:

$$\begin{aligned} &\bar{I}_1 = J^{-2/3} I_1 \,, \quad \bar{I}_2 = J^{-4/3} I_2, \\ &\bar{\lambda_1} = J^{-1/3}\lambda_1 \,, \quad \bar{\lambda_2} = J^{-1/3}\lambda_2 \,, \quad \bar{\lambda_3} = J^{-1/3}\lambda_3 \,. \end{aligned} \tag{1.56}$$

Neo-Hookean Model

One of the simplest hyperelastic material models is the Neo-Hookean model. The model is similar to Hooke's law, showing an initial linear stress-strain relationship but becoming non-linear after a certain range.

The strain energy density function for a compressible Neo-Hookean model is defined as

$$W = C_{10}(\bar{I}_1 - 3) + \frac{K}{2}(J-1)^2 \,, \tag{1.57}$$

where the initial shear modulus is $G = 2C_{10}$ and K the initial bulk modulus. These components are obtained through curve-fitting, according to stress-strain curves obtained from experimental tests.

Mooney-Rivlin Model

The Mooney-Rivlin model is an extension of the Neo-Hookean model and is available in different forms depending on the number of parameters. The number of parameters is chosen with regards to the behavior of the material. If the material stress-strain curve shows many inflection points then a higher number of parameters is necessary to capture more closely its behavior.

A two-parameter incompressible Mooney-Rivlin material is given by the following strain energy density function

$$W = C_{10}(\bar{I}_1 - 3) + C_{01}(\bar{I}_2 - 3) \tag{1.58}$$

a three parameter Mooney-Rivlin model

$$W = C_{10}(\bar{I}_1 - 3) + C_{01}(\bar{I}_2 - 3) + C_{11}(\bar{I}_1 - 3)(\bar{I}_2 - 3) \tag{1.59}$$

and a five parameter Mooney-Rivlin model

$$W = C_{10}(\bar{I}_1 - 3) + C_{01}(\bar{I}_2 - 3) + C_{20}(\bar{I}_1 - 3)^2 + C_{11}(\bar{I}_1 - 3)(\bar{I}_2 - 3) + C_{02}(\bar{I}_2 - 3)^2 \tag{1.60}$$

where C_{10}, C_{01}, C_{20}, C_{11} and C_{02} are obtained through curve-fitting. The initial shear modulus is defined as

$$G = 2(C_{10} + C_{01})\,. \tag{1.61}$$

To describe a compressible material, the following additional term containing the initial bulk modulus K can be introduced:

$$\frac{K}{2}(J-1)^2\,. \tag{1.62}$$

Ogden Model

The Ogden material model is used to describe complex material behaviors found in rubbers and biological tissues. The strain energy density function of this model is based on the principal stretches:

$$W = \sum_{i=1}^{N} \frac{\mu_i}{\alpha_i}(\bar{\lambda}_1^{\alpha_i} + \bar{\lambda}_2^{\alpha_i} + \bar{\lambda}_3^{\alpha_i} - 3) + \sum_{k=1}^{N} \frac{1}{d_k}(J-1)^2 \tag{1.63}$$

where μ_i, α_i and d_k are material constants obtained from curve-fitting. N represents the order of the model and is specified by the user, it is, however, advised that this parameter be limited to 3 in order to avoid numerical difficulties. An Ogden model with $N = 1$ will stiffen with increased strain if $\alpha_i > 2$, soften if $\alpha_i < 2$ and behave as a Neo-Hookean material model if $\alpha_i = 2$.

1.2.3 Viscoelastic Models

Viscoelasticity is a property that materials exhibit when the response depends not only on the current state of the deformation but also on the rate of deformation. These materials are characterized by the following behaviors: creep during constant load, stress relaxation under constant deformation and delayed strain recovery upon unloading. These behaviors can be reproduced with the help of mechanical models composed of spring and dashpot elements. In order to obtain a relaxation function, a spring can be connected in series with a dashpot to obtain e.g. the so called Maxwell model (Maxwell fluid) as shown in figure 1.3:

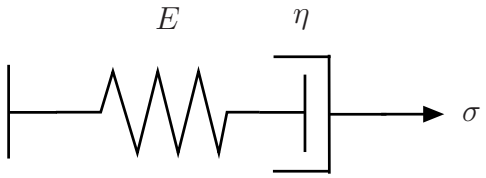

Figure 1.3: Maxwell model

where E is the stiffness of the spring and η is the viscosity in the dashpot. This model will show relaxation when a sudden strain is applied (as shown in figure 1.4) but will fail to describe the creep behavior.

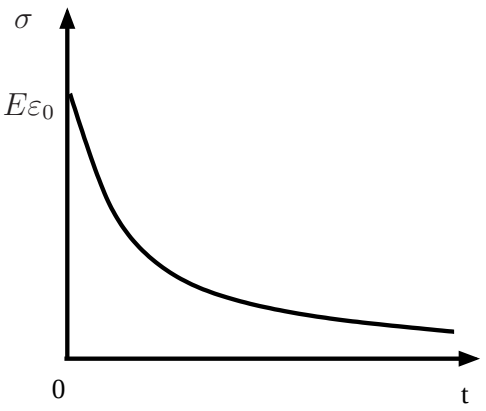

Figure 1.4: Relaxation function in the Maxwell model

On the other hand, a spring connected in parallel with a dashpot will result in the so called Kelvin-Voigt model as seen in figure 1.5.

This model reproduces the creep behavior as seen in figure 1.6 but fails to represent the relaxation behavior.

In order to capture both behaviors, the standard model is introduced which consists of a spring in parallel with a Maxwell model (figure 1.7).

To describe the response of this model, we first define α as the strain in the dashpot. We then assume that the stress in the dashpot σ^v follows a linear constitutive

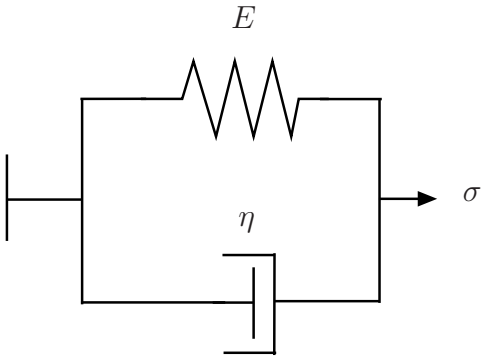

Figure 1.5: Kelvin-Voigt model

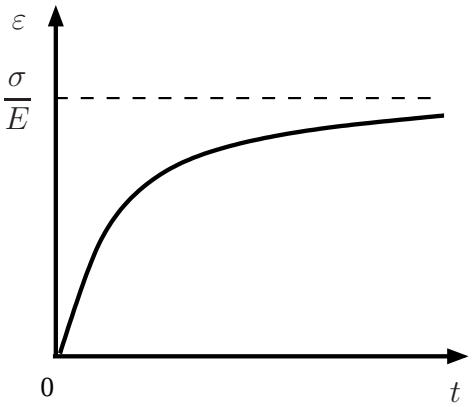

Figure 1.6: Creep function in the Kelvin model

relationship with the strain rate $\frac{\partial}{\partial t}\alpha(t)$ in the dashpot:

$$\sigma^v(t) = \eta \frac{\partial}{\partial t}\alpha(t)\,. \tag{1.64}$$

We now additionally assume for this one-dimensional model that the spring response is linear. The total stress in the device is:

$$\sigma = E_{eq}\varepsilon + \sigma^v\,, \tag{1.65}$$

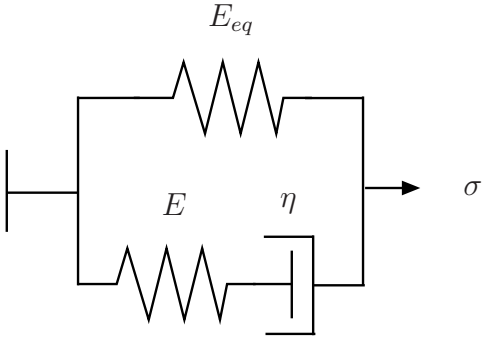

Figure 1.7: Standard model

since equilibrium requires that the stress in the dashpot be equal to the stress in the spring E:

$$\sigma^v = \eta\dot{\alpha} = E(\varepsilon - \alpha)\,. \tag{1.66}$$

The introduction of the following constants

$$\begin{aligned} E_0 &:= E_{eq} + E \qquad \text{(initial modulus)},\\ \tau &:= \eta/E \qquad\quad \text{(relaxation time)}, \end{aligned} \tag{1.67}$$

allows us to reformulate (1.65) and (1.66) into

$$\sigma = E_0\varepsilon - E\alpha\,, \tag{1.68}$$

with the internal variable α satisfying the following evolution equation:

$$\dot{\alpha} + \frac{1}{\tau}\alpha = \frac{1}{\tau}\varepsilon\,. \tag{1.69}$$

Equation (1.69) can be solved by using the integration factor $\mathrm{e}^{t/\tau}$ and using integration by parts, resulting in the following expression

$$\alpha(t) = \varepsilon(t) - \int_0^t \mathrm{e}^{-(t-s)/\tau}\dot{\varepsilon}(s)ds\,, \tag{1.70}$$

which can be introduced in (1.68) to obtain the following form:

$$\sigma(t) = \int_0^t G(t-s)\dot{\varepsilon}(s)ds\,, \tag{1.71}$$

where G is the relaxation function and is defined as

$$G(t) = E_{eq} + E\,\mathrm{e}^{-t/\tau}\,. \tag{1.72}$$

This is known as the convolution representation of viscoelasticity.

Three-Dimensional Formulation of Viscoelasticity

The viscoelastic model is based on the generalized Maxwell model (figure 1.8), where as in the case of the hyperelastic material models, the strain is split into a volumetric and a deviatoric part. The volumetric strain is defined as the trace of the strain tensor:

$$\boldsymbol{\varepsilon}_{vol} = \mathrm{tr}(\boldsymbol{\varepsilon}), \tag{1.73}$$

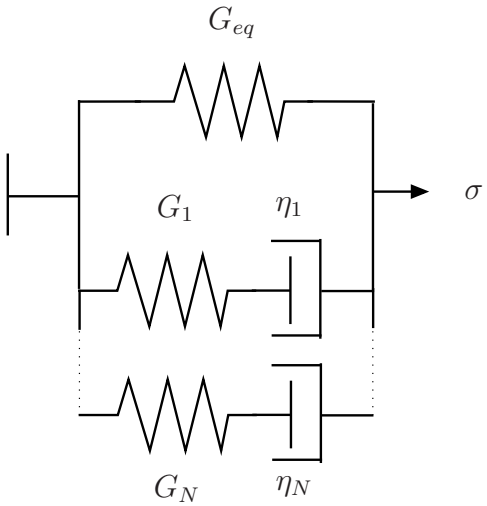

Figure 1.8: Generalized Maxwell model

while the deviatoric strain is defined as the strain with the change in volume removed:

$$\boldsymbol{\varepsilon}_{dev} = \boldsymbol{\varepsilon} - \frac{1}{3}\mathrm{tr}(\boldsymbol{\varepsilon})\mathbf{I}\,. \tag{1.74}$$

The free energy, Ψ, and dissipation function, Φ, are defined as

$$\Psi(\boldsymbol{\varepsilon}, \boldsymbol{\alpha}_1, \cdots, \boldsymbol{\alpha}_n) = \frac{1}{2}K\varepsilon_{Vol}^2 + G_{eq}\|\boldsymbol{\varepsilon}_{Dev}\|^2 + \sum_{i=1}^{n} G_i\|\boldsymbol{\varepsilon}_{Dev} - \boldsymbol{\alpha}_i\|^2\,, \tag{1.75}$$

$$\Phi(\boldsymbol{\beta}_1, \cdots, \boldsymbol{\beta}_n) = \sum_{i=1}^{n} \frac{1}{2}\frac{1}{\eta_i}\|\boldsymbol{\beta}_i\|^2\,, \tag{1.76}$$

where $\boldsymbol{\alpha}_i$ are the internal variables, $\boldsymbol{\beta}_i$ the forces in the dashpot elements, K the bulk modulus, η_i the viscosity in the dashpots, G_i the shear modulus of the springs, and G_{eq} the long term shear modulus. The free energy Ψ, and the strain energy density function W, are related by:

$$W = \rho_0\Psi\,. \tag{1.77}$$

Using Coleman's exploitation method ([3]) one obtains the following expressions:

$$\begin{aligned}
\boldsymbol{\sigma} &= (K\boldsymbol{\varepsilon}_{vol})\mathbf{I} + [2G_{eq}\boldsymbol{\varepsilon}_{dev} + \textstyle\sum_{i=1}^{n} 2G_i(\boldsymbol{\varepsilon}_{dev} - \boldsymbol{\alpha}_i)]\colon \mathbb{P} \\
\boldsymbol{\beta}_i &= 2G_i(\boldsymbol{\varepsilon}_{dev} - \boldsymbol{\alpha}_i) \\
\dot{\boldsymbol{\alpha}}_i &= \frac{1}{\eta_i}\boldsymbol{\beta}_i
\end{aligned} \tag{1.78}$$

The convolution representation can be obtained with a procedure similar to the one used with the standard model, i.e. through integration of the evolution equation.

This representation is employed by several numerical programs and has the following form:

$$\begin{aligned} \boldsymbol{\sigma} &= (K\boldsymbol{\varepsilon}_{vol})\mathbf{I} + \int_0^t 2G(t-s)\dot{\boldsymbol{\varepsilon}}_{dev}(s)ds \\ G(t) &= G_{eq} + \sum_{i=1}^{n} G_i \mathrm{e}^{-t/\tau_i} \end{aligned} \tag{1.79}$$

The function $G(t)$ is known as the shear relaxation and is defined by a series of exponential functions known as the Prony series. In a similar manner, a bulk relaxation function $K(t)$ can be incorporated into (1.79)

$$\boldsymbol{\sigma} = \int_0^t K(t-s)\dot{\boldsymbol{\varepsilon}}_{vol}(s)ds + \int_0^t 2G(t-s)\dot{\boldsymbol{\varepsilon}}_{dev}(s)ds \tag{1.80}$$

with the bulk relaxation defined as

$$K(t) = K_{eq} + \sum_{i=1}^{n} K_i \mathrm{e}^{-t/\tau_i}\,. \tag{1.81}$$

1.3 The Finite Element Method

The present work, dealing with the study of the human masticatory system, rests on an initial boundary value problem in the field of solid mechanics. The preferred method to solve this type of problems is the Finite Element Method (FEM). An initial boundary value problem (IBVP) consists of partial differential equations (PDEs) coupled with a set of restrictions called the initial and boundary conditions. The solution must solve the differential equations and satisfy both, the initial and boundary conditions. In most cases it is not possible to obtain an analytic solution. For this reason, numerical methods such as the Finite Element Method are employed, where an approximate solution is obtained by solving the problem in a "weak sense".

1.3.1 Strong Formulation of the Initial Boundary Value Problem

The IBVP in solid mechanics is defined by the strain-displacement equation, the balance of momentum and the constitutive equation. A function $\mathbf{u}(\mathbf{x}, t)$ (displacement) has to be found that fulfills the balance of momentum in the domain Ω, and satisfies the initial conditions in Ω and the boundary conditions on Γ. The balance of momentum in the current configuration is given by

$$\rho\,\ddot{\mathbf{x}} - \operatorname{div}\mathbf{T} = \rho\,\mathbf{b} \quad \text{(balance of momentum)} \tag{1.82}$$

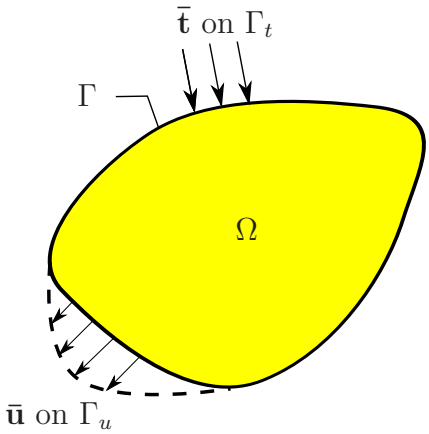

Figure 1.9: Domain of a IBVP

where ρ is the density and $\mathbf{b}$ the volume force.

$$\text{where} \begin{cases} \ddot{\mathbf{x}} = \ddot{\mathbf{u}} \\ \mathbf{T} = \mathbf{f}(\mathbf{u}, ...) \\ \mathbf{u} = \bar{\mathbf{u}} \text{ on } \boldsymbol{\Gamma}_\mathbf{u} \text{: Dirichlet boundary conditions} \\ \mathbf{u} : \mathbf{T}(\mathbf{u}, ...) = \bar{\mathbf{t}} \text{ on } \boldsymbol{\Gamma}_\mathbf{t} \text{: Neumann boundary conditions} \end{cases} \tag{1.83}$$

where $\bar{\mathbf{t}}$ is the surface load and $\mathbf{T}$ is the Cauchy stress tensor.

Note: $\Gamma = \Gamma_u \cup \Gamma_t, \Gamma_t \cap \Gamma_u = 0$

1.3.2 Weak Formulation of the Initial Boundary Value Problem

Several methods exist to obtain a weak formulation of the IBVP. In this work, the approach of the weighted residuals is presented. The method rests on introducing a weight function into the differential equation and integrating it over the entire domain: Instead of requiring the PDE to hold in the entire domain, we now only require the integral of the PDE weighted with some function to hold. In the case of solid mechanics, we begin with the balance of momentum:

$$\rho\, \ddot{\mathbf{u}} - \operatorname{div} \mathbf{T} - \rho\, \mathbf{b} = \mathbf{0}\,. \tag{1.84}$$

Since an approximate solution for $\mathbf{u}$ will be obtained, a residual $\mathbf{R}$ denoting the error is introduced:

$$\rho\, \ddot{\mathbf{u}} - \operatorname{div} \mathbf{T} - \rho\, \mathbf{b} = \mathbf{R}\,. \tag{1.85}$$

We multiply the residual with a test function $\delta\mathbf{u}$ and integrate it over the entire domain. We now require:

$$\int_{\Omega} (\rho\,\ddot{\mathbf{u}} - \operatorname{div}\mathbf{T} - \rho\,\mathbf{b})\,\delta\mathbf{u}\,\mathrm{d}v = 0\,. \tag{1.86}$$

With the help of the divergence theorem and integration by parts we reach the following expression

$$\int_{\Omega} \rho\,\ddot{\mathbf{u}}\cdot\delta\mathbf{u}\,\mathrm{d}v + \int_{\Omega} \mathbf{T} : \operatorname{grad}\delta\mathbf{u}\,\mathrm{d}v - \int_{\Gamma} \bar{\mathbf{t}}\cdot\delta\mathbf{u}\mathrm{d}a - \int_{\Omega} \rho\,\mathbf{b}\cdot\delta\mathbf{u}\mathrm{d}v = 0\,, \tag{1.87}$$

which is the weak formulation. Now we must find a function:

$$\mathbf{u} \in \varphi := \{\mathbf{u} \in {H_0}^1(\Omega^3) \mid \mathbf{u} = \bar{\mathbf{u}} \text{ on } \Gamma_u\} \tag{1.88}$$

$$\delta\mathbf{u} \in T := \{\delta\mathbf{u} \in {H_0}^1(\Omega^3) \mid \delta\mathbf{u} = 0 \text{ on } \Gamma_u\}\,, \tag{1.89}$$

where φ is the trial space containing the approximation functions for $\mathbf{u}$, and T is the weighting or test functions space $\delta\mathbf{u}$ vanishing on Γ_u.

1.3.3 Spatial Discretization

In FEM, the spatial domain of the problem is divided into a group of subdomains called the finite elements wherein the Galerkin method is applied. This division allows the use of simple shapes to approximate complex shapes. To ensure continuity between elements, nodal values are shared by adjacent elements, and shape functions are employed to interpolate these values throughout the element. Time dependency is retained by the nodal values, resulting in an algebraic problem where the system of ordinary differential equations in time is thus solved with another method. The function $\mathbf{u}$ is approximated within a single finite element by

$$\mathbf{u}(\mathbf{x},t) \approx \mathbf{u_h}(\mathbf{x},t) = \sum_{i=1}^{n} N_i(\mathbf{x})\cdot\mathbf{d}_i(t) = \mathbf{N}\cdot\mathbf{d}\,, \tag{1.90}$$

where N_i, are the shape functions, $\mathbf{d}_i$, the vectors containing the nodal displacements, and n the number of nodes per element. In the Galerkin method, the shape functions used to approximate the trial function, are also used for the test function $\delta\mathbf{u}$:

$$\delta\mathbf{u}(\mathbf{x}) = \sum_{i=1}^{n} N_i(\mathbf{x})\cdot\delta\mathbf{d}_i = \mathbf{N}\cdot\delta\mathbf{d}\,. \tag{1.91}$$

Since the time dependence is retained by the nodal values, the time derivatives have the following expressions:

$$\ddot{\mathbf{u}}_\mathbf{h}(\mathbf{x},t) = \mathbf{N}\cdot\ddot{\mathbf{d}} \quad \text{and} \quad \delta\ddot{\mathbf{u}}(\mathbf{x}) = \mathbf{N}\cdot\delta\ddot{\mathbf{d}}\,. \tag{1.92}$$

The gradient of the test function is computed with the help of a strain displacement matrix $\mathbf{B}$

$$\operatorname{grad}\delta\mathbf{u}(\mathbf{x}) = \frac{\partial\mathbf{N}}{\partial\mathbf{x}}\cdot\delta\mathbf{d} = \mathbf{B}\cdot\delta\mathbf{d}\,. \tag{1.93}$$

The domain is now discretized into elements Ω^k where $1 < k < N_{elem}$, N_{elem} is the number of elements and Γ^k are the boundaries of the elements. Summing over the elements that compose the domain and introducing the previous approximations into (1.87), one obtains the following expression:

$$\sum_{k=1}^{N_{elem}}\left\{\int_{\Omega^k}\rho\,(\mathbf{N}\cdot\ddot{\mathbf{d}})\,\cdot(\mathbf{N}\cdot\delta\mathbf{d})\,\mathrm{d}v + \int_{\Omega^k}\mathbf{T}:(\mathbf{B}\cdot\delta\mathbf{d})\mathrm{d}v \right.$$
$$\left. - \int_{\Gamma^k}\bar{\mathbf{t}}\cdot(\mathbf{N}\cdot\delta\mathbf{d})\mathrm{d}a - \int_{\Omega^k}\rho\mathbf{b}\cdot(\mathbf{N}\cdot\delta\mathbf{d})\mathrm{d}v\right\} = 0\,, \tag{1.94}$$

with the help of some transposing operations, we reach the following expression:

$$\sum_{k=1}^{N_{elem}}\left\{\int_{\Omega^k}\rho\,(\delta\mathbf{d}^\mathbf{T}\cdot\mathbf{N}^\mathbf{T})\cdot(\mathbf{N}\cdot\ddot{\mathbf{d}})\,\mathrm{d}v + \int_{\Omega^k}(\delta\mathbf{d}^\mathbf{T}\cdot\mathbf{B}^\mathbf{T}):\mathbf{T}\mathrm{d}v \right.$$
$$\left. - \int_{\Gamma^k}(\delta\mathbf{d}^\mathbf{T}\cdot\mathbf{N}^\mathbf{T})\cdot\bar{\mathbf{t}}\mathrm{d}a - \int_{\Omega^k}\rho(\delta\mathbf{d}^\mathbf{T}\cdot\mathbf{N}^\mathbf{T})\cdot\mathbf{b}\mathrm{d}v\right\} = 0\,. \tag{1.95}$$

Since the equation must hold for arbitrary values of $\delta\mathbf{d}^\mathbf{T}$, we finally arrive at

$$\sum_{k=1}^{N_{elem}}\left\{\int_{\Omega^k}\rho\,\mathbf{N}^\mathbf{T}\cdot\mathbf{N}\cdot\ddot{\mathbf{d}}\;\mathrm{d}v + \int_{\Omega^k}\mathbf{B}^\mathbf{T}\cdot\mathbf{T}\mathrm{d}v \right.$$
$$\left. - \int_{\Gamma^k}\mathbf{N}^\mathbf{T}\cdot\bar{\mathbf{t}}\mathrm{d}a - \int_{\Omega^k}\rho\mathbf{N}^\mathbf{T}\cdot\mathbf{b}\mathrm{d}v\right\} = 0\,, \tag{1.96}$$

Following an assembly process of the components of the individual elements into a global matrix, the equation can be written in the following manner resembling the more familiar form of Newton's second law:

$$\mathbf{F} = \mathbf{M}\mathbf{a}$$

$$\text{with} \begin{cases} \mathbf{F} = -\int\limits_{\Omega} \mathbf{B}^{\mathbf{T}} \cdot \mathbf{T} \mathrm{d}v + \int\limits_{\Gamma} \mathbf{N}^{\mathbf{T}} \cdot \bar{\mathbf{t}} \mathrm{d}a + \int\limits_{\Omega} \rho \mathbf{N}^{\mathbf{T}} \cdot \mathbf{b} \mathrm{d}v \\ \mathbf{M} = \int\limits_{\Omega} \rho\, \mathbf{N}^{\mathbf{T}} \cdot \mathbf{N}\ \mathrm{d}v \\ \mathbf{a} = \ddot{\mathbf{d}}\,. \end{cases} \tag{1.97}$$

1.3.4 Time Discretization

The spatial discretization results in a system of ordinary differential equations of second order, which is then solved by another method. The choice of method depends mostly in the physical behavior of the problem. These methods can be essentially classified into implicit and explicit time integration schemes:

Implicit: The time derivatives are calculated using both, the known quantities of the current time step (t_n) and the unknown quantities of the next time step (t_{n+1}), resulting in a system of algebraic equations that are solved by an iterative process. Implicit schemes are unconditionally stable and thus the time step is not limited.

Explicit: The time derivatives depend only on the current time step (t_n). If a diagonalized lumped mass matrix is used, no matrix inversion is required and the calculation of the time step becomes extremely efficient. The scheme is conditionally stable, with the time step size being limited by a stability criterion.

Implicit Time Integration Schemes

The simplest implicit time scheme is the *Backward Euler Method*, where the global nodal and velocity displacements in the next time step are approximated by:

$$\mathbf{d}_{n+1} = \mathbf{d}_n + \Delta t\, \dot{\mathbf{d}}_{n+1} \text{ and } \dot{\mathbf{d}}_{n+1} = \dot{\mathbf{d}}_n + \Delta t\, \ddot{\mathbf{d}}_{n+1}\,, \tag{1.98}$$

where $\mathbf{d}_{n+1}$, $\dot{\mathbf{d}}_{n+1}$, and $\ddot{\mathbf{d}}_{n+1}$ represent the global nodal displacements, velocities and accelerations at time step t_{n+1}, respectively. One of the most popular implicit schemes is *Newmark's Method*, where the displacements and velocites are approxi-

mated by the following expressions:

$$\begin{aligned}\mathbf{d}_{n+1} &= \mathbf{d}_n + \Delta t\,\dot{\mathbf{d}}_n + \left\{\left(\frac{1}{2}-\alpha\right)\ddot{\mathbf{d}}_n + \alpha\ddot{\mathbf{d}}_{n+1}\right\}\Delta t^2 \\ \dot{\mathbf{d}}_{n+1} &= \dot{\mathbf{d}}_n + \left\{(1-\delta)\ddot{\mathbf{d}}_n + \alpha\ddot{\mathbf{d}}_{n+1}\right\}\Delta t\end{aligned} \tag{1.99}$$

where δ and α are independent parameters that can be set by the user, but are limited to the following intervals: $0 \leq \alpha \leq 0.5$ and $0 \leq \delta \leq 1$.

Since these relations depend on unknown quantities at time t_{n+1}, a system of algebraic equations will result upon their introduction into (1.96). This system of equations can have either the nodal accelerations or the displacements as unknowns since one variable can be determined from the other with (1.98) or (1.99). The solution of the system of equations is solved, typically, with *Newton's Method*. The method consists of an iterative process where a successively better approximation is found until a predefined tolerance value is reached. The method is implemented through the linearization of the residuum $\mathbf{R}$ by taking the first terms of the Taylor's series expansions. The approximation for the i^th iteration step is given by

$$\mathbf{R}(\mathbf{d}_{n+1}) = \mathbf{R}(\mathbf{d}^i_{n+1}) + \left[\frac{\partial \mathbf{R}}{\partial \mathbf{d}}\right]\Delta\mathbf{d} = \mathbf{R}(\mathbf{d}^i_{n+1}) + \mathbf{K}_T\,\Delta\mathbf{d} = \mathbf{0}\,, \tag{1.100}$$

where $\mathbf{K}_T$ is known as the tangential stiffness matrix. The method requires the inversion of this matrix in order to calculate the update of the displacements:

$$\Delta\mathbf{d} = -\mathbf{K}_T^{-1}\,\mathbf{R}(\mathbf{d}^i_{n+1})\,. \tag{1.101}$$

The displacements for the next iteration step are then updated:

$$\mathbf{d}^{i+1}_{n+1} = \mathbf{d}^i_{n+1} + \Delta\mathbf{d}\,, \tag{1.102}$$

where the initial value for the displacements is the converged value of the last time step: $\mathbf{d}^0_{n+1} = \mathbf{d}_n$. Implicit schemes possess the advantage of being unconditionally stable. This means that the solution will not grow out of bounds for any step size. The step size is, however, limited for accuracy and convergence reasons. The step size needs to be small enough to provide accurate results and to allow the *Newton Method* to converge. Problems with a highly non-linear behavior will require a large number of iterations or, in some cases, may even fail to approach a better solution due to the inadequacy of the tangential stiffness matrix. A smaller time step may be required in some cases for the Newton Method to converge. This, however, may greatly increase the computational cost since in an implicit scheme the cost per time step is unknown. Large models are computationally very expensive because the size of the tangential stiffness matrix is directly proportional to the size of the model. Implicit schemes are usually preferred for problems with low frequency content and mild non-linearities.

Explicit Time Integration Schemes

The most basic explicit time scheme is the *Forward Euler Method*. Here, the global nodal displacements and velocities for the next step are approximated with the following expressions:

$$\begin{aligned} \mathbf{d}_{n+1} &= \mathbf{d}_n + \Delta t\, \dot{\mathbf{d}}_n \\ \dot{\mathbf{d}}_{n+1} &= \dot{\mathbf{d}}_n + \Delta t\, \ddot{\mathbf{d}}_n \,. \end{aligned} \tag{1.103}$$

The favorite explicit time scheme for solid mechanics is the *Central Difference Scheme*, where the velocities and accelerations are approximated by

$$\begin{aligned} \dot{\mathbf{d}}_n &= \frac{\mathbf{d}_{n+1} - \mathbf{d}_{n-1}}{2\Delta t}, \\ \ddot{\mathbf{d}}_n &= \frac{\mathbf{d}_{n+1} - 2\mathbf{d}_n + \mathbf{d}_{n-1}}{\Delta t^2} \,. \end{aligned} \tag{1.104}$$

Using the first definition in (1.104) we can calculate the velocity at time $t_{n+1/2}$ as

$$\dot{\mathbf{d}}_{n+1/2} = \frac{\mathbf{d}_{n+1} - \mathbf{d}_n}{\Delta t} \,, \tag{1.105}$$

which can now be used to redefine the acceleration in (1.104) as

$$\ddot{\mathbf{d}}_n = \frac{\dot{\mathbf{d}}_{n+1/2} - \dot{\mathbf{d}}_{n-1/2}}{\Delta t} \,. \tag{1.106}$$

The approximations used to calculate the displacements at time t_{n+1} are given as

$$\begin{aligned} \mathbf{d}_{n+1} &= \mathbf{d}_n + \dot{\mathbf{d}}_{n+1/2}\Delta t \,, \\ \dot{\mathbf{d}}_{n+1/2} &= \dot{\mathbf{d}}_{n-1/2} + \ddot{\mathbf{d}}_n \Delta t \,. \end{aligned} \tag{1.107}$$

The acceleration at time t_n can be calculated for both schemes according to (1.97):

$$\ddot{\mathbf{d}}_n = \mathbf{M}^{-1}\mathbf{F}_n \,. \tag{1.108}$$

We can observe that calculating the acceleration is numerically very efficient if the mass matrix $\mathbf{M}$ is diagonal, since inversion of the matrix is not required. This is accomplished through the use of a so-called *lumped mass matrix*. The employment of such a matrix is essential for explicit schemes. Most high order elements are not available in FEM programs using explicit schemes since a lumped mass matrix only

gives reasonable results for linear elements. An exception is given by second-order tetrahedral elements with modified interpolation functions.

As discussed earlier, explicit schemes are conditionally stable. In the case of the *central difference method*, the critical time step Δt_{cr} for a system of equations is given by

$$\Delta t_{cr} = \frac{2}{\omega_{max}}\,, \tag{1.109}$$

where ω_{max}, is the highest eigenfrequency of the system. The condition arises from the requirement that the discrete time step must be smaller than the time needed for a wave to travel between adjacent nodes on the spatial discretization. In large models the maximum eigenfrequency will usually be very high. As a result, the critical time step will be extremely small. Even smaller time steps may be required for accuracy reasons. A technique that allows larger time steps is known as *mass scaling*. The main idea is to add mass in order to reduce the value of the maximum eigenfrequency while affecting the general behavior as little as possible. The natural frequency of an elastic rod is obtained with the following expression

$$\omega = 2\sqrt{\frac{E}{\rho}}\,L\,, \tag{1.110}$$

where ρ is the density, E the Young's modulus and L the length of the rod. Increasing the density will reduce the natural frequency, which results in a larger time step. In a similar manner, adding nodal mass in a finite element will increase the density and therefore the time step. *Mass scaling* is particularly useful when localized small elements are reducing the overall time step or when quasi-static analyses are carried.

1.4 Contact Mechanics

The presence and importance of contact in the masticatory system is clear: During the chewing process the bolus between the teeth is ground and destroyed under forces resulting from contact, the articular disc slides between the fossa and the condyle during opening and closing of the jaw, etc. The difficulties associated with accurately modeling contact (as well as large displacements and deformations) has driven many authors with comprehensive models [4, 5], to greatly simplify the behavior of the temporomandibular joint and the forces produced in mastication, by means of nodal forces and constraints.

In this section, a short overview of contact mechanics and its treatment within the finite element method will be presented. For further details on this topic see [6].

1.4.1 Contact Kinematics

Contact is defined in the IBVP as a constraint condition where a particle of the surface of a body cannot penetrate the surface of another. Under the assumption that both bodies undergoing contact, are deformable, one characterizes the undeformed bodies at the initial time t_0 as B_0^i, where $i = 1, 2$ denotes each of the bodies, and their deformed configurations as B_t^i. The function $\boldsymbol{\chi}$ maps points $\mathbf{X}^i$ from the reference configuration onto points $\mathbf{x}^i$ in the actual configuration. The boundaries of the bodies are separated, as done previously, into Γ_u^i and Γ_t^i representing the surfaces under *Dirichlet* and *Neumann* boundary conditions. An additional surface representing the boundary under contact conditions is denoted as Γ_c^i (cf. Fig. 1.10).

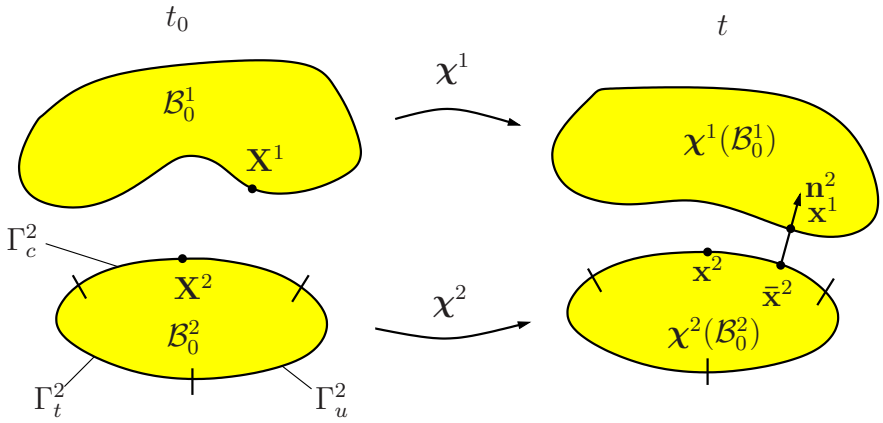

Figure 1.10: Domains of a contact problem ($\mathcal{B}_0^1$: body defined as slave, $\mathcal{B}_0^2$: body defined as master)

The surfaces may not overlap each other and together they represent the complete boundary:

$$\Gamma^i = \Gamma_u^i \cup \Gamma_t^i \cup \Gamma_c^i \text{ and } \Gamma_t^i \cap \Gamma_u^i = \Gamma_t^i \cap \Gamma_c^i = \Gamma_u^i \cap \Gamma_c^i = \emptyset \quad (i = 1, 2). \tag{1.111}$$

Since the surfaces getting into contact are not known a priori, they must be determined in every time step in the actual configuration. First, we distinguish the surfaces by defining one as the *master* surface and the other as the *slave* surface. The master surface is parameterized using convective coordinates $\boldsymbol{\xi} = (\xi^1, \xi^2)$ in both, the reference $\mathbf{X}^2 = \mathbf{X}^2(\xi^1, \xi^2)$ and actual configuration $\mathbf{x}^2 = \mathbf{x}^2(\xi^1, \xi^2)$. The tangent vectors are defined as $\mathbf{A}_\alpha^2 = \hat{\mathbf{X}}_{,\alpha}^2(\xi^1, \xi^2)$ and $\mathbf{a}_\alpha^2 = \hat{\mathbf{x}}_{,\alpha}^2(\xi^1, \xi^2)$ in the reference and actual configuration, respectively. The point $\bar{\mathbf{x}}^2 = \mathbf{x}^2(\bar{\boldsymbol{\xi}})$ on the *master* surface Γ_c^2 with the minimum distance to a fixed point $\mathbf{x}^1$ in the *slave* surface is determined by

$$\bar{\mathbf{x}}^2 = \arg \min_{\mathbf{x}^2 \subseteq \Gamma^2} \|\mathbf{x}^1 - \mathbf{x}^2(\boldsymbol{\xi})\| \,. \tag{1.112}$$

Once the point has been found, a gap function g_N determines the state between both contact surfaces

$$g_N = [\mathbf{x}^1 - \mathbf{x}^2(\bar{\boldsymbol{\xi}})] \cdot \mathbf{n}^2(\bar{\boldsymbol{\xi}}) \,, \tag{1.113}$$

where $\bar{\mathbf{n}}^2$ is the unit outward normal of the *master* surface and can be obtained by

$$\bar{\mathbf{n}}^2 = \frac{\bar{\mathbf{a}}_1^2 \times \bar{\mathbf{a}}_2^2}{\|\bar{\mathbf{a}}_1^2 \times \bar{\mathbf{a}}_2^2\|} \,. \tag{1.114}$$

The interpenetrability is then defined as

$$g_N \geq 0 \,, \tag{1.115}$$

where a negative value for g_N denotes penetration between the surfaces and a value of zero means perfect contact. In the weak form of the *Balance of Momentum*, applied surface forces are denoted with the help of the traction vector $\bar{\mathbf{t}}$. In contact mechanics, additional unknown surface forces arising from contact are introduced, which are denoted by the contact traction vector $\bar{\mathbf{t}}_\mathbf{c}$.

The contact traction forces in vector $\bar{\mathbf{t}}_\mathbf{c}$ are decomposed into normal and tangential components:

$$\mathbf{t_c} = \mathbf{t}_N + \mathbf{t}_T = (-t_N)\mathbf{n} + (-t_T)\boldsymbol{\tau} \,, \tag{1.116}$$

where t_N is the normal contact force and must be negative as a compressive force, $\mathbf{n}$ the unit normal vector, t_T the tangential forces (acting in the opposite direction of the movement) and $\boldsymbol{\tau}$ is the unit tangent vector. Normal contact forces result from the constraints introduced to avoid penetration, while tangential forces are the product of frictional constitutive equations. In non-frictional problems, only normal contact forces are present.

1.4.2 Contact Constraints

The normal constraints are mathematically formulated with the so-called *Karush-Kuhn-Tucker* (KKT) conditions:

$$1)\, g_N \geq 0, \qquad 2)\, t_N \leq 0, \qquad 3)\, t_N\, g_N = 0. \tag{1.117}$$

The first expression in (1.117) is the interpenetrability condition. The second expression demands that normal contact forces be compressive. Finally, the third expression is a complementary condition that requires contact forces to be zero if there is a gap between the bodies. If the contact forces are less than zero (meaning that compression forces are present) then no gap between the bodies can exist.

Tangential constraints are introduced with the help of constitutive equations, the best known being *Coulumb*'s friction law, where the only material parameter is the coefficient of friction μ. In this law, two different conditions exist, namely the *sticking* and *sliding* conditions. The *sticking* condition occurs when the tangential force is lower than the normal force t_N times the coefficient of *static* friction μ_s :

$$t_T \leq \mu_s \, t_N \implies \dot{\mathbf{g}}_T = 0 \quad \text{(sticking)} \,, \tag{1.118}$$

where $\mathbf{g}_T$ is the tangential slip. In this case, the tangential forces are obtained from the equilibrium equation. If the tangential forces surpass this limit a sliding motion will begin. To mantain this motion, the driving force must be greater than the normal force t_N times the coefficient of *dynamic* friction μ_d, which will be the resulting frictional force acting in the opposite direction of the sliding motion:

$$t_T > \mu_s \, t_N \implies \dot{\mathbf{g}}_T \neq 0 \,, \quad \mathbf{t}_T = -\mu_d \, t_N \, \frac{\dot{\mathbf{g}}_T}{\|\dot{\mathbf{g}}_T\|} \quad \text{(sliding)} \,. \tag{1.119}$$

The frictional problem can be solved analogously to the standard plastic problem [**?**] a trial step is performed to determine the current condition, with a return map being applied in the case of sliding. A "yield function" $\mathbf{\Phi}$ is defined

$$\mathbf{\Phi} := \|t_T\| - \mu \, t_N \,, \tag{1.120}$$

with the tangential slip defined under sliding conditions as:

$$\dot{\mathbf{g}}_T = \dot{\lambda} \frac{\mathbf{t}_T}{\|\mathbf{t}_T\|}, \tag{1.121}$$

which allows the definition of the necessary conditions for Coulomb friction law in Karush-Kuhn-Tucker form:

$$1) \, \mathbf{\Phi} \leq 0, \qquad 2) \, \dot{\lambda} \geq 0, \qquad 3) \, \mathbf{\Phi} \, \dot{\lambda} = 0. \tag{1.122}$$

These conditions enforce the maximum value of the frictional forces and ensure that no sliding occurs if the tangential forces are below the sticking condition limit. These conditions have been defined assumming that the coefficients of friction are equal ($\mu_s = \mu_d = \mu$). Usually the static coefficient of friction is, however, larger than the dynamical one and a relation is necessary for the transition from one to another. One such relation involving the relative sliding velocity $\dot{g_T}$ is given by

$$\mu(\dot{\mathbf{g}_T}) = \mu_d + (\mu_s - \mu_d) e^{c\|\dot{\mathbf{g}}_T\|}. \tag{1.123}$$

1.4.3 Inclusion of Contact Mechanics into the IBVP

The weak formulation of the IBVP in (1.87) describes a single body under *Dirichlet* and *Neumann* conditions. The introduction of the contact conditions results in an inequality equation. Since in the *Finite Element Method* these conditions are formulated as active and inactive conditions, the weak form of *balance of momentum* can be expressed as an equality equation. The *balance of momentum* for two deformable bodies undergoing contact can be expressed as:

$$\sum_{i=1}^{2} \left\{ \int_{\Omega^i} \rho^i \, \ddot{\mathbf{u}}^i \cdot \delta\mathbf{u}^i \, \mathrm{d}v^i + \int_{\Omega^i} \mathbf{T}^i : \operatorname{grad} \delta\mathbf{u}^i \, \mathrm{d}v^i - \int_{\Gamma^i} \bar{\mathbf{t}}^i \cdot \delta\mathbf{u}^i \, \mathrm{d}a^i - \int_{\Omega^i} \rho^i \, \mathbf{b}^i \cdot \delta\mathbf{u}^i \, \mathrm{d}v^i \right.$$
$$\left. - \int_{\Gamma_c^i} \mathbf{t_c}^i \cdot \delta\mathbf{u}^i \, \mathrm{d}a^i = 0 \right\}, \quad (1.124)$$

where the last term is the contact contribution. Equilibrium requires that the forces between the contact surfaces be equal and in opposite direction $\mathbf{t_c}^1 \, \mathrm{d}a^1 = -\mathbf{t_c}^2 \, \mathrm{d}a^2$ which allows the formulation of the contact contribution in the following manner:

$$\sum_{i=1}^{2} \left\{ - \int_{\Gamma_c^i} \mathbf{t_c}^i \cdot \delta\mathbf{u}^i \, \mathrm{d}a^i \right\} = - \int_{\Gamma_c^1} \mathbf{t_c}^1 \cdot (\delta\mathbf{u}^1 - \delta\mathbf{u}^2) \mathrm{d}a^1 \,, \quad (1.125)$$

with the integration being carried out only over the slave surface. Introducing (1.116) one obtains

$$- \int_{\Gamma_c^1} \mathbf{t_c}^1 \cdot (\delta\mathbf{u}^1 - \delta\mathbf{u}^2) \mathrm{d}a^1 = \int_{\Gamma_c^1} (t_N \mathbf{n} + t_T \boldsymbol{\tau}) \cdot (\delta\mathbf{u}^1 - \delta\mathbf{u}^2) \, \mathrm{d}a^1 \,. \quad (1.126)$$

We now represent the tangent force with its contravariant component t_T^α and covariant basis $\mathbf{a}_\alpha$ and expand the dot product

$$\int_{\Gamma_c^1} [t_N \mathbf{n} \cdot (\delta\mathbf{u}^1 - \delta\mathbf{u}^2) + t_T^\alpha \mathbf{a}_\alpha \cdot (\delta\mathbf{u}^1 - \delta\mathbf{u}^2)] \, \mathrm{d}a^1 \,. \quad (1.127)$$

The variations of the gap function g_N ("test functions") and the convective coordinates $\bar{\xi}^\beta$ are introduced as

$$\begin{aligned} \delta g_N &= (\delta\mathbf{x}^1 - \delta\bar{\mathbf{x}}^2) \cdot \mathbf{n} = (\delta\mathbf{u}^1 - \delta\bar{\mathbf{u}}^2) \cdot \mathbf{n} \,, \\ \delta\bar{\xi}^\beta &= m^{\alpha\beta} (\delta\mathbf{u}^1 - \delta\bar{\mathbf{u}}^2) \cdot \mathbf{a}_\alpha \,, \end{aligned} \quad (1.128)$$

where $m^{\alpha\beta}$ is the inverse of the metric of the convective coordinates system. The metric $m_{\alpha\beta}$ is given by

$$m_{\alpha\beta} = \mathbf{a}_\alpha \cdot \mathbf{a}_\beta \,. \tag{1.129}$$

The inverse of the metric $m^{\alpha\beta} = (m_{\alpha\beta})^{-1}$ allows us to obtain the contravariant vector $\mathbf{a}^\alpha$ associated with the covariant vector $\mathbf{a}_\alpha$

$$\mathbf{a}^\alpha = m^{\alpha\beta}\mathbf{a}_\beta. \tag{1.130}$$

Introducing (1.128) into (1.127) yields the weak form of the contact contribution

$$\int_{\Gamma_c^1} [t_N \delta g_N + t_{T_\alpha} \delta \bar{\xi}^\alpha] \, \mathrm{d}a^1 \,, \tag{1.131}$$

where $t_{T\alpha}$ represents the covariant component of the tangent force.

1.4.4 Regularization with Penalty Method

Several methods exist in order to satisfy the contact constraints, some of the most popular are the *Lagrange Multiplier Method*, the *Penalty Method* and the *Augmented Lagrange Method*. The available methods vary between FEM implementations (in software packages) and time integration schemes. In LS-DYNA, three distinct methods to handle contact have been implemented, namely the *Kinematic Constraint Method*, the *Penalty Method*, and the *Distributed Parameter Method*. In the present work, contact is enforced through the *Penalty Method*, which requires the gap function g_N to be reformulated into a penetration function $\bar{g_N}$

$$\bar{g_N} = \begin{cases} (\mathbf{x}^1 - \bar{\mathbf{x}}^2) \cdot \mathbf{n} & \text{if} \quad (\mathbf{x}^1 - \bar{\mathbf{x}}^2) \cdot \mathbf{n} < 0 \\ 0 & \text{if} \quad (\mathbf{x}^1 - \bar{\mathbf{x}}^2) \cdot \mathbf{n} \geq 0 \end{cases} \tag{1.132}$$

In the *Penalty Method*, normal contact forces are a product between the penetration function $\bar{g_N}$ and a penalty parameter ϵ_N whose value is defined by the user. This corresponds to a spring becoming active during penetration to push the penetrating node back to the surface. The normal contact force is defined as

$$t_N = \epsilon_N \bar{g_N}. \tag{1.133}$$

The correct enforcement of the contact constraint (no penetration) can be obtained when $\epsilon_N \to \infty$. Large values of ϵ_N may, however, lead to a badly conditioned

numerical problem. For the frictional case, a tangential penalty parameter ϵ_T is used to regularize the tangential slip velocity (Eq. 1.121):

$$\dot{\mathbf{g}}_T - \dot{\lambda}\frac{\mathbf{t}_T}{\|\mathbf{t}_T\|} = -\frac{1}{\epsilon_T}\frac{d\,\mathbf{t}_T}{dt}, \tag{1.134}$$

This equation has the following covariant form:

$$m_{\alpha\beta}\dot{\xi^{\beta}} - \dot{\lambda}\frac{t_{T_\alpha}}{\|\mathbf{t}_T\|} = -\frac{1}{\epsilon_T}\frac{d\,t_{T_\alpha}}{dt}, \tag{1.135}$$

The trial step is calculated under the assumption of stick conditions, therefore $\dot{\lambda} = 0$. If a backward Euler scheme is employed along a linear approximation of the master surface, then the trial step has the following form:

$$t_{T_\alpha}^{tr,(n+1)} = t_{T_\alpha}^{(n)} - \epsilon_T m_{\alpha\beta}(\xi^{\beta}_{(n+1)} - \xi^{\beta}_{(n)}). \tag{1.136}$$

The yield function can then be computed to determine if the contact is occurring under *sliding* or *sticking* conditions. The tangential force is defined for each case in the following manner

$$t_{T_\alpha}^{(n+1)} = \begin{cases} t_{T_\alpha}^{tr,(n+1)} & \text{if} \quad \mathbf{\Phi}_{n+1} < 0 \,(\text{sticking}) \\ \mu\, t_{N_{n+1}} \dfrac{t_{T_\alpha}^{tr,(n+1)}}{\|\mathbf{t}_{T_\alpha}^{tr,(n+1)}\|} & \text{if} \quad \mathbf{\Phi}_{n+1} \geq 0 \,(\text{sliding}) \end{cases} . \tag{1.137}$$

Chapter 2:
Geometry Creation and Discretization

The creation of a realistic finite element model requires the preparation of an accurate geometry. The anatomical components of the masticatory system are very complex and diverse, each demanding different strategies to achieve a correct representation. The next step consists of creating a mesh where each of the anatomical structures is discretized. This process involves the selection of appropriate element types in order to obtain an efficient and accurate model.

2.1 Geometry Creation

The creation of a component's geometry is a convoluted process which can be summarized in the following steps: Segmentation of the structure, edition/repair of the geometry, and conversion to a compatible CAD format. Once the geometry has been imported into a pre-processing software, it is converted into a solid volume, which can then be assembled into the overall model. Since the components of the masticatory system have complex surfaces and fit very tightly, geometries typically require adjustments before being successfully assembled. A workflow diagram of this process can be observed in Figure 2.1. Structures with geometries obtained through the segmentation process include the cortical and cancellous bone sections of the jaw, the teeth, the fossa and, to some extent, the articular disc. Geometries obtained with a different strategy are described later.

2.1.1 Image Segmentation of the Relevant Structures

Image segmentation is the process of extracting an anatomical structure from a set of CT- (computer tomography) or MRI- (magnetic resonance imaging) scans. These scans consist of a set of images/slices covering a predefined distance along an anatomical axis with a predefined distance between the individual images. The desired component is colored in each slice, these individual sketches are then assembled into a 3D representation by the segmentation software (Fig. 2.2). The University of Greifswald provided CT-scans that belonged to a patient with a recent wisdom tooth extraction. These scans were obtained using a CBCT (cone beam computed tomography) scanner. The software employed for the segmentation was "Mimics Innovation Suite 14" [7] which can automatically identify anatomical structures from medical images such as DVT-scans by their grayscale values. This

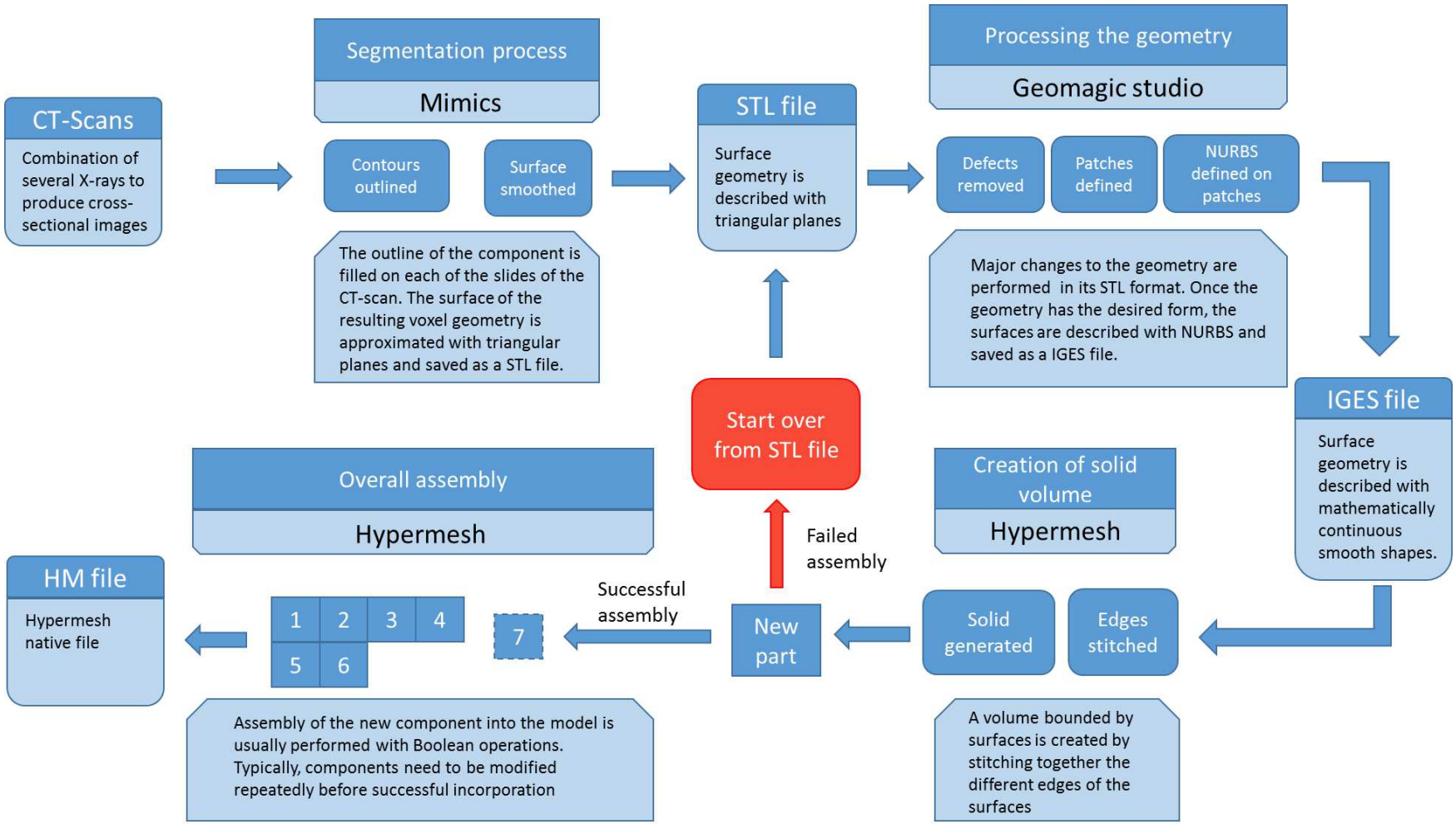

Figure 2.1: Workflow diagram of the geometry creation process.

automatic segmentation requires that the user defines a threshold for the grayscale which determines the components to be isolated from the scans. Figure 2.3 shows the result of performing an automatic segmentation on the DVT scans used in our model.

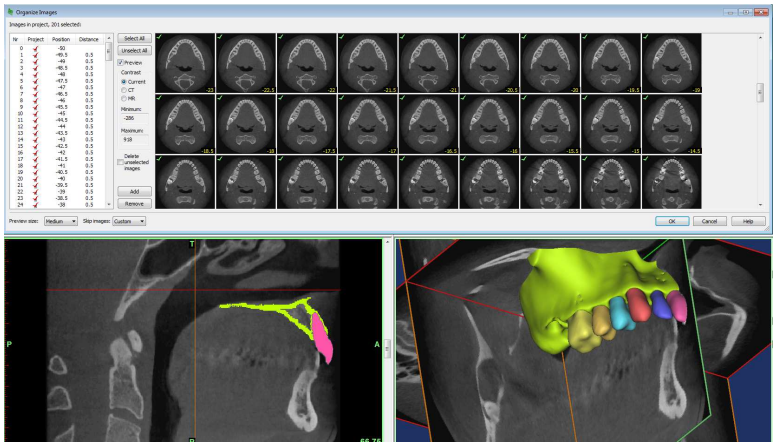

Figure 2.2: Segmentation of the maxilla

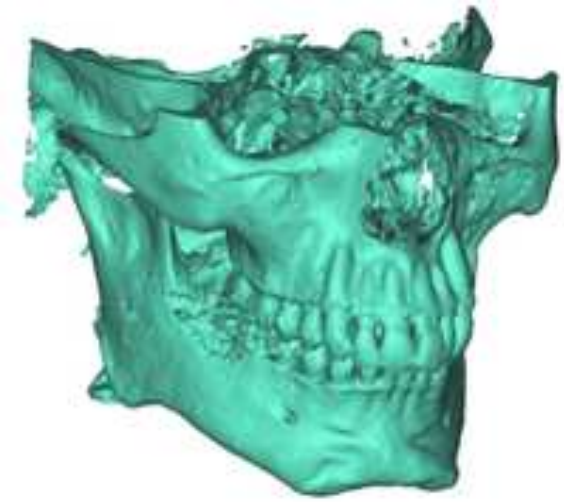

Figure 2.3: Automatically generated 3D-model of a patient's skull and teeth by segmentation

The problem, however, is that there is no automatic way of isolating a separate component, when other structures have the same grayscale. In the case of mineralized tissue, where all structures lie within the same grayscale threshold, one can observe (Figure 2.3) that not only the bone, but also the teeth are segmented. The creation of the finite element model requires, however, that the components be independently identified, so that e.g. material properties, contact areas and boundary conditions can be correctly assigned.

Furthermore, the creation of our model required the segmentation of each tooth, each periodontium, the cortical and spongy bone and the articular disc of the TMJ, separately. This required a time-consuming manual segmentation procedure where the contours of each component were outlined and stored in each slice of the scan. Afterwards, the outlines were filled. The surface of the voxel geometry is approximated with triangular planes, which results in a rough surface that can be smoothed before being exported. 3D representations of all structures were created with a high degree of accuracy (Fig. 2.4).

Figure 2.4: 3D representation of the individually segmented structures

2.1.2 Processing of the 3D Model

The result of the segmentation process is a set of STL (STereoLithography) files each associated with a corresponding component. A STL file describes the geometric surface of a 3D object using a triangular representation. In order to use these 3D-models, the STL files need to be converted into a format which can be recognized by a finite element preprocessing program such as Hypermesh [8]. The tool used for this conversion was "Geomagic Studio 12" [9], a reverse engineering software that allows a wide range of operations to modify the model. Before the files were converted, however, defects such as spikes and holes resulting from the segmentation process must be repaired (Fig. 2.5).

The STL files are converted into the IGES (Initial Graphics Exchange Specification) format (standard file for geometries) by creating several NURBS (Non-uniform rational B-spline) that closely match the surface represented by the STL file. The first step involves the creation of contour lines, which divide the model in a series of major surfaces (Fig. 2.6). The purpose of this step is to avoid having steep curvatures in a surface.

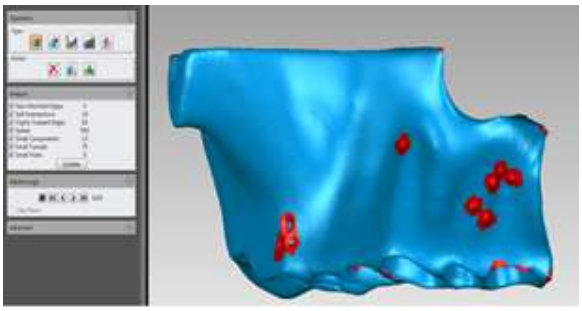

Figure 2.5: Repairing the geometry defects

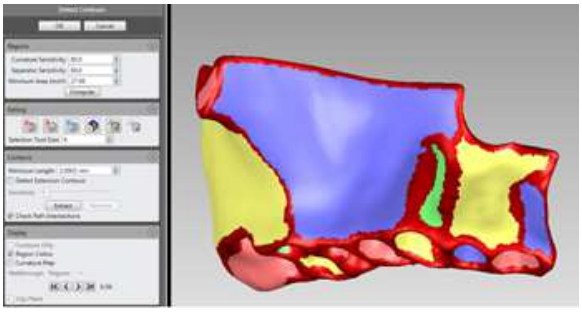

Figure 2.6: Definition of the contour lines

This step is followed by the placement of patches, quadrilateral areas where the NURBS surfaces are subsequently defined (Figure 2.7). The patch layout is governed by the major surfaces created in the last step. At this point the object is ready to be exported as an IGES object, which is compatible with most preprocessing and finite element softwares. Careful selection of the contour lines is required to obtain an acceptable distribution of the patches, and even then, in most occasions these must be manually redone.

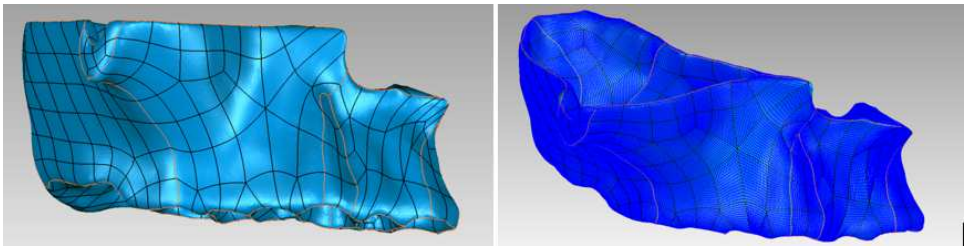

Figure 2.7: Patch distribution/grids of NURBS surfaces

2.1.3 Creation of Solid Volumes

The IGES files contain only the surfaces of the geometry, whereas a solid volume is required to create a mesh. With Hypermesh [8], solid volumes can be created

with bounding surfaces. The surfaces in the IGES file usually are missing some areas that would produce a sealed volume, which need to be created. Additionally, surface edges may have to be stitched together as they could be incorrectly imported by the software. Once a solid volume is at hand, the geometry can be joined together with the rest of the model by means of Boolean operations. If any significant change of the geometry is required, then it must be applied on the STL files, which involves repeating the process.

2.1.4 Creation of the PDL

The PDL is an extremely thin tissue that is not visible in typical scans. Its dimensions require scans obtained with high-resolution scanners in order to properly segment its geometry. Although the mechanical properties and geometries vary greatly between publications, the majority of the models depict the PDL as having a constant thickness. It is shown by [10] that the results in the stress distributions are practically insensitive to the thickness distribution throughout the PDL. They are, however, significantly affected by the overall PDL thickness.

The resolution of the available scans was not adequate to properly segment the PDL. To circumvent this problem, the geometry was obtain by means of Boolean operations. The majority of CAD programs have Boolean operations available in some form that are, typically, reserved between solids (a geometry that is completely bound by surfaces). The use of this type of operations is fundamental for the correct connectivity of the model and the modification of the geometries. Applying these operations between geometries that are described by NURBS surfaces can, however, frequently end with problems as a result of the complexity of the geometries. The successful creation of the PDL required a combination of operations between "Geomagic" and the post-processing software "Hypermesh 12". In "Geomagic" a set of teeth with a positive offset of 0.25 mm was used to cut a matching set of alveolus in the jaw and maxilla. Thus, the PDLs of all teeth had a constant thickness of 0.25 mm. The final volumes (Figure 2.8) were created in Hypermesh.

2.1.5 Creation of the Temporomandibular Joint (TMJ)

The main structures that compose the temporomandibular joint are the condyle, the mandibular fossa, both covered by a cartilage layer, and the articular disc. The condyle and the mandibular fossa were obtained during the segmentation process. The disc and its attachments were, however, not visible in the CT-scan. Creating its geometry was achieved by following shapes introduced in anatomy books. The articular disc undergoes significant movements during its natural function. Achieving an accurate movement of the disc in the model requires a smooth fit of that

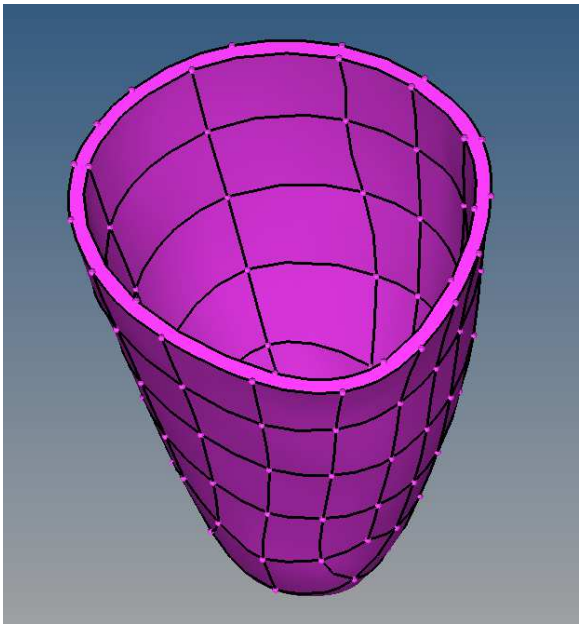

Figure 2.8: Solid representation of the PDL

the superior and inferior surfaces of the articular disc between their counterparts, the surface of the fossa and the condyle, respectively. In contact mechanics, sharp gradients in the shape of the mesh can create convergence problems. Additionally, no penetration should exist between the contact surfaces in the initial state. Several iterations were required to obtain a TMJ with apt dimensions for appropriate disc movements. The cartilage layer covering the condyle and the maxillar fossa, were created using an offset operation of 0.5 mm. The geometry of the articular capsule (attachments of the disc) was deemed too complex to create as a realistic 3D-object. Furthermore, experimental data of its behavior is scarce [11]. For this reason its function was enforced with truss elements in this model. The final structure of the TMJ can be observed in Figure 2.9.

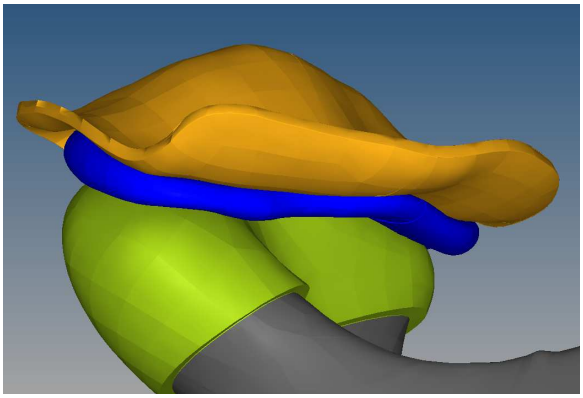

Figure 2.9: Temporomandibular joint: Cartilage of the condyle (green), articular disc (blue), and cartilage of the fossa (orange)

2.2 Mesh Generation

Once the bounding surfaces between volumes have been properly defined, the next step is to discretize the problem through the creation of a mesh. For our model, the preprocessor "Hypermesh" was used to generate the mesh. In finite element analysis, element formulation varies between software and time integration schemes. Hexahedral meshes provide both better accuracy and less computational effort, however, the process involved in their creation is considerably time-consuming. In the case of implicit schemes, high-order shape function formulations are available for hexahedral and tetrahedral elements, as well as transitional pyramid elements. These types of elements allow accurate results with a coarser mesh. In the initial stages of the model, the FEM program "ANSYS" was employed to run the simulations. The large step size possible in the implicit method allowed for smaller computational times, and a coarser mesh meant that both, the input and output files, were smaller, thus saving time during the transfer of files with the high-performance computing cluster. The advantage of the implicit method is, however, quickly lost as the complexity of the model grows. The increasing number of elements, as further components of the masticatory system were introduced, resulted in convergence problems with smaller time steps being required. It has been shown (e.g. [12]) that the introduction of contact has a minor effect on the size of the explicit time increments, but significantly reduces the size of the implicit increments. In our model, the introduction of the highly non-linear behavior of the PDL in addition to the contact of the disc with the fossa and the condyle resulted in a time step that made the implicit method impractical. The model was therefore run with LS-DYNA's explicit scheme. This resulted in a great reduction of computational time and avoided convergence problems altogether.

2.2.1 Solid Element Formulations in LS-DYNA

The transition from ANSYS to LS-DYNA required extensive modification of the mesh. Since available element formulations differ between the programs, the mesh required further local refinement in order to ensure that results were accurate. The available element formulations in LS-DYNA are shown in Table 2.1.

In LS-DYNA, hexahedral elements should be employed whenever possible with either formulations 1, 2, or 3. Hourglass control is required in the case of reduced integration. If the structure is complex, then tetrahedrons type 4, 13, 16, or 17 can be used. Type 13 should be employed in the case of large strains. In our model, the solid element formulations employed were 1, 10, and 13. Element formulation type 1 is a 8-node hexahedral element with reduced integration which requires hour glass control. Formulation 10 is a 4-node tetrahedral element with a single integration

Element formulation	Shape	Integration	Timestep size*	Remarks
-2	Hexahedron	selective reduced	1.0	suitable for poor aspect ratios, accurate formulation
-1	Hexahedron	selective reduced	1.0	suitable for poor aspect ratios, efficient formulation
1	Hexahedron	reduced	1.0	needs hourglass stabilization
2	Hexahedron	selective reduced	1.0	no hourglass stabilization required
3	Hexahedron	full	1.0	8 node quadratic brick element with nodal rotations
4	Tetrahedron	selective reduced	0.69	4 node quadratric tetrahedron with nodal rotations
10	Tetrahedron	1-point	0.82	stiff behavior (volumetric locking)
13	Tetrahedron	1-point	0.82	nodal pressure averaging, alleviated volumetric locking
16	Tetrahedron	4(5) point	0.32	10 node quadratic tetrahedron, good accuracy at moderate strains
17	Tetrahedron	4(5) point	0.27	10 node composite tetrahedron
15	Pentahedron	2 point	0.52	transition element
115	Pentahedron	1 point reduced	1.0	transition element

*for solid elements with same edge length

Table 2.1: Element formulations in LS-DYNA

point, which suffers from shear and volumetric locking. Formulation 13 is also a 4-node tetrahedral element but it employs an average element pressure to calculate the volumetric component of the internal virtual work which helps alleviate volumetric locking. However, the element is still affected by shear locking. In the next section, a brief overview of these elements is discussed.

Element Formulation Overview

In the *Finite Element Method*, the shape functions used for the approximation function in (1.90) employ an isoparametric formulation in order to map the elements from the global coordinate system into a local one. To this end, the shape functions

are constructed upon a reference element and then transferred to the global elements (Figure 2.10).

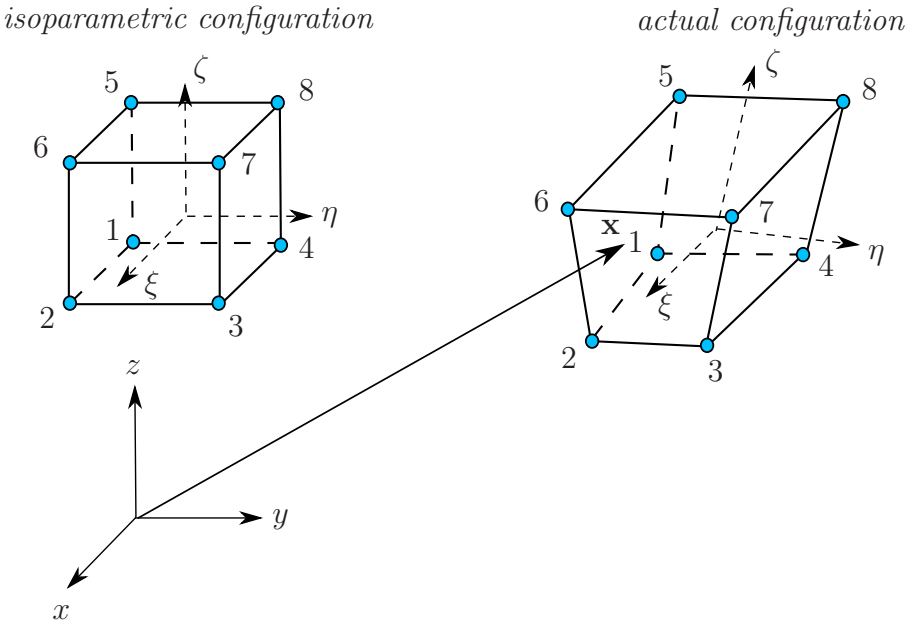

Figure 2.10: Isoparametric formulation of a brick element

The approximation function is then expressed as

$$\mathbf{u}(\mathbf{x}) \approx \mathbf{u_h}(\mathbf{x}) = \sum_{i=1}^{n} N_i(\mathbf{x}) \cdot \mathbf{d}_i = \sum_{i=1}^{n} N_i(\boldsymbol{\xi}) \cdot \mathbf{d}_i = \mathbf{N} \cdot \mathbf{d}\,. \tag{2.1}$$

As previously mentioned, n is the number of nodes that compose the element and $\mathbf{d}$ is the vector representing the nodal displacements. The interpolation matrix $\mathbf{N}$ contains the shape functions of the elements

$$\mathbf{N} = \begin{bmatrix} N_1 & 0 & 0 & N_2 & 0 & 0 & \cdots & N_n & 0 & 0 \\ 0 & N_1 & 0 & 0 & N_2 & 0 & \cdots & 0 & N_n & 0 \\ 0 & 0 & N_1 & 0 & 0 & N_2 & \cdots & 0 & 0 & N_n \end{bmatrix}, \tag{2.2}$$

and the strain-displacement matrix $\mathbf{B}$ is obtained by the following operation

$$\mathbf{B} = \begin{bmatrix} \frac{\partial}{\partial x} & 0 & 0 \\ 0 & \frac{\partial}{\partial y} & 0 \\ 0 & 0 & \frac{\partial}{\partial z} \\ \frac{\partial}{\partial y} & \frac{\partial}{\partial x} & 0 \\ 0 & \frac{\partial}{\partial z} & \frac{\partial}{\partial y} \\ \frac{\partial}{\partial z} & 0 & \frac{\partial}{\partial x} \end{bmatrix} \cdot \mathbf{N} \,. \tag{2.3}$$

The shape functions for a 8-node hexahedral element are defined as

$$N_i(\xi, \eta, \zeta) = \frac{1}{8}(1 + \xi_i\,\xi)(1 + \eta_i\,\eta)(1 + \zeta_i\,\zeta) \tag{2.4}$$

where ξ_i, η_i, ζ_i are the local coordinates of node i and can be found in Table 2.2.

i	1	2	3	4	5	6	7	8
ξ_i	-1	1	1	-1	-1	1	1	-1
η_i	-1	-1	1	1	-1	-1	1	1
ζ_i	-1	-1	-1	-1	1	1	1	1

Table 2.2: Nodal coordinates of brick element

A 4-node tetrahedral element (Figure 2.11) has the following shape functions

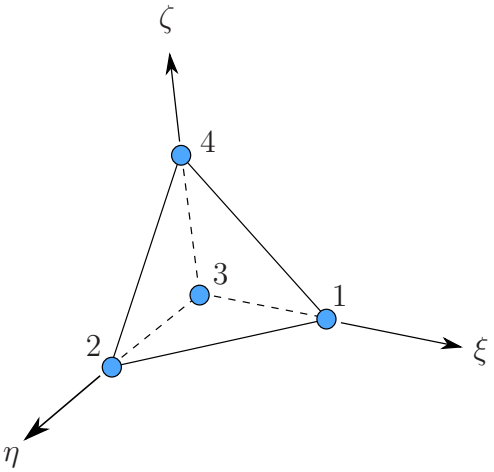

Figure 2.11: 4-node tetrahedral element

$$
\begin{aligned}
N_1(\xi,\eta,\zeta) &= \xi\,,\\
N_2(\xi,\eta,\zeta) &= \eta\,,\\
N_3(\xi,\eta,\zeta) &= 1-\xi-\eta-\zeta\,,\\
N_4(\xi,\eta,\zeta) &= \zeta\,,
\end{aligned}
\tag{2.5}
$$

where the origin of the local coordinate system is placed at one node. The range for the different coordinates, thus, is

$$
\begin{aligned}
0 &\le \xi \le 1-\eta-\zeta\,,\\
0 &\le \eta \le 1-\xi-\zeta\,,\\
0 &\le \zeta \le 1-\xi-\eta\,.
\end{aligned}
\tag{2.6}
$$

The relations between the global Cartesian coordinates x, y, z and the local element coordinates ξ, η, ζ have the following form:

$$
\begin{array}{lll}
\dfrac{\partial x}{\partial \xi} = \sum_{i=1}^{n} \dfrac{\partial N_i}{\partial \xi}\cdot x_i & \dfrac{\partial x}{\partial \eta} = \sum_{i=1}^{n} \dfrac{\partial N_i}{\partial \eta}\cdot x_i & \dfrac{\partial x}{\partial \zeta} = \sum_{i=1}^{n} \dfrac{\partial N_i}{\partial \zeta}\cdot x_i \\
\dfrac{\partial y}{\partial \xi} = \sum_{i=1}^{n} \dfrac{\partial N_i}{\partial \xi}\cdot y_i & \dfrac{\partial y}{\partial \eta} = \sum_{i=1}^{n} \dfrac{\partial N_i}{\partial \eta}\cdot y_i & \dfrac{\partial y}{\partial \zeta} = \sum_{i=1}^{n} \dfrac{\partial N_i}{\partial \zeta}\cdot y_i \\
\dfrac{\partial z}{\partial \xi} = \sum_{i=1}^{n} \dfrac{\partial N_i}{\partial \xi}\cdot z_i & \dfrac{\partial z}{\partial \eta} = \sum_{i=1}^{n} \dfrac{\partial N_i}{\partial \eta}\cdot z_i & \dfrac{\partial z}{\partial \zeta} = \sum_{i=1}^{n} \dfrac{\partial N_i}{\partial \zeta}\cdot z_i
\end{array}
\tag{2.7}
$$

According to the chain rule, the derivatives of the shape functions are given by

$$
\begin{aligned}
\frac{\partial N_i}{\partial \xi} &= \frac{\partial N_i}{\partial x}\frac{\partial x}{\partial \xi} + \frac{\partial N_i}{\partial y}\frac{\partial y}{\partial \xi} + \frac{\partial N_i}{\partial z}\frac{\partial z}{\partial \xi}\,,\\
\frac{\partial N_i}{\partial \eta} &= \frac{\partial N_i}{\partial x}\frac{\partial x}{\partial \eta} + \frac{\partial N_i}{\partial y}\frac{\partial y}{\partial \eta} + \frac{\partial N_i}{\partial z}\frac{\partial z}{\partial \eta}\,,\\
\frac{\partial N_i}{\partial \zeta} &= \frac{\partial N_i}{\partial x}\frac{\partial x}{\partial \zeta} + \frac{\partial N_i}{\partial y}\frac{\partial y}{\partial \zeta} + \frac{\partial N_i}{\partial z}\frac{\partial z}{\partial \zeta}\,.
\end{aligned}
\tag{2.8}
$$

By compiling these expressions in the "*Jacobian Matrix*" $\mathbf{J}$

$$\mathbf{J} = \begin{bmatrix} \frac{\partial x}{\partial \xi} & \frac{\partial y}{\partial \xi} & \frac{\partial z}{\partial \xi} \\ \frac{\partial x}{\partial \eta} & \frac{\partial y}{\partial \eta} & \frac{\partial z}{\partial \eta} \\ \frac{\partial x}{\partial \zeta} & \frac{\partial y}{\partial \zeta} & \frac{\partial z}{\partial \zeta} \end{bmatrix}, \tag{2.9}$$

we can rewrite Equation (2.8) as

$$\begin{bmatrix} \frac{\partial N_i}{\partial \xi} \\ \frac{\partial N_i}{\partial \eta} \\ \frac{\partial N_i}{\partial \zeta} \end{bmatrix} = \mathbf{J} \cdot \begin{bmatrix} \frac{\partial N_i}{\partial x} \\ \frac{\partial N_i}{\partial y} \\ \frac{\partial N_i}{\partial z} \end{bmatrix}. \tag{2.10}$$

The inverse relation, which is particularly useful to calculate the partial derivatives in the strain-displacement matrix, is thus given by

$$\begin{bmatrix} \frac{\partial N_i}{\partial x} \\ \frac{\partial N_i}{\partial y} \\ \frac{\partial N_i}{\partial z} \end{bmatrix} = \mathbf{J}^{-1} \cdot \begin{bmatrix} \frac{\partial N_i}{\partial \xi} \\ \frac{\partial N_i}{\partial \eta} \\ \frac{\partial N_i}{\partial \zeta} \end{bmatrix}. \tag{2.11}$$

The integrals in Equation (1.97) are transformed into the element (local) coordinate system in the following way

$$\int_{\Omega} (\cdots) \mathrm{d}v = \int_{-1}^{1} \int_{-1}^{1} \int_{-1}^{1} (\cdots) |\mathbf{J}| \, \mathrm{d}\xi \, \mathrm{d}\eta \, \mathrm{d}\zeta \,. \tag{2.12}$$

They are evaluated using numerical integration, discussed in the next section. At this point, all the relations required to solve the IBVP, are functions that either depend on the element coordinates ξ, η, ζ, or can be solved with the help of the inverse of the Jacobian.

To finish this section, the variation in formulation employed by the element type 13 to alleviate volumetric locking is discussed. In element formulation 13, the term

which contains the internal stresses $\mathbf{T}$ in equation 1.87 has its deviatoric and volumetric component evaluated separately. In the case of a hyperelastic Neo-Hookean material, the volumetric component of the strain energy density function $W_{vol}(J)$ is defined as

$$W_{vol}(J) = \frac{K}{2}(J-1)^2 \,. \tag{2.13}$$

The derivative of this expression with respect to J yields the element pressure

$$p^{(e)} = \left.\frac{\mathrm{d}W_{vol}}{\mathrm{d}J}\right|_{J^{(e)}=v^{(e)}/V^{(e)}} = K\left(\frac{v^{(e)}-V^{(e)}}{V^{(e)}}\right) . \tag{2.14}$$

where the value of $J^{(e)}$ over an element e is the ratio between the actual element volume $v^{(e)}$ and the initial element volume $V^{(e)}$. The volumetric component of the term with the internal stresses in Equation (1.87) can then be calculated with the following expression

$$\int_\Omega \mathbf{T}_{vol} : \operatorname{div}\delta\mathbf{u}\mathrm{d}v = \sum_{e=1}^{m} p^{(e)} v^{(e)} \operatorname{div}\delta\mathbf{u}^{(e)} \,, \tag{2.15}$$

where m is the number of elements over the domain. The use of Equation (2.15) results in volumetric locking for moderately large values of the Poisson ratio ν. In order to reduce the volumetric locking present in standard tetrahedral elements, an average nodal pressure tetrahedral element was proposed by [13]. First, the average nodal volumetric ratio is defined

$$J_a = \frac{v_a}{V_a} \,, \qquad v_a = \sum_{e=1}^{m_a} \frac{1}{4} v^{(e)} \,, \qquad V_a = \sum_{e=1}^{m_a} \frac{1}{4} V^{(e)} \tag{2.16}$$

where m_a is the number of elements that share node a. The average nodal pressure is then defined in the following manner:

$$p_a = \left.\frac{\mathrm{d}U}{\mathrm{d}J}\right|_{J=v_a/V_a} = K\left(\frac{v_a - V_a}{V_a}\right) \tag{2.17}$$

Subsequently, the average element pressure is defined as

$$\bar{p}^{(e)} = \frac{1}{4}\sum_{a=1}^{4} p_a^{(e)} \,, \tag{2.18}$$

which allows Equation (2.15) to be reformulated as

$$\int_\Omega \mathbf{T}_{vol} : \operatorname{div}\delta\mathbf{u}\mathrm{d}v = \sum_{e=1}^{m} \bar{p}^{(e)} v^{(e)} \operatorname{div}\delta\mathbf{u}^{(e)} \,. \tag{2.19}$$

Element formulation 13 employs this expression, which provides alleviated volumetric locking.

Numerical Integration

Analytical integration of the different functions is generally impractical. The *Finite Element Method* employs *Gaussian* quadrature to numerically evaluate the integrals. The method computes the integral of a function f through the sum of the values of the function at specific points $f(\xi_i)$ multiplied with corresponding weight parameters w_i

$$\int_{-1}^{1} f(\xi)\mathrm{d}\xi \approx \sum_{i=1}^{n_{GP}} f(\xi_i) \cdot w_i \,, \tag{2.20}$$

The accuracy of the approximation depends on the number of *Gauss* points n_{GP} used. The exact integration of a polynomial can be guaranteed by using a sufficient number of *Gauss* points. A number n of *Gauss* points will exactly integrate a polynomial of order $2n-1$.

Nesting of the individual one-dimensional integrals is carried out in order to approximate a three-dimensional domain

$$\int_{-1}^{1}\int_{-1}^{1}\int_{-1}^{1} f(\xi,\eta,\zeta)|\mathbf{J}|\,\mathrm{d}\xi\,\mathrm{d}\eta\,\mathrm{d}\zeta = \sum_{j=1}^{n_{GP}}\sum_{k=1}^{n_{GP}}\sum_{l=1}^{n_{GP}} f(\xi_j,\eta_k,\zeta_l)\,|\mathbf{J}_{jkl}|\,w_j\,w_k\,w_l \tag{2.21}$$

Table 2.3 lists the integration points for hexahedral elements. In the case of a trilinear 8-node hexahedral element, 2 *Gauss* points are required in each dimension to obtain an exact integration. This corresponds to 8 integration points in a 2 x 2 x 2 configuration (full integration).

Depending on the number of integration points, the integration can be classified into full, selective reduced or reduced integration. Using full integration has the disadvantage of being "expensive" and that the element shows pressure locking effects. Reduced integration evaluates the integral using a single point, which results in the element not exhibiting locking and in substantial savings in computational time. However, zero energy modes are present which can lead to mesh degeneration and must be handled through the use of hourglassing control. Finally, selective reduced integration uses reduced integration to calculate the hydrostatic components of the stress and full integration for the deviatoric components. This method is computationally expensive, but the elements show alleviated volumetric locking and hourglass control is not required.

The integration points for tetrahedral elements are shown in Table 2.4. 4-node linear tetrahedra are usually integrated with one integration point, while 10-node quadratic tetrahedras with four. The term reduced integration is not used for tetrahedral elements.

Scheme	**Location** (ξ_i, η_i, ζ_i) **including perturbations**	**Weights** w_i	**Number of points**
1 x 1 x 1	$(0,0,0)$	8	1
2 x 2 x 2	$\left(\pm\sqrt{\frac{1}{3}}, \pm\sqrt{\frac{1}{3}}, \pm\sqrt{\frac{1}{3}}\right)$	1	8
3 x 3 x 3	$(0,0,0)$	$\left(\frac{8}{9}\right)^3$	1
	$\left(0,0,\pm\sqrt{\frac{3}{5}}\right)$	$\left(\frac{8}{9}\right)^2\left(\frac{5}{9}\right)$	6
	$\left(0,\pm\sqrt{\frac{3}{5}}, \pm\sqrt{\frac{3}{5}}\right)$	$\left(\frac{8}{9}\right)\left(\frac{5}{9}\right)^2$	12
	$\left(\pm\sqrt{\frac{3}{5}}, \pm\sqrt{\frac{3}{5}}, \pm\sqrt{\frac{3}{5}}\right)$	$\left(\frac{5}{9}\right)^3$	8

Table 2.3: Integration points for a hexahedral element

Total number of points	**Location** $(\xi_i, \eta_i, \zeta_i, 1-\xi_i-\eta_i-\zeta_i)$ **including perturbations**	**Weights** w_i	**Number of points**
1	$\left(\frac{1}{4}, \frac{1}{4}, \frac{1}{4}, \frac{1}{4}\right)$	$\frac{1}{6}$	1
4	$\left(\frac{5-\sqrt{5}}{20}, \frac{5-\sqrt{5}}{20}, \frac{5-\sqrt{5}}{20}, \frac{5+3\sqrt{5}}{20}\right)$	$\frac{1}{24}$	4
15	$\left(\frac{1}{4}, \frac{1}{4}, \frac{1}{4}, \frac{1}{4}\right)$	$\left(\frac{16}{810}\right)$	1
	$\left(\frac{7-\sqrt{15}}{34}, \frac{7-\sqrt{15}}{34}, \frac{7-\sqrt{15}}{34}, \frac{13+3\sqrt{15}}{34}\right)$	$\frac{2665+14\sqrt{15}}{226800}$	4
	$\left(\frac{7+\sqrt{15}}{34}, \frac{7+\sqrt{15}}{34}, \frac{7+\sqrt{15}}{34}, \frac{13-3\sqrt{15}}{34}\right)$	$\frac{2665+14\sqrt{15}}{226800}$	4
	$\left(\frac{10-2\sqrt{15}}{40}, \frac{10-2\sqrt{15}}{40}, \frac{10+2\sqrt{15}}{40}, \frac{10+2\sqrt{15}}{40}\right)$	$\frac{20}{2268}$	6

Table 2.4: Integration points for a tetrahedral element

2.2.2 Truss elements and interpolation constraints

The truss element is one of the simplest elements. It consists of two nodes, each with three degrees of freedom, and can only transmit axial loads. Displacements

and velocities can be interpolated along the axis with the following expressions

$$\begin{aligned} u &= u_1 + \frac{x}{L}(u_2 - u_1)\,, \\ \dot{u} &= \dot{u_1} + \frac{x}{L}(\dot{u_2} - \dot{u_1})\,, \end{aligned} \tag{2.22}$$

where u_1 and u_2 are the displacements of the respective nodes and L is the length of the element. This expression returns u_1 with a value of $x = 0$ and u_2 when $x = L$. The strain increments can be computed with

$$\Delta\varepsilon = \frac{\dot{u_2} - \dot{u_1}}{L}\Delta t\,, \tag{2.23}$$

In LS-DYNA the strain increment is approximated using a *Central Difference Scheme* which results in the following expression

$$\Delta\varepsilon = \frac{2\,(\dot{u}_2^{\,n+\frac{1}{2}} - \dot{u}_1^{\,n+\frac{1}{2}})}{L^n + L^{n+1}}\Delta t\,. \tag{2.24}$$

The normal (internal) force N is then updated according to

$$N^{n+1} = N^n + A\,\Delta\sigma = N^n + A\,E\Delta\boldsymbol{\varepsilon}\,, \tag{2.25}$$

where A is the cross-section of the truss element. In the present model, truss elements are used to represent the muscles, tendons and disc attachments of the masticatory system. When truss elements are connected to solid elements, the connection works as a hinge, since no bending moment is transmitted. It is assumed that fibers and attachments do not transmit any moments to the bone or the disc; they are, however, attached to large surfaces. Connecting the truss elements directly to the solid elements would result in a single node carrying the load which results in a singularity. Therefore, the trusses are connected to the solid elements through the help of constraints.

The goal is to distribute the forces experienced e.g. by the tendons of the muscles over the whole attachment surface while ensuring that no artificial stiffness is introduced. For this purpose, an *interpolation constraint* is used. This constraint type interpolates the motion of a dependent node u_{dep} from the motion of a set of independent nodes according to

$$u_{dep} = \sum_{i=1}^{n_{ind}} \frac{u_i}{n_{ind}}\,, \tag{2.26}$$

where n_{ind} is the number of independent nodes. Applying a force or moment to the dependent node effectively distributes the load to the independent nodes. This

constraint is an interpolation element and not a rigid element, and as such it does not add stiffness to the structure. The element functions by transferring the loads applied at the dependent node to the center of gravity (CG) of the weighted group of independent nodes. The loads at the CG are subsequently transferred to the independent nodes according to each node's weighting factor.

2.2.3 Contact elements (Segment-to-Segment)

Several approaches are available for the discretization of the contact contribution in Eq. (1.131). In our model, the discretization is performed through the use of Node-to-Surface (NTS) contact elements. This type of element pairs the approximation of a *master surface* with a slave node and restrains the slave node from penetrating into the *master surface*. Nodes from the master surface can, however, penetrate the slave surface. A NTS contact element is composed of the nodes used to approximate the *master surface* plus the slave node. Before defining the contact element, the *slave node's* $\mathbf{n}_s$ corresponding *master surface* S_m has to be determined. This is done in two steps: First, the closest *master node* $\mathbf{n}_m$ for the given *slave node* $\mathbf{n}_s$ is found. Subsequently, the *master surface* S_m containing the closest projection point of the *slave node* between the surfaces S_i that share the *master node* $\mathbf{n}_m$ is identified. It can be shown that the node $\mathbf{n}_s$ lies in a segment $S_i\,(i = 1, 2, \cdots, n)$, if the following tests are satisfied:

$$\begin{aligned} &(\mathbf{c}_i \times \mathbf{s}) \cdot (\mathbf{c}_i \times \mathbf{c}_{i+1}) > 0\,, \\ &(\mathbf{c}_i \times \mathbf{s}) \cdot (\mathbf{s} \times \mathbf{c}_{i+1}) > 0\,, \end{aligned} \tag{2.27}$$

where the vectors $\mathbf{c}_i$, and $\mathbf{c}_{i+1}$, originate from node $\mathbf{n}_m$ and lie along the edges of segment S_i. Vector $\mathbf{s}$ is the projection from vector $\mathbf{g}$, a vector originating at node $\mathbf{n}_m$ and ending at node $\mathbf{n}_s$, onto the *master surface* (Figure 2.12). Vector $\mathbf{s}$ is calculated via the following expression

$$\mathbf{s} = \mathbf{g} - (\mathbf{g} \cdot \mathbf{m}^i)\mathbf{m}^i\,, \tag{2.28}$$

where for segment S_i:

$$\mathbf{m}^i = \frac{\mathbf{c}_i \times \mathbf{c}_{i+1}}{\|\mathbf{c}_i \times \mathbf{c}_{i+1}\|}\,. \tag{2.29}$$

Once the *master surface* has been identified, the next step consists in determining the convective coordinates $\bar{\boldsymbol{\xi}} = (\xi^1, \xi^2)$ for the point $\bar{\mathbf{x}}^2(\bar{\boldsymbol{\xi}})$ with the minimum distance to the *slave node*. Since the projection of a vector between this point and the *slave*

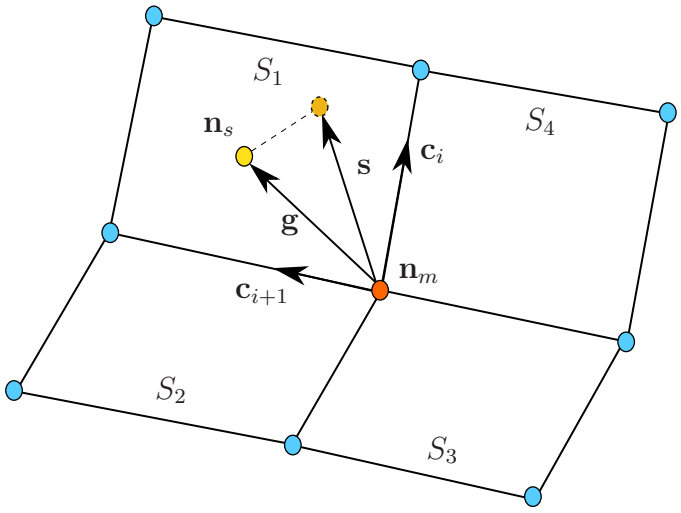

Figure 2.12: Projection of the slave node on the master surface

node onto the master surface should be zero, the point $\bar{\mathbf{x}}^2$ must satisfy the following expressions

$$\begin{aligned} \frac{\partial \bar{\mathbf{x}}^2}{\partial \xi^1}(\mathbf{n}_s - \bar{\mathbf{x}}^2) &= 0\,, \\ \frac{\partial \bar{\mathbf{x}}^2}{\partial \xi^2}(\mathbf{n}_s - \bar{\mathbf{x}}^2) &= 0\,. \end{aligned} \tag{2.30}$$

An iteration scheme is employed in order to find the convective coordinates $\bar{\boldsymbol{\xi}} = (\xi^1, \xi^2)$. The nodal vector of the contact element has the following form

$$\mathbf{x}_{nts}^T = \{\mathbf{x}^{(1)}, \mathbf{x}^{(1)}, \cdots, \mathbf{x}^{(n)}, \mathbf{x}^{(n+1)}\}^T\,, \tag{2.31}$$

where n is the number of nodes that represent the *master surface* and $\mathbf{x}^{(i)}$ are the vectors containing the nodal points; $x^{(n+1)}$ is the *slave node*. The relative displacement vector $\mathbf{x}^1 - \bar{\mathbf{x}}^2$, and the variation $\delta\mathbf{x}^1 - \delta\bar{\mathbf{x}}^2$, can be computed with the help of an approximation matrix $\mathbf{A}$

$$\mathbf{x}^1 - \bar{\mathbf{x}}^2 = -\mathbf{A}(\bar{\boldsymbol{\xi}})\mathbf{x}_{nts}\,; \qquad \delta\mathbf{x}^1 - \delta\bar{\mathbf{x}}^2 = -\mathbf{A}(\bar{\boldsymbol{\xi}})\delta\mathbf{x}_{nts}\,. \tag{2.32}$$

The approximation matrix $\mathbf{A}$ as

$$\mathbf{A}(\xi^1, \xi^2) = \begin{bmatrix} N_1 & 0 & 0 & N_2 & 0 & 0 & \cdots & N_n & 0 & 0 & -1 & 0 & 0 \\ 0 & N_1 & 0 & 0 & N_2 & 0 & \cdots & 0 & N_n & 0 & 0 & -1 & 0 \\ 0 & 0 & N_1 & 0 & 0 & N_2 & \cdots & 0 & 0 & N_n & 0 & 0 & -1 \end{bmatrix}. \tag{2.33}$$

The *master surface* is approximated through standard shape functions. Our model employs three- and four-node isoparametric surface elements to approximate the *master surfaces*. A four node surface uses the following shape functions:

$$\begin{aligned} N_1^s &= \frac{1}{4}(1-\xi^1)(1-\xi^2)\,, \qquad & N_2^s &= \frac{1}{4}(1+\xi^1)(1-\xi^2)\,, \\ N_3^s &= \frac{1}{4}(1+\xi^1)(1+\xi^2)\,, \qquad & N_4^s &= \frac{1}{4}(1-\xi^1)(1+\xi^2)\,. \end{aligned} \tag{2.34}$$

The shape functions for a three node surface element are as follows

$$\begin{aligned} N_1^s &= (1-\xi^1-\xi^2)\,, \qquad & (0 \le \xi^1 \le 1-\xi^2) \\ N_2^s &= \xi^1\,, & (0 \le \xi^2 \le 1-\xi^1) \\ N_3^s &= \xi^2\,, \end{aligned} \tag{2.35}$$

where the origin of the local coordinate system is placed at one of the nodes, as in the case of the tetrahedral element.

The surface vectors take the following form

$$\mathbf{a}_1 = \frac{\partial \mathbf{A}}{\partial \xi^1}\,\mathbf{x}_{nts}\,, \qquad \mathbf{a}_2 = \frac{\partial \mathbf{A}}{\partial \xi^2}\mathbf{x}_{nts}\,. \tag{2.36}$$

The metric tensor $\mathbf{m}$ can be obtained with equation (1.129). The normal vector is then given by the following expression

$$\mathbf{n} = \frac{\mathbf{a}_1 \times \mathbf{a}_2}{\sqrt{\det \mathbf{m}}}\,. \tag{2.37}$$

At this point, all necessary parameters to calculate the normal (Equation 1.133) and tangent (Equation 1.137) forces are available.

2.2.4 Overview of the Mesh

Most of the components of the masticatory system are represented in this study by tetrahedral elements with formulation 13 (Table 2.1). This includes the peridontium around the teeth in the maxilla (purple) and the mandible (green), the teeth (red), the cortical bone (gray), and the spongy bone (blue) (Figure 2.13).

The cartilage of the fossa and the articular disc are represented with hexahedral elements with reduced integration (element formulation type 1 in LS-DYNA). The employed hourglass control is the *Belytschko-Bindeman Assumed Strain Co-Rotational*

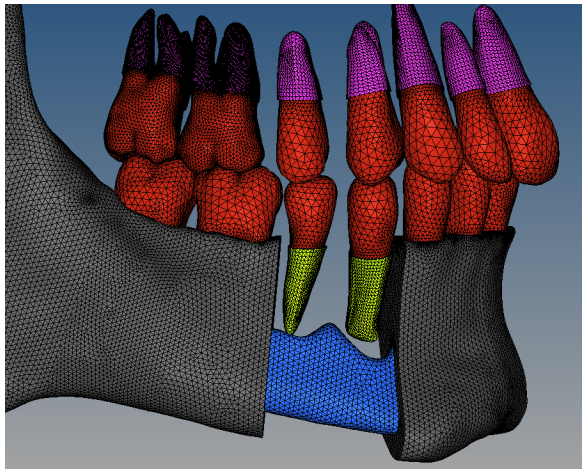

Figure 2.13: Mesh of the bone, PDL and teeth

Form (hourglass control type = 6) with the recommended hourglass coefficient for rubbers (QM = 1). For robustness reasons the cartilage of the condyle is modeled with constant stress tetrahedral elements (type 10)(Figure 2.14).

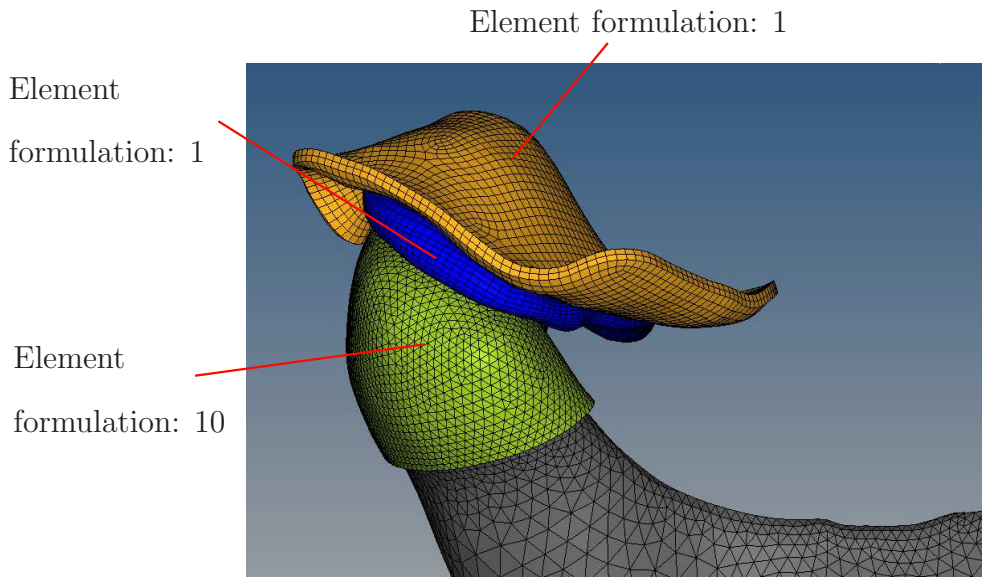

Figure 2.14: Solid element formulations used for the TMJ

As previously mentioned, truss elements are employed to represent the attachments of the articular disc, the tendons and the muscles. The inferior posterior/anterior attachments are connected to the cortical bone of the condyle while the superior attachments are connected to constrained nodes of the cartilage of the fossa. The attachments are then all connected to the articular disc through the use of interpolation elements. A pair of pulley elements was used in order to enforce each of the posterior inferior attachments to remain at the surface of the cartilage of the condyle. Forces withstood by the pulleys are distributed across the surface of the

cartilage of the condyle (left side of Figure 2.15).

The truss element representing the muscle has one side attached to a constrained node located at the origin point of the muscle and the other side to another truss representing the tendon. The tendon is attached in its other end to a constrained interpolation element positioned at the insertion point of the muscle. The surface that the interpolation element covers is an approximation of the surface where the corresponding muscle attaches. This configuration can be observed in the right side of Figure 2.15: The orange trusses represent the fibers of the muscles (explained in detail in chapter 6); the red trusses the tendons; and the blue interpolation elements distribute the forces over the surface of the bone.

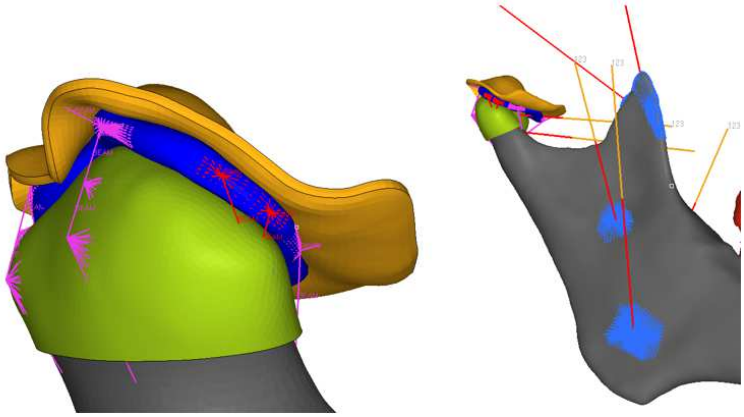

Figure 2.15: Interpolation elements are used to distribute the forces from the muscles and the attachments

To handle contact, the card `CONTACT_AUTOMATIC_SURFACE_TO_SURFACE` has been used to define all contact pairs in the model. This card employs a two-way treatment of contact: Once it finishes checking the penetration of the *slave nodes* through the *master surface*, it checks the penetration of the *master nodes* through the *slave surfaces*. In this manner, selecting which of the surfaces is the master or slave is irrelevant.

The placement of contact elements for the TMJ can be seen in Figure 2.16. Two contact pairs are defined, *i)* the surface of the cartilage of the condyle with the inferior surface of the articular disc, and *ii)* the inferior surface of the cartilage of the fossa with the superior surface of the articular disc.

Definition of contact between the teeth and bolus depends on the task being simulated. During clenching, contact is defined between each tooth and its antagonist. If the task involves a bolus, then contact is defined between the teeth and the inferior/superior part of the bolus. Only the surface considered to be in contact during occlusion is covered by the contact elements (Figure 2.17).

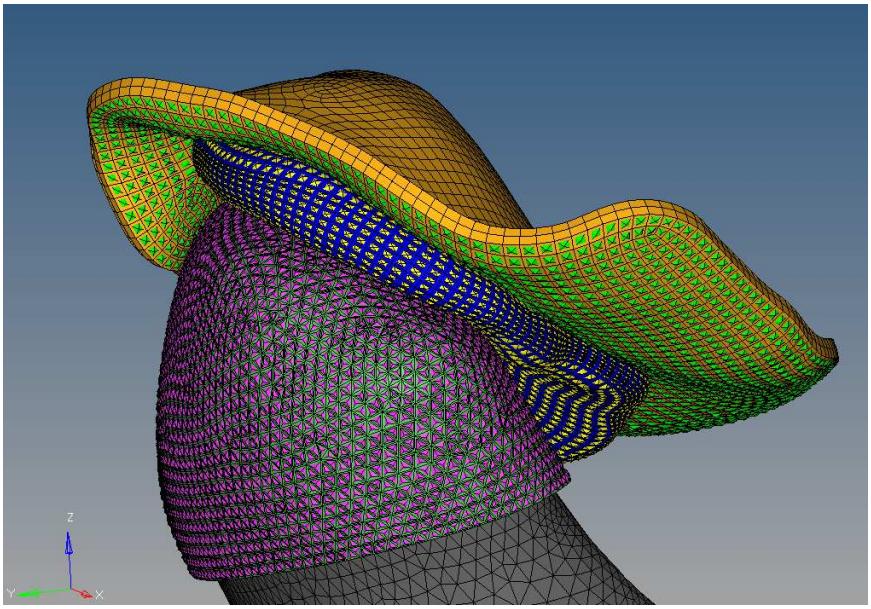

Figure 2.16: Contact surfaces in the TMJ: The contact elements on the surface of the cartilage of the condyle, the cartilage of the fossa and the articular disc are displayed in violet, green, and yellow, respectively.

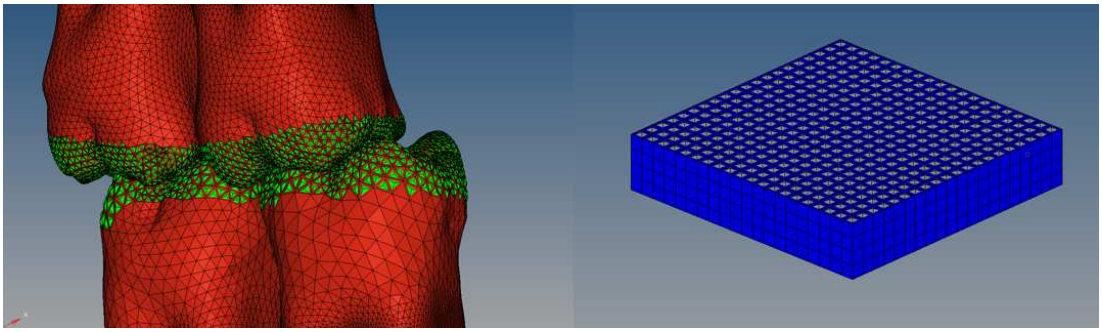

Figure 2.17: Contact elements on the surface of the teeth are shown green (left). Contact elements on the bolus are displayed in gray (right).

The final full model has approximately 3.0 million elements (around 1.2 million elements belong to the teeth and are rigid). This number of elements was reached after performing several convergence analyses. In table 2.5, the number of elements for each component are shown, for the reduced model employed in symmetrical tasks. The initial mesh had around 1.3 million elements and is depicted in figure 2.18. As mentioned previously, the geometry is divided as to have the alveoles and the ramus in independent volumes. Areas subjected to high stresses were refined, as well as complicated parts of the geometry, which could generate problems, such as the cortical bone between the alveoles. In the case that symmetry can be exploited, such as during bilateral molar biting (BMB), the number of elements is reduced by half. A frontal view of the full model with transparent elements (edges of the

elements are hidden) is shown in Figure 2.19.

Component	Element type	Elements*
Cortical bone	Tetrahedron 13	540781
Cancellous bone	Tetrahedron 13	88589
Teeth	Tetrahedron 10	679630
Articular disc	Hexahedron 1	11501
Cartilage of the fossa	Hexahedron 1	5590
Cartilage of the condyle	Tetrahedron 10	11610
PDL	Hexahedron 1	270673

*mesh for symmetrical tasks

Table 2.5: Number of elements of each component of the model

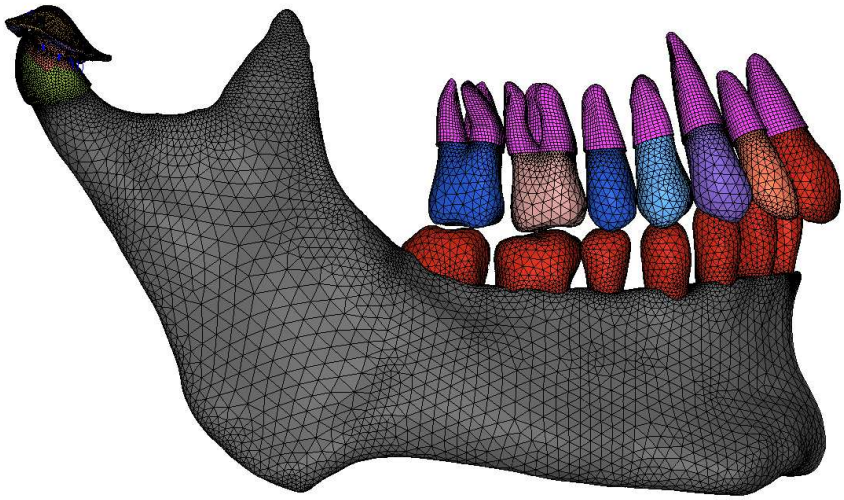

Figure 2.18: Initial mesh for symmetrical tasks, composed by around 1.3 million elements

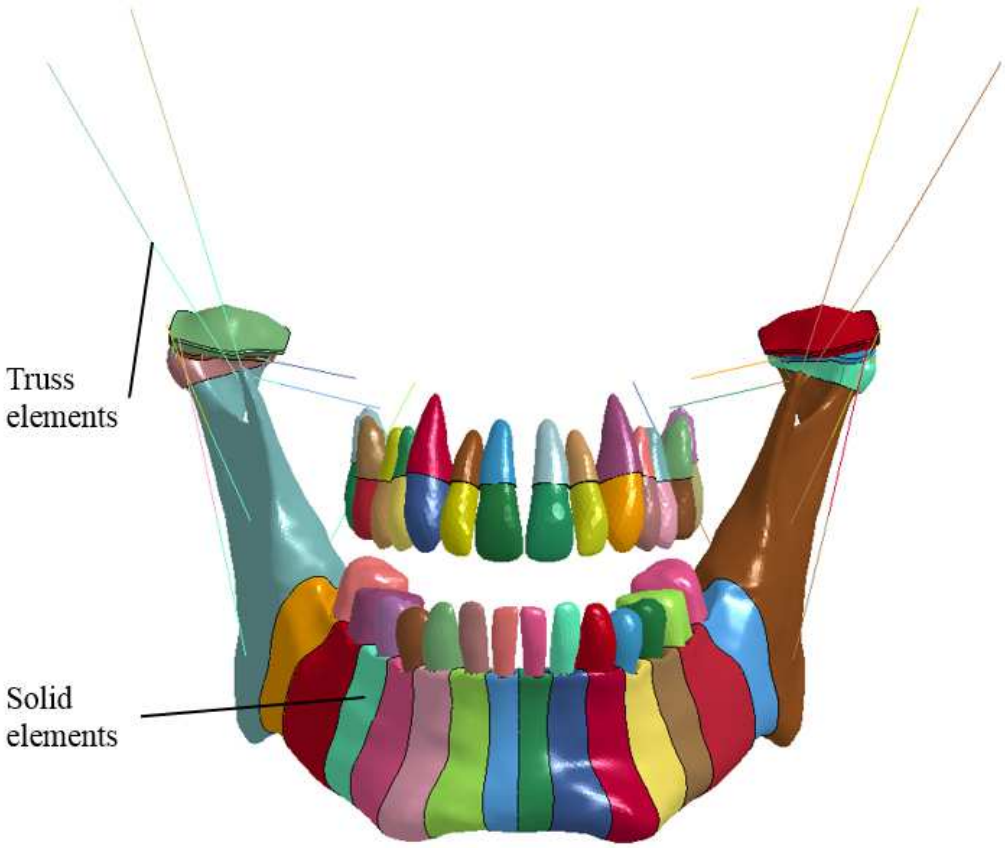

Figure 2.19: Full model used in unilateral tasks

Chapter 3:
The Bone

Bones are stiff organs that provide support and structure of the body, allow mobility and protect the different organs of the body. They are complex tissues, composed of living cells, organic matrix (mainly collagen) and minerals (salts of calcium and phosphate, mostly hydroxyapatite). The collagen gives the bone its tensile strength while the mineral components ensure its compressional strength. The bone is constantly remodeling in order to adapt dynamically to changes in its environment. This adaptation is achieved by specialized bone cells known as the osteoblasts, which synthesize bone, and the osteoclasts, which break down bone tissue through a process called bone resorption. The activity of these cells is believed to be controlled by the mechanosensing cells of the bone, the osteocytes.

3.1 Mechanical Properties of the Bone

The bone can be classified depending on its morphology into cortical and cancellous (trabecular, spongeous) bone.

The *cortical bone* forms the outer shell of most bones. It is much denser, stronger and stiffer than the trabecular structure in its interior. The available literature on the mechanical behavior of the bone is extensive. Mechanical tests with cortical bone show that Young's modulus varies between authors and depends on the type of test applied. Additionally, the elastic modulus of the bone in the tangential and radial direction is different from that in the axial direction [14, 15].

Material parameters for *cancellous bone* are more difficult to determine since the porosity of the material varies significantly between bones and age of the subject. Material coefficients spread widely from author to author [16, 17].

Properties of *mandibular cortical bone* were measured by various authors [18, 19, 20]. These properties vary along its different sections (Fig. 3.1). From the incisal region to the molar region, a maximum Young's modulus of around 20 GPa is observed when aligned with a line tangential to the inferior border of the body of the mandible. The modulus gradually decreases as the angle changes, down to 11 GPa when aligned perpendicular to the inferior border. In the area of the ramus, a maximum Young's modulus, once again of approximately 20 GPa, is observed at an angle of 120 degrees with respect to the inferior border of the ramus (almost tangent to the posterior border of the ramus). The ultimate tensile strength for cortical bone was reported

to be in the range of 135 - 192 MPa [14, 21], while the ultimate compressive strength shows a higher value of 177 - 214 MPa [21].

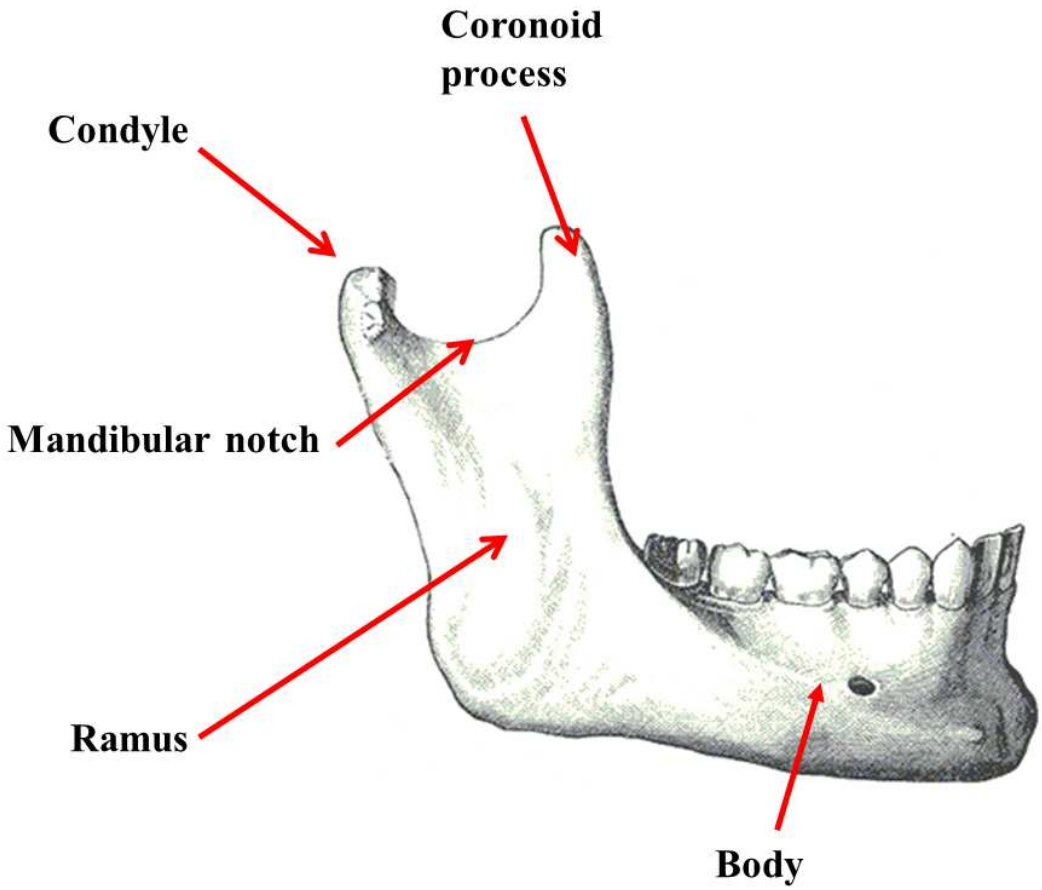

Figure 3.1: The different parts of the human mandible. (Source: www.theodora.com)

The *mandibular cancellous bone* also shows anisotropic properties, with different values of Young's modulus in the radial, tangential and axial directions, and has remarkable variance at different sites of the mandible [22, 23, 24]. The elastic modulus goes from a value of 0.047 GPa, up to a value of 2.2 GPa. However, a linear elastic isotropic model was used in our model. The Young's modulus of cortical bone was taken from Tanaka et al. [25] and the apparent Young's modulus of cancellous bone from O'Mahony et al. [22]. These are presented in table 3.1.

The bone that surrounds the teeth is called the alveolar bone. It can be classified into four different types [26] depending on its composition, ranging from class 1, being mainly cortical bone, to class 4 which is composed almost completely of trabecular bone. In this model, the alveolar bone was modeled as cortical bone (Fig. 3.2) since its gray-scale value on the CT-scans was essentially indistinguishable from that of the cortical bone.

Bone type	Young Modulus [GPa]	Poisson's ratio
Cortical bone	13.7	0.3
Cancellous	2.0	0.3

Table 3.1: Mechanical properties used for the bone in our model

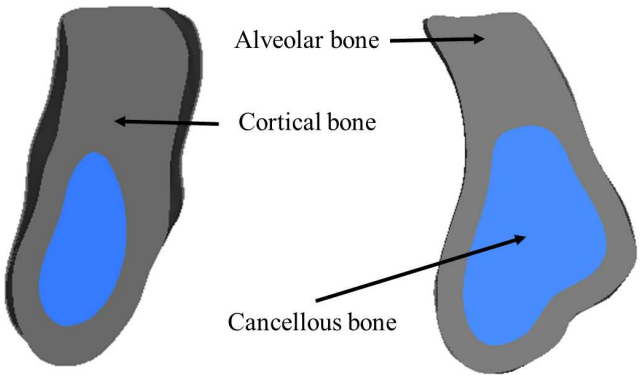

Figure 3.2: Sectional view of the jaw bone at the molar region (left) and between the central incisors (right). The bone surrounding the teeth (alveolar bone) has been modeled as cortical bone

3.2 Simulations and Results

Since the bone shows higher resistance to loads under compression than under tension, the first and third principal stresses were examined. The behavior of the bone was studied during jaw opening, bilateral molar biting and unilateral molar biting.

3.2.1 Jaw Opening

The opening muscles were activated to their maximum level in order to open the jaw. It can be observed that due to the action of the lateral pterygoid muscle (detailed in the muscles' chapter), stresses in the mandible are almost completely compressive on the palatinal surface and tensile on the buccal surface. In figure 3.3, a lateral view of the jaw, displaying the first principal stresses, and a medial view, indicating the third principal stresses, are shown. The highest tensile stresses, with values around 15 MPa, can be observed at the lateral side of the ramus, tensile stresses can also be observed in the mandibular notch and the buccal surface of the mandibular body. The highest compressive stresses, with a value of approximately -17 MPa, are found at the posterior part of the ramus, notable compressive stresses are also seen at the palatinal surface of the mandibular body.

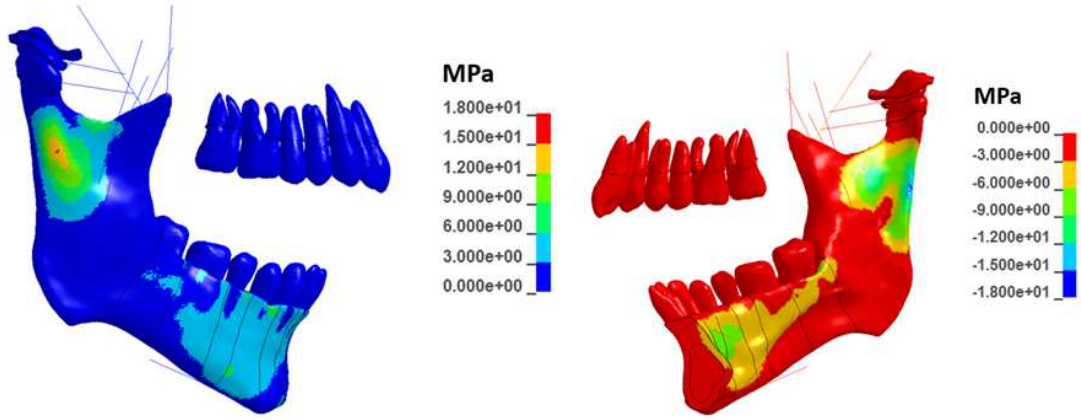

Figure 3.3: First (left) and third (right) principal stresses in the mandible during opening

3.2.2 Biting Tasks

Bilateral molar biting was performed with a biting force of 300 N. The first principal stresses in the bone can be observed in figure 3.4. The third principal stress is shown in figure 3.5. Areas under high tension in the jaw include the posterior part of the mandibular notch, the coronoid process and the anterior border. The posterior part of the ramus is the area under highest compression. Compression can also be observed at the posterior part of the coronoid process. These areas of tension and compression agree with those obtained by Korioth et al. [4] and Kober et al. [27]. Some discrepancies are visible, however, in the tension present in the coronoid process, which is absent in Kober's model. Nevertheless, a direct comparison cannot be made since *unilateral premolar biting* tasks have not been performed with our model. This task was also performed with a biting force of 800 N. The resulting maximum stress, for both cases, can be seen in table 3.2.

Bite force [N]	Von Mises stress [MPa]
300	34
800	89

Table 3.2: Maximum Von Mises stress on the mandible during BMB of 300 and 800 N

An almost linear relationship between biting force and stress can be observed. This is due to the use of a linear material model for the bone.

In order to be able to compare our results more closely with those of Korioth [4], a unilateral molar biting task was performed calibrating the forces seeking a similar joint/bite force ratio. This was not possible, however, since such forces in our model

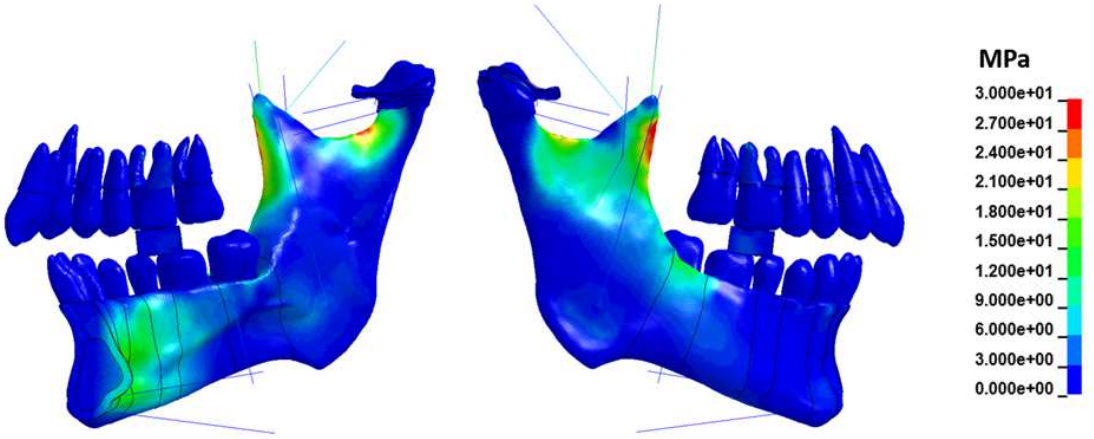

Figure 3.4: First principal stress during a bilateral molar biting force of 300 N. Medial (left) and lateral view (right)

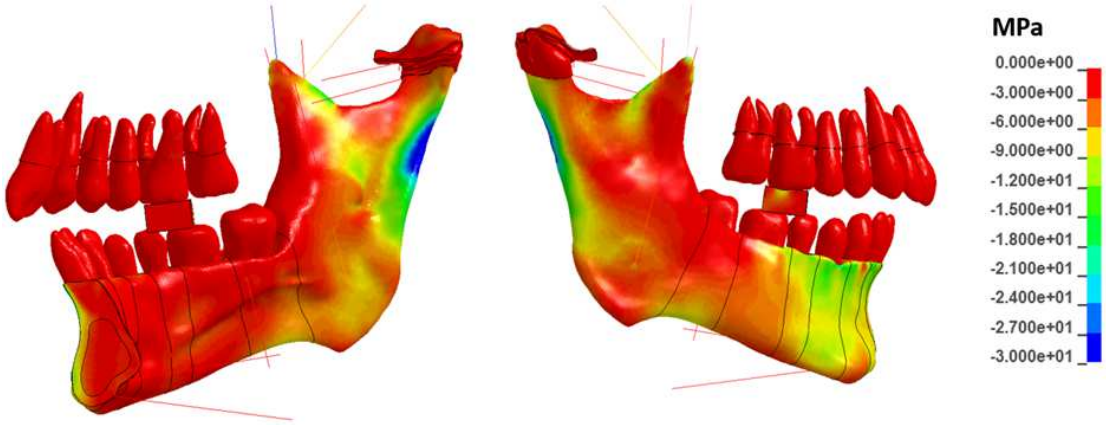

Figure 3.5: Third principal stress during a bilateral molar biting force of 300 N. Medial (left) and lateral view (right)

result in an unstable balance of the joint. In figure 3.6, the first principal stresses of the jaw are depicted for unilateral molar biting. Here a 10 x 10 x 2 (mm) bolus was placed between the molars, and the muscle forces increased until a bite force of 300 N was reached. The bolus was modeled as a linear elastic material with a Young's modulus of 20 MPa, equivalent to the elastic modulus of an almond under compression, and a Poisson's ratio of 0.47 [28]. The resulting third principal stresses can be seen in figure 3.7.

However, the following discrepancy can be observed: For a biting force of 526 N the maximum values for both, first and third principal stresses, reported by Korioth et al. are of approximately 25 MPa and -25 MPa, respectively. In our model, this value is already exceeded under a bite force of 300 N. The obtained stresses remain, however, still below the ultimate tensile stress (135 MPa) and the ultimate

compressive stress (-205 MPa) of the bone.

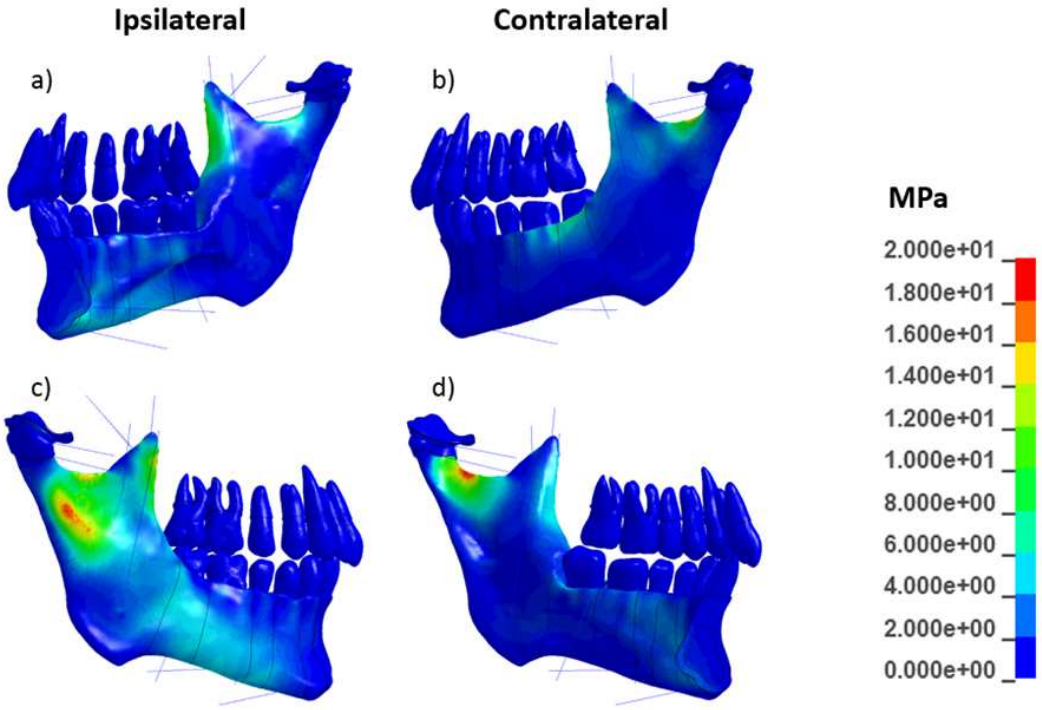

Figure 3.6: First principal stress in the jaw under a unilateral molar bite force of 300 N: a) medial view ipsilateral side, b) lateral view contralateral side c) lateral view ipsilateral side and d) medial view contralateral side

When *unilateral biting* is performed with a reduced force of 150 N, compressive stresses are larger at the contralateral side, since this joint brings the system in balance (forces on the joints are studied in chapter 5) with both sides having practically the same muscle forces (Fig. 3.8). As the biting force increases, the muscle forces at the ipsilateral side become larger than at the contralateral side. Although joint forces remain larger at the contralateral side, the compressive stresses in the posterior part of the ramus become larger at the ipsilateral side.

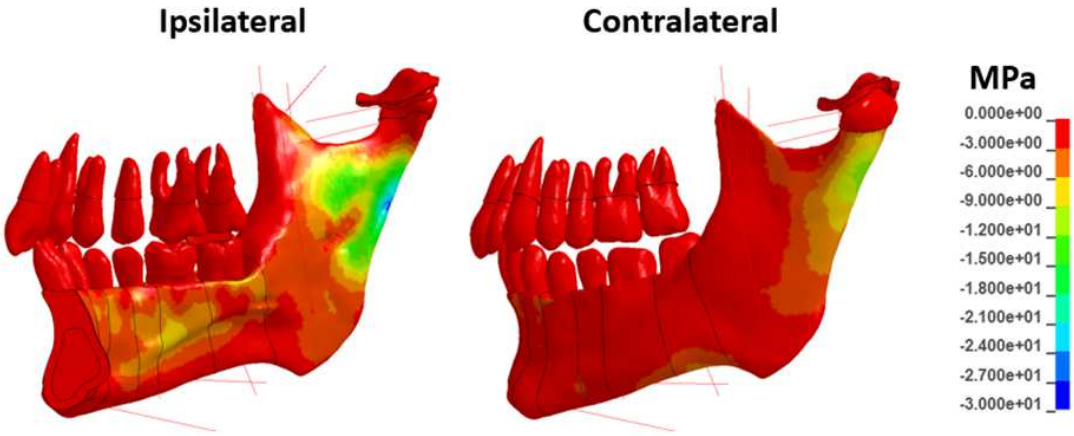

Figure 3.7: Third principal stress in the jaw under a unilateral molar bite force of 300 N in the ipsilateral (medial view) and contralateral side (lateral view)

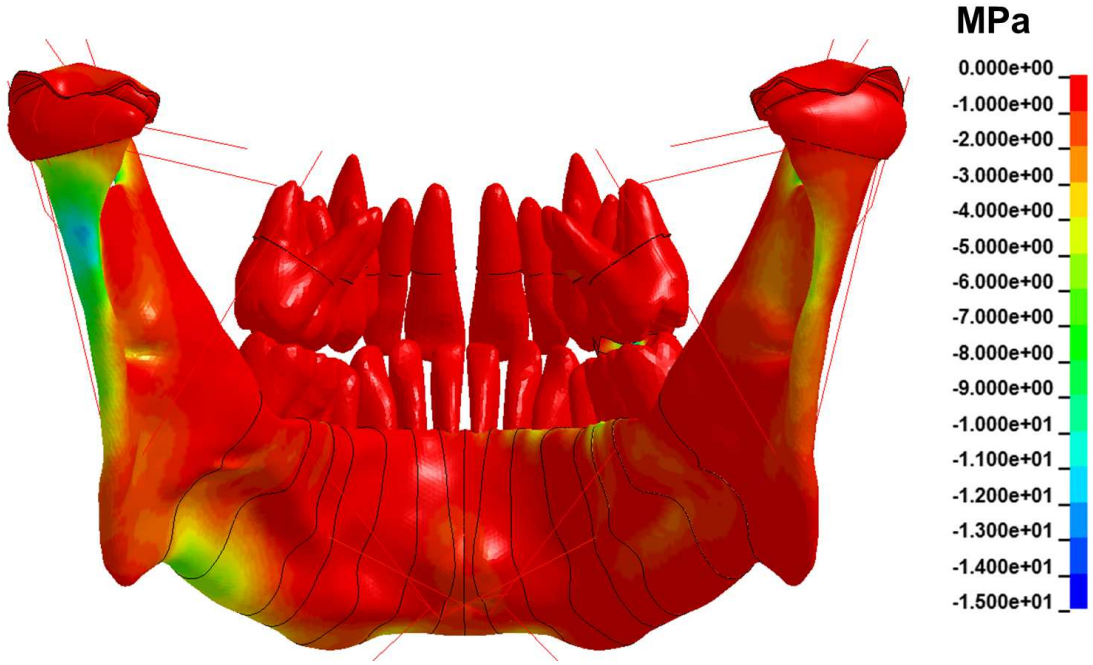

Figure 3.8: Third principal stress in the jaw under a unilateral molar bite force of 150 N (posterior view)

3.3 Conclusions

The stress present in the jaw depends on how the reaction forces are distributed between the joint and the teeth involved in the biting process. Data of the distribution of forces during biting tasks vary considerably in the literature. This originates from the difference in direction, application point and level of the muscle forces. The range of possible bite and joint forces has been studied for example in ([29, 30]). Throckmorton [29] showed that modifying the muscles' parameters gives a range of 38-123 N of joint force for a biting force of 196 N. The current model has been calibrated to match the results by Rues et al. [31], since these biting and muscle forces were experimentally measured.

Simulations, Korioth for instance, where the bite force is notably larger than in the joint, have an orientation of the total force of the closing muscles towards the anterior direction. This requires that the joint force exerted on the condyle possesses a large posterior component in order to reach balance. In a static model, this balance is easily reached since the condyle is completely constrained. In our dynamic model, however, joint forces are restricted to the normal direction of the fossa. This type of reaction force results in a very unstable position of the disc, since an increase of the posterior forces (mild activation of the posterior temporalis) results in the disc quickly displacing to its maximum posterior position. This is the most stable position of the disc, since the temporomandibular ligament and the attachments of the disc ensure that no further posterior displacement is possible. This observation suggests that joint forces have a considerable effect on the stabilization of the articular disc during high biting forces. The degree of jaw opening also plays a role in the distribution of forces between the joint and the teeth, since the distribution of forces changes due to the shift of angle and sarcomere length of the muscles.

In our model, stresses were found to be larger than those found in Korioth's model even when a much smaller biting force was employed. It is difficult to evaluate if the distribution of force is responsable for this discrepancy, since having a very small force in the joint while mantaining high forces on the teeth would require the system to be in a conditionally stable position, which would demand a control scheme for the activation levels of the muscles. The discrepancy can perhaps be caused by an additional reason: Korioth's model incorporates the anisotropy of the bone, which according to Kober et al. [27] reduces the stresses in the jaw. Stresses in the model do not exceed the maximum failure stresses of the bone, even under very high biting forces.

It was observed that when higher values of Young's modulus are employed for the spongious bone, up to a value of 10 GPa, results remain essentially the same since the loads on the mandible are carried almost exclusively by the cortical bone which has a higher second moment of area along with a much higher elastic modulus. The

use of such values for the trabecular bone of the mandible was seen in some works (e.g. Tanaka et al.[25]), these were likely taken from values corresponding to other bones of the body, such as the femur or the tibia.

Chapter 4:
The Periodontal Ligament

The periodontal ligament (PDL) is the tissue that binds the teeth to the alveolar bone and governs short-term tooth mobility. The PDL is composed of bundles of connective tissue fibers (Sharpey's fibers), specific cells, vasculature, nerves and ground substance. Sharpey's fibers connect the alveolar bone to the cementum of the teeth [32]. Occlusal forces are absorbed by the oblique fibers, which cover most of the surface of the tooth. The remaining fiber bundles located at the top and bottom of the PDL, counteract tipping and rotating forces (Fig. 4.1).

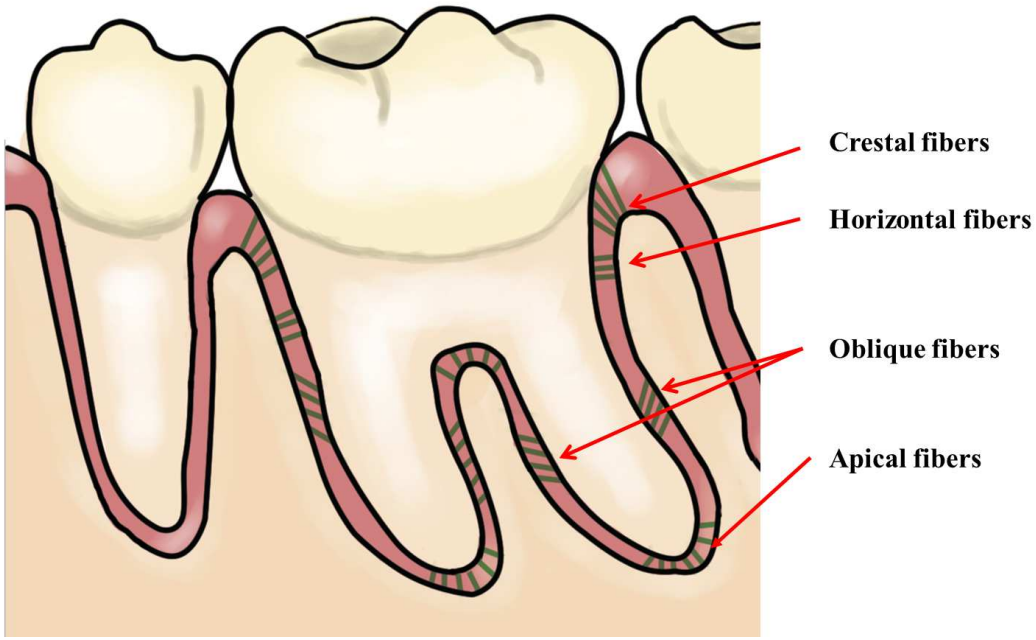

Figure 4.1: The periodontal ligament binds the tooth to the alveolar bone. The vast majority of Sharpey's fibers are oriented in an oblique manner

The cells in the PDL continuously affect its structural behavior; they synthesize and absorb the collagen fibers as well as the surrounding alveolar bone. This process constantly reshapes the geometry of the PDL and the alveoles in order to adapt to the loads applied to the teeth [33]. The vasculature of the PDL plays an important role by its functional properties, because occlusal forces are also resisted by means of the tissues' fluids (blood vessels and ground substance) and its movement. When the teeth are loaded, fluids contained in the PDL will flow to the alveolar bone (the rich vascular supply of the PDL penetrates the alveolar bone), giving the tissue dissipation properties. As soon as the fluid flow is fully utilized the PDL becomes

essentially incompressible, and hydraulic pressure distribution occurs [34, 35]. Since the deformation that occurs in the teeth and the alveolar bone is very small when compared to the deformation of the PDL, the former is usually disregarded when studying the mobility of the tooth [36].

Current studies of the PDL face the following issues: First, the discrepancies in the literature relating to the mechanical properties of the PDL complicate the interpretation of results obtained with numerical models [37]. In addition, these models require their implementation into a finite element solver, typically a time consuming task. Secondly, simplified loading conditions of the masticatory system where forces that do not reproduce realistic biting forces are often employed. Many works regarding the study of the PDL place a vertical/horizontal nodal force at the tooth in order to load the PDL. In other cases, a constraint is applied to the tooth in order to restrict its movement while forces from the muscles are applied to the jaw.

4.1 Material Model of the PDL

The development of material models for the PDL has had several approaches in the literature. Some authors [38] calibrated material models to match the stress-strain results obtained from uniaxial tests on the PDL. These types of tests only expose the resistance of the PDLs fibers to tension, and therefore fail to measure the compressive response of the tissue. Due to the confined nature of the PDL, the bulk parameter plays a fundamental role in its behavior. Materials calibrated following curves obtained from these tests, will result in unsatisfactory force-displacement results differing from those seen in Parfitt [39] and Lenz et al. [40].

The model of Natali et al. [41] shows good agreement with the force displacement curves but unfortunately the material parameters are not disclosed. Other authors implemented their own material models which produce results that closely match the results from the Parfitt experiment [42, 43, 44]. In the course of this work, two hyperelastic material models were used for the PDL: A first-order Ogden and a polynomial form that follows the work from Su et al.[44].

Hyperelastic material models assume that the material behavior can be described by means of a strain energy function, from which the stress-strain relationship can be derived. The strain energy function for the Ogden material model is defined in LS-DYNA as

$$W = \sum_{i=1}^{3} \sum_{j=1}^{n} \frac{\mu_j}{\alpha_j} (\lambda_i^{\alpha_i} - 1) + K(J-1)^2 \,. \tag{4.1}$$

where W is the strain energy potential, λ_i are the deviatoric principal stretches, μ_j and α_j are material parameters, J is the determinant of the elastic deformation

gradient and K the bulk modulus. In LS-DYNA, the bulk modulus is computed using Poissons ratio ν and Young's modulus E. The parameters that produced the best agreement with the experimental results for both, vertical and horizontal loads, were found with a parameter study and are presented in Table 1.

$\boldsymbol{\mu_1}$ [MPa]	$\boldsymbol{\alpha_1}$ [MPa]	$\boldsymbol{\nu}$ (Poisson's ratio)
0.5-2.5 E-03	150	0.46

Table 4.1: Material parameters for the first order Ogden model (for $\boldsymbol{\mu_1}$ a range is proposed, the lower and upper limit values were employed in the following simulations)

The strain energy function for the polynomial form proposed by Su et al. [44] is

$$\begin{aligned} W =& C_{10}(\bar{I}_1 - 3) + C_{20}(\bar{I}_1 - 3)^2 + C_{30}(\bar{I}_1 - 3)^3 + \\ & \frac{1}{D_1}(J-1)^2 + \frac{1}{D_2}(J-1)^4 + \frac{1}{D_3}(J-1)^6 \end{aligned} \tag{4.2}$$

where C_{10}, C_{20}, C_{30}, D_1, D_2, D_3 are material parameters, $\bar{I}_1$ is the first invariant of the right Cauchy strain tensor with the volumetric component removed, and J is the determinant of the deformation gradient. Material parameters used are the same as proposed in [44] for the volumetric finite strain viscoelastic model. The Ogden material model is readily available as material 77 in LS-DYNA while the polynomial form had to be implemented within this study. Both material models do not take into account the direction of the fibers inside the PDL, as they are isotropic and homogeneous.

4.2 Simulations and Results

The calibration of the material model was performed under several conditions. First, the materials were tested under axial and horizontal forces in order to compare them to the experimental results available in the literature. The materials were subsequently tested under more realistic conditions: i.e. during incisive biting as well as during unilateral molar biting.

4.2.1 Axial and Horizontal Forces on a Maxillary Incisive Tooth

The displacement that the teeth undergo under a particular force can be accurately measured in vivo. Lenz et al. [40] produced the following graphs (Fig. 4.2 and 4.3)

which show the range of displacements of an incisive tooth under intrusive axial and horizontal loads by compiling the experimental results from different authors.

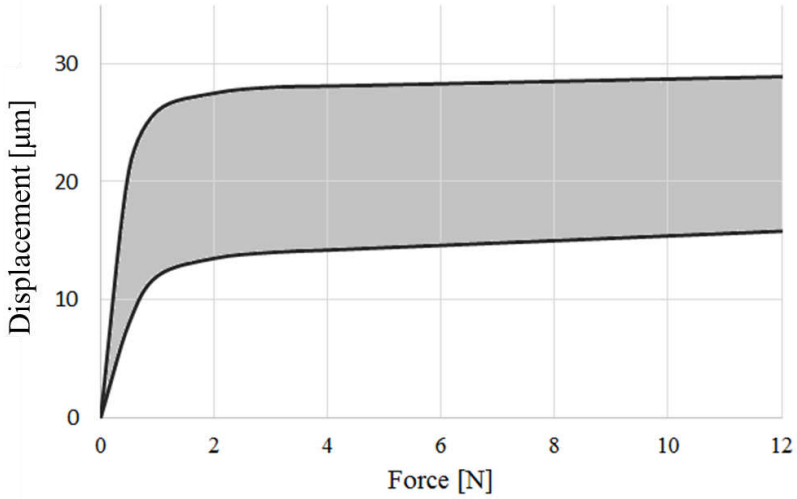

Figure 4.2: Range of displacements of an incisive tooth under axial load

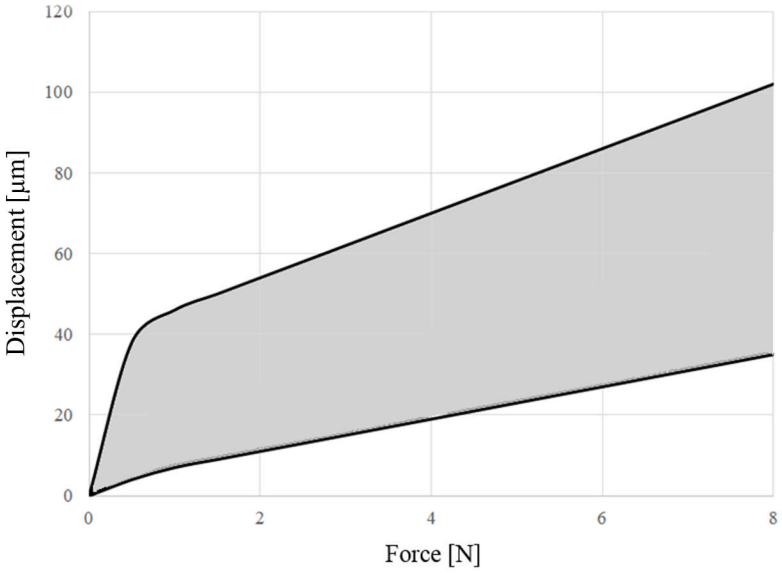

Figure 4.3: Range of displacements of an incisive tooth under horizontal loads

In order to test the materials under axial and horizontal loads, simulations were run in an isolated maxillary tooth (Fig. 4.4). The PDL is meshed with 5000 hexahedral elements with reduced integration while the tooth is modeled as a rigid body. Nodes that are in contact with the alveolar bone are constrained. To take into account the influence of the alveolar nerve, nodes residing in its diameter have not been constrained.

Three material models were tested, the polynomial form and two Ogden models. The latter was analyzed for two different values of the parameter μ_1. For Ogden

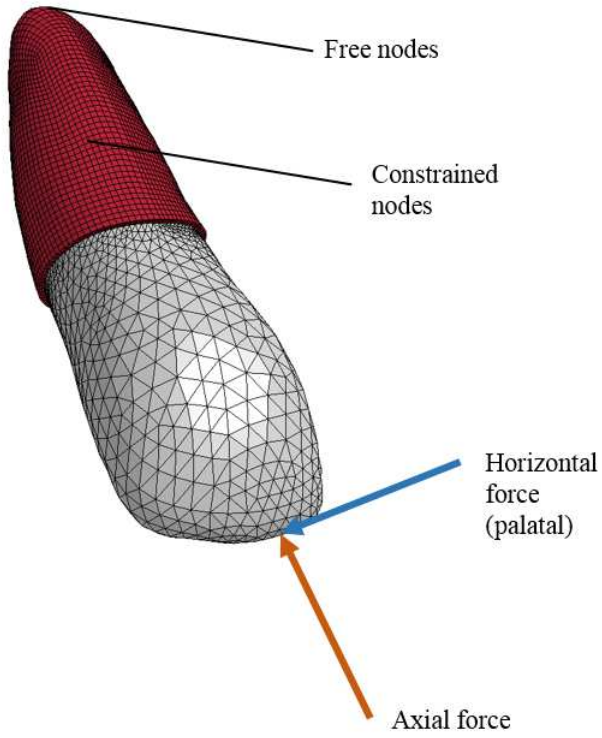

Figure 4.4: Maxillary tooth (grey elements) and PDL (red elements)

A μ_1 = 2.5E-03 MPa, for Ogden B μ_1 = 0.5E-03 MPa were chosen. In the axial case, the force is applied at the tip and along the axis of the tooth. Results can be observed in Figure 4.5.

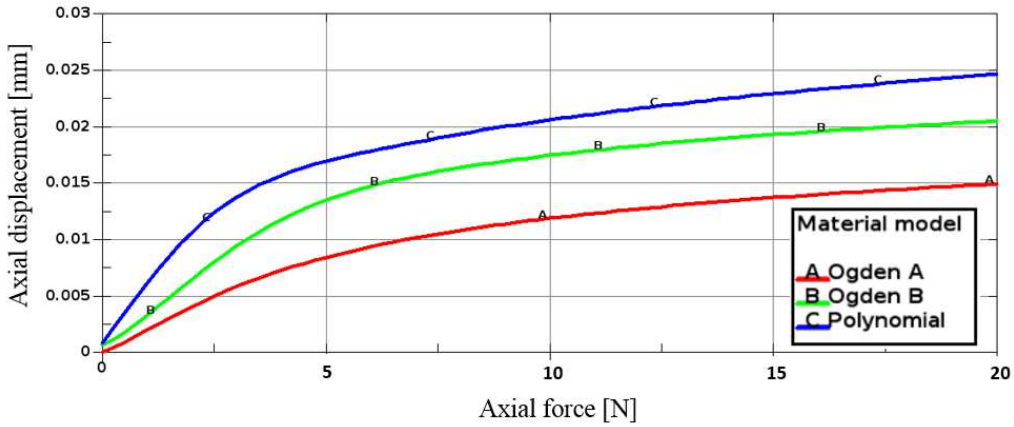

Figure 4.5: Axial displacements of a maxillary tooth under axial intrusive loads

It is evident, by comparison with the experimental results in figure 4.2, that the polynomial shows better agreement, especially in the range from 0 to 5 N. At this range, the PDL shows an extremely non-linear behavior that is rather difficult to

capture. Both material models exponentially stiffen as deformation occurs, creating difficulties in the numerical solver. Material model Ogden B shows that lowering the value of μ_1 leads to a better response for the axial case, but results in the material becoming less stable and in creating a response very close to the maximum upper limit for the horizontal case, as seen in Figure 4.6.

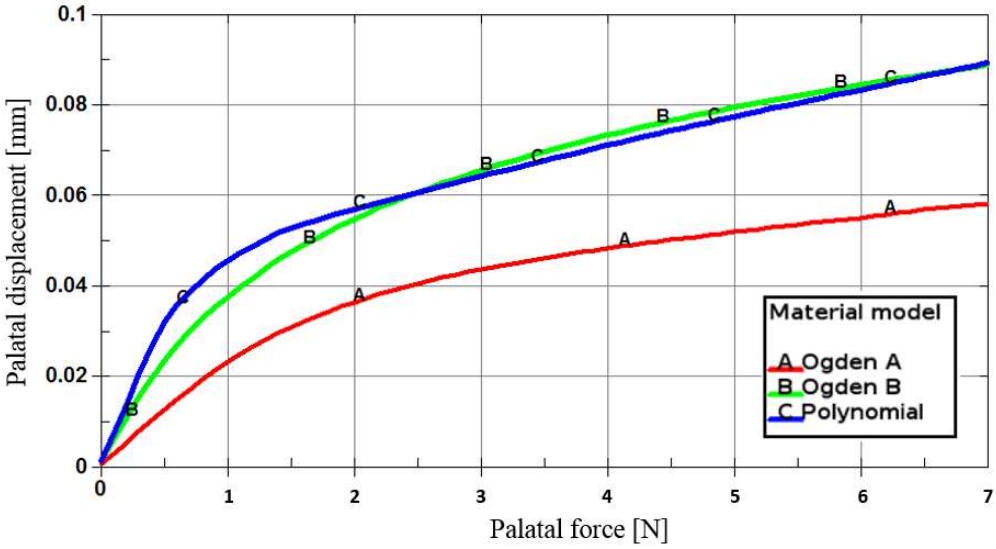

Figure 4.6: Horizontal displacements of a maxillary tooth under palatal (oriented towards the palate or tongue) loads

During a palatal force the polynomial form and Ogden model B produce very similar results, with both being very close to the superior limit of the displacement observed in Fig. 4.3. In this case, displacements reported by material Ogden A are placed in the middle of the range of the experimental results.

4.2.2 Incisive Biting

A bolus with dimensions of 32 x 16 x 4 mm was placed between the incisive teeth (Figure 4.7). Muscles were activated to open and close the jaw in a time of 500 ms. 15 nodes were vertically constrained at the center of the anterior border of the bolus in order to introduce a moment to keep the bolus from rotating. This moment replicates the constraint that food (e.g. griped by the hands) has during incisive biting. The closing muscles were activated around 5% of their maximum capacity to produce a resultant biting force of 28 N. Further activation of the closing muscles was deemed unnecessary since occlusion is imminent. Contact occurs at 245 ms, with the four mandibular incisive (Teeth 41, 42, 31 and 32) and two central maxillary incisive (Teeth 11 and 21) teeth taking part in the biting process. Due to the bolus dimensions, the lateral maxillary incisive teeth do not come into contact with the bolus.

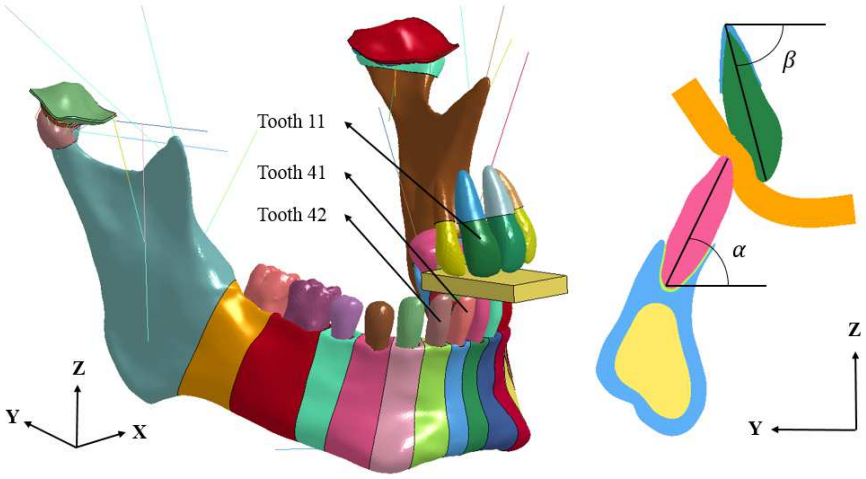

Figure 4.7: Configuration used for incisive biting (left). Sectional view of teeth 11 and 41 during biting (right)

Forces on the teeth, computed from the contact elements, are shown in Fig. 4.8, 4.9 and 4.10. It can be observed in the figures, that forces are not evenly distributed between the lower incisives. Forces are lower in the lateral mandibular incisives as they lack leverage since their antagonists, teeth 12 and 22, do not take part in the biting process. Since forces are reported with respect to the global coordinate system, the angle of the teeth must be taken into account. The mandibular teeth rotate along the jaw during opening and closing. The angle of the incisive teeth α at times 245, 300 and 500 ms is 61.2, 66.2 and 67.3 degrees, respectively. Angle β of the maxillary teeth remains almost constant at a value of 73.6 degrees.

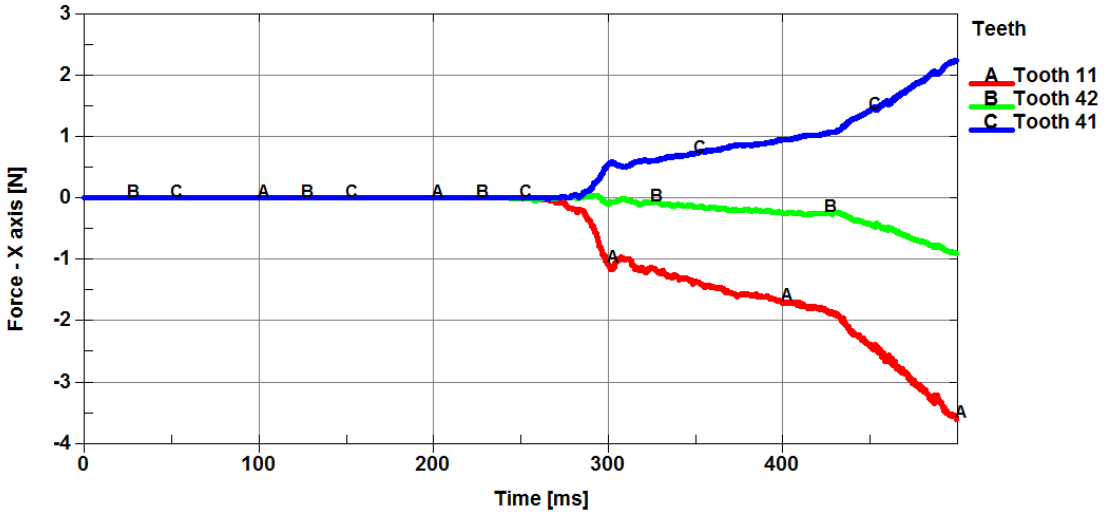

Figure 4.8: Forces in the x-axis during incisive biting. Biting finished at 500 ms

Forces on tooth 11 are almost perpendicular to its axis resulting in a high moment

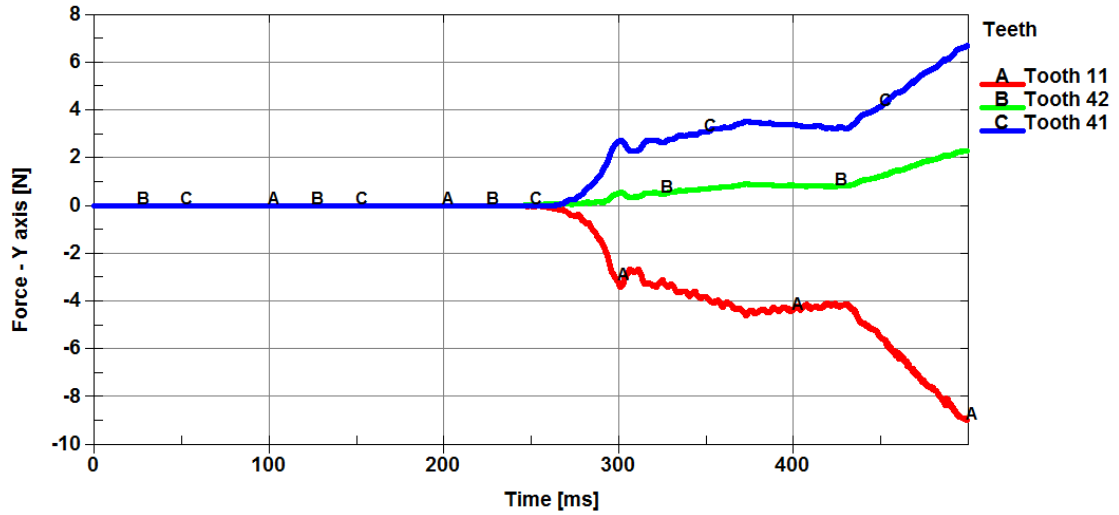

Figure 4.9: Forces in the y-axis during incisive biting. Biting finished at 500 ms

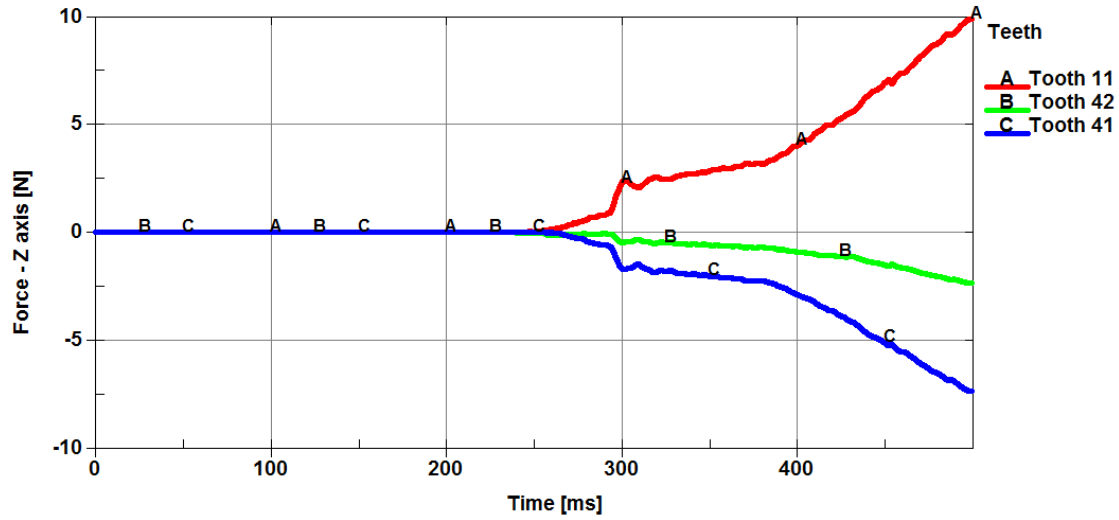

Figure 4.10: Forces in the z-axis during incisive biting. Biting finished at 500 ms

during the duration of the biting process. On the other hand, teeth 41 and 42 are under forces aligned with the axis of the tooth for most of the time, with the force in the posterior direction increasing as the bolus deforms and becomes trapped between the maxillary and mandibular teeth.

4.2.3 Unilateral Molar Biting (UMB)

Unilateral molar biting was performed by placing a 10 x 15 x 2 mm bolus between teeth 16 and 46 (Fig. 4.11). The jaw opening muscles were activated from time 0 to 220 ms up to 15 % of their maximum capacity achieving an opening between

the incisive teeth of 12 mm. Jaw closing muscles and contact elements in the bolus were then activated. Activation levels of the closing muscles remain low until a time of 430 ms has been reached. At this point, the bolus is firmly placed between the teeth and higher activation levels are then used to reach a biting force of 150 N. Activation levels of the closing muscles were taken from Schindler et al. [45] for the case where the contralateral side doesn't reach the bolus, which corresponds to unilateral molar biting.

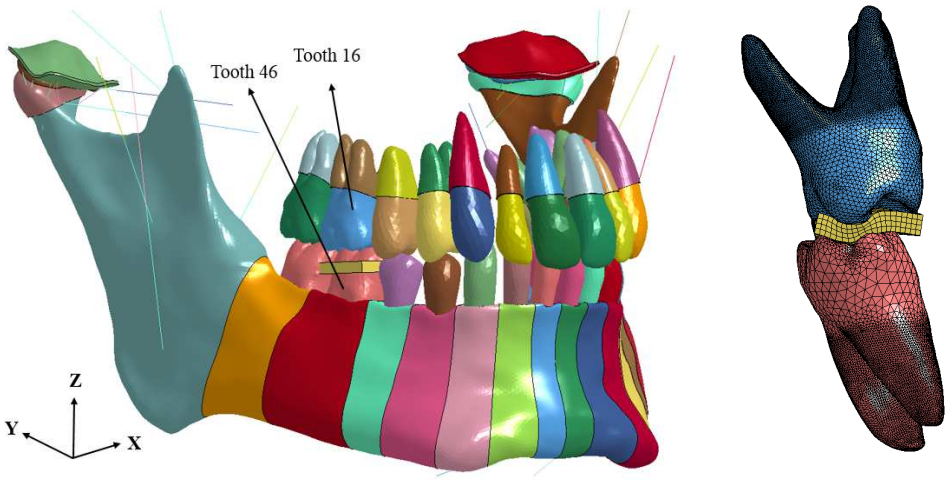

Figure 4.11: Model configuration for unilateral molar biting. The right figure displays the final condition of the bolus and configuration of the molars 16 and 46 involved in the task. The bolus has no interaction with the teeth until the jaw has opened sufficiently and no overlap exists between the volumes of teeth and the bolus

Forces developed on the lower first molar tooth (46) are shown in Fig. 4.12. It can be observed that in the initial phase of UMB, the resulting force on tooth 46 is partially aligned with the direction of its root. As the bolus deforms, the posterior and lateral forces vanish and an almost pure vertical force remains. The application point of the resulting force was determined to be between the buccal cusp and the groove in the mandibular molar and between the lingual cusp and the groove in the maxillary molar (Figure 4.13).

4.2.4 Stresses in the PDL

The first principal stresses developed in the PDL during the intrusive loads used to produce the displacements of Figure 4.5, are displayed in Figure 4.14a. The third principal stresses can be seen in Figure 4.14b. In both cases the applied force is 20 N.

We can observe in these figures that a compressive response occurs at the apex of

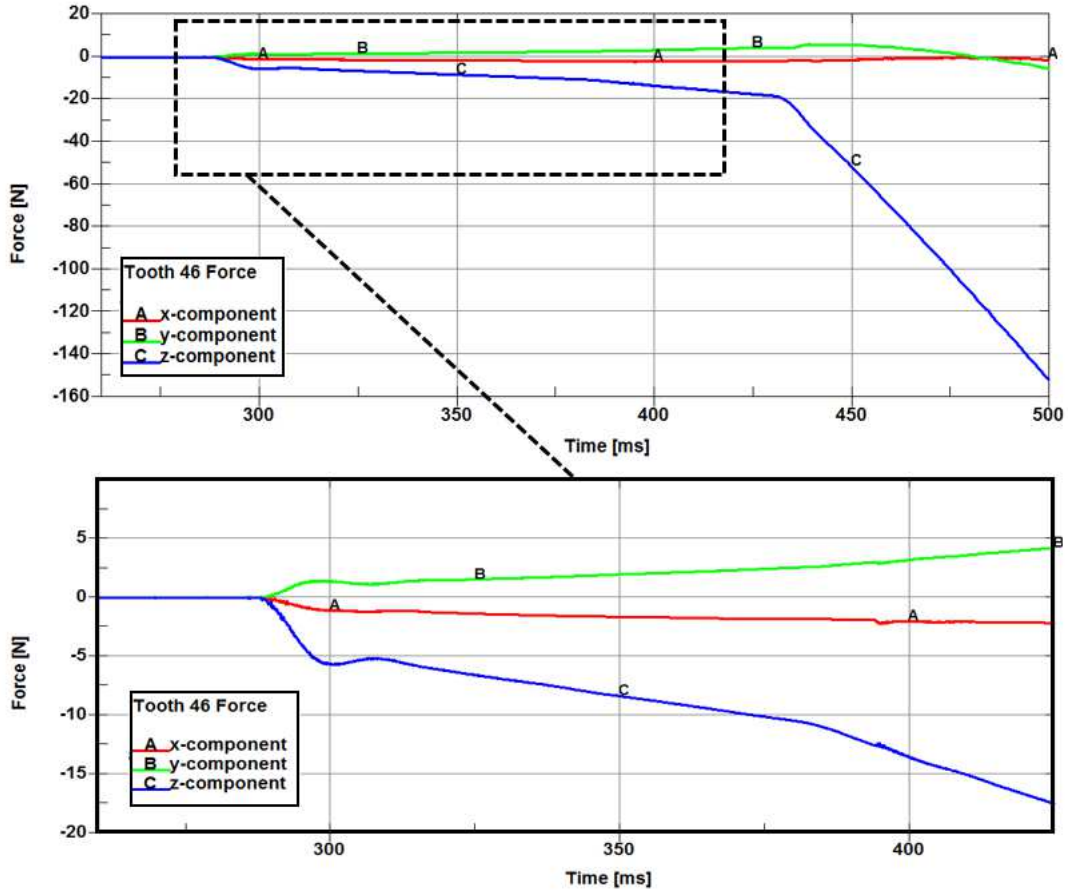

Figure 4.12: Forces in tooth 46 during unilateral molar biting. The figure below is a closer look at the initial range, when posterior and lateral forces are significant

the tooth, while tension is present in the oblique fibers of the PDL. We additionally observe that the distribution between compressive and tensile response is different between the material models, with the polynomial model carrying the load mostly by means of compression and with the Ogden model A rather through means of tension. For this reason, in this particular task a higher concentration of stress is observed in the polynomial model because the apex, a relatively small area of the PDL, is the only site that can resist compression.

During incisive biting, tooth 11 must resist at all times the moment produced by the anterior forces at the tip of the tooth. We observe that the horizontal and apical fiber bundles, responsible for counteracting tipping and rotating forces, are under high stresses (Figure 4.14c). The polynomial model delivers higher compressive stresses in order to counteract the moment in the tooth (Figure 4.14d).

Stresses in the first molar are shown in figures 4.15 and 4.16. In both models, tensional stresses appear over the lingual surface of the roots, whereas compressive stresses show at the lingual side of the root bifurcation. As in the previous cases,

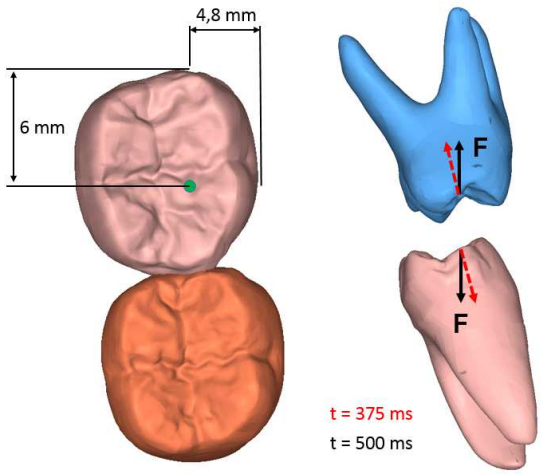

Figure 4.13: Resultant force application point on the mandibular first molar (left). The molar (light pink) is 10.3 mm wide and 11.5 mm long. The second mandibular molar (orange) is displayed for orientation purposes. Posterior view of the molars and resulting force during unilateral molar biting (right)

the polynomial model exhibits higher compressive stresses.

Maximum and minimum stresses as calculated by the polynomial model and by the Ogden model A are presented in Table 4.2.

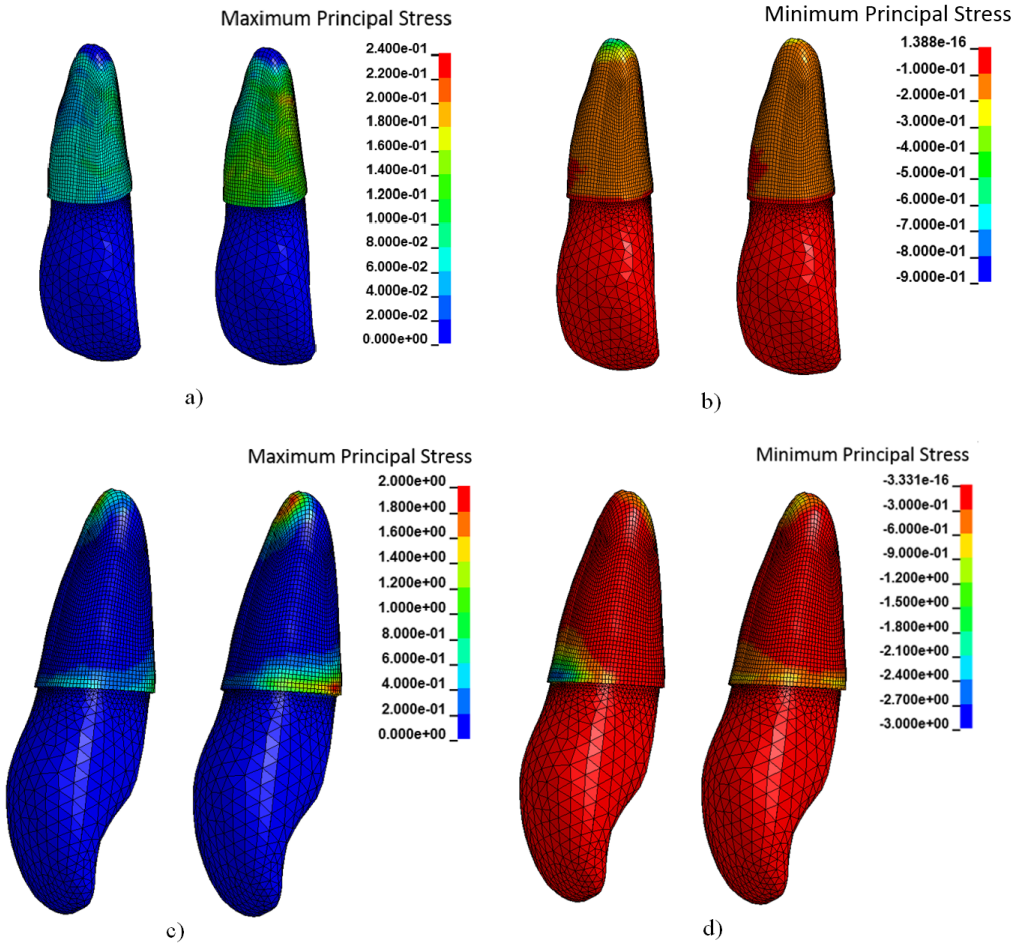

Figure 4.14: Comparison of stresses between the polynomial model (placed left in each picture) and Ogden model A (placed right in each picture). First principal stresses (a) and third principal stresses (b) in the PDL developed during a tooth-aligned axial load of 20 N. First principal stresses (c) and third principal stresses (d) during incisive biting (resulting force on each tooth is 14 N)

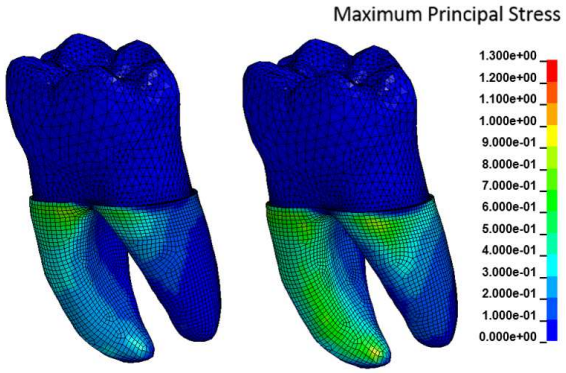

Figure 4.15: First principal stresses in the PDL developed during unilateral molar biting with 80 N for the polynomial model (left) and the Ogden model A (right)

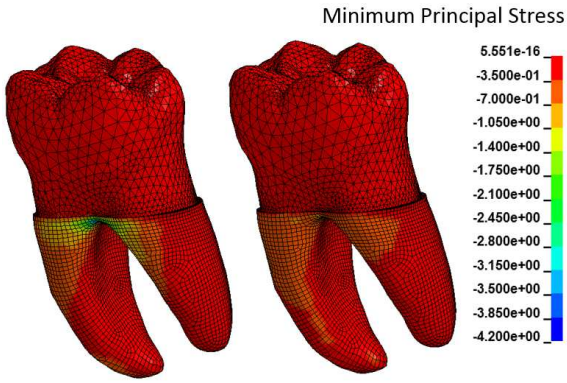

Figure 4.16: Third principal stresses in the PDL developed during unilateral molar biting with 80 N for the polynomial model (left) and the Ogden model A (right)

Material model	**Case**	**Maximum stress [MPa]**	**Minimum stress [MPa]**
Polynomial model	Axial	0.13	-0.85
	Incisive biting	2.11	-3.20
	UMB	0.97	-4.19
Ogden model A	Axial	0.24	-0.25
	Incisive biting	2.66	-1.27
	UMB	1.35	-0.86

Table 4.2: Maximum and minimum stresses for the polynomial model and Ogden model A

4.3 Conclusions

The forces obtained with the complete model during the biting tasks show that the smaller incisive teeth are aligned to minimize the moment produced during biting, while their counterparts, the maxillary teeth, must withstand higher moments. The maxillary teeth are able to carry these loads due to their greater size and hence, larger PDL surface. Resulting forces in the first molar during UMB are mostly intrusive and do not produce large moments. The morphology of the molars, which show a small tilt suggesting the capacity to resist lateral forces, are most likely adapted for the mastication process.

The conditions of the teeth in both tasks can be easily reproduced in a simplified model with the presented data. For incisive biting, the forces in Figures 4.8, 4.9 and 4.10 must be applied at the respective resultant force application point. For the mandibular incisive teeth, the point is found at the tip of the tooth, for the maxillary incisive teeth the point is located in the middle of the lingual fossa.

In the case of the mandibular teeth, the force must be modified to take into account the rotation of the teeth. In the case of UMB, the resulting force is mostly vertical and its application point is placed between the groove and the cusp that fits in the antagonist's groove. Both, the polynomial and Ogden model A, can reproduce the experimental results compiled by Lenz et al. [40]. However, using parameters that produce good results for the case of an axial intrusive force, means that the material may be too soft in the case of a palatal horizontal force. The material parameters for Ogden model B are inside the range of both cases, but the material is too stiff during small forces in the axial case.

The PDL employs different mechanisms to resist tensile (Sharpey's fibers) and compressive (hydrostatic pressure) forces. For this reason, the stresses shown are the maximum (tensile) and minimum (compressive) stresses. The two material models behave in a different manner, the polynomial model exhibits a higher compressive response to forces applied to the teeth. On the other hand, the Ogden material shows mostly tensile stresses when an identical load is applied. Since the areas under compression are smaller, the polynomial model shows greater concentration of stresses. Evaluating the stress in the PDL is difficult since in vivo measurements of its properties are very limited. Experimental results [46] on porcine PDL have shown a tensile failure stress of about 8 MPA. Although tensile stresses shown here do not exceed these values (Table 4.2), higher biting forces which the muscles are able to produce would make the principal stresses exceed this value. Due to the relatively large surface surrounding the PDL (398 mm^2 for tooth 46) over which the forces are distributed, lower stresses are expected in the PDL. A similar comparison cannot be done with the compressive stresses since the PDL handles these loads indirectly through the fluids it contains, and as such a maximum compressive stress

that the tissue can withstand cannot be experimentally determined. Despite this, it is unlikely that the majority of a biting load would be resisted by compressive stresses at the root bifurcation of the molar as suggested by the polynomial model.

In order to capture the highly non-linear behavior of the PDL, the two material models have an exponential stiffening response to strain. This creates, however, a concentration of stresses in areas that deform first since a small change in strain results in a large difference in stiffness, and subsequently any further loading will be mostly carried by the stiffer elements. For both materials, the parameter that affects the values of the stress the most is the bulk modulus. The closer the material is to becoming incompressible, the better the forces are distributed and thus lower absolute values are obtained for both, the maximum and minimum stress. In the case of the Ogden model, the hydrostatic stress has a linear relationship with the relative volume J and any increase in the Poisson's ratio will result in the material being too stiff. For the polynomial model, however, the relationship is exponential, which should allow the material, by using the appropriate parameters, to become incompressible as the strain increases. In reality, the parameters used for the polynomial model by Su et al. [44] result in a quicker response (stiffening) to shear strain than to volumetric strain, making the material more compressible as it deforms. It is to note, that both material models require that the time step size be reduced as the strain increases due to the rising non-linearity of the material behavior. Additionally, oscillations in both materials were damped by adding viscoelasticity to the model in order to avoid numerical instabilities.

Both materials models reproduce the mobility of the teeth in an accurate manner for typical motions and tasks of the masticatory system. It was observed, that the employed simplified geometries of the PDL were sufficient to capture realistic displacements. This helps to reduce considerably the amount of time to create the geometries of the PDL, as only the surface of the tooth is required to create its corresponding alveole. Future studies regarding the influence of the small movements of the teeth during near interscupation can be performed with these material models. In the case of very small forces, the parameters can be further calibrated, although with the corresponding penalty of requiring a smaller time step.

Chapter 5:
The Temporomandibular Joint

The temporomandibular joint (TMJ) is a synovial joint which articulates the mandible to the skull. It is mainly composed of the mandibular condyles, the mandibular / glenoid fossae, the articular discs, the capsules, the ligaments and the lateral pterygoid muscles. The articulating surfaces of the condyles and the mandibular fossa are covered with articular cartilage, which together with the synovial fluid allows for a very low coefficient of friction and a uniform transmission of compressive forces to the bone [47]. The articular cartilage of the TMJ contains both, collagen fibers of type I and of type II, which classifies it as a fibrocartilage, in contrast to most other synovial joints composed mainly of hyaline cartilage. Cartilage is composed mainly of an extracellular matrix of collagen fibers filled with ground substance. Due to the low permeability of the tissue, compression forces rapidly increase fluid pressure, which in turn carries the major part of the load through hydrostatic pressurization [48]. The collagen fibers of the cartilage, on the other hand, resist the stretching of the tissue from tensile forces [49]. The proportion of type of collagen fibers present in the articular cartilage, depends upon the functional demand of the joint [50]. The articular disc, also composed of fibrocartilage, lies between the mandibular condyle and the fossa, dividing the synovial joint in two compartments. It distributes loads and dissipates the energy caused from impact loads. The disc allows relative motions between the condyle and the temporal bone. In the case of the condyle, translational as well as rotational movements are possible. The articular disc is connected to the articular surfaces through the joint capsule. The attachments of the joint capsule can be divided as shown in figures 5.1 and 5.2 into medial, lateral, anterior and posterior attachments. These attachments offer the disc a certain range of movement and at the same time avoid extreme displacements that may result in its dislocation.

The temporomandibular ligament supports the joint when high posterior forces occur and limits the posterior displacement of the mandible. It also constrains the movement of the condyle during jaw opening [51]. It is composed of two bundles of fibers which attach at the zygomatic arch and the neck of the mandible. The lateral pterygoid muscle attaches to the condyle, and in the majority of cases also directly to the articular disc. The lateral pterygoid muscle is the main responsible for the anterior incursion of the condyle and the disc.

The complexity of the joint makes it very susceptible to problems and disorders. Around 20-30 percent of the population are affected by some type of temporo-

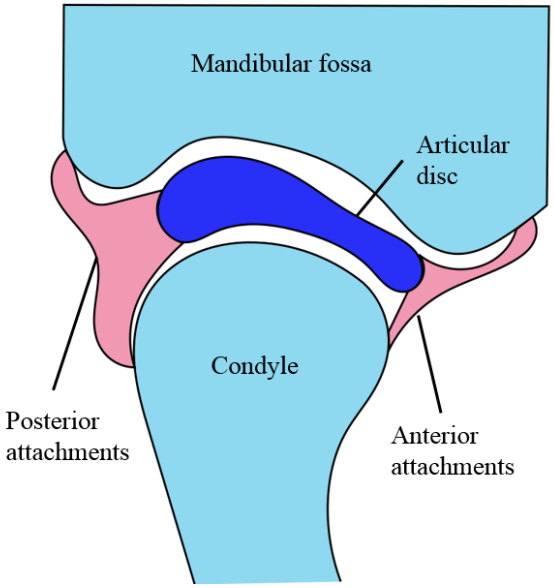

Figure 5.1: Sagittal view of the temporomandibular joint (TMJ) showing the anterior and posterior attachments of the joint capsule

mandibular disorder (TMD), such as pain, clicking, bruxism, limited mobility, articular disc dislocation, etc. [52, 53]. One of the most frequent treatments employed for TMD is splint therapy [54], with more than 3 million splints made just in the United States. The purpose of the splint is to create a mechanical obstruction in order to restrict dysfunctional forces. Since the activation level and the capacity to

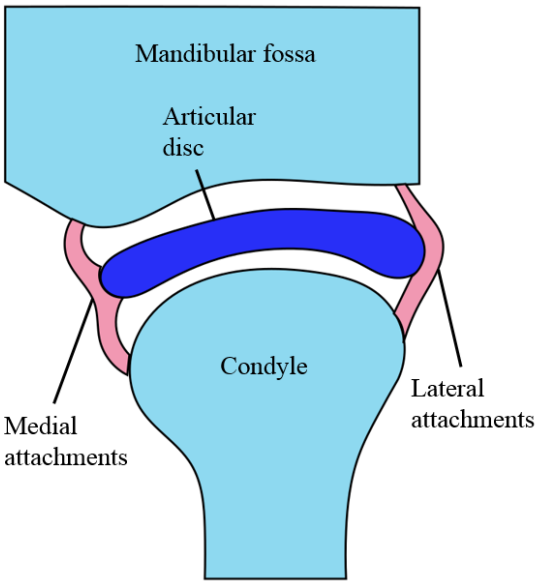

Figure 5.2: Coronal view of the temporomandibular joint (TMJ) showing the medial and lateral attachments of the joint capsule

produce muscle force is affected by its current length, splints can be employed in different situations, for instance, to achieve muscle relaxation in the case of muscle hyperactivity or to protect the teeth and the mandible during bruxism. Differences in muscle recruitment and activation levels when gap variations are introduced in the masticatory system were studied by Schindler et al. [45]. The introduction of these gap variations also changes the development of bite and joint forces. These forces and the behavior of the TMJ, particularly of the articular discs, were further studied with the present model. The model was run as a dynamic problem, in order to accurately capture the relative displacements undergone by the TMJ. These displacements are crucial to determine the response of the TMJ to given loads. Understanding the effects that result from the introduction of these limiting gaps, will allow a more detailed comprehension of the effectiveness of the use of splints as therapy for joint disorders.

5.1 Physiological Movement of the TMJ

The motion of the TMJ during jaw opening can be observed in Fig. 5.3. During the initial phase, the condyle undergoes mostly a rotational movement, with a translational component becoming more prevalent as the jaw continues to open. The inferior stratum of the posterior attachments (retrodiscal tissue) and the superior anterior attachments will steadily abandon their state of tension until they become completely relaxed in the final phase of the motion. Similarly, tension in the superior stratum of the posterior attachments and the inferior anterior attachments increases until the fibers are stretched to their maximum capacity. Tension in the anterior inferior attachments pulls the disc anteriorly and keeps it above the condyle, while the superior stratum of the posterior attachments limits the anterior incursion of the disc.

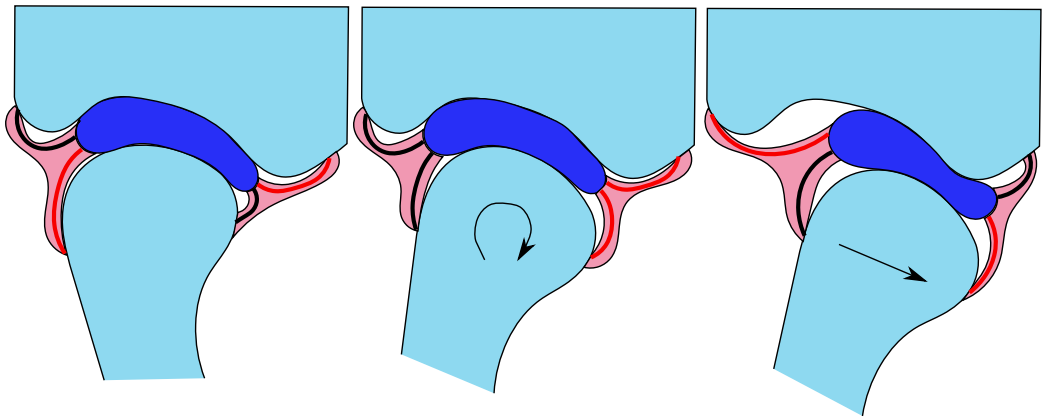

Figure 5.3: Motion of the TMJ during jaw opening. Relaxed and tense fibers are represented by red lines and black lines, respectively

Jaw closing follows the inverse process. Here, as the condyle returns to its posterior position, the inferior stratum of the posterior attachments build up tension in order to avoid anterior disc dislocation while the superior anterior attachments limits the posterior displacement of the disc. These attachments work together with the temporomandibular ligament counterbalancing the posterior forces developed by the muscles during strong biting forces. As can be observed in Fig. 5.4, the temporomandibular ligament pivots the condyle in order to force it into a trajectory that ensures the handling of strong posterior forces by the articular disc.

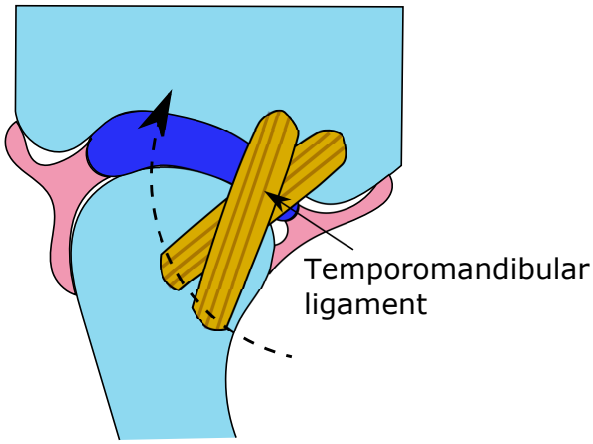

Figure 5.4: The temporomandibular ligament pivots the condyle and constraints it to a trajectory that ensures that posterior forces can be handled by the articular disc

The motion followed by the condyle during opening is a consequence of the presence of the temporomandibular ligament and the passive response of the muscles. Once these tissues cannot be stretched any further, the condyle translates anteriorly to relax them and allow further jaw opening.

5.2 Modeling the TMJ

Several strategies have been employed to model the TMJ. In the following, focus was given to works where the geometry of the articular disc and its movement relative to the condyle were modeled. Koolstra & van Eijden meticulously studied the TMJ. They created a model [55] that used a combined FE and rigid body analysis, where the joint consists of an articular disc and cartilage tissue represented by solid finite elements. The jaw itself is modeled as a rigid body. In this model, the disc is attached to the condyle by means of inextensible wires, which represent the lateral and medial attachments of the joint capsule. Displacements in Koolstra's model are a result of forces that originate from the activation of the muscles, which were also closely studied by Koolstra & van Eijden [56]. These authors also studied

the viscoelastic behavior of the articular disc, and determined its decay constants [57]. Perez et al. executed numerous investigations of the TMJ [58, 59, 60]. In their studies, the TMJ consists of the articular disc and the lateral and medial attachments, which are represented with solid elements as part of the geometry of the disc. The attachments connect the condyle to the disc and allow displacements of the disc. Their work focuses on the incorporation of a material model that captures the anisotropy of the articular disc. A poroelastic material model is used with different parameters for the anterior, middle and posterior part of the disc. The cartilage tissue, however, is omitted in their model.

In our model, the TMJ consists of the articular disc, the cartilage of the fossa, the cartilage of the condyle, the lateral, medial, posterior and anterior attachments of the disc, and the temporomandibular ligament. With the exception of the lateral and medial attachments, all these components are deformable.

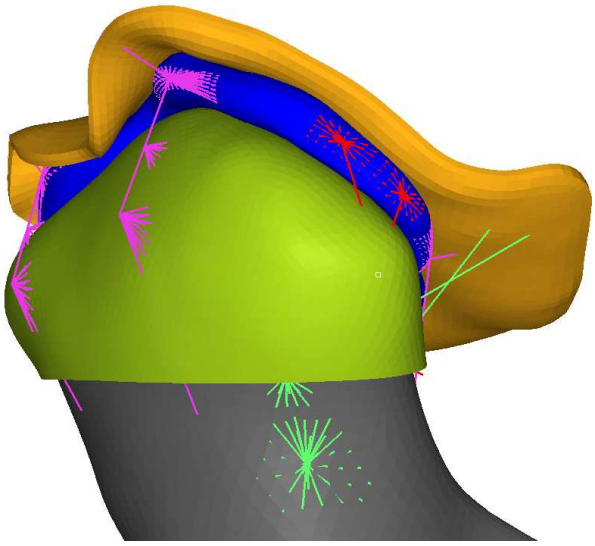

Figure 5.5: Configuration of the TMJ: cartilage of the fossa (yellow solid elements), articular disc (blue solid elements), cartilage of the condyle (green solid elements), anterior and posterior attachments (fuchsia truss elements), lateral attachments (red truss elements), and temporomandibular ligament (green truss elements)

The joint modeling underwent several revisions before reaching its current state. In the literature, the attachments of the disc are often simplified with one or two springs attached to a constrained point in space in order to limit the movement of the disc. However, this approach results in an unrealistic behavior during jaw opening. A considerable amount of time was employed recreating different representations of the joint, until finally following the steps of Koolstra's model. At the beginning, the model included only the medial and lateral attachments. However, due to the dislocation of the disc during high biting forces, it was decided to introduce the attachments that played a role constraining the border movements of the joint. The

joint was continuously updated as long as different tasks showed the limitations of the model.

5.2.1 Articular Disc and Cartilage

Since soft tissue is not visible in CT-scans, the geometry of the articular disc could not be obtained through a segmentation process. To procure its geometry, the space between the condyle and the mandibular fossa was outlined while following anatomy books in order to determine the space occupied by the disc. This resulted in an articular disc with a rather even thickness than what is observed in reality, as the disc thickness varies considerably between its anterior, middle and posterior part (Fig. 5.6). The articular disc was meshed with over 11.000 hexahedral elements. The geometry for the articular cartilage of both the mandibular fossa and the condyle was created with an offset operation of 0.5 mm [61, 62]. The cartilage of the fossa and the condyle were included because of their role in evenly distributing the forces to the bone. A Mooney-Rivlin hyperelastic material model whose parameters were taken from Koolstra & van Eijden [55] was used for the cartilage and articular disc. The viscoelastic behaviour of the disc was also included, with decay constants taken from [57]. Node-to-surface contact elements were used to define the contact between the disc and the cartilage of the fossa as well as the contact between the disc and the cartilage of the condyle. In both cases, friction was defined as non-existent since frictional forces are minimal due to the presence of the synovial fluid.

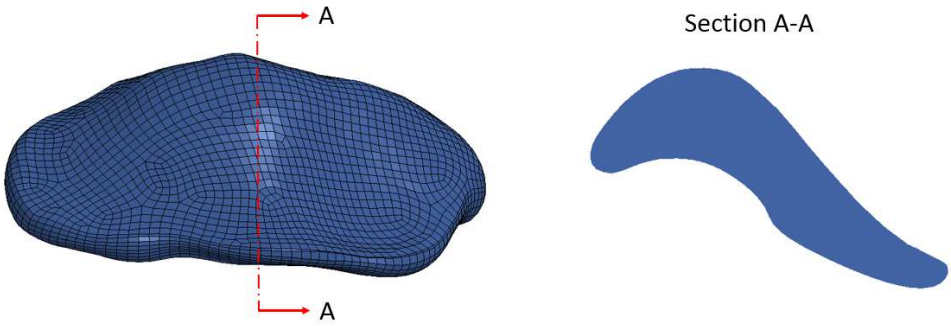

Figure 5.6: Frontal (left) and sectional (right) view of the articular disc

5.2.2 Attachments and Ligaments

The jaw experiences a significant posterior force when the closing muscles are activated. Koolstra activated the lateral pterygoid muscles in order to bring the system into balance and avoid the disc from extreme dislocations. The measurement of muscle activation levels in [45] shows that the lateral muscles are mostly inactive during

the biting process. To ensure joint stability during strong muscle forces, inclusion of the posterior and anterior attachments of the capsule as well as the temporomandibular ligament was deemed necessary. All attachments and ligaments were modeled using trusses with a material model that only produces resistance during tension. The attachments of the capsule were represented each with a pair of trusses, except the posterior inferior attachments of the capsule, where pulley elements were employed to keep the trusses on the surface of the condyle, in order to produce an appropriate response from the fiber (Fig. 5.5). The temporomandibular ligament was modeled using a pair of trusses in order to represent the deep and superficial part, which are differently oriented. The extent of the trusses was estimated from the area covered by the attachments on the disc. This area was further calibrated a) to ensure that the range of movement of the joint was not unrealistically limited, and b) at the same time to provide the stability required during strong muscle forces. The area of the trusses for the attachments amounts to approximately $12\,\mathrm{mm}^2$. Similarly, for the temporomandibular ligament, the area of its trusses was estimated to be around $15\,\mathrm{mm}^2$.

The attachments of the capsule were given an elastic modulus from the stress-strain curve obtained by Tanaka [63]. However, the inferior posterior and the superior anterior attachments are tense when the mouth is closed. This is the initial configuration of the model. For this reason, a positive offset, determined by measuring the length of the trusses during jaw opening (when the fibers are relaxed) was set. Since the task of the medial and lateral attachments of the capsule is to keep the disc on the surface of the condyle, they were modeled as inextensible wires as in [55]. The temporomandibular ligament was modeled using the material parameters from Palomar [58].

The stylomandibular and sphenomandibular ligaments were not included in the model since they mostly prevent excessive protrusion of the mandible, which was not in the scope of this study.

The introduction of the remaining attachments allows the model to perform biting tasks without having to activate the lateral pterygoid muscles in order to bring the jaw into balance. In this manner, more accurate forces in the joint are achieved.

5.3 Simulations and Results

5.3.1 Jaw Opening

The distinctive process that the TMJ undergoes during jaw opening helps to evaluate whether the different components of the masticatory system were properly configured. Jaw opening was achieved by activating the lateral pterygoid and di-

gastric muscle during an interval of 75 ms (a detailed view of the modeled muscles can be found in chapter 6). The TMJ undergoes a realistic behavior during jaw opening as shown in figure 5.7: a rotational motion of the condyle is followed by a translational one and the articular disc moves along with it. A gap of 35 mm between the incisive teeth was achieved when reaching an activation level of 100% for the opening muscles. This gap is slightly lower than the natural range of maximum mouth opening [64] which is around 52.8 +/- 7.4 mm for adult men. The gap is limited in our model by the approach to fix the position of the hyoid bone, resulting in the digastric muscle quickly losing capacity to generate force as it contracts, and by the resistance of the TMJ ligament and the muscles.

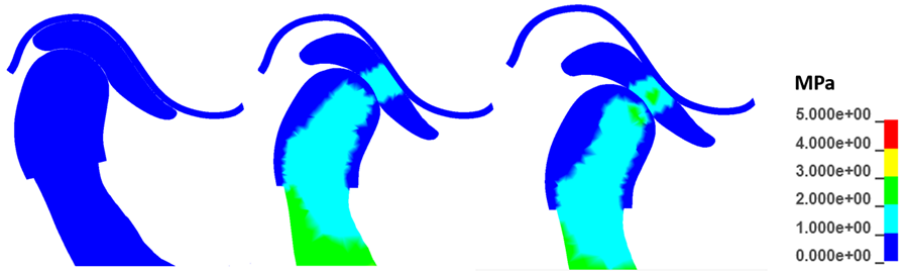

Figure 5.7: Motion of the condyle and disc, and von Mises stresses in the TMJ during jaw opening

Resulting forces in the TMJ and stress levels on the disc during jaw opening are similar to those obtained by Koolstra & van Eijden [55]. The joint forces in our model are somewhat lower since Koolstra's model includes the rest of the suprahyoid muscles (mylohyoid, geniohyoid). The resulting joint force is displayed in Fig. 5.8.

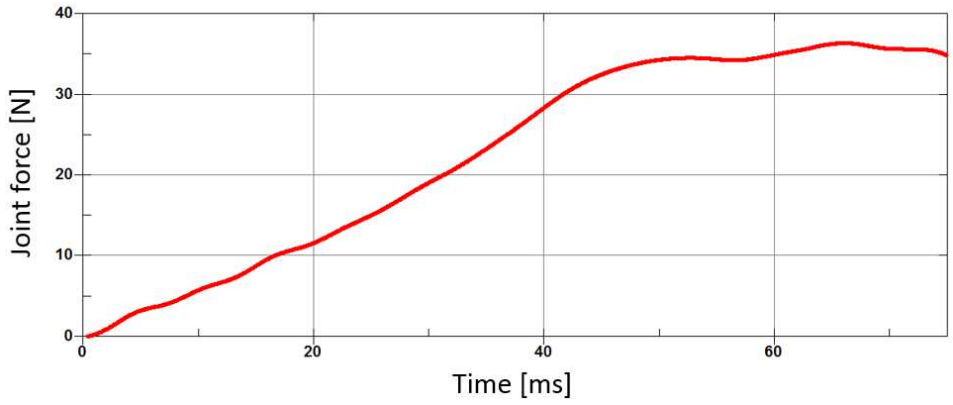

Figure 5.8: Von Mises stress in the TMJ during jaw opening

5.3.2 Variational Gap Constraint

The configuration used for the study is shown in figure 5.9. The gap was established by a rigid spacer. The spacer on the contralateral side remains in the same position for each case, while the rigid body on the ipsilateral side is lowered by $0, 100, 200$, or $300\,\mu$m. For this task, the jaw is opened slowly from 0 to 225 ms, resulting in a gap between the first molars of circa 5 mm, just enough to bring the lower molars below the rigid bodies. At this point, the contact elements become active and low magnitudes are set for the closing muscles, until a time of 430 ms. These two phases were performed in order to minimize the kinetic energy in the model and avoid sudden movements or impacts. Once the bolus is firmly trapped between the teeth, then the closing muscles are activated to their final magnitudes.

150 N Bite Force

For this task, the employed activation magnitudes and the resulting force of the muscles are shown in table 5.1 and 5.2. They were obtained by averaging the activation levels from several patients, needed to produce a total biting force of 150 N. These activation levels were experimentally measured by Schindler et al. [45].

Figure 5.10 presents the resulting forces on the joint and on the rigid bodies. Employing the average activation levels produced in the case of 0, 100, 200 and 300 μm, a resulting force on the rigid bodies of 170, 164, 150 and 156 N, respectively. As expected, as the gap increases, the force distribution changes, with a higher share being shifted to the ipsilateral rigid body and the contralateral joint.

Stresses on the disc can be observed in Figures 5.11 and 5.12. When no gap is introduced, the stresses on both discs occur between the middle and posterior part of the disc. In this case, both condyles are positioned in a very stable position, since no further posterior displacement is possible due to the TMJ ligament and the attachments of the disc. The resulting force on the mandible then points in posterior direction. Additionally, a large area of the articular disc is in contact with both the condyle and the mandibular fossa, thus allowing for a better distribution of the forces in the joint. As the gap increases, stresses in the ipsilateral joint continuously shift to the center of the disc. The rising forces in the contralateral side increase the compressive stresses, with the compressive stress reaching a magnitude of -1.67, -1.73, -1.79, and -1.86 MPa.

Muscle	0 μm	100 μm	200 μm	300 μm
Temporalis Anterior I	38 %	37 %	34 %	36 %
Temporalis Posterior I	39 %	20 %	19 %	18 %
Masseter I	13 %	18 %	17 %	25 %
Medial Pterygoid I	7 %	5 %	6 %	6 %
Lateral Pterygoid I	0.1 %	1 %	1 %	1 %
Temporalis Anterior C	36 %	37 %	33 %	31 %
Temporalis Posterior C	38 %	20 %	17 %	14 %
Masseter C	15 %	20 %	19 %	22 %
Medial Pterygoid C	9 %	7 %	10 %	10 %
Lateral Pterygoid C	0.1 %	2 %	1 %	4 %

I: Ipsilateral, C: Contralateral

Table 5.1: Average activation levels of the muscles to produce a bite force of 150 N for each introduced gap

50 N Bite Force

The previous task was repeated with a smaller biting force. In this case, however, the use of averaged activation levels of the muscles (obtained by averaging the muscle activation levels of several patients who performed the same task) resulted in a much higher biting force of around 80 N. On the other hand, the use of healthy patients' specific activation levels produced biting forces very close to the target of 50N, with three different patients resulting in biting forces of 50 $\pm$ 2.5 N, and no patient from those used for the average, surpassing a biting force of 65 N. The activation levels and muscle forces, typical of a single patient are shown in tables 5.3 and 5.4.

The resulting forces for all cases are presented in figure 5.13. A similar behavior as for a 150 N biting force is used, can be observed. However, in the 300 μm case, no contact is observed at the contralateral side. Since the experimental measurements show that in this case contact occurs in both sides, albeit with very low forces at the contralateral side, it may be concluded that the model cannot entirely capture the correct behavior of the system. This can be attributed to the fact that the employed geometry and muscles' activation levels originate from different patients.

The principal (minimum) stresses on the disc can be observed in figures 5.14 and

Muscle	**Force [N]**			
	0 μm	100 μm	200 μm	300 μm
Temporalis Anterior I	58	56	50	53
Temporalis Posterior I	49	25	24	22
Masseter I	23	32	28	35
Medial Pterygoid I	6.5	4.8	5.5	5.5
Lateral Pterygoid I	0.1	0.5	0.6	0.4
Temporalis Anterior C	55	56	50	48
Temporalis Posterior C	47	25	21	18
Masseter C	26.5	35	30	39
Medial Pterygoid C	8.2	6.5	13	17
Lateral Pterygoid C	0.1	1.1	0.6	2

I: Ipsilateral, C: Contralateral

Table 5.2: Force exerted by each muscle to produce a bite force of 150 N for each introduced gap

5.15. The highest compressive stresses in the case of 0, 100, 200, and 300 μm gap constraints are -0.85, -1.06, -0.99, and -0.99, respectively.

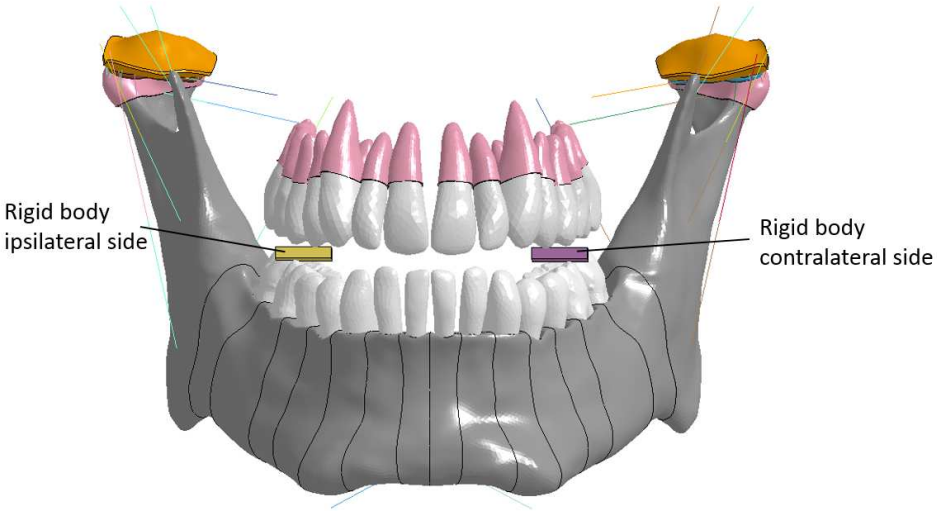

Figure 5.9: Variational gaps were introduced with rigid bodies. The ipsilateral side is displaced downwards in each case

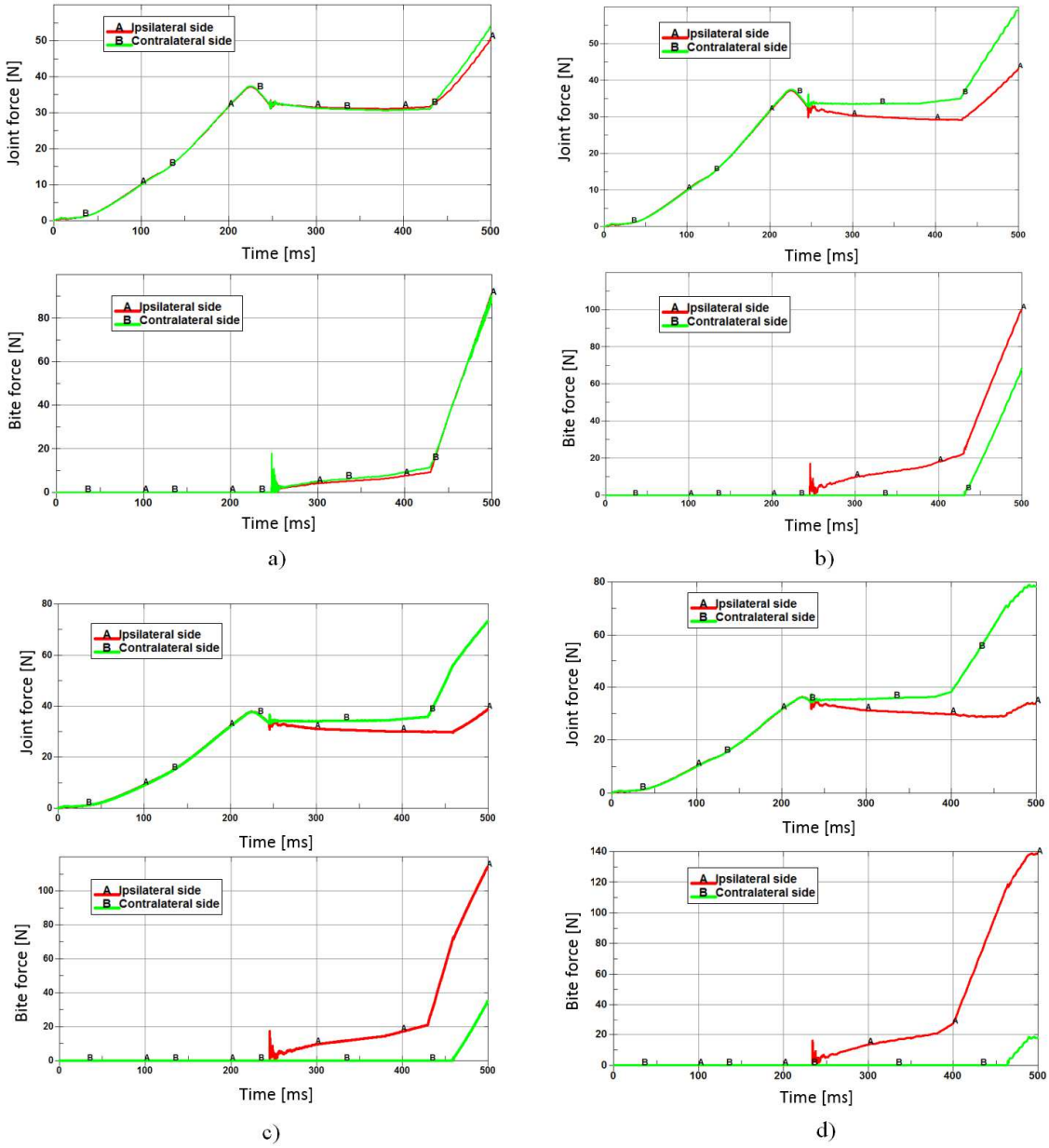

Figure 5.10: Forces on the joint and the rigid spacers, when the two sides are leveled (a), and when a gap of 100 (b), 200 (c), or 300 μm (d) is introduced. Activation levels of the muscles belong to a 150 N bite force (oscillations observed here arise from the impact between the teeth and the rigid spacer)

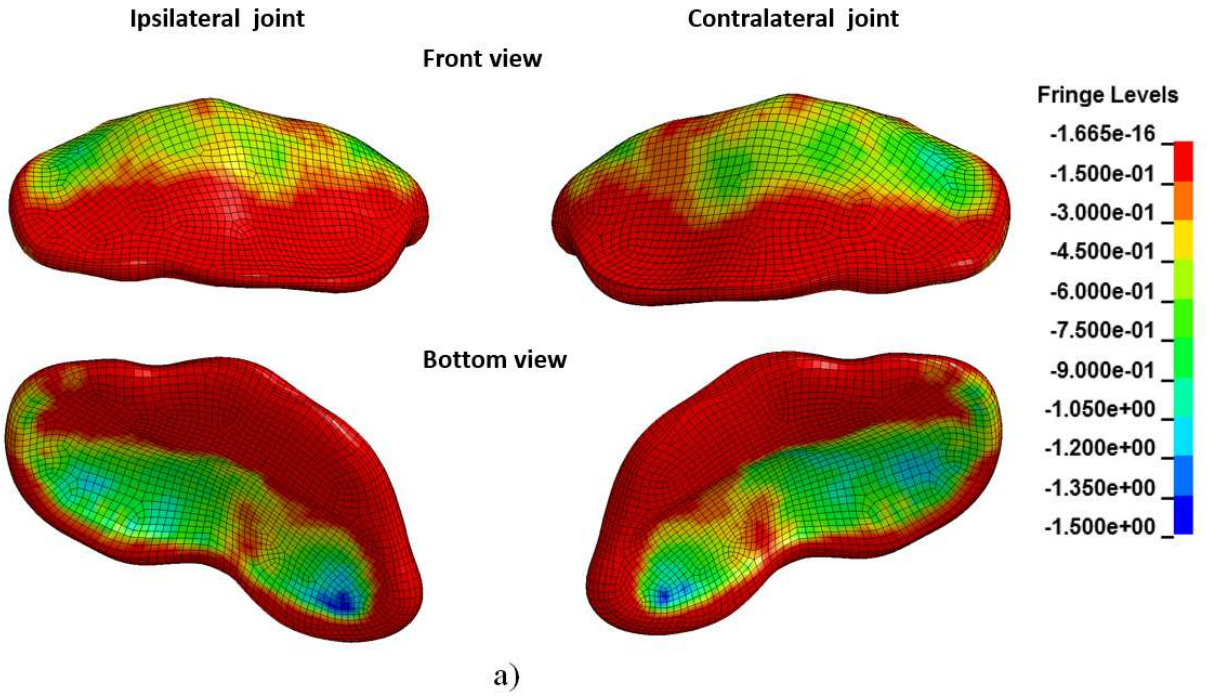

Figure 5.11: Third principal stresses in the articular disc during a target bite force of 150 N and a gap of 0 (a) and 100 μm (b)

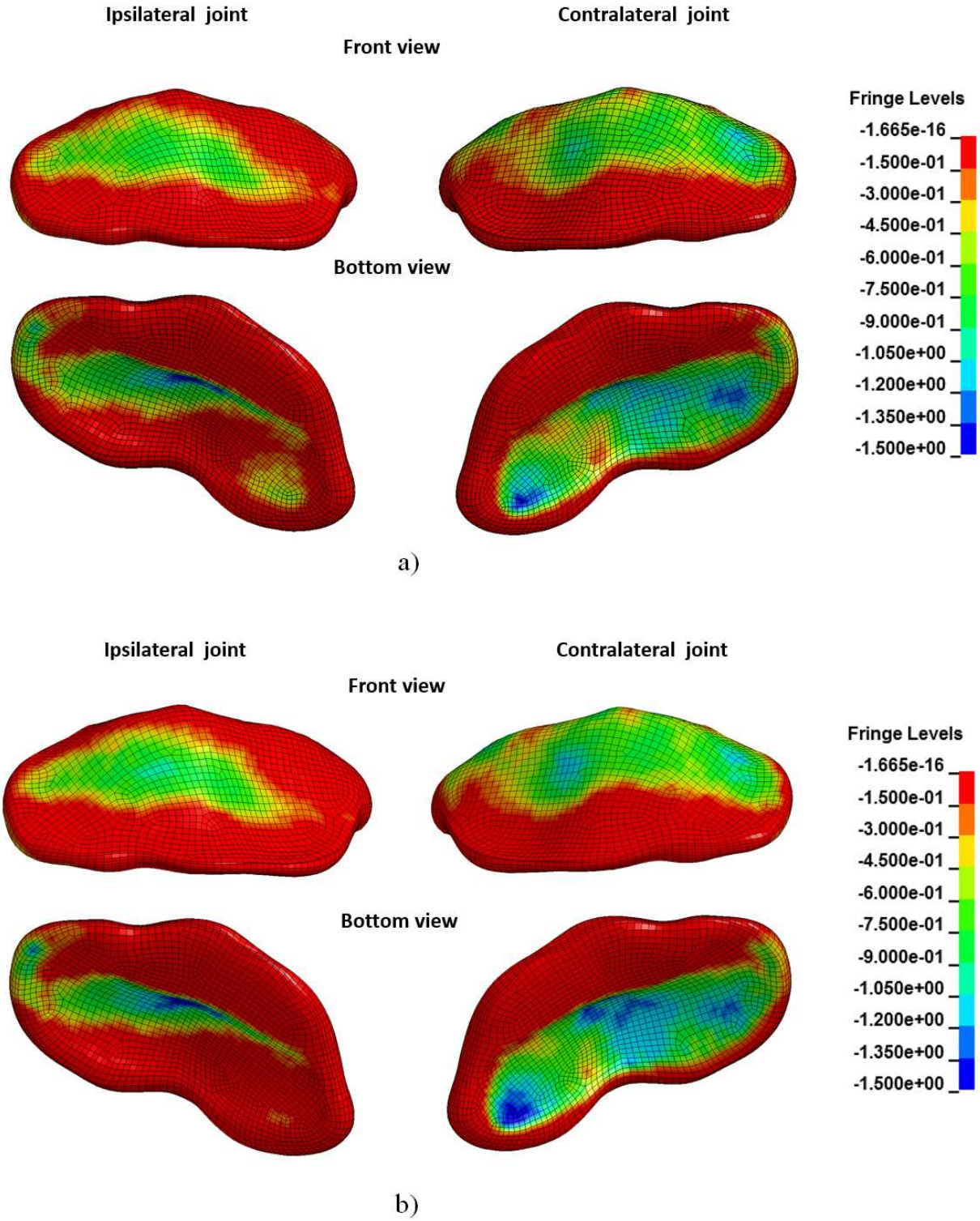

Figure 5.12: Third principal stresses in the articular disc during a target bite force of 150 N and a gap of 200 (a) and 300 μm (b)

Muscle	0 μm	100 μm	200 μm	300 μm
Temporalis Anterior I	13.0 %	10.6 %	7.4 %	6.4 %
Temporalis Posterior I	6.7 %	5.5 %	7.3 %	9.8 %
Masseter I	6.2 %	6.2 %	3.7 %	3.0 %
Medial Pterygoid I	1.7 %	3.9 %	4.4 %	2.0 %
Lateral Pterygoid I	0.5 %	0.6 %	0.6 %	0.6 %
Temporalis Anterior C	13.2 %	10.4 %	11.4 %	11.9 %
Temporalis Posterior C	2.7 %	3.8 %	5.0 %	5.3 %
Masseter C	6.9 %	6.8 %	5.5 %	6.0 %
Medial Pterygoid C	2.3 %	3.6 %	5.2 %	5.8 %
Lateral Pterygoid C	0.4 %	0.4 %	0.6 %	0.5 %

I: Ipsilateral, C: Contralateral

Table 5.3: A healthy patient's activation levels of the muscles to produce a bite force of 50 N for each introduced gap

Muscle	**Force** [N]			
	0 μm	100 μm	200 μm	300 μm
Temporalis Anterior I	20.0	16.3	12.0	10.0
Temporalis Posterior I	9.0	7.2	9.0	12.5
Masseter I	11.0	11	6.6	5.5
Medial Pterygoid I	2.1	4.0	5.0	2.5
Lateral Pterygoid I	0.2	0.3	0.3	0.3
Temporalis Anterior C	21.0	16.3	18.0	18.7
Temporalis Posterior C	3.8	5.1	6.5	7.0
Masseter C	12.5	12.1	10.0	11.0
Medial Pterygoid C	2.5	3.7	5.0	5.4
Lateral Pterygoid C	0.2	0.2	0.3	0.2

I: Ipsilateral, C: Contralateral

Table 5.4: Force exerted by each muscle to produce a bite force of 50 N for each introduced gap

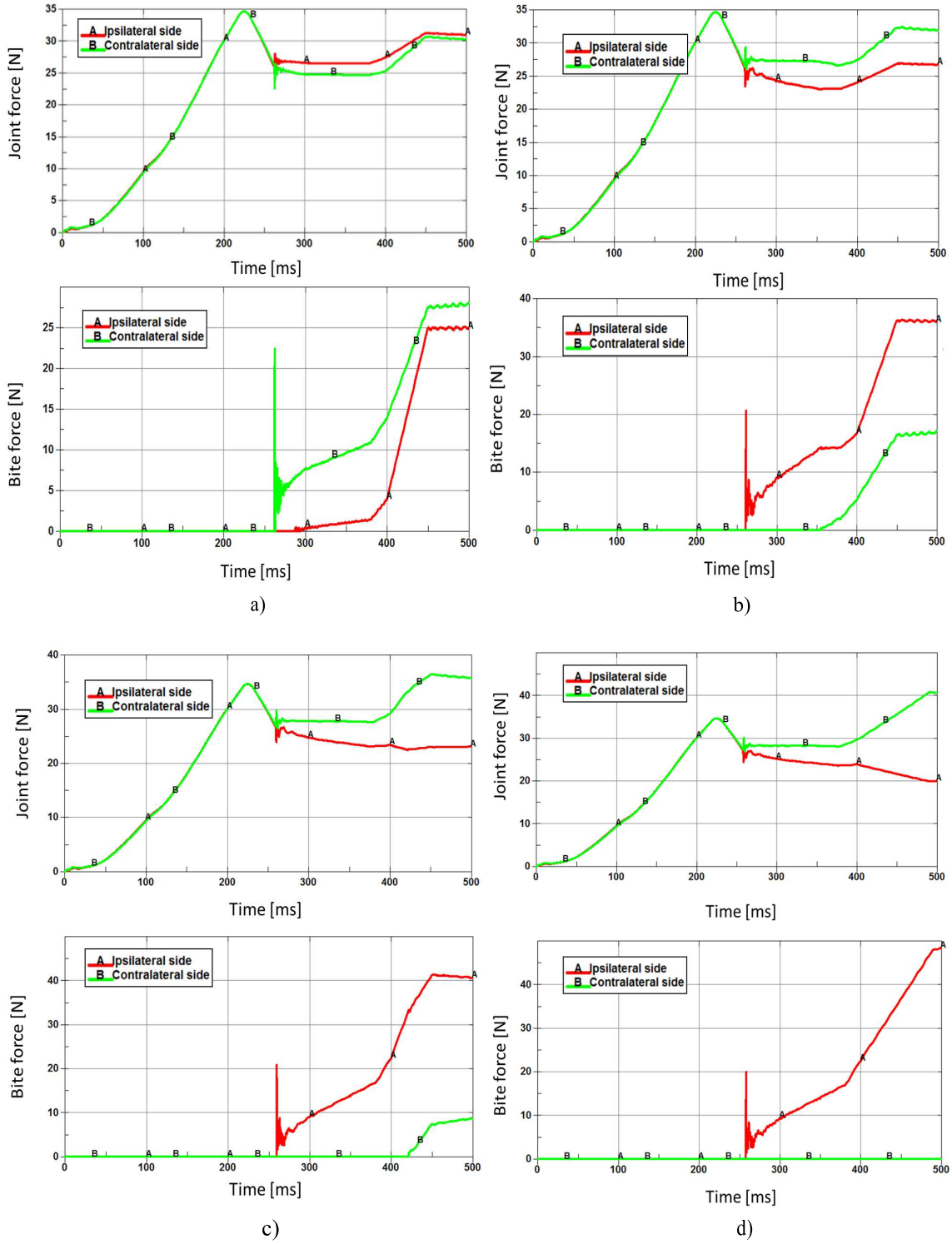

Figure 5.13: Forces on the joint and the rigid spacers, when the two sides are leveled (a) and when a gap of 100 (b), 200 (c), or 300 μm (d) is introduced. Activation levels of the muscles belong to a 50 N biting force (oscillations observed here arise from the impact between the teeth and the rigid spacer)

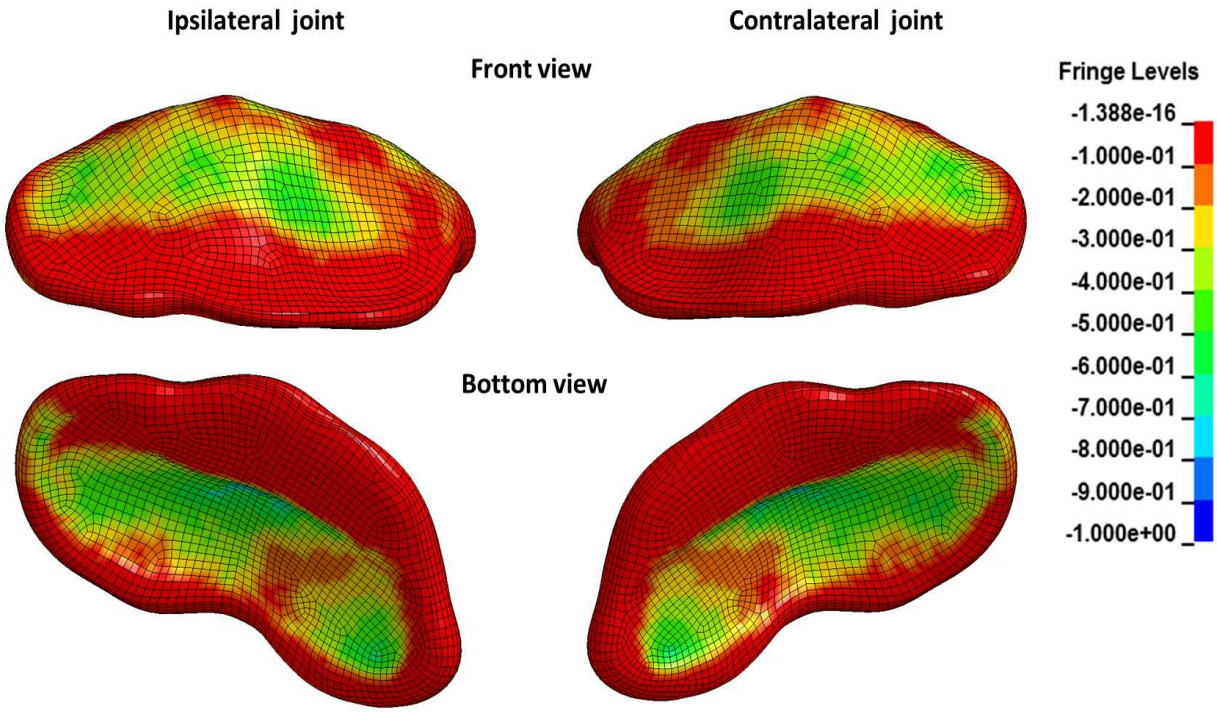

a)

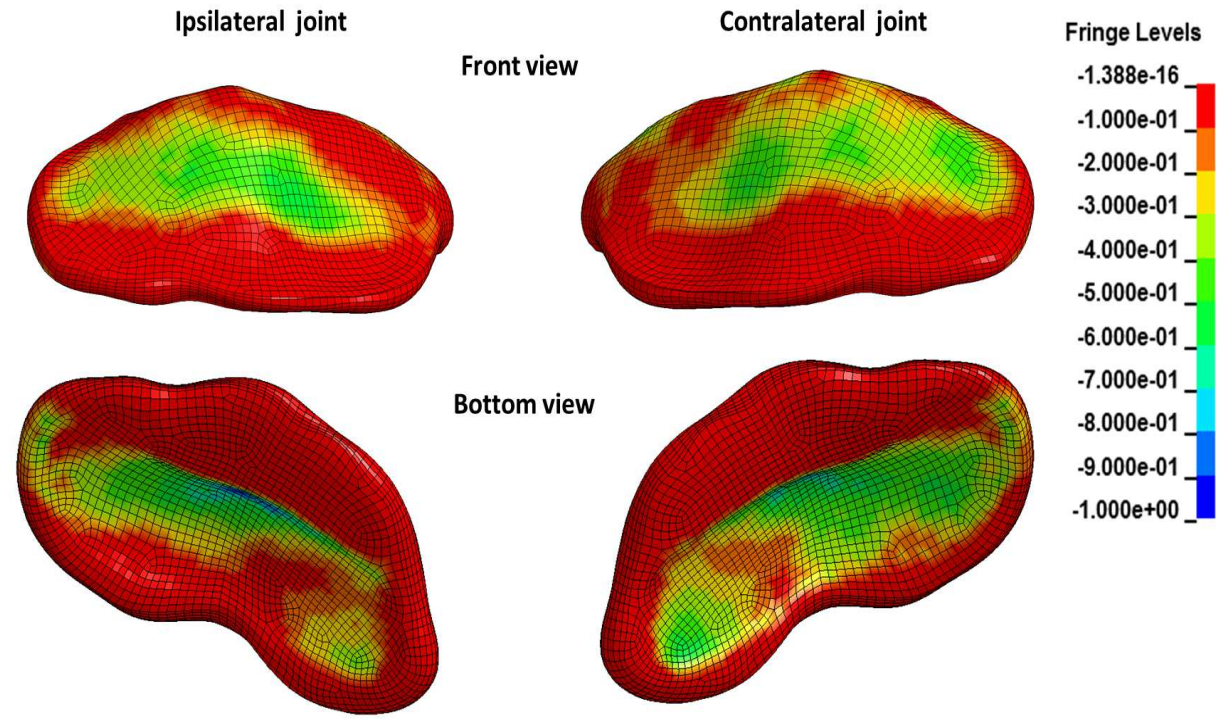

b)

Figure 5.14: Third principal stresses in the articular disc during a target biting force of 50 N and a gap of 0 (a) and 100 μm (b)

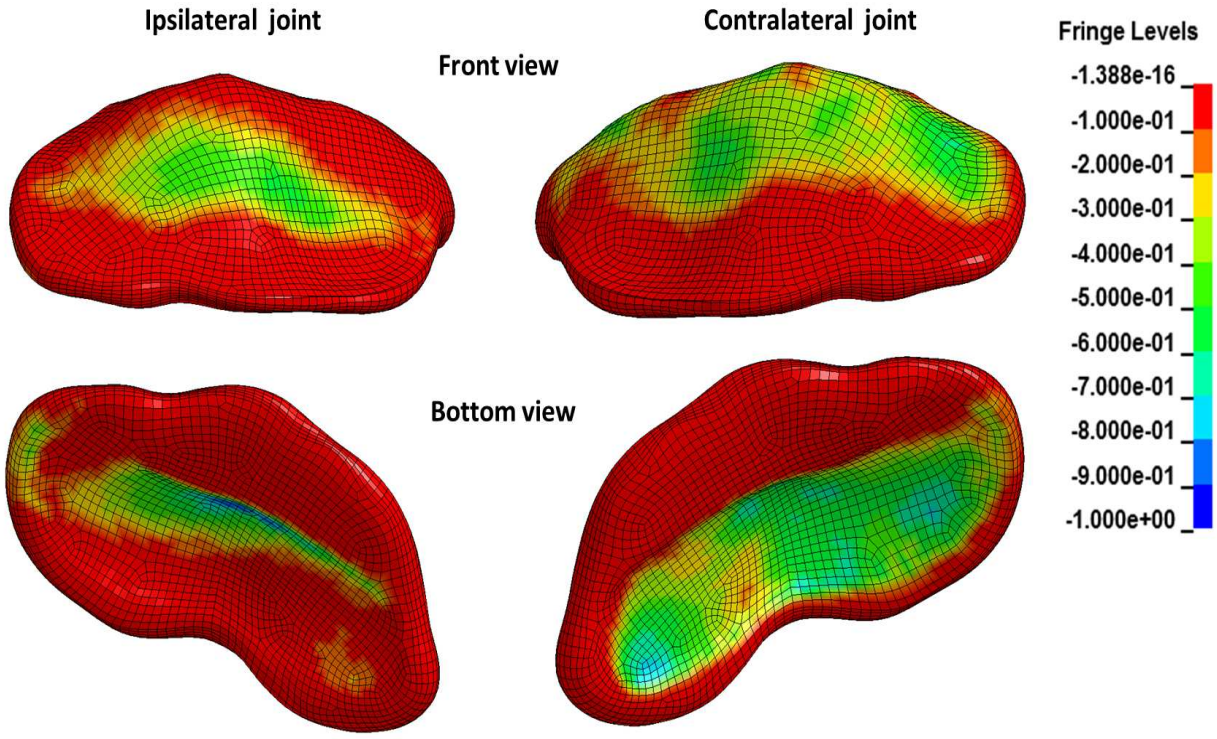

a)

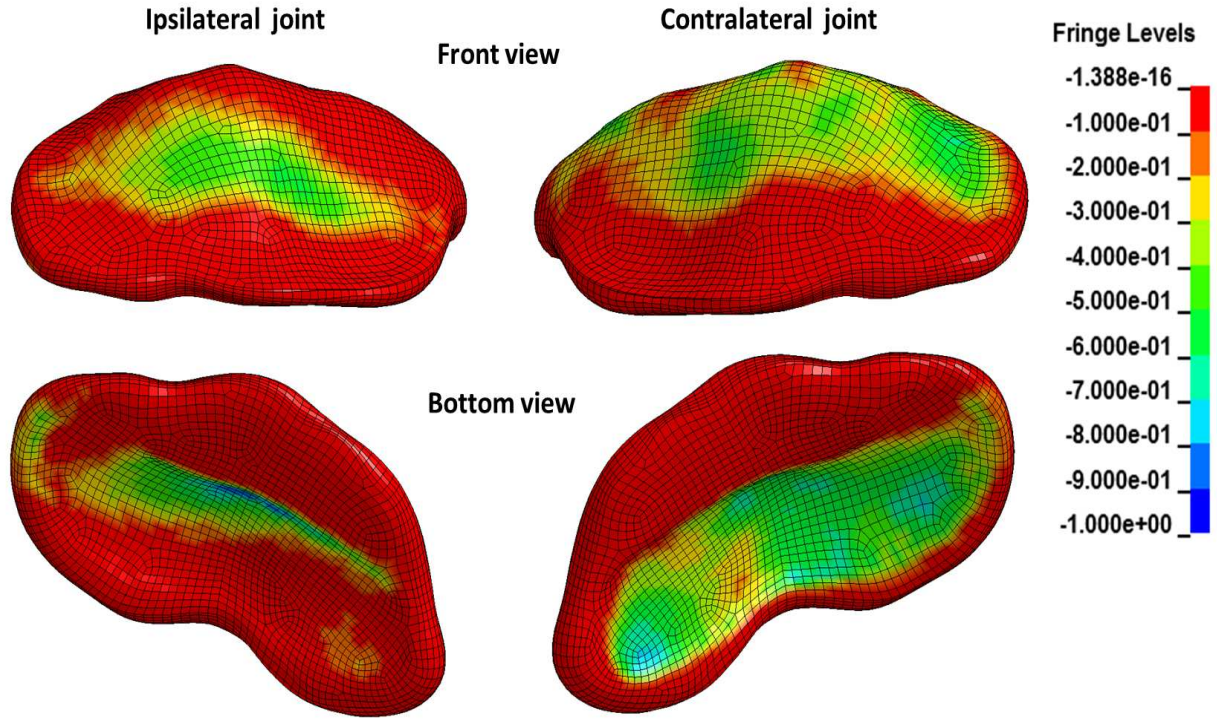

b)

Figure 5.15: Third principal stresses in the articular disc during a target biting force of 50 N and a gap of 200 (a) and 300 μm (b)

5.4 Conclusions

The motion observed during jaw opening is governed by the constraints imposed by the TMJ ligament and the passive resistance of the muscles. As the condyle rotates, the resistance from these tissues becomes too large for the opening muscles to overcome. The condyle then displaces anteriorly in order to continue jaw opening without further stretching the TMJ ligament, the superficial masseter, and the medial pterygoid muscles. Since the physiological motion of the TMJ during opening is well known, its reproduction can be used as a preliminary review of the correct calibration of the different components. In our model, the reproduction of this motion suggests that the material parameters proposed by Palomar [58] for the temporomandibular ligament result in the tissue behaving too stiff, since they do not allow the condyle to slide downwards the articular fossa properly, restricting the disc from displacing anteriorly. The parameters provided by Palomar et al. are an approximation made by these authors because of the lack of experimental data in the literature. To allow the articular disc to displace further and reach the articular tubercle, the parameter C_1 of the Mooney-Rivlin material had to be reduced here to 4.0 MPa. Stresses in the disc during jaw opening (Fig. 5.7) occur in the center of the disc. In this particular task, the shape of the disc may play an important role, since a thinner middle section would allow a larger surface of the disc to remain in contact with both, the articular tubercle and the condyle, thus resulting in lower stresses magnitudes.

A very similar change of force distribution on the rigid spacers was also observed in the experimental measurements of Schindler et al. [45]. The contralateral side overcomes the introduced gap through, mostly, the deformation of the articular disc. The model shows that further widening of the gap would be too difficult to overcome, since forces on the contralateral rigid spacer are minimal, while the force in the contralateral joint already surpasses by more than twice the amount in the ipsilateral joint. When the gap is introduced, a decrease in the activity of the temporalis muscle occurs, while activity in the masseter muscle increases. This phenomenon, along with the reduced forces that occur in the ipsilateral joint, lowers the posterior displacement of the ipsilateral condyle and shifts the stresses to the center of the disc. On the other hand, the higher forces withstood by the contralateral joint deform its disc and displace the condyle posteriorly. As a result, in all cases the contralateral condyle is held at its most posterior position by the TMJ ligament and the disc atttachments. Subsequently, the stress patterns on the disc are similar, compression mostly in the posterior and middle parte of the disc, but with different magnitudes.

When performing the task with the lower biting force of 50 N, a higher deviation of the target force is observed when averaging the activation levels. Since the muscles

are working in the *ascending limb* of the characteristic curve (explained in the next chapter), raising the activation level of muscles that are close to their optimal length will result in a much higher response than of those that have already significantly contracted. Due to the lower forces, a shift of compressive stresses from the middle to the posterior part of the disc is observed when a gap of 200 μm is introduced.

Overall behavior of the masticatory system is captured rather well by the current model, showcasing the basis for more refined studies to be performed with the finite element method for therapies involving the TMJ. The use of splints clearly changes drastically the distribution of forces in the masticatory system. Discs showing wear or damage may be relieved with splints because they may limit forces in the joint or shift the stresses to a more resilient region of the disc. Improvements to the geometry of the current model could be performed with the help of MRI-scans, although it is unknown if the effort to create such complex geometry is justifiable. Although more sophisticated material models for the articular disc can be found in the literature, the current hyperelastic model was considered sufficient for the scope of this work.

Chapter 6:
The Masticatory Muscles

The muscles of the masticatory system govern the kinetics of the system, and, along with the temporomandibular joint and temporomandibular ligament, its kinematics. The muscles are responsible for motion through their capacity to produce force and, additionally, help restrict certain movements through their passive response to stretching. The capabilities of the muscles are directly related to their physiological structure. The physiological characteristics of the muscles of the human masticatory system were extensively investigated by van Eijden [65].

The role of the masticatory muscles has been studied with the help of mathematical models using the line of action of the muscles in order to determine the resulting bite and joint forces [66, 67, 56]. As the possible combinations in muscle forces to produce a specific biting force are practically unlimited, optimization strategies are often employed, where either the overall muscle energy levels or the forces in the joint are minimized.

The employment of electromyography (EMG) is one of the most prevalent method to estimate muscle forces. The process of predicting muscle forces on the basis of its measured electrical activity has been studied extensively. In [68, 69, 31], biting forces and activation levels of the muscles were simultaneously measured. A calibration process was then employed for a large number of parameters in order to obtain the appropriate muscle forces to match the experimental biting force.

Mathematical models of the muscle that require a small number of parameters have also been developed [70, 71, 72]. These models reproduce the characteristic behavior of the muscles, discovered by Hill in 1938 [73, 74], and can output forces with the activation levels of the muscles as only input.

These models have been employed in dynamical models of the human masticatory system [75, 55, 76, 77, 57] to study the role of the muscles for the motion of the human jaw. Three-dimensional finite element modeling of the muscles has also been employed to study the dynamics of chewing [78, 79].

In the following section, the principal characteristics of the muscles are presented along Hill's muscle model which was employed in this work to reproduce the behavior of the muscles. The muscles of the masticatory system are then introduced as well as the material data used in the model to represent each of these muscles. The different configurations present in the literature are compared in order to closely study the effect of each parameter on the behavior of the stomatognathic system.

6.1 Muscle Properties

The muscles are structures capable of producing force and are composed of elastic elements which give them a passive response to stretching. The principal characteristics considered when modeling the muscles, are the force-length and the force-velocity relationships.

6.1.1 Force-Length Relation: Active and Passive Forces

Striated muscles are composed of fibers, which are in turn made up of many smaller myofribils. Each myofibril is composed of a series of sarcomeres connected to each other through structures called Z-discs. The sarcomeres consist of a combination of actin (thin) and myosin (thick) protein filaments which can slide past each other. The connections between these two filaments are known as cross-bridges. The production of force occurs during the working stroke of the myosin head while bonded to the actin filaments. This cross-bridge mechanism was proposed as the so-called sliding filament theory by A.F Huxley [80] and H.E. Huxley [81]. The number of possible bonded myosin heads, and thus, the possible force to be exerted, depends on the existing overlap between the actin and myosin filaments along the length of the sarcomere.

Gordon et al. [82] studied the relation between force production and sarcomere length on isolated fibers of a frog muscle. Measurements of the filaments' lengths reported around 1.6 μm for the thick filament and 0.95 μm for the thin filament. Through measurements of the remaining components (width of the Z-disc, H-zone, etc.) a theoretical force-length relationship was established (Fig. 6.1). As can be observed on the graph, at a distance larger than 3.65 μm, the formation of cross-bridges is no longer possible and production of force can no longer take place. The zone below this length, up until reaching 2.25 μm, is known as the *descending limb*. Once this length has been reached, the number of potential cross-bridges, and thus force production, reaches its maximum. Here a plateau region can be observed, where force production is optimal. At a length of around 2 μm, a decrease of force production will occur with further shortening, due to interference of thin myofilaments as they begin to overlap. This zone, until shortening to 1.27 μm, below which force production is no longer possible, is known as the *ascending limb*.

Although the lengths of thick filaments are nearly constant in different animal species, the thin myofilaments lengths have been observed to vary significantly between species. Walker and Schrodt [83] and Herzog et al. [84] studied the length of the myofilaments in apes, cats and humans. Taking into account the differences in their length, a theoretical force-length property was derivated for human muscles as observed in figure 6.2. The passive response of the muscle was measured with

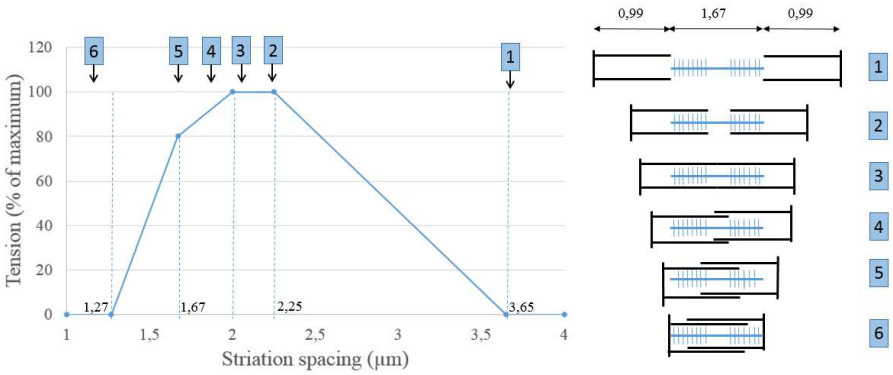

Figure 6.1: Theoretical force-length relation of fibres of a frog muscle

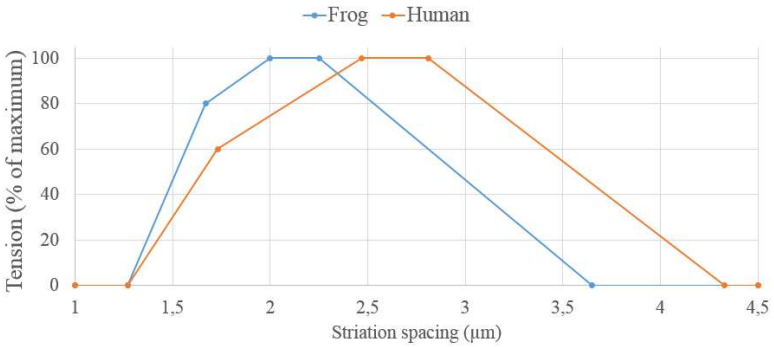

Figure 6.2: Comparison of force-length relation between frog and human muscles

standard uniaxial tensile tests by stretching it to different lengths without providing any type of stimulation. In figure 6.3, the force produced by the contractile element is shown with a blue line, the passive response in red and the total combined force with a black line.

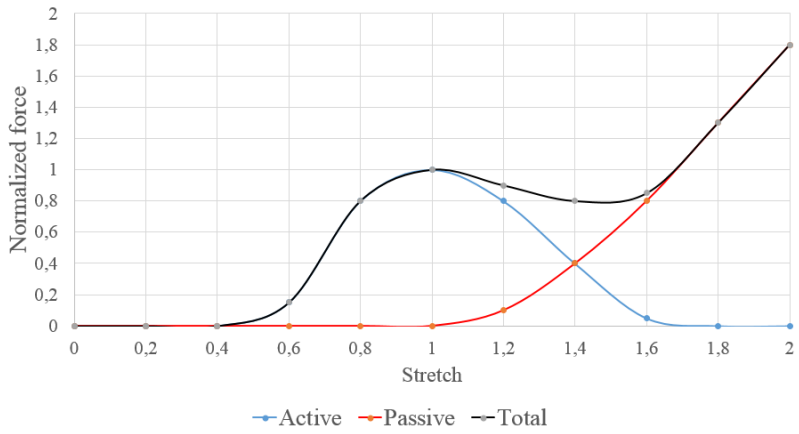

Figure 6.3: Force-length relation for active, passive and total force exerted by the muscle. As the muscle stretches, total force diminishes for a short range since the active force wanes, and then rises as the passive force continues to increase

6.1.2 Force-Velocity Relation

Muscles produce less force during quick contractions than when shortening occurs at a low pace. This reduction is a consequence of part of the force being employed to overcome an inherent viscous resistance when the muscle is shortening. This non-linear relation was observed by Hill [73] when studying the heat production of isolated frog muscles. The lengthening part of the relation (Fig. 6.4) was obtained by applying a load larger than the *maximum isometric force* to the muscle. The result was an elongation of the muscle at a constant speed, but with a much lower speed as expected when applying an extrapolation of the Hill equation. The slope of the force-velocity curve is about six times larger during lengthening than during shortening, and the curve is thus, not continuous at velocity $V = 0$. This relationship is presented in Fig. 6.4 and was developed by Otten [85].

When a force of about 1.8 times the *maximum isometric force* is applied, the muscle loses its ability to withstand stretching.

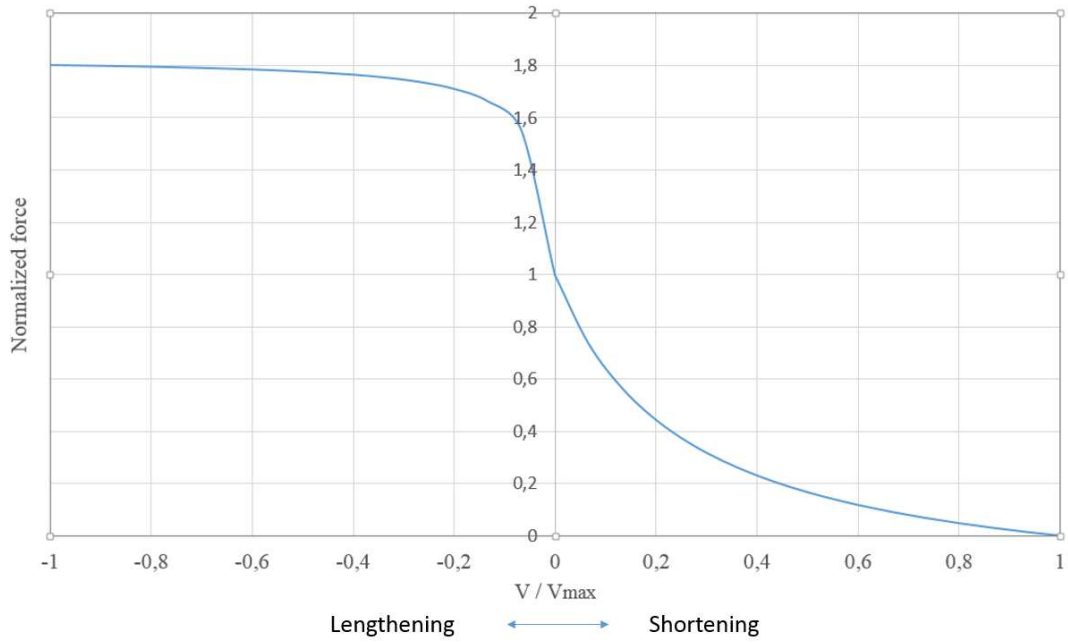

Figure 6.4: Force-velocity relation of a muscle with respect to its maximum isometric force

6.1.3 The Hill Muscle Model

The three-element Hill type muscle model consists of a contractile element (CE) and two spring elements, one placed in parallel (PE) and the other in series (SE). The parallel element simulates the passive response of the muscle, while the element in series tries to capture the muscle behavior observed in quick-release experiments. The element in series is usually disregarded when the muscle element is placed in series to a structure representing the tendon.

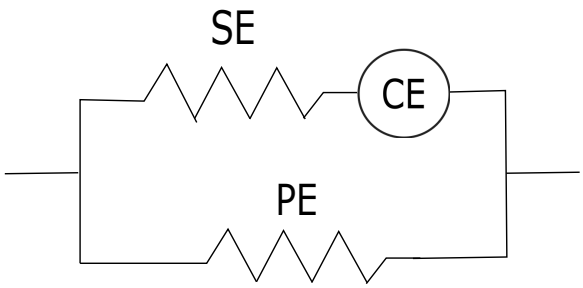

Figure 6.5: 3-element Hill muscle model

6.2 Modeling the Masticatory Muscles

The muscles that belong to the masticatory system are usually classified depending on their role to either open or close the jaw. The jaw opening muscles are shown in figure 6.6 and are listed in the following:

Lateral pterygoid can be divided into a superior and an inferior head. The superior head originates from the infratemporal crest of the greater wing of the phenoid bone and inserts onto the neck of the condyle; in 60% of subjects it additionally inserts onto the articular disc and fibrous capsule of the TMJ. The inferior head originates from the surface of the lateral pterygoid plate and inserts onto the neck of the condyle. This muscle protrudes the mandible during jaw opening and is also responsible for the lateral excursions of the jaw during chewing.

Digastricus consists of two bellies united by an intermediate tendon. The posterior belly, which is the longest one, originates from the digastrics groove medial to the mastoid process, it then becomes a tendon which passes through a fibrous loop attached to the hyoid bone. This tendon is followed by the anterior belly, which inserts into the lower border of the mandible. the digastricus depresses the mandible during jaw opening.

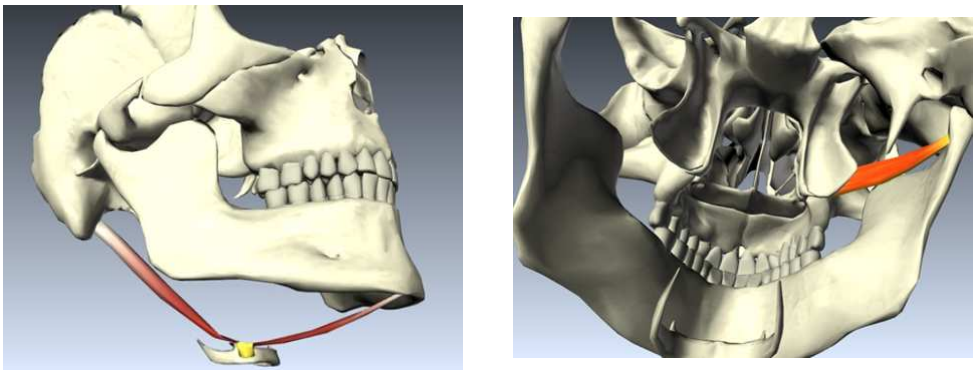

(a) Digastric **(b)** Lateral pterygoid

Figure 6.6: Opening muscles (www.biodigitalhuman.com)

Some authors include the rest of the suprahyoid muscles, namely the geniohyoid, the mylohyoid and the stylohyoid. These muscles are assumed to play an insignificant role for the masticatory system in this work for reasons detailed later. The closing muscles are the following (Fig. 6.7):

Masseter consists of a superficial and a deep head. The larger, superficial head, originates from the anterior two-thirds of the zygomatic arch and inserts into

the angle of the mandible and the inferior half of the lateral surface of the ramus of the mandible. The smaller, deep head originates from the third of the lower border of the zygomatic arch. It inserts into the upper half of the ramus and the lateral surface of the coronoid process of the mandible. This muscle elevates the mandible.

Temporalis originates from the temporal fossa and inserts onto the top and medial surface of the coronoid process of the mandible. This muscle both elevates and retracts the mandible.

Medial pterygoid originates above the medial surface of the lateral pterygoid plate and the pterygoid fossa. It inserts into the lower and back part of the medial surface of the ramus and angle of the mandible. This muscle elevates the jaw and also assists the lateral pterygoid during lateral movements of the mandible.

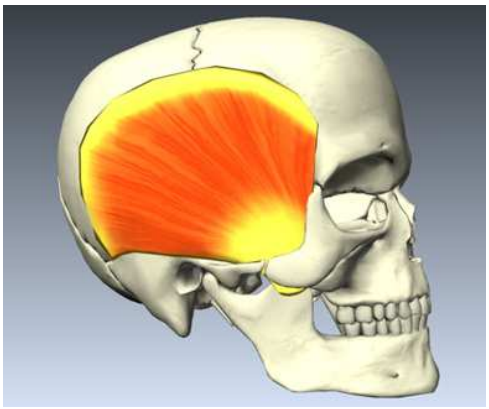

(a) Temporalis

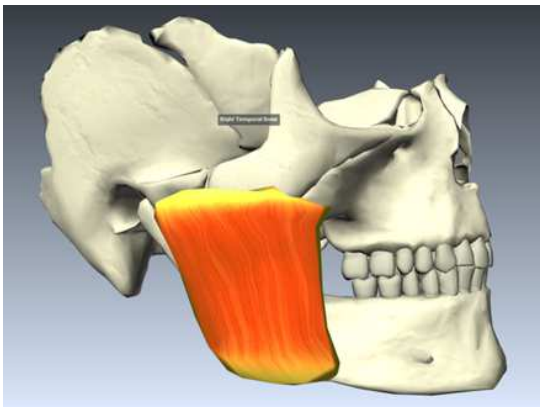

(b) Masseter

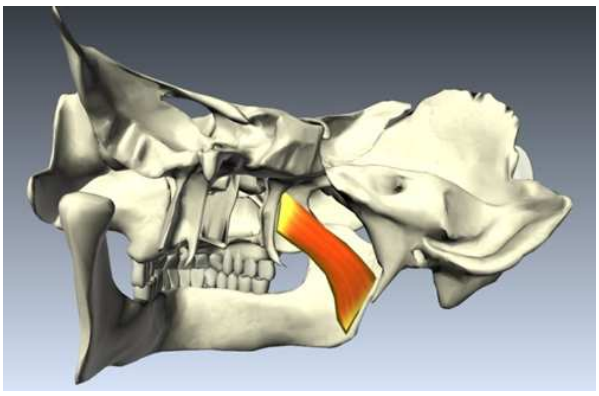

(c) Medial pterygoid

Figure 6.7: Closing muscles (www.biodigitalhuman.com)

Several models for muscles can be found in the literature [75, 55, 76, 77, 57, 78, 79]. In our model, muscles are represented by two truss elements in series, one

representing the fibrous part of the muscle and the other the tendon. The fibrous part is represented by Hill's muscle model while the tendons, since they undergo very small deformations, are represented by inextensible wires. In total, eight muscle components were employed to represent the following muscles (on each side): two for the temporalis (anterior and posterior part), two for the masseter (superficial and deep part), two for the lateral pterygoid (superior and inferior head), one for the medial pterygoid and one for the digastric.

The coordinates for the origin and insertion points were obtained by locating them directly on the geometry. In the case of the origin points of the temporalis and digastric muscle, cephalometry and coordinates published by other authors [65] were employed to determine their position. The coordinates of origin and insertion for the different muscles are presented in Table 6.1. Only the anterior belly of the digastric muscle is represented in the model. In order to take into account the contraction possible by its posterior belly, the muscle fiber lengths of both bellies were added to the single element representing the digastric muscle. This results in the very small length of the tendon observed in the table. The *muscle fiber length* of any muscle can be calculated by subtracting the *tendon length* from the *total muscle length* (distance between the origin and insertion points).

Muscle	**Origin**			**Insertion**			**Tendon length**
	x	y	z	x	y	z	
Masseter							
Superficial part	-57.0	-26.0	29.0	-46.5	5.4	-14.1	21.7
Deep part	-59.0	-3.0	31.0	-44.4	2.2	1.6	16.6
Temporalis							
Anterior part	-65.0	-14.0	84.0	-46.0	-8.4	29.2	29.2
Posterior part	-79.0	41.0	75.0	-45.4	-2.9	25.0	37.1
Lateral pterygoid							
Superior head	-27.2	1.3	22.0	-47.1	24.1	26.6	9.2
Inferior head	-23.3	-0.8	17.0	-48.1	24.7	23.3	11.9
Medial pterygoid	-17.3	-4.5	21.5	-41.0	5.6	-18.4	29.9
Digastricus	-17.0	-5.0	-52.0	-5.2	-51.2	-40.3	3.0

Table 6.1: Coordinates of origin and insertion points of the masticatory muscles

The Frankfurt plane can be located with the help of the coordinates appearing in table 6.2. The orientation of the coordinate system is given in figure 4.7.

Anatomical position	**Coordinates**	
	y	z
Superior margin of the external acoustic meatus	39.1	31.0
Inferior margin of the orbits	-41.9	42.4

Table 6.2: Coordinates of the Frankfurt plane

6.2.1 Muscle Configuration

The muscles are represented using LS-DYNA muscle model (Material 156), the principal characteristics of the muscle are incorporated following the work of van Ruijven & Weijs [71], where the force is expressed as

$$F(t) = F_{max}[A(t)FL(t)FV(t) + FP(t)]\,. \tag{6.1}$$

Here F_{max} is the maximum isometric muscle force, $A(t)$ the instantaneous activation level, $FL(t)$ the force-length factor, $FV(t)$ the force-velocity factor, and $FP(t)$ the parallel elastic force. The maximum force F_{max} a muscle can produce depends on the number of sarcomeres working in parallel, which can be estimated on the basis of the cross-sectional area of the muscle. It is obtained by multiplying its physiological cross-sectional area (PCSA) with a value of 18.8 - 40 N/cm^2 [86, 87, 88]. A value of 30 N/cm^2 was used [88] in our model. The PCSA of each masticatory muscle was obtained from van Eijden et al. [65].

The force-length factor $FL(t)$, the force-velocity factor $FV(t)$, and the parallel elastic force $FP(t)$ are defined as a function of the sarcomere length $Ls(t)$.

The instantaneous sarcomere length is given by

$$Ls(t) = [Lm(t) - (Lm_i - Lf_i)]\frac{Ls_i}{Lf_i}\,, \tag{6.2}$$

where $Lm(t)$ is the instantaneous muscle length, Lm_i the initial muscle length, Lf_i the initial muscle fiber length and Ls_i the initial sarcomere length. The parameters required to calculate the sarcomere lengths (Lm_i, Lf_i and Ls_i) were also taken from van Eijden et al. [65].

The force-length factor is defined as

$$FL(t) = 0.41Ls(t)^3 - 4.40Ls(t)^2 + 14.80Ls(t) - 15.05\,, \tag{6.3}$$

The force-velocity factor is specified by

$$FV(t) = \begin{cases} \left\{ \dfrac{12.5 - \dfrac{Vs(t)}{2.73}}{12.5 + \dfrac{Vs(t)}{0.49}} \right\} & Vs(t) \geq 0 \\ 1.5 - 0.5 \left\{ \dfrac{12.5 + \dfrac{Vs(t)}{2.73}}{12.5 - 2\dfrac{Vs(t)}{0.49}} \right\} & Vs(t) \leq 0 \end{cases} , \tag{6.4}$$

where $Vs(t)$ is the sarcomere velocity. The maximum velocity has been defined as $V_{max} = 12.5\, s^{-1}$.

Finally, the parallel elastic force follows the following expression

$$FP(t) = 0.0014 \exp\left(6\frac{Ls(t) - 2.73}{2.73}\right) . \tag{6.5}$$

The parameter values of the previous expressions were calculated through curve fitting with experimental data. The active and passive behavior of the muscles described by the previous equations can be observed in Fig. 6.8. These curves match the experimental results observed on the digastric muscle of a rabbit by Muhl et al. [88]. In this expression, the muscle loses its capacity to produce force when it has contracted to a stretch of 0.67. In comparison, the theoretical behavior (Fig. 6.1) shows that the muscle is still able to produce force under a striation space of 1.27 μm which corresponds to a stretch of 0.6.

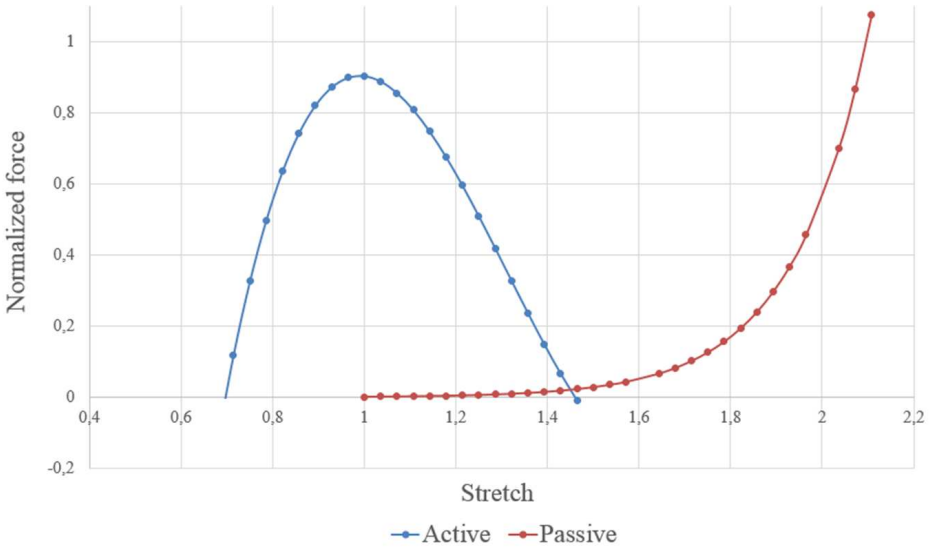

Figure 6.8: Force-length relationship employed by van Eijden

Some authors performed tests on the muscles of rats and humans [89, 90] showing a limited capacity to contract below a stretch of 0.70, other experiments performed

in frog and cat muscles show [91, 82], however, a capacity to continue exerting force even below a stretch of 0.5. A deviation is also observed with the passive response, with a normalized force of 100% only being reached after a stretch of 2 has been surpassed, whereas most studies show this force is reached with a stretch of 1.5.

The force-velocity relationship can be observed in Fig. 6.9. In this relation, the maximum tension developed during maximum lengthening velocity, has a value of around 1.45 F_{max}.

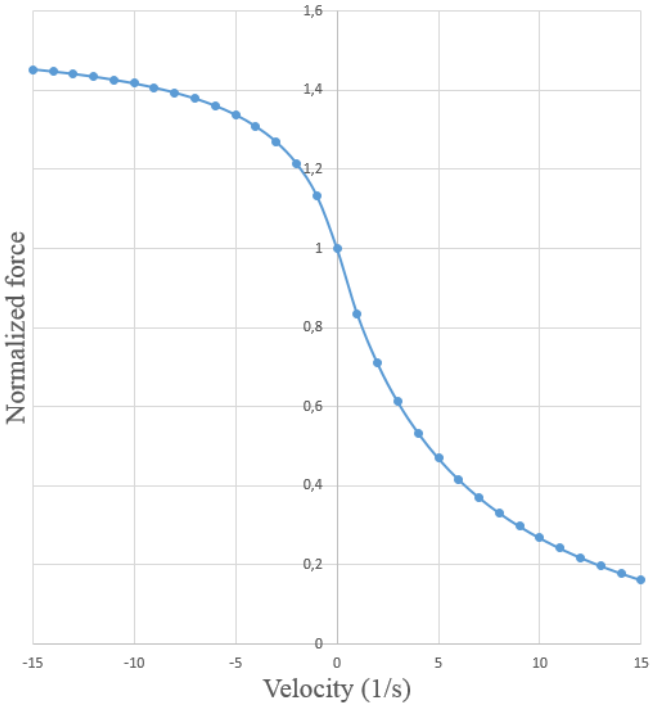

Figure 6.9: Force-velocity relationship employed by van Eijden

The initial state assumed in this model is *maximum intercuspation*. Different values for the stretch ratio of the different muscles in this state were presented by Koolstra [75, 55] and are shown in table 6.3. Here, the effects of using different initial stretch values for the muscles is studied.

It is usually assumed that the working range of all muscles is inside the *ascending limb*, to ensure the stability of the system. In his works, Koolstra employed two different configurations for the stretch ratio of the muscles during occlusion, which can be observed in table 6.3. We can deduce that during *maximum intercuspation* the deep masseter muscle is not capable of producing any force in both configurations, as its stretch ratio is already below the *ascending limb*. In the first configuration, the optimal length, given by the value 1.0, for the closing muscles occurs when the degree of jaw opening is around 20 degrees and the optimal length for the opening muscles occurs during occlusion. This places all muscles' working range inside the

Muscle	Stretch ratio at occlusion	
	Conf. 1 [75]	Conf. 2 [55]
Superficial Masseter	0.78	0.98
Deep Masseter	0.62	0.56
Anterior Temporalis	0.74	1.08
Posterior Temporalis	0.82	1.08
Medial Pterygoid	0.80	1.11
Superior Lateral Pterygoid	1.00	0.82
Inferior Lateral Pterygoid	1.00	0.91
Digastric	1.00	1.14

Table 6.3: Stretch ratio of jaw muscles during maximum intercuspation as given in Koolstra's works

ascending limb. For the second configuration, most of the closing muscles are near the optimal length during occlusion and jaw opening results in a loss of force for most muscles.

6.3 Simulations and Results

6.3.1 Force-Length Characteristics of the Muscle

We analyzed the significance of the different force-length characteristics of the muscle available in the literature based on opening of the jaw and unilateral molar biting. For this, three models were calibrated with different muscle characteristics. Two models were calibrated employing Koolstra's relationships, each with a different initial stretch configuration. *Model 1* employs configuration 1 and *Model 2* uses configuration 2. The third model was calibrated with the theoretical active-length relationship of humans from Fig. 6.2, combined with the passive-length response in Fig. 6.3. This model uses the first stretch configuration (Conf. 1 in table 6.3) since this is the most usual assumption for the working range of the muscles.

A cut view of the condyle during maximum jaw opening in each model can be observed in Fig. 6.10. Forces developed in the joint in each case can be seen in figure 6.11. As expected, the highest joint forces are in *Model 3* since the passive responses of the muscles begin at much lower strains. The lowest joint forces are

present in *Model 2* since the lateral pterygoid is able to exert less and the digastricus is able to exert more force due to their initial stretch configuration, in comparison to *Model 1*.

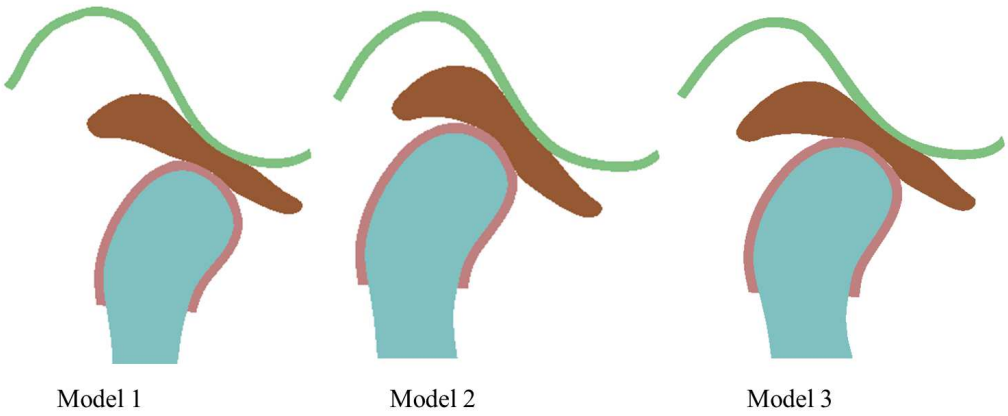

Figure 6.10: Joint configuration when the opening muscles' activation levels are at their maximum, for the three models

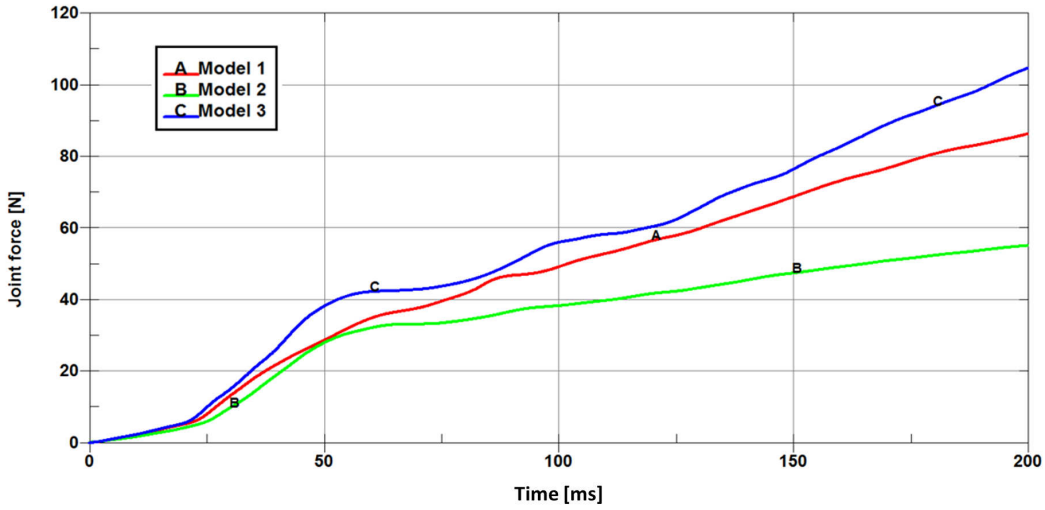

Figure 6.11: Joint forces during maximum opening phase

The condylar anterior displacement can be observed in figure 6.12. In this graph, due to the employed coordinate system, negative values correspond to anterior displacements. The highest anterior displacement is observed in *Model 1*, the lowest displacement in *Model 2*. This result was expected as the muscle responsible for the protrusion of the mandible is the lateral pterygoid. The same behavior is observed for the condyle's vertical displacement (Fig. 6.13), where *Model 1* achieves the largest and *Model 2* the lowest vertical displacement.

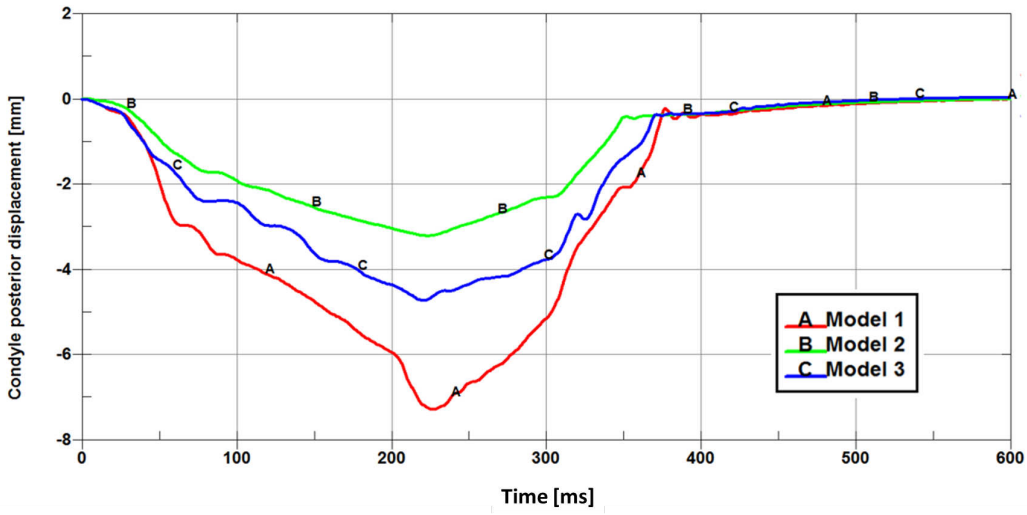

Figure 6.12: Anterior displacement of the condyle

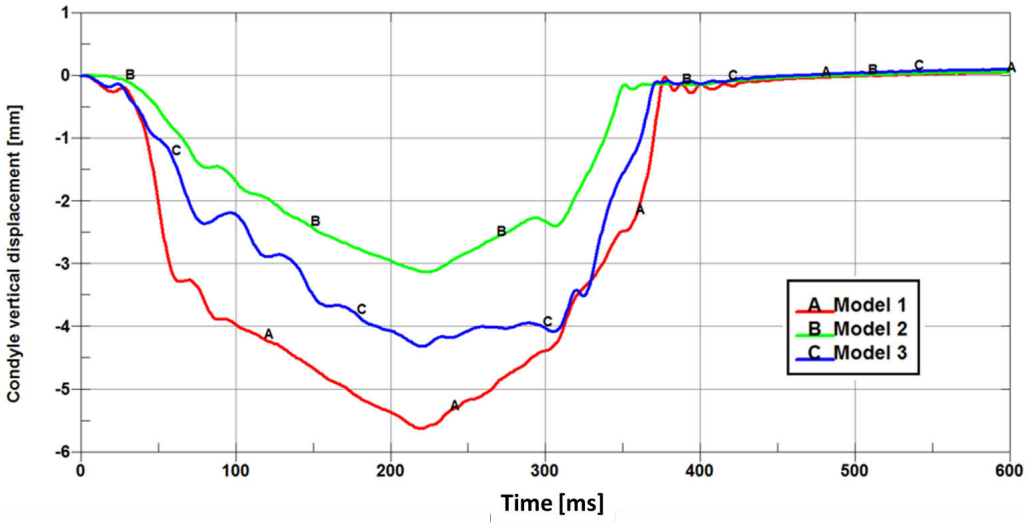

Figure 6.13: Vertical displacement of the condyle

The vertical displacement of the central mandibular incisive tooth can be observed in Fig. 6.14. Clearly all models reach a similar degree of opening. *Model 1* and *Model 2* have the least amount of muscle passive resistance. *Model 1* has less available force for the digastric muscle due to its initial stretch ratio. However, since in this model the lateral pterygoid can exert a higher force, it achieves further condylar displacement, which reduces the stretch of the TMJ ligament as well as the masseter and medial muscles, alleviating their passive resistance. In the case of *Model 3*, the passive resistance of the muscles is compensated by the much larger available active force of this configuration.

In figure 6.15 we can observe the biting force and the force in each of the joints

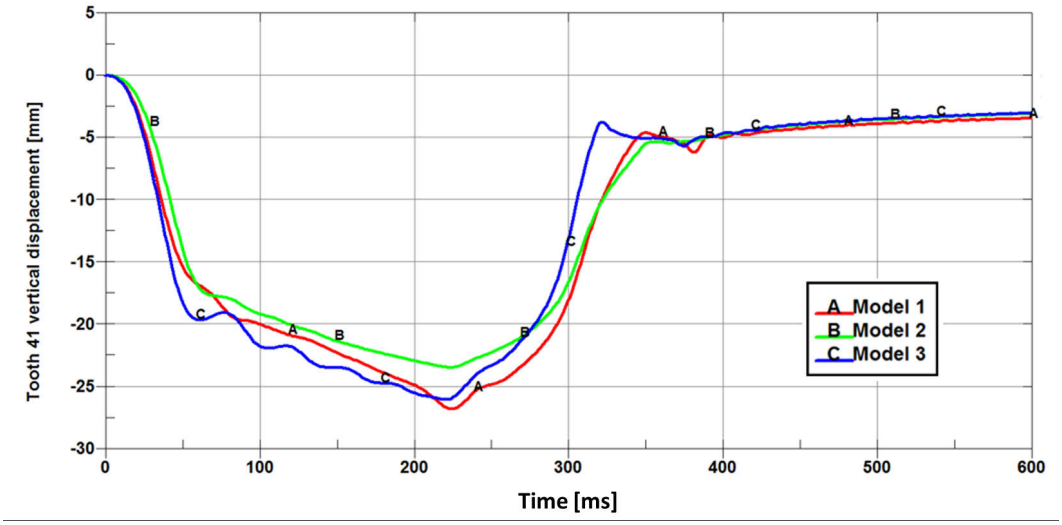

Figure 6.14: Vertical displacement of the central mandibular incisive teeth

during unilateral molar biting with a target force of 150 N. We can observe that *Model 1* can produce a biting force of only 80 N with the assigned activation levels. In the case of *Model 2* and *Model 3*, however, a biting force of 140 N is obtained which is very close to the target force.

6.3.2 Influence of Bolus Size on Joint and Bite Forces

In the case of *Model 1* and *Model 3*, the muscles work in the *ascending limb*, an increase in bolus size will result in stronger biting forces until the muscles begin to enter the *descending limb* range. In the case of *Model 2*, the source for an increase in biting force will be the deep masseter muscle, since the other closing muscles will begin to depart from their optimal range.

To study the stability of *Model 2*, a bilateral molar biting (BMB) was performed with a bolus of thickness 2 *mm* placed between molars 16 and 46, having a distance of 2 *mm* from the maxillary tooth. The bolus is lowered 2 mm in a time interval of 100 ms, at times 500, 650 and 800 ms. Activation levels of the muscles for BMB to produce a total biting force of 200 N (100 N in each side) were taken from Rues et al. [31] and are reached at time t = 500 ms. The study was repeated with the bolus having an initial distance of 6 *mm* from the maxillary tooth which results in a total gap distance of 8 mm between the molars.

Forces on the joint and the bolus can be observed in Fig. 6.16. The study was repeated with 8 *mm* in order to show that at this range the resulting forces agree with those found in [31] i.e. a force of 120 N in the joint corresponds to a 200 N biting force (100 N in the model due to the use of symmetry). It was observed that

in the studied range the configuration is stable, as the biting force increases at all times as the jaw opens.

From Table 6.4, the stretch ratios of the muscles at each of the different gaps can be read. It is to note, that the increase of force production of the deep masseter keeps the system stable, as all other muscles continuously lose their capacity to produce force. In the case of the medial pterygoid, the muscle can barely produce force in any of the cases.

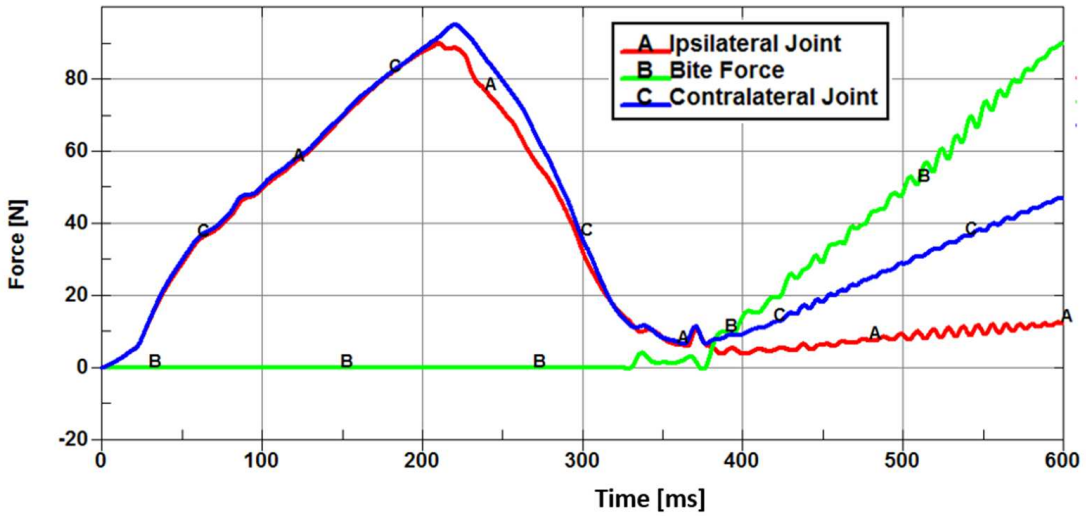

a)

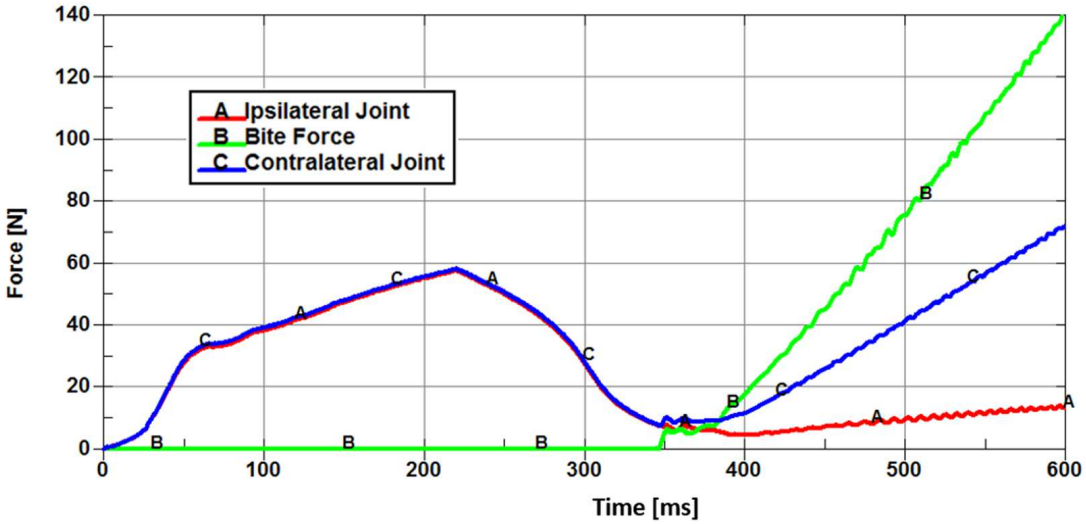

b)

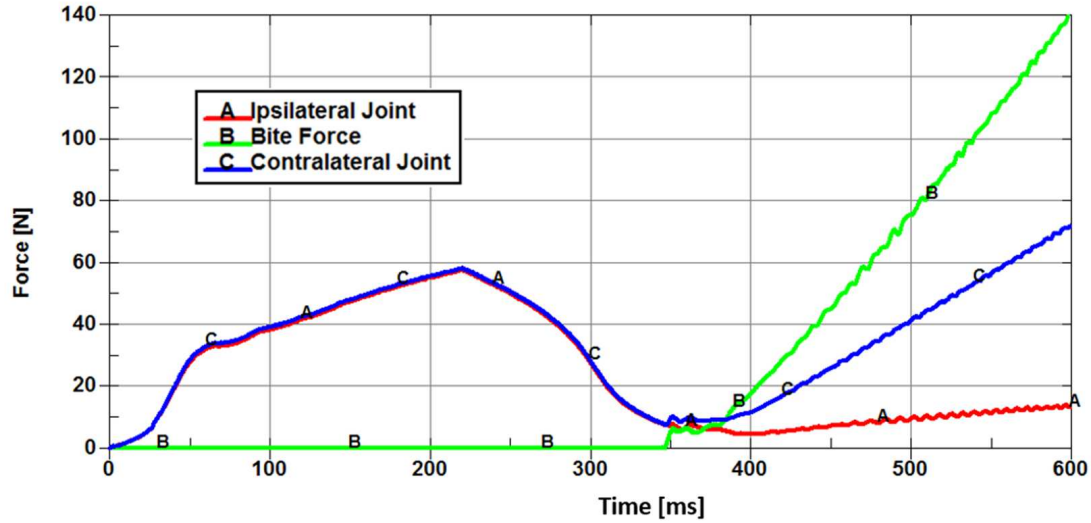

c)

Figure 6.15: Forces on the bolus and the joints in a) Model 1, b) Model 2 and c) Model 3, during unilateral molar biting with a target bite force of 150 N

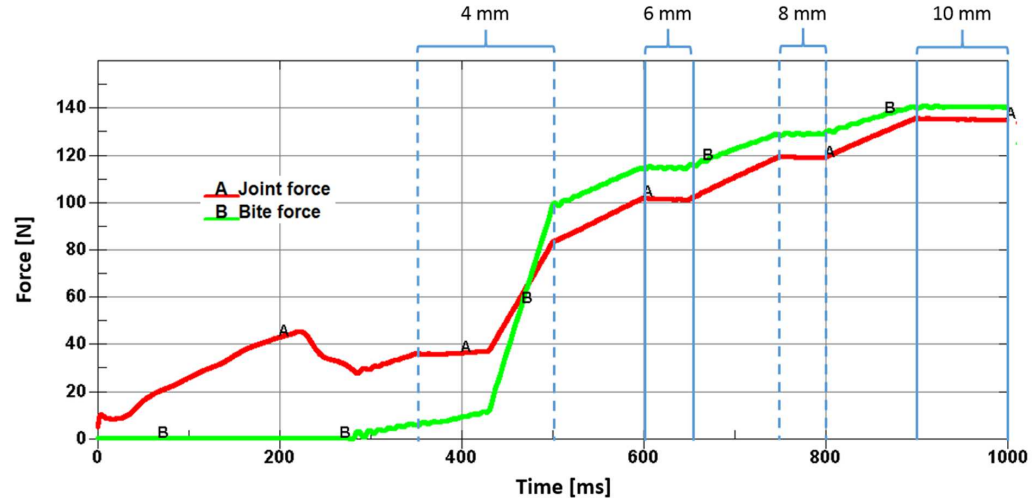

a)

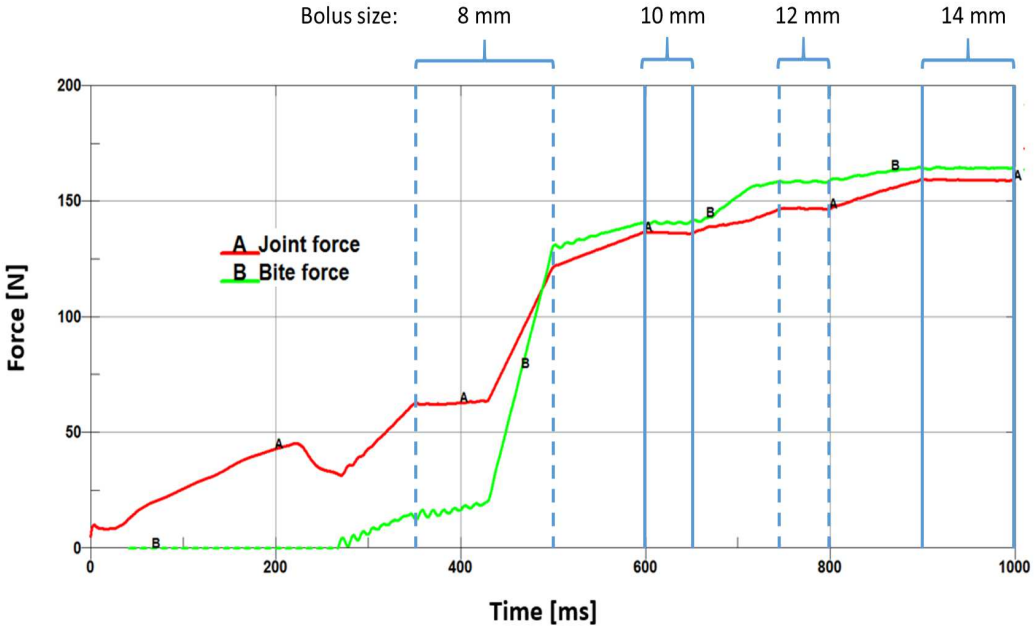

b)

Figure 6.16: Effect of the height of the bolus on the forces on the bolus and the joint. The height of the bolus at times 500, 650 and 800 ms is in graph a) 4, 6, 8 and 10 mm and in graph b) 8, 10, 12 and 14 mm, respectively

Muscle	**Stretch ratio with a gap of [mm]**					
	4	6	8	10	12	14
Superficial Masseter	1.07	1.11	1.15	1.20	1.24	1.29
Deep Masseter	0.62	0.65	0.68	0.72	0.75	0.79
Anterior Temporalis	1.14	1.18	1.22	1.28	1.32	1.37
Posterior Temporalis	1.13	1.15	1.18	1.20	1.23	1.26
Medial Pterygoid	1.23	1.30	1.36	1.42	1.49	1.57

Table 6.4: Stretch of the muscles with different gaps between the second molars

6.3.3 Influence of Origin Point on Joint and Bite Forces

The origin points of both, the temporalis and the masseter muscles, are difficult to determine since these muscles are attached to a rather large area of the skull. Here three different origin points were assigned to both muscles to study their effect on the joint and biting forces. For both muscles, the origin point was displaced along the horizontal plane by *15 mm* both, positively and negatively. Activation levels of the muscles were the same as in the previous task, and a bolus of 2 mm was placed directly in contact with molar 16.

The results for each case can be observed in figures 6.17 and 6.18. An anterior displacement of the origin point of the superficial masseter results in practically no change of the joint force and the biting force (Fig 6.17 b). A posterior displacement of the same origin point results in a small reduction of both forces (Fig 6.17 c).

In the case of the anterior temporalis, as in the case of the masseter, no significant changes were observed (Fig 6.18 b). A slight reduction of biting and joint forces is seen when its origin point is displaced anteriorly, and a slight increase of joint force and decrease of bite force when the origin point is displaced posteriorly (Fig 6.18 c).

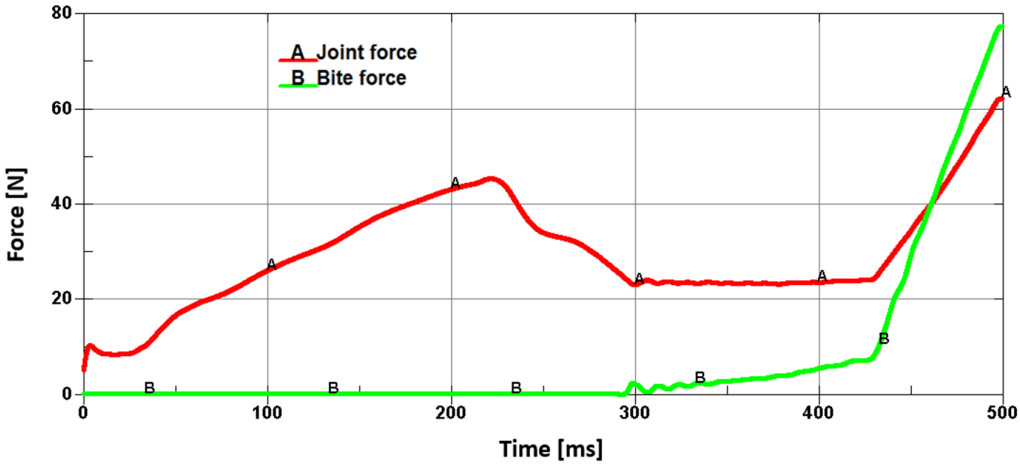

a) Original position

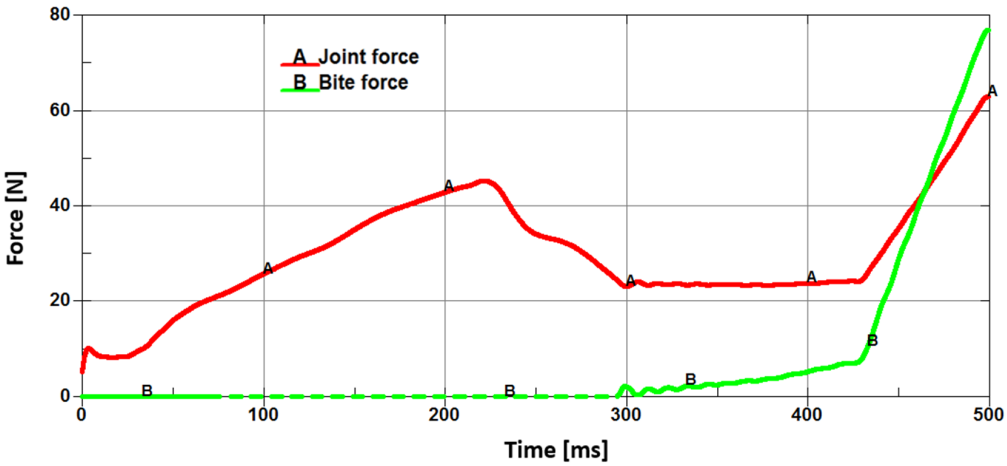

b) Superficial masseter origin point displaced anteriorly

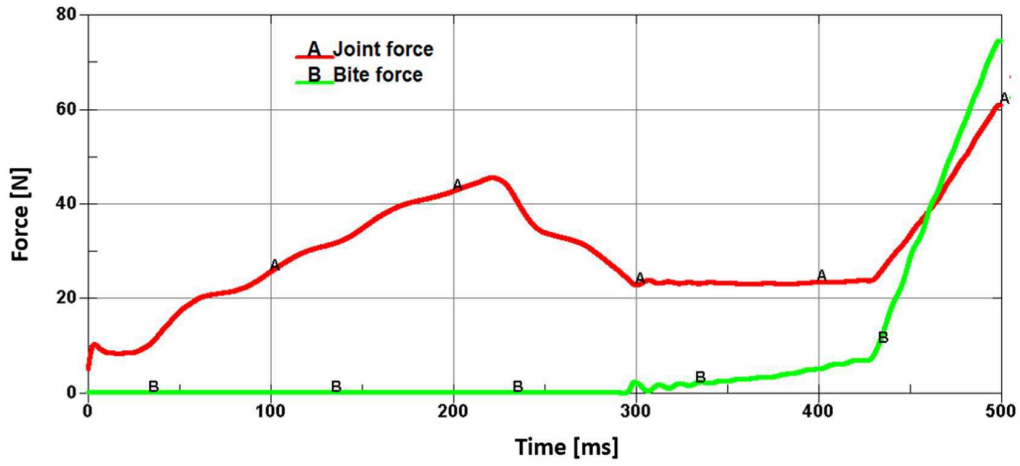

c) Superficial masseter origin point displaced posteriorly

Figure 6.17: Effect of the origin point of closing muscles on the forces on the bolus and the joint. a) Original position, b) superficial masseter origin point displaced anteriorly, c) superficial masseter origin point displaced posteriorly

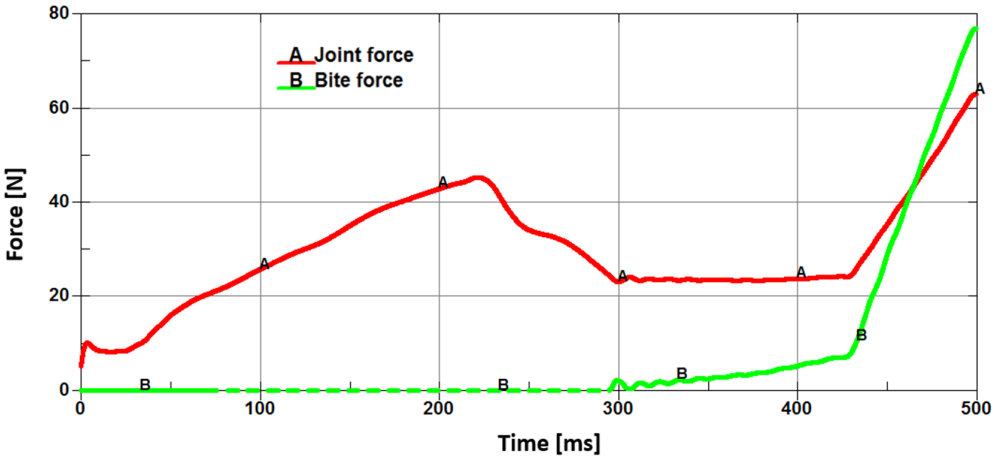

a) Original position

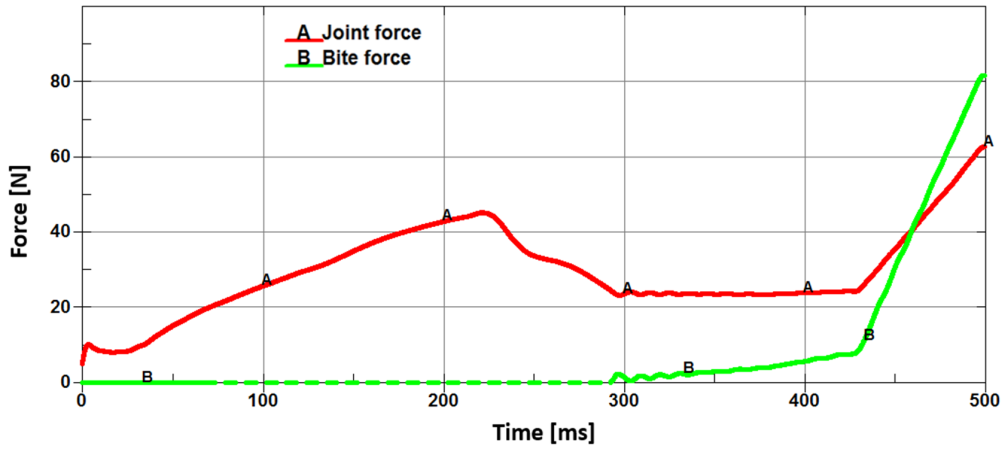

b) Anterior temporalis origin point displaced anteriorly

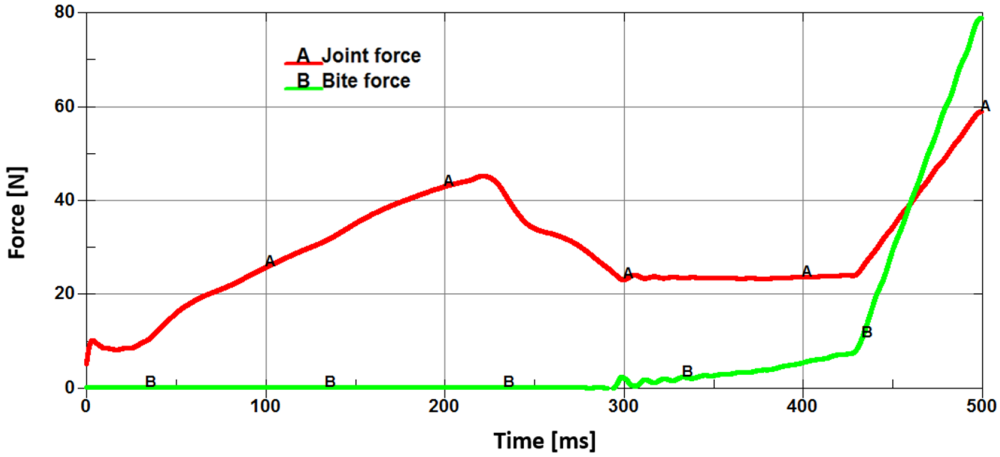

c) Anterior temporalis origin point displaced posteriorly

Figure 6.18: Effect of the origin point of closing muscles on the forces on the bolus and the joint. a) Original position, b) anterior temporalis origin point displaced anteriorly, c) anterior temporalis origin point displaced posteriorly

6.4 Conclusions

The present model employs forward dynamics, where forces are used to predict resultant displacements and reaction forces. Inverse dynamics are more widely used in the field of biomechanics, as motion data is easier to acquire. The choice of using forward dynamics arises from the difficulties of properly modeling contact when using inverse dynamics, as small variations in the measured motions will result in considerable differences in the resultant contact forces. This propagation of error is further exacerbated when highly non-linear materials are employed, as the response of the material depends on its current state of strain. For this reason, it was found to be more appropriate to estimate the muscle forces from their measured electric activities in order to determine the resultant forces.

To validate the model, the resulting biting force in the bolus should match those observed experimentally. The experimentally measured activation levels can produce satisfactory results (correct biting force) with different muscle configuration/characteristics. Selecting the properties of the muscles is, for this reason, not straightforward.

During jaw opening, it can be hypothesized that lower joint forces than those produced by *Model 1* and *Model 3* are expected since the condyle is able, in reality, of further displacement. In these two models, the reaction forces in the joint do not allow for further movement and the disc is considerably deformed. Further studies regarding jaw opening were not carried out since the displacement of the hyoid bone which was no considered in this model, plays a certain role for force direction of the digastric muscle and experimental data regarding the different muscles attached to this bone are scarce.

During UMB, the force-length characteristics and stretch ratio used in *Model 1* are unable to produce the biting force observed in experimental results. On the other hand, *Model 2* and *Model 3* are able to produce a biting force close to that observed in the experimental tests. When assuming that the muscles work in the *ascending limb*, the force-length factor must allow for significant force production during muscle contraction, which is severely limited by the force-length factor proposed by Ruijven[71].

All three of the models were found to be stable and able to produce a larger force when the jaw is opened further. In the case of *Model 2*, the increase of force production in the deep masseter is able to compensate for the rest of the closing muscles. Additionally, it was observed that the medial pterygoid functions only in a very limited range in this model. The employed model in the rest of the simulations of this work was *Model 2*, as it reproduces biting forces accurately and does not excessively limits the movement of the joint.

The relatively small variation of the origin point of the temporalis and masseter muscles, studied with *Model 2* did not produce a significant effect in the ratio of biting and joint force. This was an unexpected result, since in static models of the literature a larger effect can be observed. This may be a result of the dynamic treatment of our model, which allows the condyle to reposition itself during the operation of the masticatory system. The opening of the jaw was shown to possess a higher influcence of the joint / biting force ratio, mostly because of the limited working range of the medial pterygoid muscle in this particular configuration.

Chapter 7:
The Mastication Cycle

Mastication is the process that involves the synchronous activation of the muscles of the masticatory system in order to crush the bolus with the surface of the teeth. Due to the direct influence mastication has in the quality of life [92], masticatory performance as well as the diverse factors that affect it (among them chewing kinematics, early contact, dentition, etc.) have been extensively studied. However, the direct influence of these factors is still not completely understood.

Current techniques employed in prosthetic rehabilitation, particularly those relying in CAD/CAM techniques, only use kinematic data to reconstruct biomechanically effective and interference-free tooth profiles. It is assumed that so-called border movements recorded for patients and implemented in mechanical and virtual articulators avoid unwanted short-range contact of antagonistic teeth during chewing or bruxing.

To ensure that damaging tooth contacts during critical short-range contact of antagonistic teeth are avoided, data on the occlusal displacements caused by kinetic loading of the masticatory system during the chewing of food, and the resulting deformations and micro- movements of the complete jaw system, are needed. Presently such data are unavailable.

During chewing of a food bolus between the teeth, occlusion is usually not reached abruptly but is, rather, a kinetic process: After first contact with the food bolus the teeth undergo gliding (translation and rotation) relative to each other before reaching the final configuration. During this phase the load distribution on the participating teeth, the stress distribution in the periodontium, and the mutual alignment of the teeth will change continuously from first contact to the end of the power stroke.

The finite-element method has been widely employed to study the stomatognathic system. Due to complexity of the masticatory system, however, most of the studies that rely on this method usually focus on a particular component in order to simplify the problem and to reduce the computational effort required. Investigations where most of the components of the system have been modeled can also be found [5, 4, 93, 94], but usually concentrate on rather limited motions of the jaw.

In a fairly recent work by Commisso et al. [95], the chewing motions were reproduced by using a comprehensive model, but the model did not include a deformable bolus. In the present work, the powerstroke of the chewing cycle is simulated by

calibrating the model kinetically to match the kinematics of the chewing motion, with a deformable bolus being placed between the teeth.

7.1 Kinematics of the Chewing Cycle

Several studies have analyzed the shape and duration of the chewing cycle under different circumstances. Differences can be observed between males and females [96, 97], with age difference [98], with the type of bolus [99, 100] and among patients with different mastication performance [101]. On the other hand, it has been observed that blocking the nerves to eliminate the perception of the jaw joints and the periodontal ligament, results in virtually no change [102].

Recording the kinematics of the chewing cycle is usually performed by recording the movement of a point in the jaw, usually on the chin (Bhatka et al. [99], Lepley et al. [101]) or a point of the lower central incisors (Piancino et al.[100], Schindler et al. [102], Buschang et al.[97]) over the course of several mastication cycles. The principal characteristics of the mastication cycle recorded from different authors are quoted in table 7.1.

Author	**Cycle duration [ms]**	**Max velocity [mm/s]**	**Vertical displacement [mm]**	**Lateral displacement [mm]**
Buschang et al. [97]	835-972	99.6	17.8	4.87
Bhatka et al.[99]	751-790	121.0	12.7	4.41
Schindler et al.[102]	-	-	20	6
Piancino et al.[100]	617	152	18.8	4.4
Lepley et al. [101]	750	97.9	10.3	5.2

Table 7.1: Cycle duration, maximum velocity and maximum vertical and lateral excursions of the chewing cycle measured by different authors. The studies employ different types of bolus, including real foods that change physical properties and break down during mastication as well as chewing gums. In our model, the bolus was modeled as a linear elastic material

It can be seen that the recorded paramaters can differ significantly between authors. Typically, the duration of the opening phase of the cycle is longer than the closing phase, but the opposite was observed by Lepley et al. [101]. The trajectory followed by the recorded point was also found to take different shapes. Maximal extrusion

and velocity was found to be related to the size and hardness of the bolus, with the jaw storing more kinetic energy when more resistant boluses are chewed.

7.2 Simulations and Results

Due to the evident complexity of the chewing process, simplified simulations of the chewing cycles were performed. Two simulations were executed: The first focuses only in the opening and closing movement of the jaw, while the second simulation incorporates the lateral excursion of the jaw observed in the chewing process. Geometries employed in both simulations are identical. A bolus with a thickness of 2 mm was crushed between the second molars to observe the movements of the teeth and the direction and magnitude of the resulting biting force. The bolus has a Young's modulus of 20 MPa, equivalent to the elastic modulus of an almond under compression, and a Poisson's ratio of 0.47 [28].

7.2.1 Single Chewing Cycle: Simplified Model

Activation levels of the muscles were calibrated to slightly open the jaw during a period of 220 ms, producing a gap between the molars wide enough for the bolus to fit. The bolus was placed between molar teeth 16 and 46. Contact elements in between become active at t = 230 ms. At t = 259 ms, molar 46 made contact with the bolus and rigid body rotation of the bolus was observed until time t = 278 ms, when the cusps of the molars completely captured the bolus. The closing muscles were then slightly activated until time t = 400 ms to ensure stability, i.e. a firm grip of the bolus between the molar teeth. The activation levels were subsequently increased to finally obtain a realistic bite force of 150 N at 600 ms. Activation levels were taken from Schindler et al. [69].

The resulting force on tooth 16 in each direction, from frontal and sagittal perspectives, can be observed in figure 7.1. During the initial phase of biting, when the bolus is being captured by the teeth, the resulting force is partially aligned with the direction of the roots. As both, force and deformation, increase, the resulting force becomes almost completely vertical relative to the Frankfort horizontal plane. In both planes this results in a force vector at a substantial angle to the occlusal plane (Fig. 7.1). In principle, the spatial kinetic behavior can be described as partial spiral movement leading to short-range intercuspation. The force evolution on tooth 16 over time (Fig. 7.2) and the points of application of the resultant force are also shown in figure 7.1. The points were estimated by using the resulting forces and moments on both teeth, by means of an iterative process.

Because the PDL of molar 16 is constrained at its border with the maxillary bone,

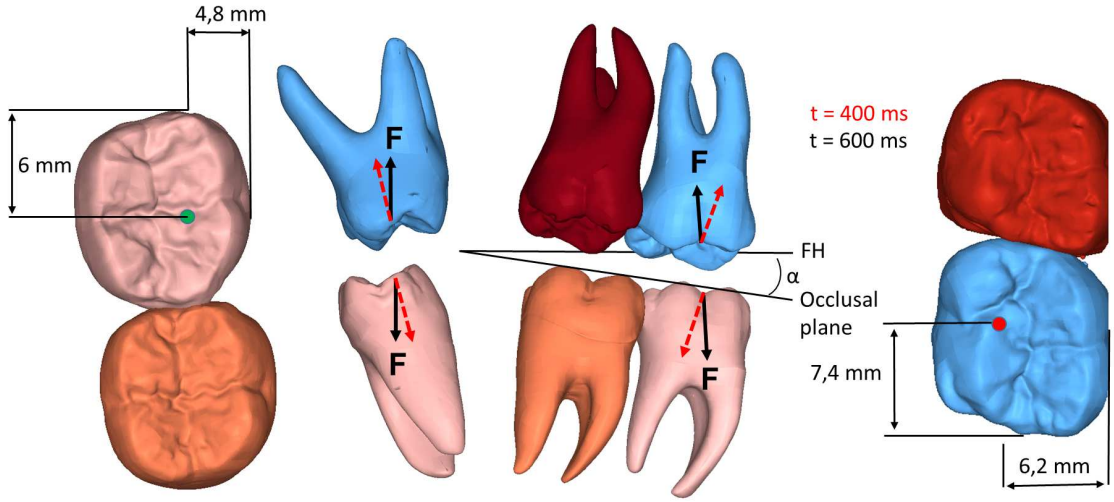

Figure 7.1: The force directions on teeth 16 and 46 at t = 400 ms and 600 ms, and estimated resulting force application points (red and green dots). F = force, FH = Frankfort horizontal plane, α: sagittal angle between FH and occlusal plane

displacements of this tooth are completely governed by its PDL. The displacement components of the resulting force application point for tooth 16 are plotted in figure 7.4. In the lateral-medial direction we observed a positive lingual displacement of 3.25 μm until t = 400 ms. At this point the displacement decreased until the initial conditions were reached at t = 500 ms. In the anterior-posterior direction, up to t = 400 ms a negative labial displacement was observed; this reached a magnitude of 20 μm, then slowly returned to a value of 5 μm from this point. Displacements in the vertical direction increased continuously up to approximately 16 μm.

From t = 400 to 600 ms, as activation levels were increased to reach the target force, the level of the mandibular molar rose by 1 mm, substantially deforming the bolus (Fig. 7.5). It can be estimated from figure 7.3 that an average gap of approximately 2 mm remained between the upper and lower molars at the end of the simulation because of the rather stiff bolus.

The first principal stress in the PDL of tooth 16 at different times during the biting process is depicted in figure 7.6. At t = 400, 500, and 600 ms the maximum stresses were 0.42, 1.89, and 7.07 MPa, respectively; the minimum stresses were -0.25, -0.92, and -3.56 MPa, respectively.

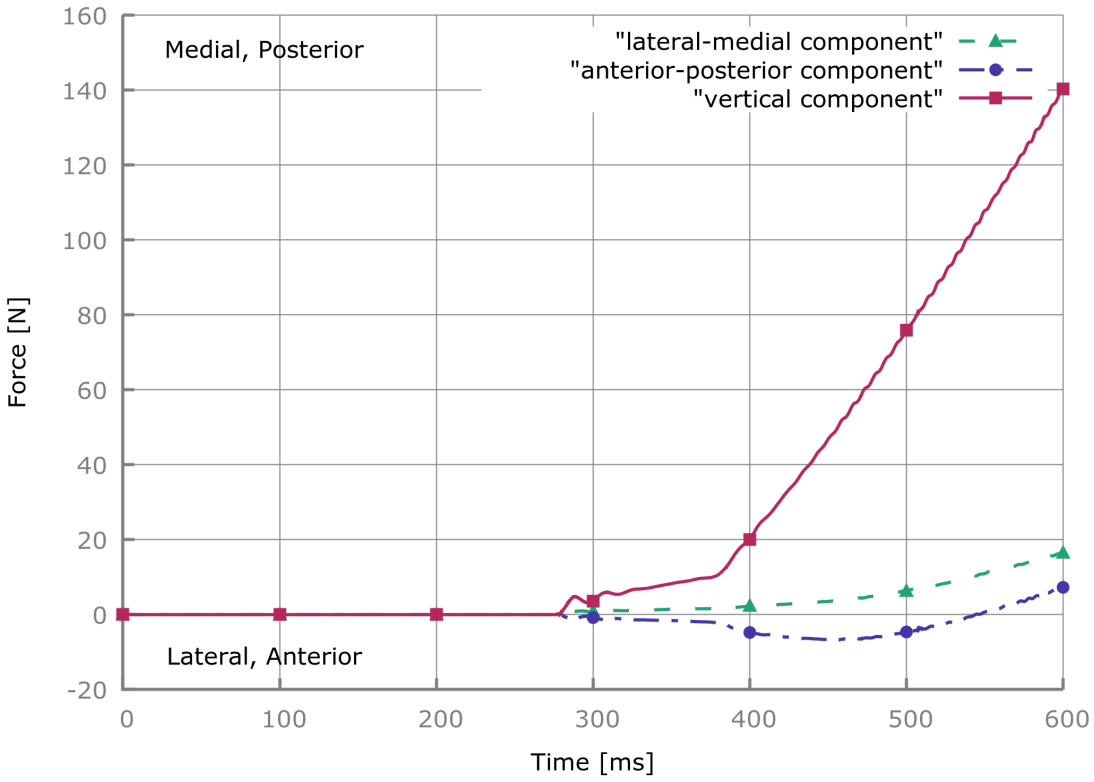

Figure 7.2: Development of force components on tooth 16 in the lateral-medial, anterior-posterior, and vertical directions over time

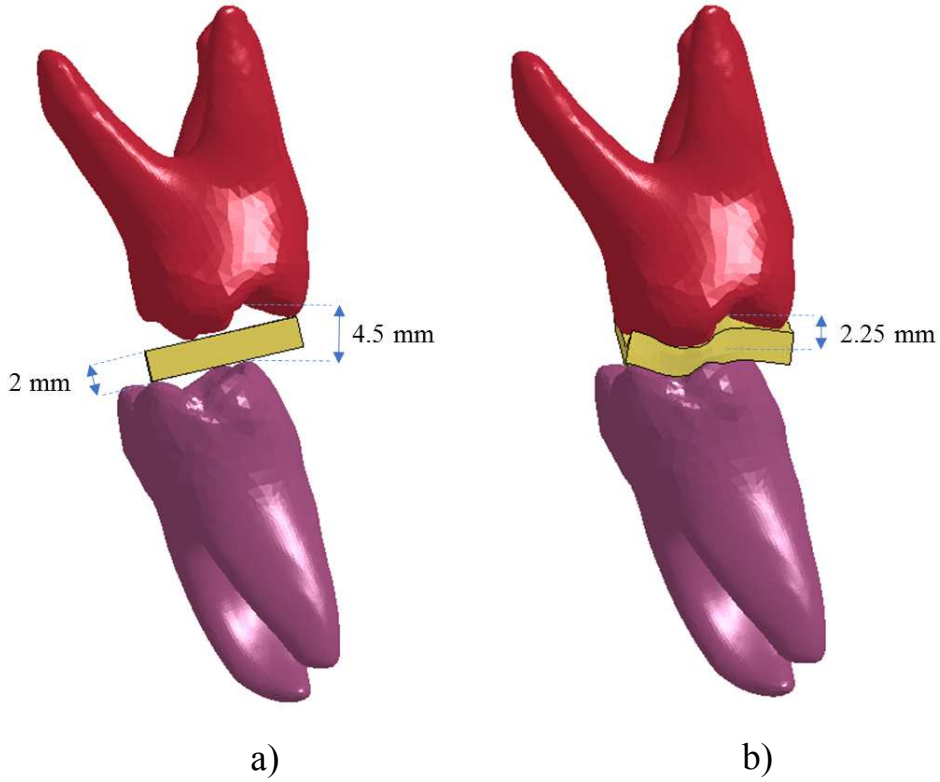

Figure 7.3: Posterior view of teeth 16 and 46 during the biting process. Views at the a) initial and b) final phase of the biting process

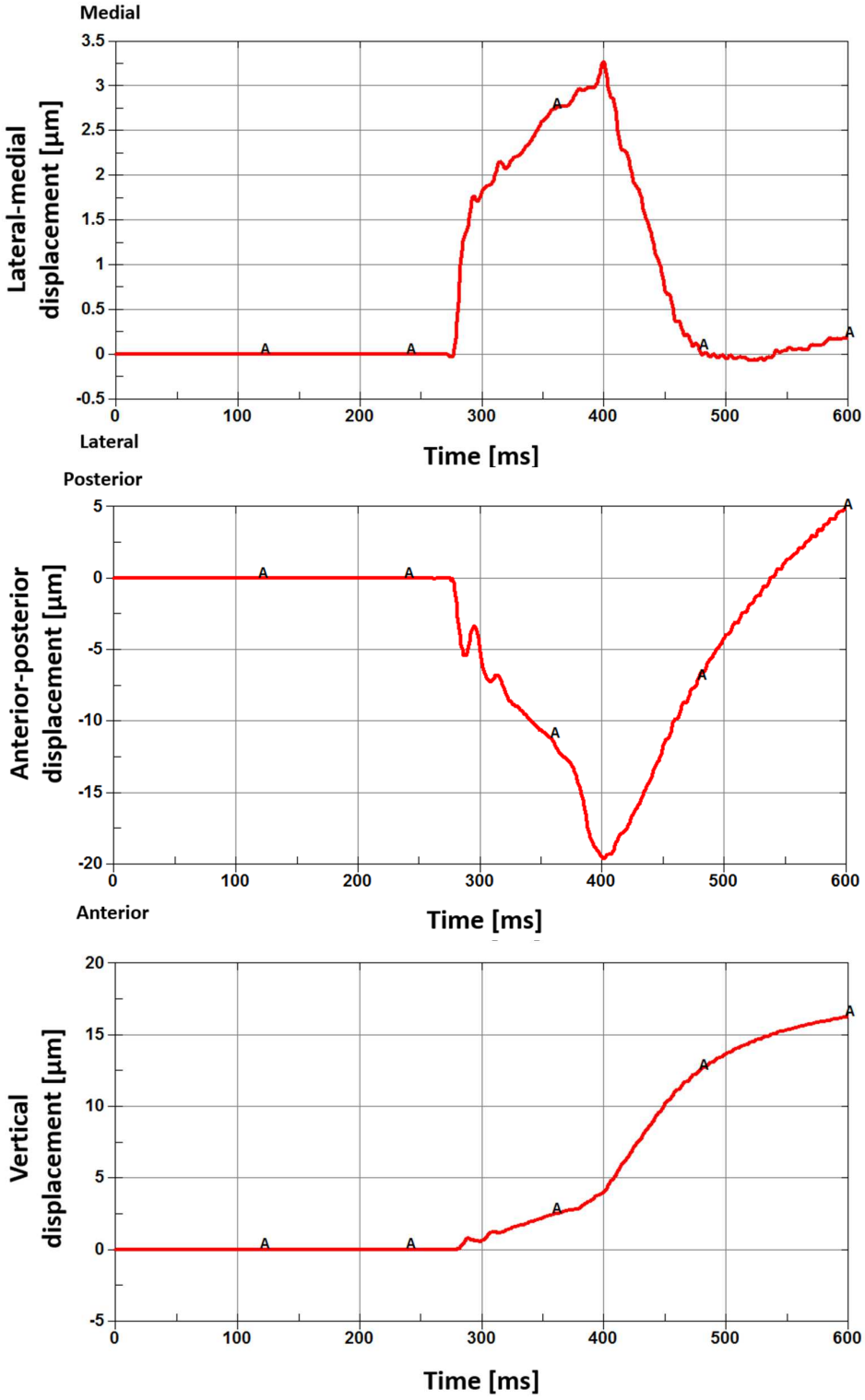

Figure 7.4: Displacement components of the force application point of molar 16 in the lateral-medial, anterior-posterior, and vertical direction

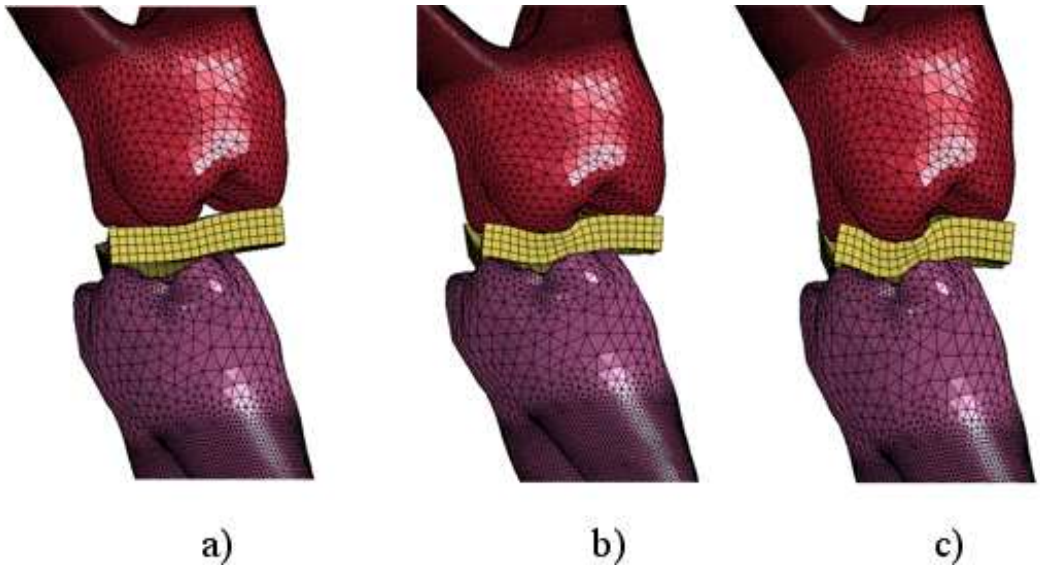

Figure 7.5: Posterior view of the biting process. Views at times a) 400 ms, b) 500 ms, and c) 600 ms

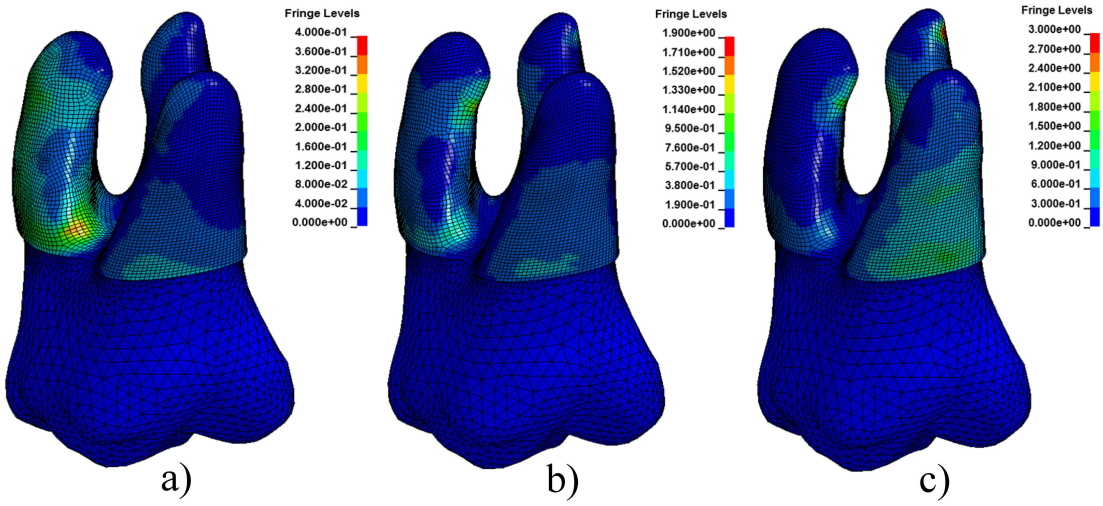

Figure 7.6: First principal stresses in the PDL of tooth 46 at times a) 400 ms, b) 500 ms, and c) 600 ms

7.2.2 Single Chewing Cycle: Enhanced Model

For a more realistic simulation of the chewing cycle, several aspects of the cycle were prescribed: The duration of the complete cycle was set as 800 ms, with the opening phase and closing phase lasting 450 and 350 ms, respectively. The maximal vertical displacement was specified as 15 mm, the maximal lateral excursion as 4 mm, and the maximum velocity was chosen as 150 mm/s.

The creation of smooth movements, such as the chewing cycle, is exceedingly difficult with the model. Stable forces in the jaw are very difficult to produce as the passive forces of the muscles that oppose the movement increase exponentially, as well as the muscle responsible for the movement is continuously losing its capacity to produce force. The dissipation of energy occurring from the force-velocity factor was considered to be inadequate, since very light activation levels of the muscles would accelerate the jaw to a velocity where the muscle produces almost no force, and an irregular movement results as the passive resistance of the muscles quickly inverts the movement of the jaw. Even a slight activation of the antagonist muscles (in this case the closing muscles) did not introduce sufficient dissipation for a smooth movement to take place. For this reason, a damping constant with a value of 0.05 MPa/sec was incorporated into the Hill model.

In figure 7.7 the motion executed by the lower incisor tooth can be observed in both, anterior and lateral view. The shape of the movement from the frontal view follows the general motion but lacks the roundness observed in measurements observed as e.g by Bhatka et al. [99]. The lateral view shows that the closing part of the chewing cycle has a path with a notable offset in the anterior direction. Measurements show that the opening and closing path are very similar in the anterior and posterior directions.

Displacements and velocities in the lateral and vertical directions are shown in figure 7.8. These follow the behavior from the curves seen in Bhatka et al. [99] but are, however, not quite as smooth. The lateral velocity has significant sudden changes resulting in an uneven curve. Since contact with the non-destructible bolus occurs at time 670 ms, sudden deceleration occurs shortly after.

Activation levels of the muscles used to obtain this motion, are displayed in figure 7.9. In order to simplify the task at hand, the opening and closing muscles were activated with the same levels at both sides. In this manner, the vertical velocity of the jaw could be calibrated using fewer paramaters. The lateral movement of the jaw was controlled using the lateral pterygoid muscles. As observed, the motion of the chewing cycle was obtained with rather low activation levels of the muscles.

The displacements in the lateral-medial, anterior-posterior and vertical directions of molar 16 during this chewing cycle can be seen in figure 7.10. Displacement in the

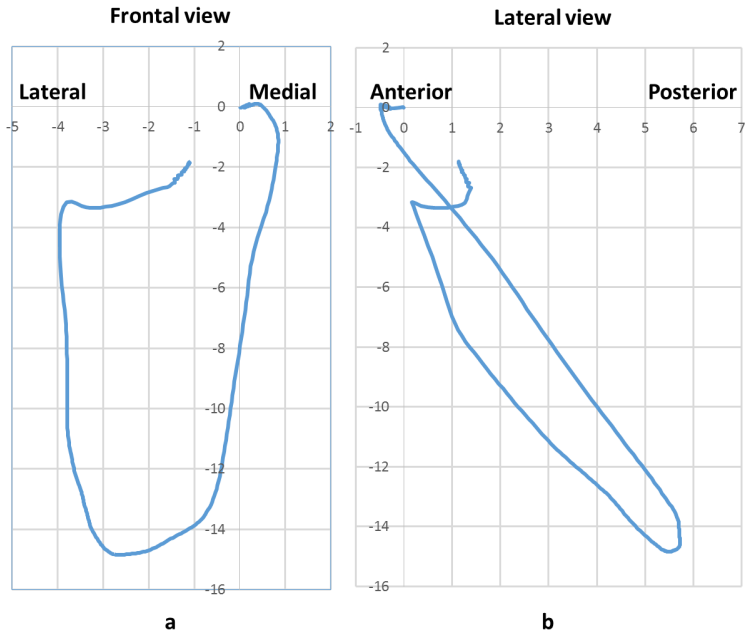

Figure 7.7: Displacements (in mm) of the tip of the central incisor (tooth 41) during a single chewing cycle; a) front view, b) lateral view

latero-medial direction are small although forces in the same direction are significant. As in the simplified chewing case, the rotation of the tooth is prevented due to the vertical forces introducing a moment in the opposite direction. Displacements in the anterior-posterior direction are initially large but are countered subsequently by the vertical forces, too. Vertical displacements are similar to those observed in the simplified chewing task, although smaller since a lower biting force is reached in this case.

The forces on molar 16 are shown in figure 7.11. Due to the chewing motion, there is a higher proportion of force in the medial direction, however, as in the simplified chewing task, vertical forces dominate. The antero-posterior component of the force is not significant in this case. The resultant biting force developed in this simulation due to the kinetic energy stored in the jaw is of around 10 N. The resulting biting force of approximately 90 N is reached here by activating the closing muscles to a value of 10%. The lateral force is developed by deactivation of the lateral pterygoid at the contralateral side, which results in the stored energy in this joint, in the disc and its attachments, bringing the condyle to its posterior position.

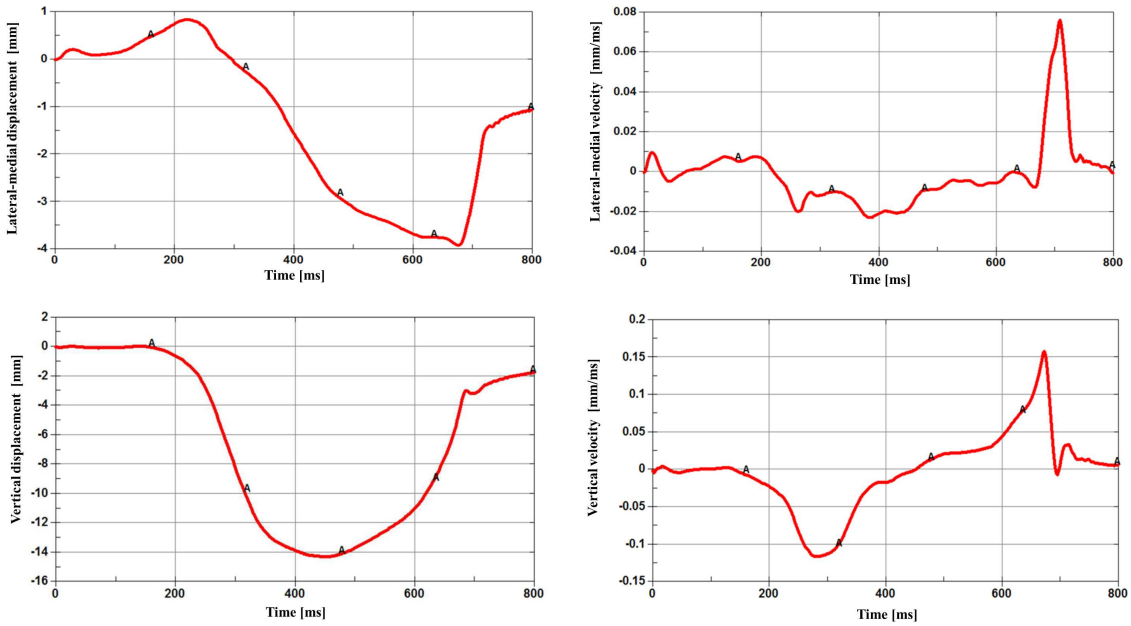

Figure 7.8: Displacements and velocities in the lateral-medial direction (upper row) and in the vertical direction (bottom row) of the tip of the central incisor (tooth 41) during a single chewing cycle

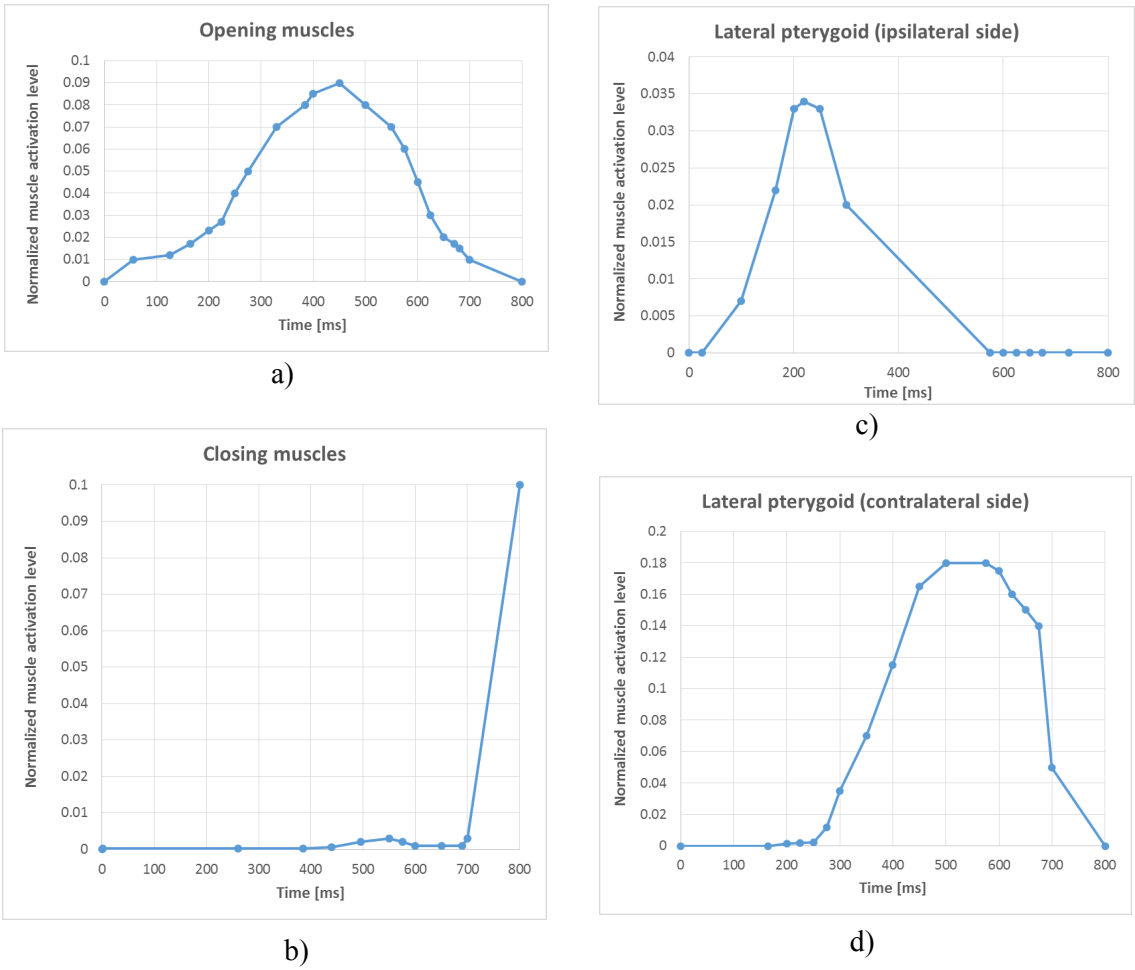

Figure 7.9: Activation levels for the a) opening, b) closing, c) ipsilateral lateral pterygoid, and d) contralateral lateral pterygoid muscles

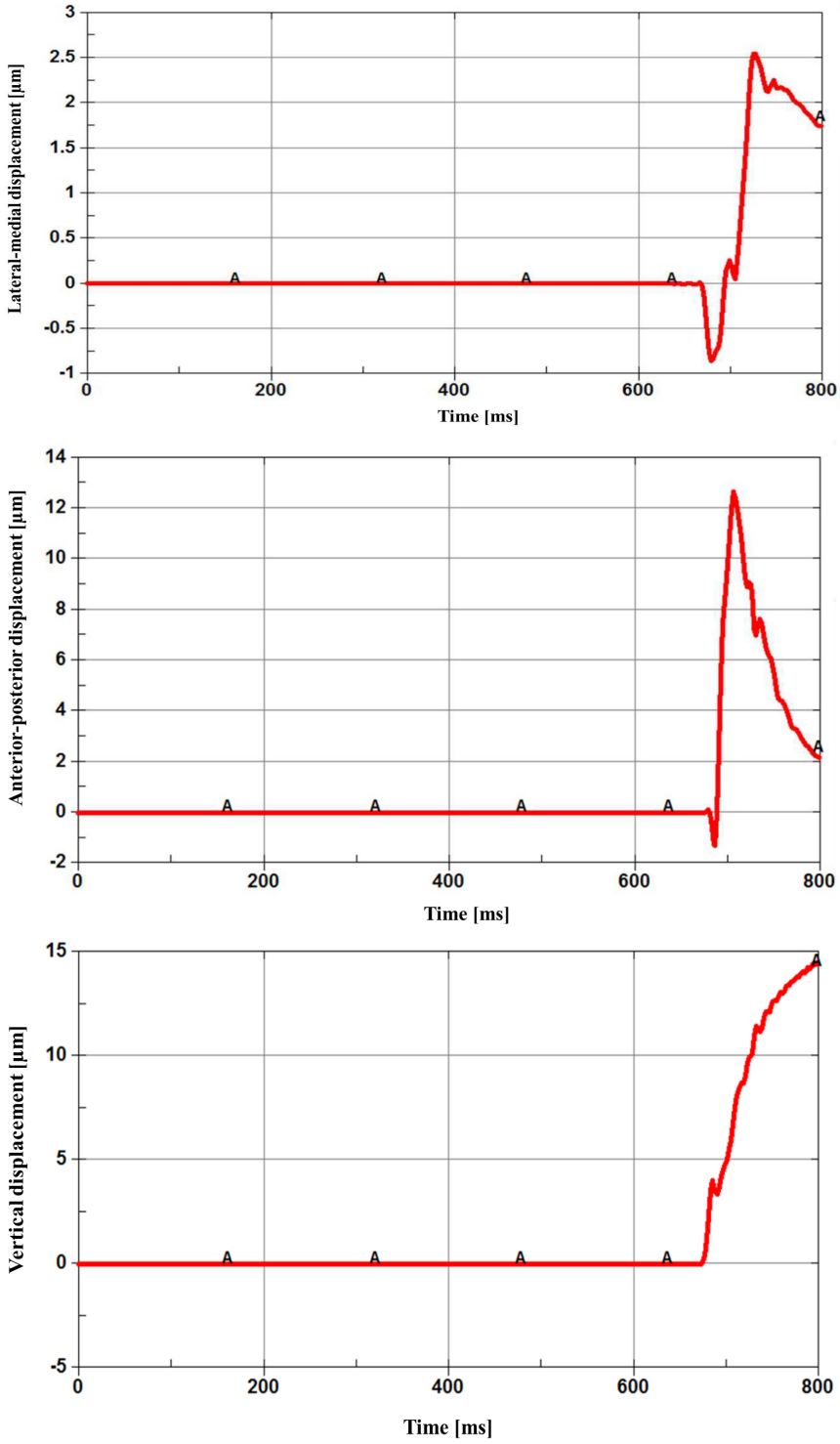

Figure 7.10: Displacement of tooth 16 during the single chewing cycle

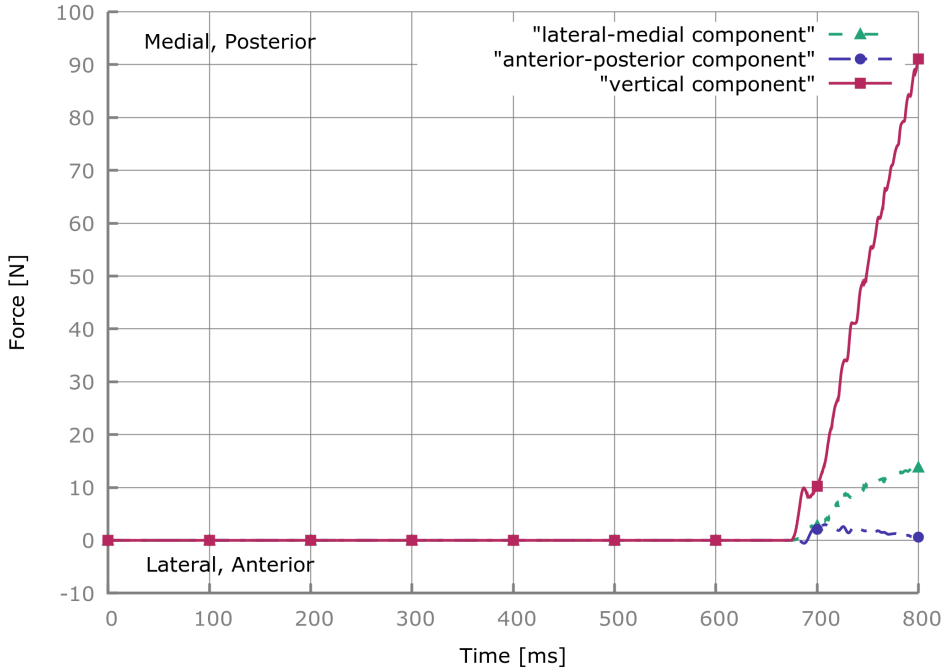

Figure 7.11: Development of force components on tooth 16 in the lateral-medial, anterior-posterior and vertical directions over time during a single chewing cycle

7.3 Conclusions

In contrast to widely held beliefs, axial loading of the molar teeth can be observed only at the very beginning of the power stroke and not during the path into short-range intercuspation. This finding is in agreement with previous experimental data reported by Schindler et al. [102], and Rues et al. [103]. It was also observed that small mediolateral and anteroposterior movements of the molars are brought into balance when intrusive forces are applied.

Although the force on the teeth is not completely horizontal as in the experimenal setting, its horizontal component of 5 N produced a mesial displacement of approximately 20 μm. This displacement is inside the range of the experimental results reported by Yoshida et al. [104]. The forces developed on the molars are mostly intrusive and do not produce large moments during the initial phase of biting. Because of the geometry of the molar and its antagonist, tooth 16 experiences a lingual force which increases slightly during the complete biting process. This results in an initial lingual tilting of tooth 16. As soon as the vertical force increases, the tooth begins to tilt in the buccal direction, because of the moment generated by the resulting force. In the anterior-posterior direction, anterior tilting of the molar is observed until t = 400 ms because of the anteriorly directed force acting on the tooth. Although this force continues to increase in the anterior direction until t = 460 ms, the moment produced by the vertical force tilts the molar in the posterior direction. The reversal of the anterior force at t = 460 ms is a result of a partial spiral motion of the molar following the inward movement of the jaw during the power stroke. It might be assumed that the complex kinetic behavior of the molars and the jaw when the antagonists are in close proximity, is affected more by the self-guiding properties of the occlusal profiles (cusps and fossae) of the teeth than by persistent changes in the co-contraction pattern of the jaw muscles involved.

Reproducing the kinematics of the chewing cycle proved to be a very challenging task. As an initial step to simplify the complex motion, opening and closing muscles were activated identically at both sides to control the vertical displacement of the jaw. The exception in this approach were the lateral pterygoid muscles, which were used to create the lateral movement of the cycle. Naturally this approach is not an ideal strategy since EMG measurements show that the activity of the muscles at the ipsilateral side is different from that at the contralateral side. This simulation allows, however, to understand the effect of the different components on the resulting motions.

It was observed that during opening, once the rotation of the condyle has reached a certain amount, the inferior part of the retrodiscal tissue begins to hinder further rotation, since due to the pulley elements the tissue begins to fold over itself. This undesired behavior shows that the pulley elements are not suitable as a mechanism

to keep the tissue at the surface of the condyle. In reality, the inferior stratum of the retrodiscal tissue offers no resistance to jaw opening. This behavior is easier to observe when only one of the condyles is displacing anteriorly, as the initial tension of the attachment has great influence on the ability of the lateral pterygoid muscle to laterally accelerate the mandible. This limitation may be one of the reasons for the lack of a smooth velocity behavior in medio-lateral direction.

With the current model, a motion can be performed that reproduces the general characteristics of the chewing cycle. However, the very final stage of the cycle cannot be captured since the used bolus is non-destructible. This forces the teeth as well as the jaw to follow a less resistant path at this stage, which displaces the jaw posteriorly.

As in the simplified case, movements in the mediolateral and anteroposterior directions are balanced as the intrusive force raises. A small lateral movement of the maxillary molar occurs due to the medial motion in the final stage of the chewing cycle. A significant posterior displacement of the molar is observed upon contact with the bolus, caused by the posterior displacement of the jaw, and is, therefore, not reflecting a realistic behavior. Although the intrusive forces are significantly lower, the vertical displacement of the maxillary molar is very similar to that of the simplified model due to the non-linear behavior of the PDL.

As expected, there is a larger component of force in the medial direction when the chewing motion is reproduced. In our model, the joint and its attachments seek constantly to bring the joint to its initial position during the chewing task.

Among the future goals of this work, is the implementation of real muscle activations measured with EMG during actual chewing tasks, and the introduction of destructible boluses. However, the present simulations have shown that corrections are required with respect to the behavior of the inferior retrodiscal tissue in order to obtain a realistic response from the model during more complex tasks.

Chapter 8:
Final Conclusions

Due to the complexity of the stomatognathic system, a myriad of complications can occur to hinder its proper operation, such as temporomandibular joint disorder, malocclusion, periodontitis, an so forth. The focus of many scientific investigations center on the functional, psychological and aesthetic impact of these complications in the well-being and quality of life of patients.

In the field of biomechanics, the different components of the masticatory system have been studied independently. For each component, there are large discrepancies concerning their material properties measure in experiments as well as different approaches on how to properly model them.

Models incorporating the majority of the components are numerous, but due to the restrictions of computational power and the complexity of the diverse components, most were performed as static analyses or with simplified boundary conditions. In this study, a model comprising the fundamental components of the stomatognathic system, was run as a transient analysis, in order to capture its dynamical behavior and enhance the comprehension of the system.

The creation of the model involved several steps, starting with the creation of accurate and compatible geometry files for the preprocessor software. The process of creating the geometry begins with the segmentation of CT-scans, which uses the gray-threshold on each of the images of the set to assign boundaries and create a 3D object. The next step involves repairing all defects present in the object. Finally, a conversion of format (from STL file) is performed in order to obtain a geometry more suitable for meshing (IGES format). This was achieved with the aid of three programs, which added great complexity to the process, because any modification of the geometry would usually require that the process be started anew, including re-meshing and verification of proper element connection. Due to the resolution of the CT-scans, several simplifications were introduced to the model: The PDL was endowed with constant thickness and the capsule of the temporandibular joint was represented with truss elements. These difficulties could be handled with the use of high resolution CT-scans. However, devices that can produce such images are extremely costly and are currently limited to small samples. Certainly, the future development and adoption of such devices will greatly reduce the work expenditure required to establish such geometries as well as enhance their accuracy.

The periodontal ligament Some of the most distinguished studies in the litera-

ture were followed in order to model components such as the muscles, the temporomandibular joint and the bony structures of the mandible. In the case of the PDL, however, due to the complexity of the tissue, no sufficient agreement was found between the different studies in order to select a specific modeling approach. The primary objective of this work, was that displacements observed during experimental tests were correctly reflected by the model. Since the PDL is extremely sensitive to forces at its resting configuration and very stiff after displacements have occurred, material models depicting the tissue as linear, were immediately discarded. The high non-linear behavior of the PDL can e.g. be captured through the use of hyperelastic material models. Several models employing such materials are available in the literature and show an appropriate response. One of these models was implemented and compared to a self-calibrated hyperelastic material model readily available in most finite element softwares. Although both models showed displacements in the range of those experimentally observed, the concentration of stress generated in the hyperelastic material models was deemed unrealistic, as the first principal stresses (tensile stresses) present during high force biting tasks, would exceed the failure stress of collagen fibers present in the PDL.

Since the PDL is a tissue completely confined between the tooth and the alveolar bone, its compressibility plays a fundamental role as small displacements of the teeth create large volumetric strains in the PDL. The closer the material model is to being completely incompressible, the better the forces are distributed, but at the same time the displacements of the teeth quickly diminish as the volumetric strain in the PDL is constrained. To provide for displacements occurring in the real tissue, the material must be allowed to compress. Thus, the material does not distribute the forces as effectively as a saturated tissue, and a concentration of stresses occur in the model as the elements that deform first become exponentially stiffer than those that deform later.

In the PDL, the fluid flows from and to the alveolar bone and gets trapped as the collagen fibers deform. The development of better material models for the PDL would require to discard the use of hyperelastic material models and adopt the use of poroelastic material models in order to correctly capture the role of the fluids inside the PDL. Works where the PDL has been modeled with such materials can be found in the literature, however, with rather simplified geometric models. Incorporating such models correctly, would require that the bones are also modeled as poroelastic, as the fluids in the PDL flow to and from the bone during the normal operation of the masticatory system.

Since the material models employed here can reproduce the displacements of the teeth under loads, they can also be used to study the effects of a reduction of tooth mobility on the masticatory system, when implants are introduced.

The temporomandibular joint The temporomandibular joint is a very complex structure. The challenges regarding its modeling begin with its geometry: The structure consists of an articular disc surrounded by a capsule that attaches it to both, the condyle and the maxillary fossa. In the literature, the geometry of the capsule is seldom created and usually only the lateral and medial attachments of this structure are represented. Since in the present model the complete mobility of the joint was one of the principal objectives, all attachments of the capsule were represented as well as the temporomandibular ligament, in order to prevent the dislocation of the disc during posterior displacement of the condyle. These structures require careful calibration: the superior posterior and inferior anterior attachments are under tension during occlusion (which corresponds to the initial configuration in our model), while the rest of the attachments are relaxed. If the attachments are not properly adjusted, they can severely limit the movement of the condyle.

The contact between the different components of the joint was one of the main reasons behind the use of an explicit time integration scheme. Since the disc moves between opposite surfaces, a small time step was required to properly capture the behavior as well as for the convergence of the implicit solver, this made the implicit scheme impractical for this study. Treating the problem as a dynamic problem allowed a more refined calibration, as it could be thus determined whether the attachments or muscles (through their passive response) were limiting the proper behavior of the system.

The most stable position of the jaw occurs when the condyle has reached its most posterior position. This can be observed during high biting forces, when the posterior forces of the temporalis muscle drive the condyle into this position. In this situation, the attachments of the capsule and the temporomandibular ligament play a fundamental role ensuring the stability of the system. These tissues can, however, severely limit the motion of the condyle during jaw opening if not properly calibrated. This phenomenon cannot be observed in static simulations, because constraints placed in the joint will always balance the system, whereas the surface of the mandibular fossa cannot produce any anterior force to balance the system.

It was observed that the geometry and the material models employed for the joint give it a remarkable capacity to evenly distribute the forces throughout the surface of the articular disc. Therefore, as forces in the joint increase, peak stress remains relatively low. During jaw opening, however, higher concentration of stresses were observed since a smaller area of the condyle remains in contact with the disc. Nevertheless, this could be due to the approximately constant thickness of the articular disc has in our model, whereas in reality its middle area is thinner.

The study performed with a gap introduced between the two sides of the mandible, revealed that significant changes of the stress patterns in the disc occur. This shows

the potential therapeutic effect of the introduction of splints, translating the stresses from damaged/weared areas to more robust/healthy parts of the disc. Further studies can be performed with the current model, introducing slight modifications to study disorders of the TMJ such as for instance disc dislocation.

It was also revealed that the modeling of the joint still suffers from limitations, as the experimental results, specifically the distribution of bite force between the sides, could not be perfectly replicated with the model.

The muscles In literature, many assumptions are made to simplify the muscles and avoid over-complicating the model. In most static models, forces are applied directly at the insertion points of the muscles. These are usually applied as a single point or distributed over the insertion area to avoid singularities. In our model, however, the orientation and the length of the muscles change along the position of the jaw, which directly affects the direction and magnitude of their forces. In the literature, Hill's muscle model is extensively used to capture the principal characteristics of the muscle behavior, namely its passive response and the influence of length and velocity to its capacity to exert force.

Data of the masticatory muscles regarding their insertion and origin points, their cross-section area and ratio of tendon to muscle fibers can be obtained directly from the literature, which shows mostly agreement in these aspects. Some of the muscles have large insertion/origin areas. Therefore some authors use several muscle components to represent what is considered as a single muscle. Choosing suitable muscle parameters, such as their force-length, force-velocity and passive response is a more delicate matter. In the literature, the operation ranges of the muscles and their response to stretching show significant variance. In this study, different curves representing each of the muscle's characteristic behaviors, namely its force-length and force-velocity relationship as well as its passive response, were employed. Various configurations using different combinations of these curves were defined and their effect on the system studied. Additionally, the origin points of the muscles were also modified to analyze their impact.

Due to the current difficulty to obtain experimental data on many of the facets of the muscles, several assumptions had to be made made in order to evaluate whether a particular configuration is producing the desired results: a) The passive response of the muscles should help to guide and not to restrict the realistic motion of the jaw observed in the literature, b) the muscles should ideally work within the range of the *ascending limb* to ensure stability of the system, and, perhaps most important, c) the use of experimental activation levels of the muscles should reproduce the experimental biting force.

As expected, even when some of the muscles are working outside their *ascending*

limb, the configurations remain stable due to the great capacity of the other closing muscles to produce force. Different muscle configurations were also able to produce the experimental biting forces with the measured activation levels. The opening jaw motion, however, shows that some of these configurations (those with a strong passive response) limit the forward motion of the condyle, creating excessive stresses in the disc.

In the literature, discrepancies can be observed regarding the ratio of joint to bite forces. The calculation of muscle forces, usually when EMG-measurements are not available, is done generally with optimization methods under the assumption of minimizing either joint or muscle forces. These assumptions result in high biting forces and low joint forces. Experimental results in the literature suggest that joint forces are higher, as also observed in this model, which may help stabilize the condyle during high biting forces. The high mobility, and thus, unstable nature of the articular disc can not be explored in static analyses of the masticatory system. The effects of altering the origin points, and consequently, the orientation of the forces was shown not to affect significantly the resulting bite/joint force ratio. However, orientation as investigated in Röhrle et al. [79] might play a significant role. The activation levels and the degree of jaw opening, however, have a bigger role influencing this ratio. The position of the jaw affects both, the angle and the magnitude of muscle force, through their force-length factor.

The bones The cortical bone has a greater capacity to carry compressive stresses than tensile stresses. For this reason, the stresses investigated were the first and third principal stresses. During opening, overall small levels of stresses were observed in the jaw, where the highest tensile stresses arose at the lateral side of the ramus, while the highest compressive stresses occurred at the posterior part of the ramus. During biting, areas exposed to highest tensile forces were the posterior part of the mandibular notch and the anterior part of the coronoid process. The region with the highest compressive stresses was, as during opening, the posterior part of the ramus. These stress patterns have previously been observed in the literature, too.

The stress levels observed where significantly below the levels for cortical bone failure. However, some models in the literature show lower magnitudes, which suggest that some of the assumptions in our model should possibly be revised.

The mastication cycle

Before incorporating the activity of the muscles measured via EMG during chewing, two simplified chewing tasks were performed in order to study the overall behavior of the model. The first simplified chewing task consisted in simple opening/closing of the jaw without any lateral movement and with a deformable bolus. The second

task incorporated the lateral motion of the chewing cycle and aimed to reproduce the kinematics of the cycle which had been experimentally measured by other authors. This task was simplified in the sense that the closing muscles were activated identically at both sides.

The first simulation showed that due to the geometry of the teeth in contact, the initial forces developed on the bolus follow the general direction of the root of the molars. As the bite force raises, tipping of the molars is reduced as it is balanced by the increasing intrusive force. As the bolus deforms between the teeth, the biting force becomes almost purely vertical.

In the second simulation, introduction of the lateral motion of the chewing cycle proved difficult since it revealed that the inferior stratum of the retrodiscal tissue non realistically resists the excursion of the condyle. Since this tissue should only resist posterior displacements of the condyle, further simulations of the chewing cycle will require the improvement of the model in this respect. Nevertheless, the general behavior of the cycle was well captured by the model. As expected, during chewing medial forces are developed in the bolus. Although the forces of the closing muscles are the same on both sides of the jaw, significant lateral force can be produced by deactivating the contralateral lateral pterygoid, as the joint brings the condyle back to its posterior position.

The previous simulations showed that reproduction of more complex motions of the lower jaw can be achieved by the model with the proper activation levels of the muscles. The behavior of the teeth is very similar for both cases, as the vertical force balances the tipping movement. However, several aspects of the model require attention: A destructible bolus is required to study the final aspect of the mastication process, the temporomandibular joint requires further revision in order to enable more smooth lateral movements of the jaw.

Limitations

The current model contains the following limitations:

- Although great effort was put into the implementation of a correct material model for the PDL, the results of the simulations revealed that hyperelastic material models are not particularly suitable to predict the stresses in the tissue.
- The hyoid bone is fixed in this model, reducing the capacity of the digastric muscle to continue exerting force. The hyoid bone is unique in the sense that it essentially hangs freely not being fixed to other bones but suspended by several muscles. To properly model its movement, the modeling of several muscles, such as the sternohyoid muscle and suprahyoid muscles along with the sternoclavicular joint, would be required. This would be, on its own, a

very complex system to model.

- The cortical bone was modeled as isotropic, although it is clearly anisotropic. It was modeled under the assumption that the loads would be carried by the longitudinal fibers of the jaw which have the highest elasticity modulus.
- The capsule of the TMJ and the bilaminar zone were modeled with trusses, without considering the behavior of fluids inside the synovial cavity. The friction between the articular disc and the articular surfaces was considered, however, to be non-existent due to the presence of synovial fluids.

Benefits of the model for medical studies

The modeling of biological systems requires the assumption of a great number of parameters which cannot be measured, however the intervention required by current technology to accurately measure the properties of in vivo materials, makes it ethically impossible. Some of the parameters employed in this work (e.g. viscoelastic paramaters of the articular disc) rely on studies performed in human cadavers whose material properties are different than those found in vivo. Other parameters (e.g characteristic behavior of muscles, elastic parameters of the retrodiscal tissue) are obtained from animals who have been dispatched immediately prior the study, in order to minimize changes in the behavior of their tissues. Naturally, parameters taken from animals need to be modified since they will differ from those of human beings. The uncertainty behind the numerous components of a biomechanical system may lead authors to simplify its components as well as the overall problem to avoid introducing complications into a time constrained project. Although several complex models can be found in literature, the ample majority of studies relies on very simplified representations of the biomechanical systems.

The simulation of more complex tasks, such as mastication coupled with the experimental measurement of the muscles' activation levels, gives a larger insight into the behavior of the overall system. Properties of the attachments of the disc, the passive response of the muscles and the ligaments of the mandible, can be scrutinized further by observing the constraints they impose on mandibular movements. The use of more complex models also helps to identify those parameters might require further experimental measurements.

With the current model, existing treatments can be studied in order to optimize them. Additionally, the proof-of-principle of a new treatment can be analyzed. Of particular interest, is the current search of criteria for the design of dental implant crowns, which involves the minimal movements of the teeth in the close-up range with respect to the jaws.

The transition into more complex models becomes easier as complex models themselves become more abundant in the literature, especially when their limitations are

made explicit, as it allows to compare the different available approaches.

Future work

Further development of this model will focus on the simulation of a more realistic power stroke of the chewing process. The model will be improved by implementing experimental data from simultaneous recordings of chewing forces, jaw movements, and the muscle's EMG activity which is under present investigations. Furthermore, the introduction of a destructible bolus that can more closely recreate the behavior of typical foods, will allow to study the significance of tooth mobility during comminution. The inferior part of the retrodiscal tissue as well as other attachments of the disc, will be modeled using solid elements.

Among the main objectives of future investigations will be the determination of the displacements of the posterior teeth during critical short-range interaction of the antagonists below 2 mm tooth separation. Thus, realistic kinetic data for occlusal freedom will be obtained, an indispensable step in avoiding interferences during mastication of different foods. This issue is of high importance particularly for CAD/CAM-produced, wear-free, all-ceramic dentures.

Bibliography

[1] G. A. Holzapfel, *Nolinear Solid Mechanics: A Continuum Approach for Engineering*. John Wiley & Sons, 2001.

[2] W. Ehlers, *Continuum Mechanics, Institut fuer Mechanik (Bauwesen), Lecture Notes of COMMAS Core Course*. Lehrstuhl II, Universitaet Stuttgart, 2009.

[3] B. D. Coleman and M. Gurtin, "Thermodynamics with internal state variables," *Journal of Chemical Physics*, vol. 47, no. 2, pp. 597–613, 1967.

[4] T. W. P. Korioth, D. P. Romilly, and A. G. Hannam, "Three-dimensional finite element stress analysis of the dentate human mandible," *American Journal of Physical Anthropology*, vol. 88, pp. 69–96, 1992.

[5] X. Ding, S. Liao, X. Zhu, H. Wang, and B. Zou, "Effect of orthotropic material on finite element modeling of completely dentate mandible," *Materials and Design*, vol. 84, pp. 144–153, 2015.

[6] A. Konyukhov and K. Schweizerhof, *Computational Contact Mechanics: Geometrically Exact Theory for Arbitrary Shaped Bodies*. Springer, 2013.

[7] Materialise, *Mimics 14.12 Reference guide*, 2011.

[8] Altair, *Hyperworks 12 Reference guide*, 2013.

[9] 3D Systems, *Geomagic Studio 12 Reference guide*, 2010.

[10] A. Hohmann, C. Kober, P. Young, C. Dorow, M. Geiger, A. Boryor, F. M. Sander, C. Sander, and F. G. Sander, "Influence of different modeling strategies for the periodontal ligament on finite element simulation results," *American Journal of Orthodontics and Dentofacial Orthopedics*, vol. 139, no. 6, pp. 775–783, 2011.

[11] V. P. Williard, B. Arzi, and K. A. Athanasiou, "The attachments of the temporomandibular joint disc: A biochemical and histological investigation," *Archives of Oral Biology*, vol. 57, no. 6, pp. 599–606, 2012.

[12] F. J. Harewood and P. McHugh, "Comparison of the implicit and explicit finite element methods using crystal plasticity," *Computational Materials Science*, vol. 39, pp. 481–494, 2007.

[13] J. Bonet and A. J. Burton, "A simple average nodal pressure tetrahedral element for incompressible dynamic explicit applications," *Communications in Numerical Methods in Engineering*, vol. 14, no. 5, pp. 437–449, 1998.

[14] D. T. Reilly and A. H. Burstein, "The elastic and ultimate properties of compact bone tissue," *Journal of Biomechanics*, vol. 8, no. 6, pp. 393–405, 1975.

[15] S. Lettry, B. Seedhorn, E. Berry, and M. Cuppone, "Quality assessment of the cortical bone of the human mandible," *Bone*, vol. 32, no. 1, pp. 35–44, 2010.

[16] J. L. Neil, T. C. Demos, J. L. Stone, and W. C. Hayes, "Tensile and compressive properties of vertebral trabecular bone," *Transactions of the annual meeting of the Orthopaedic Research Society*, vol. 8, p. 344, 1983.

[17] L. Røhl, E. Larsen, F. Linde, A. Odgaard, and J. Jørgensen, "Tensile and compressive properties of cancellous bone," *Journal of Biomechanics*, vol. 24, no. 12, pp. 1143–1149, 1991.

[18] G. Odin, C. Savoldelli, P.-O. Bouchard, and Y. Tillier, "Determination of young's modulus of mandibular bone using inverse analysis," *Medical Engineering and Physics*, vol. 32, no. 6, pp. 630–637, 2010.

[19] H. Abe, K. Hayashi, and M. Sato, *Data book on mechanical properties of living cells, ttissues, and organs*. Tokyo: Springer-Verlag, 1996.

[20] F. J. Arendts and C. Sigolotto, "Standard measurements, elasticity values and tensile strength behavior of the human mandible, a contribution to the biomechanics of the mandible - I," *Biomed Tech (Berl)*, vol. 34, no. 10, pp. 248–255, 1989.

[21] A. Kemper, C. McNally, E. Kennedy, S. Manoogian, and S. Duma, "The material properties of human tibia cortical bone in tension and compression: implacations for the tibia index," in *Proceedings of the 20th International Technical Conference on the Enhanced Safety of Vehicles*, (Lyon, France), pp. 07–0470, 2007.

[22] A. M. O'Mahony, J. L. Williams, J. O. Katz, and P. Spencer, "Anisotropic elastic properties of cancellous bone from a human edentulous mandible," *Clinical Oral Implants Research*, vol. 11, no. 5, pp. 415–421, 2000.

[23] E. B. W. Giesen, M. Ding, M. Dalstra, and T. M. G. J. van Eijden, "Mechanical properties of cancellous bone in the human mandibular condyle are anisotropic," *Journal of Biomechanics*, vol. 34, no. 6, pp. 799–803, 2001.

[24] C. H. Turner, S. C. Cowin, J. Y. Rho, R. B. Ashman, and J. C. Rice, "The fabric dependence of the orthotropic elastic constants of cancellous bone," *Journal of Biomechanics*, vol. 23, no. 6, pp. 549–561, 1990.

[25] E. Tanaka, D. Rodrigo, M. Tanaka, A. Kawaguchi, T. Shibazaki, and K. Tanne, "Stress analysis in the tmj during jaw opening by use of a three-dimensional finite element model based on magnetic resonance images," *International Journal of Oral and Maxillofacial Surgery*, vol. 30, no. 5, pp. 421–30, 2001.

[26] U. Lekholm and G. Zarb, *Tissue Integrated Prostheses: Osseointegration in Clinical Dentistry*, ch. Patient selection and preparation, pp. 199–209. Chicago: Quintessence Publishing, 1985.

[27] C. Kober, B. Erdmann, R. Sader, and H. F. Zeilhofer, "Simulation of the human mandible: Comparison of bone mineral density and stress/strain profiles due to masticatory muscles' traction," in *Proceedings of the 10th workshop "The Finite Element Method in Biomedical Engineering, Biomechanics and Related Fields"*, 2003.

[28] S. Wiliams, B. Wright, V. den Truong, C. Dauber, and C. Vinyard, "Mechanical properties of foods used in experimental studies of primate masticatory function," *American Journal of Primatology*, vol. 67, no. 3, pp. 329–346, 2005.

[29] G. S. Throckmorton, "Quantitative calculations of temporomandibular joint reaction forces - II. the importance of the direction of the jaw muscle forces.," *Journal of Biomechanics*, vol. 18, no. 6, pp. 453–461, 1985.

[30] J. H. Koolstra, T. M. G. J. van Eijden, W. A. Weijs, and M. Naeije, "A three-dimensional mathematical model of the human masticatory system predicting maximum possible bite forces," *Journal of Biomechanics*, vol. 21, no. 7, pp. 563–576, 1988.

[31] S. Rues, J. Lenz, J. Türp, K. Schweizerhof, and H. Schindler, "Muscle and joint forces under variable equilibrium states of the mandible," *Clinical Oral Investigations*, vol. 15, no. 5, pp. 737–747, 2011.

[32] H. Feneis, "Anatomy and physiology of the normal gingiva," *Deutsche Zähnarztliche Zeitschrift*, vol. 7, no. 8, pp. 467–476, 1952.

[33] A. Heimlich, "Tissue changes incident to tooth movement," *International Journal of Orthodontia and Dentistry for Children*, vol. 21, no. 11, pp. 1022–1026, 1935.

[34] A. Kristiansen and K. Heyeraas, "Micropuncture measurements of interstitial fluid pressure in the rat periodontal ligament," *Proceedings of the Finnish Dental Society*, vol. 85, no. 4-5, pp. 295–300, 1989.

[35] M. Bergomi, J. Cugnoni, H. Wiskott, P. Schneider, M. Stampanoni, J. Botsis, and U. Belser, "Three-dimensional morphometry of strained bovine periodontal ligament using synchrotron radiation-based tomography," *Journal of Anatomy*, vol. 217, no. 2, pp. 126–134, 2010.

[36] M. Nishihira, K. Yamamoto, Y. Sato, H. Ishikawa, and A. Natali, "Mechanics of periodontal ligament," in *Dental Biomechanics* (A. Natali, ed.), Taylor & Francis, 2003.

[37] T. Fill, R. Toogood, P. Major, and J. Carey, "Analytically determined mechanical properties of, and models for the periodontal ligament: Critical review of literature," *Journal of Biomechanics*, vol. 45, no. 1, pp. 9–16, 2012.

[38] H. Huang, W. Tang, B. Yan, and B. Wu, "Mechanical responses of periodontal ligament under a realistic orthodontic loading," *Procedia Engineering*, vol. 31, pp. 828–833, 2012.

[39] G. Parfitt, "Measurement of the physiological mobility of individual teeth in an axial direction," *Journal of Dental Research*, vol. 39, no. 3, pp. 608–618, 1960.

[40] J. Lenz, H. Schindler, and H. Pelka, *Die keramikverblendete NEM-Konuskrone*. Berlin: Quintessenz-Verlags-GmbH, 1992.

[41] A. Natali, P. Pavan, and C. Scarpa, "Numerical analysis of tooth mobility: formulation of a non-linear constitutive law for the periodontal ligament," *Dental Materials*, vol. 20, pp. 623–629, 2004.

[42] G. Limbert, J. Middleton, J. Laizans, M. Dobelis, and I. Knets, "A transversely isotropic hyperelastic constitutive model of the PDL. Analytical and computational aspects," *Computer Methods in Biomechanics and Biomedical Engineering*, vol. 6, pp. 337–345, 2003.

[43] G. Pietrzak, A. Curnier, J. Botsis, S. Scherrer, A. Wiskott, and U. Belser, "A nonlinear elastic model of the periodontal ligament and its numerical calibration for the study of tooth mobility," *Computer Methods in Biomechanics and Biomedical Engineering*, vol. 5, pp. 91–100, 2002.

[44] M.-Z. Su, H.-H. Chang, Y.-C. Chiang, J.-H. Cheng, L.-J. Fuh, C.-Y. Wang, and C.-P. Lin, "Modeling viscoelastic behavior of periodontal ligament with nonlinear finite element analysis," *Journal of Dental Sciences*, vol. 8, pp. 121–128, 2013.

[45] H. J. Schindler, J. Lenz, J. C. Türp, K. Schweizerhof, and S. Rues, "Small unilateral jaw gap variations: equilibrium changes, co-contractions and joint forces," *Journal of Oral Rehabilitation*, vol. 36, pp. 710–718, 2009.

[46] A. Natali, P. Pavan, E. Carniel, and C. Dorow, "A transversally isotropic elasto-damage constitutive model for the periodontal ligament," *Computer Methods in Biomechanics and Biomedical Engineering*, vol. 6, no. 5-6, pp. 329–336, 2003.

[47] E. L. Radin and I. L. Paul, "Response of joints to impact loading," *Arthritis and Rheumatism*, vol. 14, no. 3, pp. 356–362, 1971.

[48] V. Mow, W. Y. Chen, and F. H. Chen, "Structure and function of articular cartilage and meniscus," in *Basic Orthopaedic Biomechanics and Mechanobiology* (V. Mow and R. Huskes, eds.), Williams & Wilkins, 3rd ed., 2003.

[49] W. Hukins, R. Aspden, and Y. Yarker, "Fiber reinforcement and mechanical stability in articular cartilage," *Engineering in Medicine*, vol. 13, pp. 153–156, 1984.

[50] M. Tuominen, T. Kantimaa, P. Pirttiniemi, and A. Poikela, "Growth and type-II collagen expression in the glenoid fossa of the temporomandibular joint during altered loading: A study in the rat," *European Journal of Orthodontics*, vol. 18, pp. 3–9, 1996.

[51] J. W. Osborn, "The temporomandibular ligament and the articular eminence as constraints during jaw opening," *Journal of Oral Rehabilitation*, vol. 16, pp. 323–333, 1989.

[52] T. V. Macfarlane, A. S. Blinkhorn, R. Davies, J. Kincey, and H. V. Worthington, "Oro-facial pain in the community: prevalence and associated impact," *Community Dentistry and Oral Epidemiology*, vol. 30, pp. 52–60, 2002.

[53] J. C. Llodra-Calvo, M. Bravo-Pérez, and F. J. Cortés-Martinicorena, "Encuesta de salud oral en españa (2000)," *Revista Consejo Odontólogos Estomatólogos*, vol. 7, pp. 19–63, 2000.

[54] S. Ebrahim, L. Montoya, J. W. Busse, A. Carrasco-Labra, and G. H. Guyatt, "The effectiveness of splint therapy in patients with temporomandibular disorders : A systematic review and meta-analysis," *The Journal of the American Dental Association*, vol. 143, no. 8, pp. 847–857, 2012.

[55] J. Koolstra and T. van Eijden, "Combined finite-element and rigid-body analysis of human jaw joint dynamics," *Journal of Biomechanics*, vol. 38, no. 12, pp. 2431–2439, 2005.

[56] J. H. Koolstra, T. M. G. J. van Eijden, W. A. Weijs, and M. Naeije, "A three-dimensional mathematical model of the human masticatory system predicting maximum possible bite forces," *Journal of Biomechanics*, vol. 21, no. 7, pp. 563–576, 1988.

[57] J. Koolstra and T. van Eijden, "Consequences of viscoelastic behavior in the human temporomandibular joint disc," *Journal of Dental Research*, vol. 86, no. 12, pp. 1198–1202, 2007.

[58] A. P. del Palomar and M. Doblaré, "Finite element analysis of the temporomandibular joint during lateral excursions of the mandible," *Journal of Biomechanics*, vol. 39, no. 12, pp. 2153–2163, 2006.

[59] A. P. del Palomar and M. Doblaré, "The effect of collagen reinforcement in the behavior of the temporomandibular joint disc," *Journal of Biomechanics*, vol. 39, pp. 1075–1085, 2006.

[60] A. P. del Palomar and M. Doblaré, "An accurate simulation model of anteriorly displaced tmj discs with and without reduction," *Medical Engineering & Physics*, vol. 29, no. 2, pp. 216–226, 2007.

[61] T. Hansson and T. Öberg, "Arthrosis and deviation in form in the temporomandibular joint: A macroscopic study on a human autopsy material," *Acta Odontologica Scandinavica*, vol. 35, no. 1, pp. 167–874, 1977.

[62] T. Hansson, T. Oberg, G. E. Carlsson, and S. Kopp, "Thickness of the soft tissue layers and the articular disc in the temporomandibular joint," *Acta Odontologica Scandinavia*, vol. 35, pp. 77–83, 1977.

[63] E. Tanaka, K. Hanaoka, M. Tanaka, T. van Eijden, T. Iwabe, Y. Ishino, A. Sasaki, and K. Tanne, "Viscoelastic properties of bovine retrodiscal tissue under tensile stress-relaxation," *European Journal of Oral Sciences*, vol. 111, no. 6, pp. 518–522, 2003.

[64] M. Mezitis, G. Rallis, and N. Zachariades, "The normal range of mouth opening," *Journal of Oral and Maxillofacial Surgery*, vol. 47, no. 10, pp. 1028–1029, 1989.

[65] T. van Eijden, J. Korfage, and P. Brugman, "Architecture of the human jaw-closing and jaw-opening muscles," *The Anatomical Record*, vol. 248, pp. 464–474, 1997.

[66] J. C. Barbenel, "The biomechanics of the temporomandibular joint: A theoretical study," *Journal of Biomechanics*, vol. 5, pp. 251–256, 1972.

[67] J. W. Osborn and F. A. Baragar, "Predicted pattern of human muscle activity during clenching derived from a computer assisted model: Symmetric vertical bite forces," *Journal of Biomechanics*, vol. 18, no. 8, pp. 599–612, 1985.

[68] J. H. Koolstra and T. M. G. J. van Eijden, "Application and validation of a three-dimensional mathematical model of the human masticatory system in vivo," *Journal of Biomechanics*, vol. 25, no. 2, pp. 175–187, 1992.

[69] H. J. Schindler, S. Rues, J. C. Türp, K. Schweizerhof, and J. Lenz, "Jaw clenching: Muscle and joint forces, optimization strategies," *Journal of Dental Research*, vol. 86, no. 9, pp. 843–847, 2007.

[70] J. M. Winters and L. Stark, "Muscle models: What is gained and what is lost by varying model complexity," *Biological Cybernetics*, vol. 55, pp. 403–420, 1987.

[71] L. van Ruijven and W. Weijs, "A new model for calculating muscle forces from electromyograms," *European Journal of Applied Physiology*, vol. 61, no. 5, pp. 479–485, 1990.

[72] F. E. Zajac, "Muscle and tendon: Properties, models, scaling, and application to biomechanics and motor control," *Critical reviews in Biomedical Engineering*, vol. 17, no. 4, pp. 359–411, 1989.

[73] A. V. Hill, "The heat of shortening and the dynamic constants of muscle," *Proceedings of the Royal Society B Biological Sciences*, vol. 126, no. 843, pp. 136–195, 1938.

[74] A. V. Hill, "The mechanics of active muscle," *Proceedings of the Royal Society B Biological Sciences*, vol. 141, pp. 104–117, 1953.

[75] J. H. Koolstra and T. M. G. J. van Eijden, "Dynamics of the human masticatory muscles during a jaw open-close movement," *Journal of Biomechanics*, vol. 30, no. 9, pp. 883–889, 1997.

[76] C. C. Peck, G. Langenbach, and A. Hannam, "Dynamic simulation of muscle and articular properties during human wide jaw opening," *Archives of Oral Biology*, vol. 45, pp. 963–982, 2000.

[77] G. E. J. Langenbach and A. G. Hanamm, "The role of passive muscle tensions in a three-dimensional dynamic model of the human jaw," *Archives of Oral Biology*, vol. 44, pp. 557–573, 1999.

[78] O. Rhrle and A. J. Pullan, "Three-dimensional finite element modelling of muscle forces during mastication," *Journal of biomechanics*, vol. 40, no. 15, pp. 3363–3372, 2007.

[79] O. Rhrle, J. B. Davidson, and A. J. Pullan, "Bridging scales: a three-dimensional electomechanical finite element model of skeletal muscle," *SIAM Journal on Scientific Computing*, vol. 30, no. 6, pp. 2882–2904, 2008.

[80] A. F. Huxley and R. Niedergerke, "Structural changes in muscle during contraction: Interference microscopy of living muscle fibers," *Nature*, vol. 173, pp. 971–973, 1954.

[81] H. Huxley and J. Hanson, "Changes in the cross-striations of muscle during contraction and stretch and their structural interpretation," *Nature*, vol. 173, pp. 973–976, 1954.

[82] A. M. Gordon, A. F. Huxley, and F. J. Julian, "The variation in isometric tension with sarcomere length in vertebrate muscle fibres," *The Journal of Physiology*, vol. 184, pp. 170–192, 1966.

[83] S. M. Walker and G. R. Schrodt, "I segment lengths and thin filament periods in skeletal muscle fibers of the rhesus monkey and the human," *The Anatomical Record*, vol. 178, no. 1, pp. 63–81, 1974.

[84] W. Herzog, T. leonard, J. M. Renaud, J. Wallace, G. Chaki, and S. Bornemisza, "Force-length properties and functional demands of cat gastrocnemius, soleus, and plantaris muscles," *Journal of Biomechanics*, vol. 25, no. 11, pp. 1329–1335, 1992.

[85] E. Otten, "A myocybernetic model of the jaw system of the rat," *Journal of Neuroscience Methods*, vol. 21, pp. 287–302, 1987.

[86] B. M. Nigg and W. Herzog, *Biomechanics of the Musculo-skeletal System.* Wiley, 1994.

[87] W. Weijs and B. Hillen, "Cross-sectional areas and estimated intrinsic strength of the human jaw muscles," *Acta morphologica Neerlando-Scandinavica*, vol. 23, no. 3, pp. 267–274, 1985.

[88] Z. F. Muhl, A. F. Grimm, and P. L. Glick, "Physiologic and histologic measurements of the rabbit digastric muscle," *Archives of Oral Biology*, vol. 23, no. 12, pp. 1051–1059, 1978.

[89] R. D. Woittiez, P. A. Huijing, and R. H. Rozendal, "Influence of muscle architecture on the length-force diagram: A model and its verification," *Pflügers Archiv*, vol. 397, no. 1, pp. 73–74, 1983.

[90] C. N. Maganaris, "Force-length characteristics of in vivo human skeletal muscle," *Acta Physiologica Scandinavica*, vol. 172, pp. 279–285, 2001.

[91] I. E. Brown, E. J. Cheng, and G. E. Loeb, "Measured and momodel properties of mammalian skeletal muscle. II. the eeffect of stimulus frequency on force-length and force-velocity relationships," *Journal of Muscle Research and Cell Motility*, vol. 20, pp. 627–643, 1999.

[92] M. C. Bortoluzzi, J. Traebert, R. Lasta, T. D. Rosa, D. L. Capella, and A. A. Presta, "Tooth loss, chewing ability and quality of life," *Contemporary Clinical Dentistry*, vol. 3, no. 4, pp. 393–397, 2012.

[93] C. Salvoldelli, P. Bouchard, R. Loudad, P. Baque, and Y. Tillier, "Stress distribution in the temporo-mandibular joint discs during jaw closing: A high-resolution three-dimensional finite-element model analysis," *Surgical and Radiologic Anatomy*, vol. 34, pp. 405–413, 2012.

[94] M. Hirose, E. Tanaka, M. Tanaka, R. Fujita, Y. Kuroda, E. Yamano, T. M. van Eijden, and K. Tanne, "Three-dimensional finite-element model of the human temporomandibular joint disc during prolonged clenching," *European Journal of Oral Sciences*, vol. 114, pp. 441–448, 2006.

[95] M. Commisso, J. Martinez-Reina, J. Ojeda, and J. Mayo, "Finite element analysis of the human mastication cycle," *Journal of the Mechanical Behavior of Biomedical Materials*, vol. 41, pp. 23–35, 2015.

[96] R. E. Youssef, G. S. Throckmorton, E. I. Ellis, and D. P. Sinn, "Comparison of habitual masticatory activity before and after orthognathic surgery," *Journal of Oral and Maxillofacial Surgery*, vol. 55, pp. 699–707, 1997.

[97] P. H. Buschang, H. Hayasaki, and G. S. Throckmorton, "Quantification of human chewing-cycle kinematics," *Archives of Oral Biology*, vol. 45, pp. 461–474, 2000.

[98] C. H. Gibbs, N. A. Wickwire, A. P. Jacobson, H. C. Lundeen, P. E. Mahan, and S. M. Lupkiewicz, "Comparison of typical chewing patterns in normal children and adults," *American Dental Association*, vol. 105, pp. 33–42, 1982.

[99] R. Bhatka, G. S. Throckmorton, A. M. Wintergerst, B. Hutchins, and P. Buschang, "Bolus size and unilateral chewing cycle kinematics," *Archives of Oral Biology*, vol. 49, pp. 559–566, 2004.

[100] M. G. Piancino, P. Bracco, T. Vallelonga, A. Merlo, and D. Farina, "Effect of bolus hardness on the chewing pattern and activation of masticatory muscles in subjects with normal dental occlusion," *Journal of Electromyography and Kinesiology*, vol. 18, pp. 931–937, 2008.

[101] C. Lepley, G. Throckmorton, S. Parker, and P. H. Buschang, "Masticatory performance and chewing cycle kinematics — are they related?," *The Angle Orthodontist*, vol. 80, pp. 295–301, 2010.

[102] H. J. Schindler, E. Stengel, and W. E. L. Spiess, "Feedback control during mastication of solid food textures — a clinical- experimental study," *The journal of prosthetic dentistry*, vol. 80, no. 3, pp. 330–336, 1998.

[103] S. Rues, J. Lenz, J. C. Türp, K. Schweizerhof, and H. J. Schindler, "Forces and motor control mechanisms during biting in a realistically balanced experimental occlusion," *Archives of Oral Biology*, vol. 53, pp. 1119–1128, 2008.

[104] N. Yoshida, P. G. Jost-Brinkmann, and Y. Yamada, "Initial tooth movement under extraoral force and considerations for controlled molar movement," *The Angle Orthodontist*, vol. 65, pp. 199–208, 1995.